Characteristics of shear localization in brittle-ductile deformation of rocks: An experimental study

A thesis submitted for the degree of

Doctor of Philosophy (Science) of

Jadavpur University

By

Manaska Mukhopadhyay

Department of Geological Sciences
Jadavpur University
Kolkata-700032, India

September
2022

যাদবপুর বিশ্ববিদ্যালয়
কলকাতা - ৭০০০৩২, ভারত

JADAVPUR UNIVERSITY
KOLKATA-700 032, INDIA

FACULTY OF SCIENCE : DEPARTMENT OF GEOLOGICAL SCIENCES

CERTIFICATE FROM THE SUPERVISOR

This is to certify that the thesis entitled "**Characteristics of shear localization in brittle-ductile deformation of rocks: An experimental study**" submitted by **Sri. Manaska Mukhopadhyay** who got his name registered on **08/10/2015** for the award of **Ph. D. (Science)** degree of Jadavpur University, is absolutely based upon his own work under the supervision of **Professor Nibir Mandal** and that neither this thesis nor any part of it has been submitted for either any degree / diploma or any other academic award anywhere before.

.....

N. Mandal 27/09/2022

(Signature of the Supervisor(s) date with official seal)

NIBIR MANDAL
Professor
Dept. of Geological Sciences
Jadavpur University
Kolkata - 700 032

Website : www.jaduniv.edu.in
E-mail : hod.geology@jadavpuruniversity.in

HOD Phone : 033 2457 2719
Office : 033 2457 2268

Dedicated to….

Ma, Baba and Chhotka

ACKNOWLEDGMENT

I take this opportunity to express my gratitude to everyone who have been a constant support for me throughout my doctoral research tenure. I am thankful for aspiring guidance, constructive criticism and ever friendly advice and encouragement during this period.

First of all, I want to sincerely acknowledge my supervisor Professor Nibir Mandal, for the constant support, encouragement, and providing an academically rich environment for carrying out my research work. I am grateful to him for his valuable and illuminating discussions and guidance over several occasions throughout the research period. More than everything, I remain indebted to him for enriching me with his precious scientific ideas, opinions and suggestions in various research problems in this doctoral work.

I am grateful to Professor Ashok Arya, BARC, Mumbai for his support, encouragement and the guidance he provided as a Co-PI in my project. I specially thank Board of Research for Nuclear Sciences (BRNS) for the funding and comprehensive support.

My gratitude to the several reviewers who improved this study through their insightful reviews of my research communications.

My sincere thanks goes to Mr. Pradip Kr. Kar and Milan Mondal (S. K. Enterprise) for their full and continued support in terms of planning, designing, implementing and servicing of the rock deformation machines in our High Pressure and Temperature Laboratory. Their enthusiasm and energy has always put an additional motivation in working with existing machines, and planning new experimental designs.

I enjoy and admire all the enlightening and joyous moments with my colleagues at HPT Lab. I am lucky to get help, guidance and support from seniors like Dr. Koustav Chatterjee, Dr. Sujoy Dasgupta, Dr. Amiya Baruah, Dr. Urmi Dutta at the beginning of my doctoral period. Dr. Pratik Das, Anjan Chaudhury, Dr. Nilkamal Barai has offered me help and advice every time I asked them for. I must specially mention Dr. Puspendu Saha for his generous support and valuable inputs, both academically and personally. It has been a memorable and great pleasure for me to share my laboratory activities and academic accomplishments with my other laboratory colleagues Dr. Shamik Sarkar, Sudip Kumar Mandal, Dr. Giridas Maiti, Dr. Ritabrata Dasgupta, Dip Ghosh, Joyjeet Sen, Nandan Roy, Arnab Roy, Pramit Chatterjee, Ayan Patsa and Gouri Sankar Mukherjee. I specially thank Dip, Arnab and Pramit for their support and co-operation in writing and completing this thesis work.

I sincerely thank Department of Geological Sciences, Jadavpur University for providing all the infrastructural facilities for carrying out my research work.

Finally, I am forever indebted to my parents and my extended family members for their wholesome support and encouragement.

Manaska Mukhopadhyay

TABLE OF CONTENTS

Abstract

Most of the crustal rocks are mechanically heterogeneous due to various types of inherent micro- to macro-scale heterogeneities, e.g., compositional or physical flaws in the form of hard objects, weak zones, voids or pre-existing fractures. Such heterogeneities can greatly influence the modes of brittle as well as ductile deformations under geological conditions. Using laboratory experiments a part of this thesis aims to explore their role in controlling the mechanism of shear localization in elasto-plastic rocks. Commercially available polymers: polymethylmethacrylate (PMMA) and polystyrene (PS) were used as rock analogues (elasto-plastic rheology) in the experiments. Both PMMA and PS show a characteristic property of plastic strain induced permanent optical birefringence, which has been utilized to delineate continuum scale high-strain zones in models. Compression tests were performed on models with desired heterogeneities under plane strain conditions to systematically investigate the problem of heterogeneity-controlled shear band formation. It is demonstrated from PS model experiments that a transition in the plastic creep mechanism gives rise to a spectrum of shear band structures: homogenous to narrow sharp high-strain zones. This study identifies weak mechanical flaws as a crucial parameter to govern the transition in the mode of deformation localization. Homogenous models, without any pre-existing flaws produced uniformly distributed narrow shear bands (NB), symmetrically oriented at ~41°-44° to the compression axis. On the other hand, heterogeneous models produce a completely different band pattern, forming localized composite bands (CBs), with a core of densely packed NBs (at ~46°-49° with compression axis), flanked by transition zones on either side. In addition, decreasing the strain rate from $\dot{\varepsilon}$ (3×10^{-5} sec^{-1} to 2×10^{-5} sec^{-1}) is found to transform the CBs to well-defined HBs, with a homogenously sheared core bounded by a narrow gradational zone shear localisation. The experimental results are substantiated by numerical simulations to propose the possible mechanism of the shear band growth. PMMA model experiments also showed similar influence of mechanical flaws (incipient cracks) in deformation localization. Their initial geometry (orientation and crack length) critically controls the brittle – ductile transition of deformation localization around them.

Another major direction of this thesis deals with an in-depth topological study of irregular slip surfaces produced by shear localization in brittle-ductile rocks. Field observations in the Singhbhum Shear Zone revealed a type of slickensides in deformed quartzites, characterized by the absence of any hard asperity, which rules out the possibility of mechanical wearing as a possible mechanism of their formation. This thesis reports this unique type of slickensides through extensive field, and analogue experimental study (by sand-talc / talc models) and explores the factors controlling the shear fracture roughness. Shear fractures, in pure talc models, produced by plastic yielding display strong linear roughness, which become more prominent with increasing fracture orientation (θ) to the compression direction (θ = 30° - 60°). A new computational technique, based on optical image analysis, has been developed to map the surface geometry from field casts and experimental models. From 1D fractal dimension calculations, it is demonstrated ΔD (difference in 1D fractal dimension across and along the slip direction) can be used as an

effective mathematical parameter to quantify shear/fault surface roughness. Estimated ΔD from slickensides in naturally deformed quartzites and equivalent laboratory models is found to range from 0.38 to 0.95. Based on field observations, analogue experiments and numerical model simulations, mechanical wave instabilities at the soft interface between two walls is proposed as a potential mechanism for roughness generation in the form of linear irregularities.

Geodetic and seismological evidences suggest that, during shear failure the slip is not quite homogenous, rather it is quite complex, spatially as well as temporally. Such heterogeneous slip distributions have a serious implication in earthquake seismology as well as heterogeneous movements in a single event of faulting, as widely reported in the recent literature. This doctoral work provides a geometrical analysis of slip heterogeneity on fault surfaces. Two distinct roughness domains were identified on sheared quartzites from Singhbhum Shear Zone, marked by strong and weak or no roughness anisotropy. Using analogue laboratory experiments on brittle-ductile models under pure shear condition, the present study shows that shear localization on fault surfaces is partitioned into two domains: i) *slip zones*, defined by slip-parallel lineations and, ii) discrete domains showing little or no slip (called *stuck zones*). The two zones occur with varying geometrical patterns on shear surfaces. A series of analogue laboratory experiments was performed to find the factors governing slip versus stuck zone growth during a fault movement. The experiments indicate the initial fault inclination (θ) to the principal compression direction as one of the crucial factors in dictating their competitive growth. In general, increasing θ facilities the slip zones to dominate over the stuck zones. A fractal analysis is presented to show the use of ΔD in delineating these two roughness domains with contrasting anisotropy, slip zones with slip-parallel linear irregularities (strongly anisotropic), whereas stuck zones devoid of such linearity in their roughness (isotropic). Consequently, ΔD yields the lowest value (0.0036) in stuck zones, and the highest value (0.1735) in the slip zones. The field analysis is supported by experimental data (ΔD = 0.0024 and 0.2118 in stuck and slip zones, respectively).

The thesis finally draws conclusions on the following studies: i) effects of inherent mechanical heterogeneities on the mechanism of shear band formation; ii) control of applied strain rates in the transition of shear band mechanisms; iii) topological characterization of shear fractures in naturally deformed massive quartzites in a ductile shear zone, providing new explanation for the origin of non-abrasive slickenlines; and iv) dependence of shear surface roughness heterogeneities, controlled by slip versus stuck zone growth as a function of the initial shear surface orientation; and v) effectiveness of ΔD as a measure of the degree of anisotropy in surface roughness.

Chapter 1
Introduction

1.1. Deformation of rocks: standard rheological models

Understanding the mechanical responses of rock bodies to a system of forces is the key step to model or theorize the geological processes in tectonic belts. Direct observations as well as extrapolated geological evidences suggest that the responses occur in two ways: rigid body motion and non-rigid body deformation. Rigid body movements generally do not produce any internal structural features, but play an important role in a range of tectonic processes, such faulting, lithospheric plate motion, where they involve movement by translation or rotation. This kind of kinematics in rock bodies, translational or rotational faulting, porphyroblast rotation on grain scale to plate motion does not involve any internal deformations. However, rocks are generally deformable under most of the geological conditions and such deformation processes are extremely complex due to their rheological attributes. Understanding the factors controlling the rheology of rocks as well as minerals under varied geological environments has thus emerged a challenging area of research in solid earth sciences.

In 1660 Robert Hooke found that in many elastic solids, the applied stress is proportional to the given strain. Based on this observation, Hooke's law states a linear relation between stress (σ_{ij}) and strain (ε_{ij}) tensors at a point in a continuum,

$$\sigma_{ij} = C_{ijkl}\varepsilon_{kl} \qquad (1.1)$$

where C_{ijkl} represents the elastic constant tensor of rank 4, consisting of 81 components. Equation (1.1) indicates that the elastic rheology of a solid rock or a mineral can be extremely complex due

to their anisotropic elastic properties. For example, the elasticity of a foliated rock is rheologically more complex than a massive granite, as the presence of foliation introduces a mechanical anisotropy in the rock. For isotropic solids, Eq. (1.1) simplifies to,

$$\sigma_{ij} = \lambda\theta\delta_{ij} + 2\mu\varepsilon_{ij}, \qquad (1.2)$$

where θ is the volume strain (dilation). δ_{ij} is called Kroncker delta; δ_{ij}= 1 when i = j and 0 when i ≠ j. λ, μ are the most important rheological quantities, known Lame's parameters to describe the elasticity of an isotropic solid. Crustal rocks behave like an ideal Hookean elastic solid in a limited range of geological conditions, such as high strain rates, and low pressure and temperatures (near-surface conditions). It is a well-known fact that geological deformations generally occur on large time scales, in the order of millions of years at elevated pressures and temperatures. Such long-time scale deformations no longer occur in an elastic regime, but in a viscous flow regime. Consequently, a range of viscous rheological models have been used to study deep-crustal tectonic processes. According to the classical theory of Newton, the stress tensor in a flowing viscous fluid is linearly proportional to the strain rate tensor. Considering a rheologically isotropic viscous fluid, the relation can be expressed by

$$\sigma_{ij} = -p\delta_{ij} - \frac{2}{3}\eta\dot{\theta}\delta_{ij} + 2\eta\dot{\varepsilon}_{ij} \qquad (1.3)$$

p is the hydrostatic pressure; $\dot{\theta}$ is the volume strain rate and η the coefficient of viscosity. Fluids obeying Eq. (1.3) are described Newtonian fluids. This equation is applicable for Stokes fluids. Saint Venant showed that many solids with continued deformation reach a critical state when they no longer strain elastically, but begin to deform permanently in a steady state stress condition. This property of solids beyond the elastic range is called *plastic rheology*. The critical stress at which such permanent deformation starts to occur is termed as the yield stress.

Earth materials hardly behave like an ideal elastic (time independent) solid or a Newtonian viscous (time dependent) fluid or a perfectly plastic solid. Geological evidences suggest their complex rheological responses. To describe their non-deal behavior, geoscientists use various complex linear rheological models developed by combining the three types of rheological attributes, visualized in terms of mechanical models: a helical spring to represent the perfectly

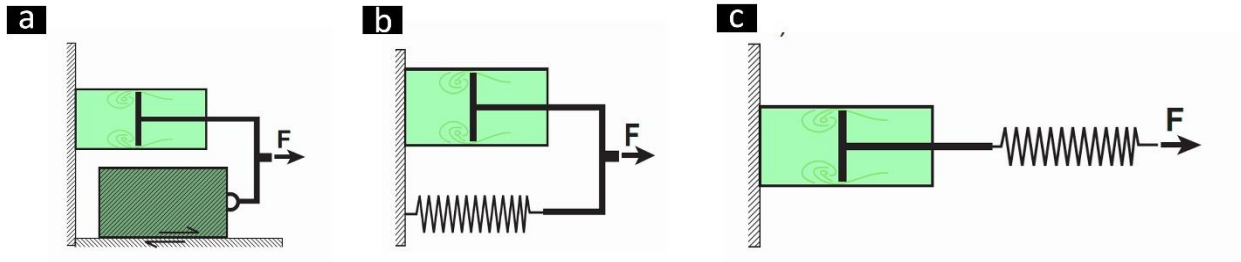

Figure 1.1. Schematic representations of various combination of rheological models of, a) Bingham; b) Kelvin ; and c) Maxwell material

elastic rheology, a dashpot to linear Newtonian rheology and a friction block on a horizontal surface to define the threshold condition of a perfectly plastic strain. Their different combinations simulate different rheological characteristics of materials. For example, a mechanical model with a friction block and a dashpot in series represents Bingham rheology (Fig. 1.1.a). Another rheological class, called Kelvin (or Voigt) rheology, comprises a spring in parallel combination with a dashpot (Fig 1.1.b). Unlike an ideal elastic solid, Kelvin substances undergo elastic deformations as a function of time. Interestingly, most of the rocks, especially porous materials and soils show Kelvin behavior, as reflected in attenuation of elastic waves during earthquake events. Maxwell (elastico-viscous) rheology is another complex rheology, represented by combing a spring and a dashpot in series (Fig 1.1.c). It is evident that the Earth as a whole follow this rheological behavior, where it responds elastically on short time scales, whereas viscously on long time scales. For example, seismic waves propagate through the mantle, implying its elastic state,

i.e. solid state on a time scale of few seconds. The same mantle takes part in heat flow by a convection process that indicates its fluid state on million years' time scales. Figure 1.2. shows a

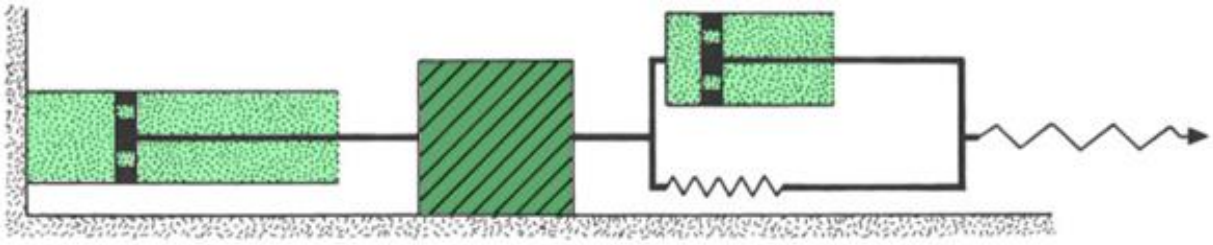

Figure 1.2. Mechanical model of a complex substance. The model consists of an elastic element, a Kelvin element, a friction block and a viscous element

generalized rheological scheme represented by a dashpot, a friction block, a Kelvin element and a spring.

A direction of rheological studies use rock deformations experiments at elevated pressures and temperatures, replicating a deep-earth environment. Earlier workers demonstrated from rock experiments that rocks generally undergo a rheological transition from brittle to ductile under high confining pressures (Handin & Hager, 1957; Paterson, 1958; Robertson, 1955). Similarly, some studies also reported the same rheological transition with increasing temperature (Griggs et al., 1960; Handin & Fairbairn, 1955; Handin & Hager, 1958). The transition from brittle to ductile is not usually sharp, rather takes place on a spectrum of rheological change, ranging from brittle to ductile through intermediate transitional zone. Most of the earlier studies mentioned above used rocks like marbles or limestones, and found out that at low confining pressure these behave as brittle material, which changes to ductile at higher confining pressures, even at room temperature.

1.2. Deformation localization

Progressive deformations in crustal rocks often produce linear zones of large finite strain strains, as compared to their host, which are described as *shear zones*. Earlier studies used the term, shear zones to mean strain localization entirely in the ductile regime. However, Ramsay (1980) used the term to deformation localization along linear zones in both brittle (sharp fractures and faults) and ductile (folds and foliation) regimes. He subdivided shear zones in three types: 1. *brittle shear zone*, (strain localization entirely by fracturing; 2. *brittle-ductile shear zone* (strain localization by a combination of both brittle fracture and ductile deformation); and, 3. *ductile shear zone* (strain localization by continuous ductile deformation without macroscopic fracturing).

1.2.1 Shear localisation in solids under compression

It is quite common in solids, including metals, polymers, granular aggregates and natural rocks, that an essentially gradual and smoothly varying deformation changes to a highly localized pattern, commonly known as *shear bands*, on sufficient loading in the plastic field. From

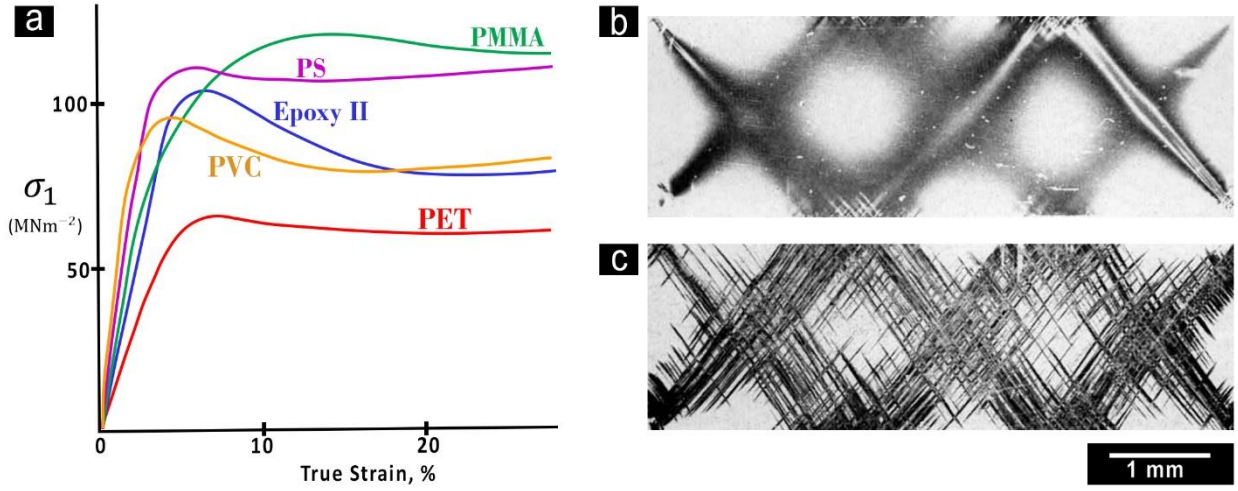

Figure 1.3. a) Stress-strain curves of polymer samples under plain strain compression (*after Bowden and Jukes (1972*) ; b & c) Diffused and narrow shear bands in PS model at elevated and lowered temperature respectively, in pure shear experiments (*after Bowden and Raha 1970*)

laboratory experiments with polymers (e.g., PMMA, PS, Epoxy II, PVC and PET) Bowden and Jukes (1972) claimed that solids can suffer viscoelastic strains (~ upto 10%) before they reach the yield point. Their experiments clearly revealed that plastic strains localize preferentially along bands oriented at angle more than 45° to the compression direction. The stress strain curves in these plastic creep experiment showed a maximum stress rise (the upper yield stress) followed by a strain softening, and further by a slow strain hardening at larger strains (Fig.1.3.a). Interestingly, several workers from rock deformation experiments reported similar creep behavior for different types of rocks, such as marble (Barnhoorn et al., 2004; Paterson, 1958; Schmid et al., 1980). On thin sections the deformed polymers revealed shear bands with varying strain distribution patterns. PMMA and PVC models produced shear bands with diffused boundaries (i.e., gradational strain variation); in contrast, PS and PET produced thin bands with sharp boundaries (abrupt strain variation). The two types of bands: diffuse and sharp formed at different inclinations to the compression direction. Bowden and Raha (1970), in their experiments on PS, also showed a

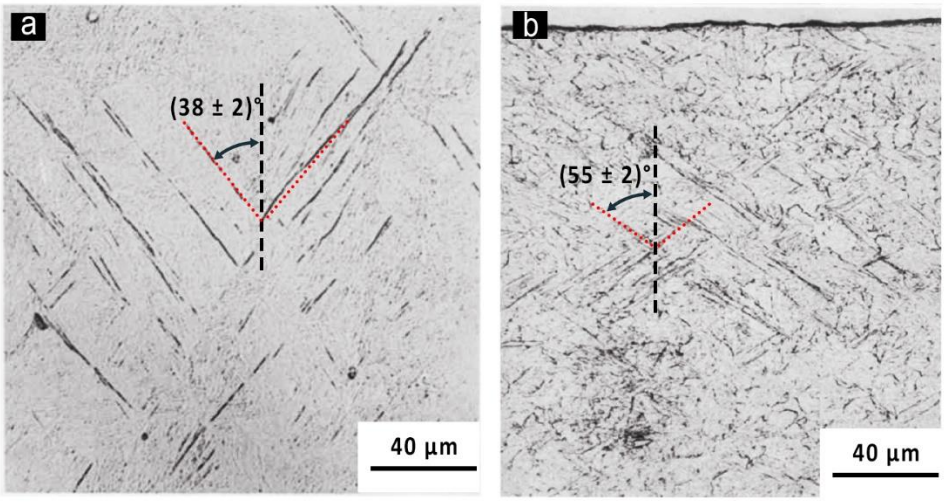

Figure 1.4. a) Aged Maraging Steel deformed under plain strain tension, with a finite strain of 0.057. Note that narrow shear bands generate with an angle of (38 ± 2)° with the tension axis (vertical); b) Aged Maraging Steel deformed under plain strain compression, with a finite strain of 0.054. Note that narrow shear bands generate with an angle of (55 ± 2)° with the compression axis (vertical) (*after Anand and Spietzig, 1980*)

transition from sharp narrow to diffused thick shear bands at elevated temperatures (65°C) and reduced strain rates (4 x $10^{-3}$$sec^{-1}$). The shear bands formed at angles more than 45° to the principal compression direction. Their dihedral angle was not constant in different experiments. To account for such a varying dihedral angle, Bowden and Jukes (1972) used a simple equation:

$$tan\,\acute{\alpha} = tan\,\alpha\,\frac{(1+\varepsilon_1)}{(1+\varepsilon_2)} \qquad (1.1)$$

where, α is the angle between the compression direction and shear plane normal in the relaxed specimen, ά is the value of α when shear bands form at yield point, ε_1 and ε_2 are the nominal elastic strains. Their experimental analyses revealed a dihedral angle of ~98°, which is considerably higher than those in other polymers. Anand and Spitzig (1980) extensively studied shear band formation in ultrahigh strength maraging steel under tension as well as compression. Their experiments produced sharp conjugate bands, symmetrically oriented to the stress direction, showing a dihedral angle of ~79^o. In their experiments deformations localized along narrow shear bands both in tension and compression tests formed at a strain just beyond a diffused necking (for tension tests). Their theory predicts the initiation of shear bands as a bifurcation of deformation in an otherwise homogenous continuum, deforming homogenously and as a rate-independent elasto-plastic body. Unlike the polymers (PMMA and PVC, which produced diffused bands), the steel samples produced sharper bands ~1-2 μm wide. They also noted that the angle between the shear bands to the tensile axis is (38 ± 2)°, which increases to (55 ± 2)° (with the compression axis) in case of steel models subject to compressive stress. Interestingly, the shear bands tend to increase their inclination with the principal compression direction; however, the narrow shear bands in deformed steel do not change their inclination with increasing strain. Progressive model deformations show that the shear bands multiply with increasing bulk deformation, and at the same

time they grow in length. The material was found to be capable of sustaining considerable deformation after the initiation of shear bands before the final failure. In a subsequent study, Anand and Spietzig (1982) theoretically predicted the angle between shear band and compression axis (θ) for different materials. For theoretical analysis, starting from an undeformed state, the model was subjected to a biaxial stress. They provided a constitutive equation for θ:

$$\theta = \pm \arctan \sqrt[4]{\frac{(1+\mu)(1+\beta)\left(1-\frac{\tau}{G}\right)}{(1-\mu)(1-\beta)\left(1+\frac{\tau}{G}\right)}} \qquad (1.2)$$

where, β is a shear induced dilatancy factor, τ is shear stress, G is instantaneous shear modulus and μ is a pressure sensitivity parameter. The study provided a comparison of the orientation of the shear bands with respect to the principal compression direction for maraging steel, polystyrene and Leighton Buzzard Sand with the experimental observations.

Material	**Observed**	**Predicted**
Maraging Steel	~ ±55°	~ ±48°
Polystyrene	~ ±40°	~ ±41°
Leighton Buzzard Sand	~ ±25°	~ ±25°

Table 1.1. Comparison of experimentally observed and theoretically predicted shear band orientation with respect to the principal compression direction in plain strain pure shear experiments with different materials. (*after Anand, 1984*)

The results of the granular Leighton Buzzard Sand were found to be almost similar to the results of some recent studies using GRAM (Granular Rock Analogue Materials), which is also a granular aggregate of rock analogue materials (Tran et al., 2019, 2020). They also showed from their pure

compression experiments that the principal shear bands and their secondary bands make angles of ~32°-34° with the compression axis.

1.2.2 Shear localization in simple shear

Logan et al. (1979) reported a set of shear bands from experimental shear zones in the brittle field. The band structures had constant orientations, with slight variations in their proportion

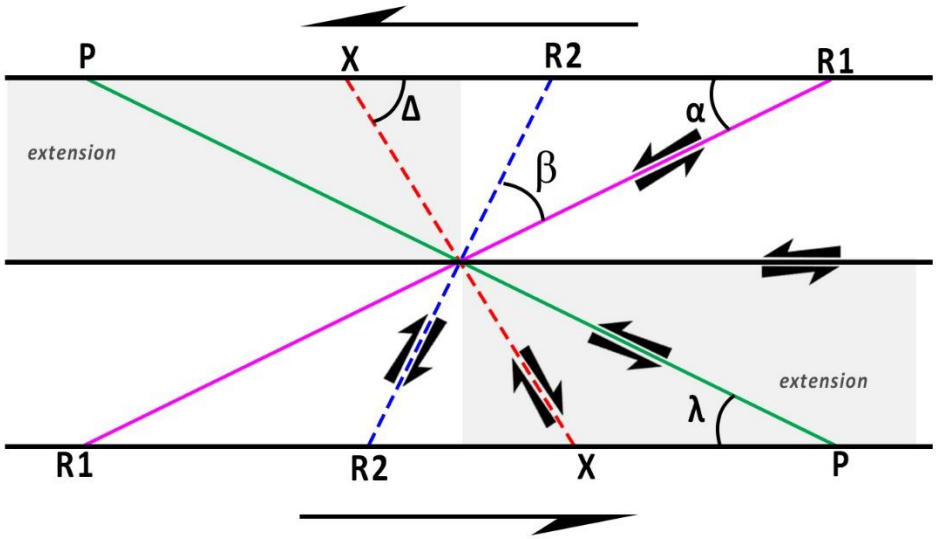

Figure 1.5. Fracture array and geometrical relationships of shear bands formed in a brittle shear zone. The shear sense is denoted by the arrows (after *Logan et aI., 1979*).

and orientations, depending on the confining pressure, pore pressure, displacement rate, gouge thickness and materials. The bands occur in four prominent sets (brittle shear bands): Riedel bands (R), thrust-type band (P) and shear-parallel bands (Y or D). The Riedel generally occurs as conjugate sets oriented at low and high angles to the shear direction, designated as R1 and R2, respectively (Fig 1.5). Both R1 and P shear bands have the same sense of shear (synthetic shear), which is similar to that of the regional deformation or the shear sense in the shear zone boundary.

Mandl (1988) suggested that, there is a zone of local compression between two overlapping R shears. As a result, a corresponding extensional zones also exist at high angle to it. Another synthetic shear is the Y or D band. Sometimes, these bands can coalesce with one another to form their anastomosing network, leaving undeformed materials in between them. Other workers also reported similar band structures from experimental studies using a wide range of boundary conditions (Rutter et al., 1986 ; Shimamoto, 1986). Many workers performed shear box experiments with clay cakes (Reidel, 1929; Morgenstern and Tchalenko, 1967), sand and other granular materials (Mandl et al., 1977; Mandl, 1988) and in rock models (Bartlett et al., 1981). A number of classical studies on natural fault zones also documented similar type of brittle shear band patterns (Dengo, 1982; Rutter et al., 1986; Chester and Logan, 1987).

Similar to brittle shear zones, ductile shear zones show a long narrow zone of intense strain localisation causing predominantly ductile deformation, which eventually involve remarkable grain size reduction and formation of lineated and well-banded rocks. The grain size reduction is often reflected from mylonites, a fine-grained rock produced by shearing in ductile shear zones. Ductile shear zones can further be classified into two types based on the deformation of the walls: 1) Discrete shear zones, where shear zones cut across wall rocks otherwise undeformed on both sides, and 2). shear zones, where one or both walls have suffered penetrative deformation. Although in true sense, the term “ductile” means a continuous deformation without any macroscopic fracturing, many workers have reported that ductile shear zones may also develop similar kinds of fabric (shear bands), e.g., R1, R2 and P similar to the brittle shear zones (Finch et al., 2014; Haakon Fossen & Cavalcante, 2017; Fusseis et al., 2006; Fusseis & Handy, 2008; Mukherjee & Koyi, 2010; Paterson & Wong, 2005). C-bands, which are similar to Y (or D) bands for brittle shear zones, form parallel to the shear direction. Within anastomosing structure of a

mylonitic shear zone, S-C fabrics are often found as major shear bands, where c-bands remain parallel and maintain a constant orientation, whereas the S bands marks the foliation and rotates with progressive shearing so that the angle between the S-C fabric set gradually gets reduced (Ramsay and Graham, 1970). On further shearing, as the ultramylonite stage is reached, the C- and S- fabrics become somewhat parallel and their individual identity is lost. Berthe et al. (1979) advocated that even if their identity is lost at the later stages, these two sets of shear bands are present even in the lesser deformed rocks, where they form at an angle of around 45° to each other. This proves that the deformational bands are non-coaxial and the acute angle between the set points towards the shear sense. In the subsequent chapters we will see some of the most common brittle and ductile deformation localisation structures related to shear zones.

Permeability in rock matrix at the interior of the Earth, mainly in the lower crust to upper mantle, can be modified by the formation of shear bands due to stress enhancements, leading to migration of melts or fluids. This relationship between fluid or melt segregation and migration and shear band localisation due to stress build up has a substantial impact on dynamics of subduction zones, lower crustal shear zones, plumes and MORs. The transport of melt to the surface occurs via a range of mechanisms from percolation through channels in permeable viscous rock (Kelemen & Dick, 1995) to movement along pre-existing open fissures or fractures (Rubin et al., 1999; Suhr, 1999). Holtzman et al., (2003) used several combinations of olivine, anorthite, chromite and MORB as sample materials, and deformed in a simple shear condition. They noticed a wide range of melt-distribution pattern as a direct manifestation of shear band localisation in the deformed samples. On one hand, the shear deformation redistributed the haphazardly placed melt-filled pockets into a much stronger preferred orientation, though on a grain scale. On the other hand, the melts are completely separated into melt-rich bands with the same preferred orientation, but much

larger in size, more than grain scale and is oriented at ~20-25° to the shear plane. In their experiments they proposed that shear localisation led to fewer larger bands and numerous smaller bands in the system. Benjamin K. Holtzman et al., (2005) further proposed that under shear deformation, melt bands generate a bimodal distribution pattern of angles (0°-30°). According to their study, the larger and wider bands localize at angles significantly higher than the narrower bands.

1.3. Modes of deformations in brittle regimes

1.3.1 Fracture

The most important manifestation of brittle failure is macroscopic fracturing of materials, forming planar or subplanar discontinuities that can develop in response to either external or internal stresses. Fractures are primarily of two types: i. tensile fractures (Mode I), and ii. shear fractures (Mode II and III). Mode II fracture is a sliding mode, where the slip is perpendicular to the fracture edge. There is another type of sliding mode, called tearing mode (Mode III), where shear fractures have slip parallel to the fracture tip line. In natural systems as well as in experiments, fractures often evolve in a complex manner, involving both slide and separation kinematics, termed as a hybrid mode. Tensile fractures ideally generate perpendicular to the principal tensile stress axis (minimum stress axis: σ_3). In nature, joints and fissures are the most common examples of tensile fractures (Mode 1), and they generally in near-surface low pressure and temperature environments. Shear fractures (Mode 2 or 3) in crustal rocks show fracture-parallel slip and generates ideally at around 20°-30° to the principal compressive stress, often in conjugate sets.

1.3.2. Fault Damage Zones

In recent years the brittle-tectonics research witnessed growing interests in studying the internal architectures of fault systems, described as fault damage zones (FDZ). Several studies focus upon the structural aspects of FDZs with an objective to understand their growth mechanism (Segall and Pollard, 1983; Granier, 1985; Cruikshank et al., 1991; Kim et al., 2000, 200). A FDZ is a tabular fault parallel zone showing intense fracturing to form a fracture population (Cowie and Scholz, 1992 ; McGrath and Davison, 1995). Their studies not only give us valuable information about fault propagation and growth (McGrath and Davison, 1995 ; Vermilye and Scholz, 1999; Kim et al., 2001 a), but also act as effective permeable zones to drive a wide range of geological processes, such as fluid flows (Sibson, 1996; Martel and Bogger, 1998), earthquake initiation and termination (Aki, 1989; Thatcher and Bonilla, 1989) and melt migration. The structure, type and extent of FDZs are governed by various factors, e.g., depth of faulting, host rock lithology, fault displacement and fault interaction and influence of preexisting structures (Mitchell & Faulkner, 2009). They generally act as covering layer of the main fault core (FC), relatively a narrow zone running parallel the fault trend. The entire FC-FDZ packet is hosted in un-fractured host rocks (Fig 1.6). FCs typically record high strains, manifested in intensely sheared, fine grained rocks, e.g., breccias, gouge, cataclasites and/or ultracataclasites (Chester et al., 1993; Cowie and Scholz, 1992; Kim et al., 2004; Scholz, 1987; Sibson, 1977; Wibberley and Shimamoto, 2003). They also occur as wide zones with strands of multiple fault cores (Faulkner et al., 2003; Faulkner et al., 2008). Ideally, a single FDZ shows a three-layer architecture: a fault core, surrounded by a transitional zone of fractured rock (FDZ), which is in turn bounded by undeformed host rock (Wall) which is almost devoid of any deformation localisation features.

The evolution of a FDZ depends on several factors, such as early fault tip migration, Andersonian fracturing, fault tip linkage, cumulative fault damage with increasing deformation

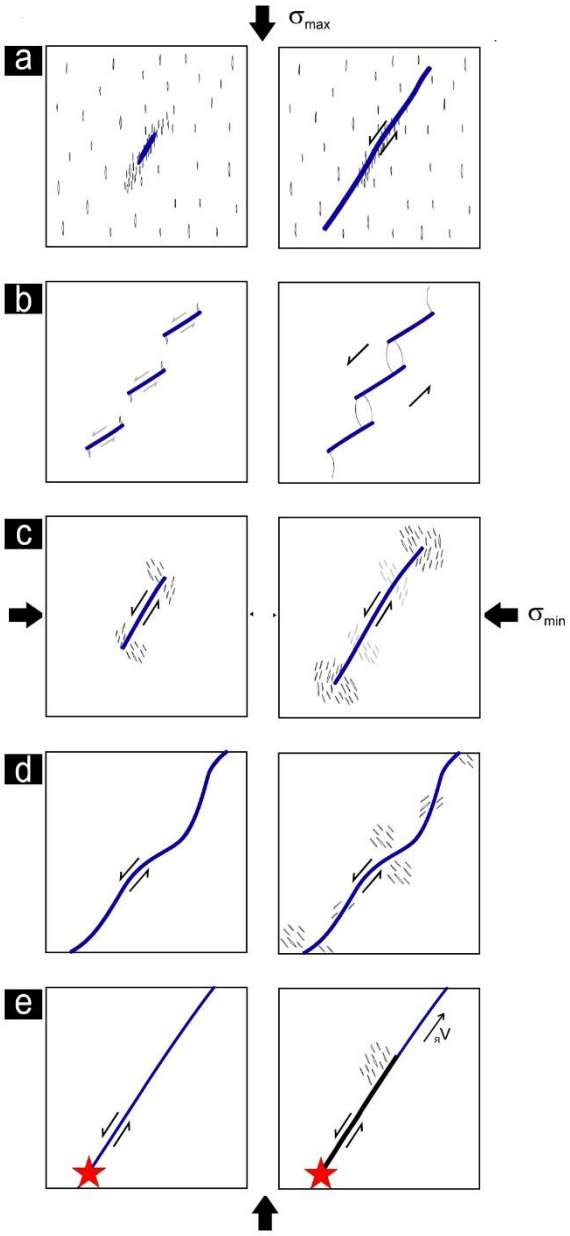

Figure 1.7. Schematic diagram illustrating various models that may be responsible for creating off-fault damage. (*modified from Wilson et al. (2003), Blenkinsop (2008) and Mitchell and Faulkner (2009)*).

and continued stress events. Five primary models have been proposed to explain the growth of a fault damage zone.

Model 1: This follows the Andersonian model of fracturing which assumes a simple, homogenous stress state in the crust. Classical coulomb failure pattern suggests that faults will

form at angles of ~25–30° with respect to the maximum principal deformational stress (Anderson, 1942; Scholz, 2002) and through interaction and coalescence of other preexisting tensile microcracks (Engelder, 1974, Healy et al., 2006, Lockner et al., 1991, Paterson and Wong, 2005, Rutter and Hadizadeh, 1991, and Scholz, 2002). These microcracks are parallel to principal compressive stress and are distributed throughout the rock (Fig 1.7.a).

Model 2: Extensional fractures, from multiple preexisting faults, typically known as wing cracks, interact and coalesce with each other giving rise to huge damage zones (Blenkinsop, 2008, Engelder, 1989, Pollard and Segall, 1987 and Rispoli, 1981) (Fig 1.7.b). This model will have a similar orientation as the previously discussed Andersonian model but will be localized only around the fault system.

Model 3: The third model deals with the development of the 'process zone' surrounding the fault tip (Scholz et al., 1993 and Vermilye and Scholz, 1998). As the process zone migrates, it creates a damage zone of microfractures in its surroundings. The size of the process zone depends on the magnitude of stress around the fault tip, which in turn determines the width of the total damage zone itself (Fig 1.7.c). Microfracture density generally decreases with distance from the fault plane, as the stress concentration decreases away from the fault tip.

Model 4: This model proposes that large fault damage zones can form by reactivation and cumulative damage from continued slip on pre-existing fault surfaces (Chester and Chester, 2000 ; Scholz, 1987). Fracture damage may occur due to juxtaposition of fault irregularities and repeated cycles of stress events (Chester and Chester, 2000; Flinn, 1977; Wilson et al., 2003). Chester and Chester (2000) showed that locally the maximum compressive stress orientations varies from parallel to perpendicular from the fault plane (e.g. Chester and Fletcher, 1997 ; Saucier et al., 1992), and as a result the microfracture orientations vary correspondingly (Fig 1.7.d).

Model 5: The fifth model of fault damage origin is related to earthquake rupture events (Rudnicki, 1980 and Wilson et al., 2003). Ideally the microfractures created by an earthquake event from a rupture tip should form in a similar orientation to the fractures formed by the migrating fault tip model. Rice et al. (2005) showed that the rupture velocity is a guiding factor that controls the dynamic stress field from a propagating slip pulse. In some cases, where the rupture propagation exceeds the shear wave velocity (supershear earthquake), produces microfractures at a relatively high angle and forms on one side of the fault (Fig 1.7.e).

. FDZs cannot be treated as a localized feature, rather they grow as a distributed zone surrounding the preexisting crack or flaw. The damage zone around a fault system can be further subdivided into three main types depending upon the place of their formation. They are the tip damage zone dominated by mode II deformation, the boundary (wall) damage zone and the linking damage zone.

1.3.3. Tip damage zone

The deformation that occurs at the preexisting fault tips due to localized differential slips results in the formation of the tip damage zone. This damage zone includes various features like the formation and propagation of wing cracks and horsetail or pinnate fractures dominated by mode II deformation, and the synthetic branch fault and antithetic fault system dominated by mode III deformation.

1.3.4. Linking Damage Zone

A portion of the FDZ that lies in between two sub parallel, non-coplanar fault segments, ie, the overlapped portion of the two closely spaced faults is termed as the linking damage zone. (Fig 1.8) This portion experiences the more complex and intense fracturing as compared to the other two portions of the damage zone as this portion evolves from the interaction of two adjacent fault tip damage zone (Zhang et al., 1991; Kim et al., 2003). Linking damage zone shows mainly two basic types of deformation, the extensional (fractures, pull aparts, rotated blocks, strike slip duplexes) and the contractional (rotated blocks, connecting faults) depending upon the type of forces it is experiencing.

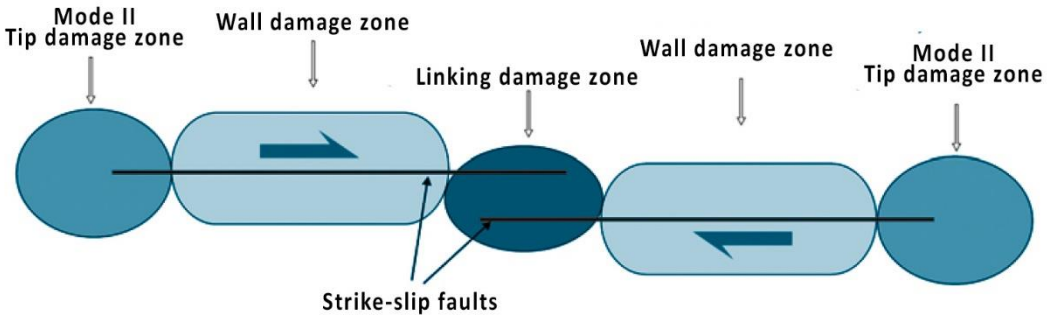

Figure 1.8. Schematic diagram of the principal locations of damage zones around a strike-slip fault zone in map view. Damage zones are classified into three main types; tip damage zone, linking damage zone, and wall damage zone. (After *Kim et al., 2004*)

1.3.5. Wall damage zone

A wall damage zone is often distributed along the whole trace of a fault, with such damage resulting both from the abandonment of tip damage zones and development of new structures in the walls of faults (Kim et al, 2004). There are three main types of wall damage zone: Wedge shaped damage zone, long narrow damage zones, and asymmetric damage zones (Dibblee, 1977)

1.4. The present thesis: aims and objectives

The present thesis aims to provide a detailed account of the different modes of deformation localisation in elasto plastic rocks containing inherent mechanically weak flaws in the form of incipient cracks, void, and fractures. This study uses mainly laboratory experiments, supported by actual field observations to theorize the mechanisms of strain localization under compressive as well as shear stresses. It is demonstrated from experimental results that inherent mechanical heterogeneities can greatly influence the various modes of deformation localization in brittle to brittle-ductile and ductile regimes. Using commercially available polymers (polymethylmethacrylate (PMMA) and polystyrene (PS) as rock analogue materials (elasto-plastic rheology) a direction of this thesis shows the factors controlling the shear band growth mechanisms. Another major direction deals with the study of slip surfaces produced by shear localisation in brittle-ductile rocks. Commercially available talc-fine sand mixtures were used in experiments to reproduce shear fractures, with an objective to undertake roughness analysis and compare the findings with those revealed from field samples. The origin of a unique type of slickensides, first reported by Means (1987) remained unexplained. This thesis reproduces them in laboratory models and demonstrates that they are non-abrasive, and produced by a sort of mechanical instability. A detailed description of the controlling parameters of shear-surface roughness in the form of linear geometrical irregularities is provided. The third aspect of this thesis concerns a geometrical analysis of slip heterogeneity on fault surfaces, which generally largely influence seismic patterns of a fault system. Using analogue experimental models, this study shows that shear localizes heterogeneously in a slip surface, which was well supported by field data.

The thesis is presented in eight chapters. The next chapter (***Chapter 2***) discusses the basic experimental and theoretical concepts of deformation localisation. This includes all the classical theories of failure criterion, major rock deformation experiments and some theoretical study of shear band formation. ***Chapter 3*** describes the experimental methods used in this doctoral thesis. It also discusses the details of the experimental model materials, their physical, chemical and rheological properties. The experimental setups and data processing techniques used for the necessary analysis are also discussed in this chapter. ***Chapter 4*** provides a roughness analysis on slip surfaces, both observed in the field as well as simulated in the laboratory. The details of field study, observation and sample analysis are described here in this section. Detailed roughness analysis was done to understand the effect of rheology and other parameters in the evolution of surface roughness. A unique type of slickenside was studied which was first mentioned by Means (1987) and was not described since then. Finally, this chapter proposes a type of mechanical instability as the probable mechanism for the formation of this type of slickenside. ***Chapter 5*** extends this roughness study into a much more detailed investigation regarding shear surface heterogeneity in a single rupture event. Experimental as well as field sample studies were carried out to quantitatively examine the slip zone patterns on a shear surface, and two prominent zones were delineated as striated (slip zones) and non-striated (stuck zones). ***Chapter 6*** investigates the role of mechanical heterogeneities in deformation localisation in the form of shear bands. Compressional experiments were conducted using polymers as rock analogues. Models with inherent flaws were deformed and were compared with homogenous blocks to understand the effect of the heterogeneities in dictating the deformation localisation. The effect of strain rate was also studied. The problem was investigated through numerical model simulations. In ***Chapter 7***

their main results are presented. The entire work is finally discussed in ***Chapter 8***, highlighting the major conclusions.

Chapter 2
Mechanics of shear failure: a review

2.1. Introductory note

The study of shear failure is crucial to understand many tectonic structures, e.g., faults, boudinage, disjunctive cleavage and deformation bands, and lithospheric plate boundaries, e.g., transform and transcurrent zones. Geological observations suggest that shear fractures can form in a wide range of pressure (P) and temperature (T) conditions, from low P-T conditions at upper crustal (brittle) regimes, to elevated P-T conditions near the brittle-plastic transition at greater depths. However, the mode of shear failure changes with varying physical environments; the failure generally gives rise to sharp fractures in shallow crustal deformations, whereas wide deformation bands, shear zones or cataclastic zones in brittle-ductile transition to ductile regimes at greater depths. Shear failures in the geological conditions are coupled with a variety of secondary processes, for example, permeability enhancement and intense fluid flows. Many rocks with primary porosity show porosity reduction preferentially in deformation bands produced by shear failure. The deformation bands can thus act effective barriers to fluid flows in porous rocks. These structural barriers can trap hydrocarbons to form good petroleum reservoirs. Similarly, fault damage zones develop fine grained cores with little or no porosity. The damage zones on either side of the fault core can act as a good storage of fluid materials, but not in the core region, which can hardly permeate fluids due to lack of sufficient porosity. Another major direction of shear

failure study concerns geophysical interpretations of earthquakes that are essentially triggered by slip events on faults. However, there are many natural faults which are aseismic, producing virtually no perceptible earthquakes. The mode of shear failure at the fault tips critically control aseismic versus seismic character of faults. Understanding the mechanics of shear failure and their controlling factors is thus the crucial step to interpret all these geological and geophysical phenomena. This chapter provides a theoretical framework of shear failure mechanics, highlighting different mechanical criteria used to define the critical state of such failure.

2.2. Failure criteria

2.2.1 Coloumb-Navier Failure Criterion

Many granular rocks and geological materials undergo shear failure in brittle regimes to produce conjugate sets of shear fractures symmetrically oriented with respect to the principal compression axes. Experiments suggest that the effective differential stress and the frictional strength of granular materials are the key dynamic parameters to govern such failure processes (Handin, 1969; Lockner and Byerlee, 1977; Heiland, 2001; Hou et al., 2020; Feng et al., 2021). Under a given pressure condition, the shear failure can occur at a threshold value of the differential stress for which the shear stress on the failure plane exceeds the cohesive strength and the frictional resistance. As the confining pressure increases with depth, rocks at deeper regions require much higher differential stress to initiate fracturing. In 17th century, French scientist, Charles Augustin de Coulomb, proposed that shear failure in granular materials occurs along the plane of maximum shear stress (τ_{max}) when τ_{max} reaches the cohesive strength. However, Coulomb's criterion faces

serious limitations. 1) The criterion implies that shear fractures develop always at an angle of 45° to the compression, irrespective of the stress condition and materials properties. The angle is generally found to be less than 45° in both naturally deformed rocks and experiments. 2) According to this criterion, the compressive and tensile strengths of materials should be equal. In reality, they are unequal; the compressive strength is usually greater than the tensile strength. Navier later modified Coulomb's theory into a version that overcomes these shortcomings. The new criterion, called Coulomb-Navier criterion predicts that shear failure occurs in granular materials along planes at which the magnitude of shear stress (τ) satisfies the following condition:

$$|\tau| = \tau_0 + \sigma \tan\varphi, \qquad (2.1)$$

σ is the normal stress across the fracture, tanφ represents the coefficient of internal friction and τ_o is the cohesive strength of the material. The criterion in Eq. (2.1) suggests that shear failure occurs along planes of maximum effective shear stress ($|\tau| - |\sigma \tan\varphi|$). The shear fracture thus forms at an angle.

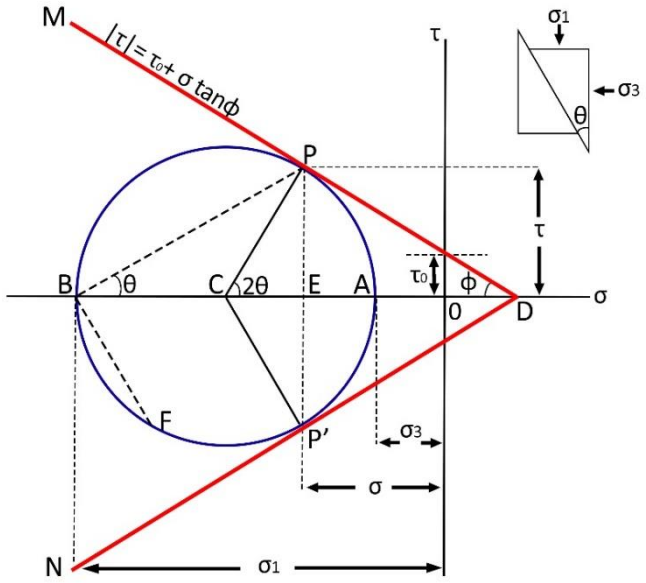

Figure 2.1. Mohr Circle representing Mohr-Coulomb Criteria (After *Ghosh, 1993*)

$$\theta = \frac{\pi}{4} - \frac{\varphi}{2} \qquad (2.2).$$

Equation (2.2) explains the common occurrence of shear fractures at angles less than 45^{o}, as observed in experiments as well as naturally deformed rocks. The criterion can also account for the orientations of the principal types (normal, reverse and strike-slip) of tectonic faults, as predicted by Anderson's theory (Anderson, 1951).

To visualize the state of stress, German engineer Otto Mohr introduced the concept of stress circle, called the Mohr's circle, which is often used to demonstrate the condition of shear failure in a stress space defined by normal (σ) and shear (τ) stress components (Fig. 2.1.). In this figure the two straight lines: DM and DN that represent the Coulomb-Navier criterion bounds the stability field. These two lines are also called Coulomb failure envelope. They are oriented at angle $\pm\varphi$ with the σ-axis, forming an intercept $\pm\tau_0$ with the τ axis. According to the criterion, the stress condition at any point on them marks the threshold state at which the body is on the verge of shear failure. The Mohr circle that represents the state of stress in the body must touch DM at P at the moment of shear failure. The normal to the shear fracture is at an angle θ to the compression direction, i.e., the σ-axis. From the diagram, it follows,

$2\theta = 90° - \varphi,$

$\theta = 45° - \varphi/2,$ (2.3)

where φ is the angle of internal friction. Equation (2.2) derived from the Mohr construction agrees with Eq. 2.3. The Coulomb-Navier criterion explains the orientations of shear fractures and faults

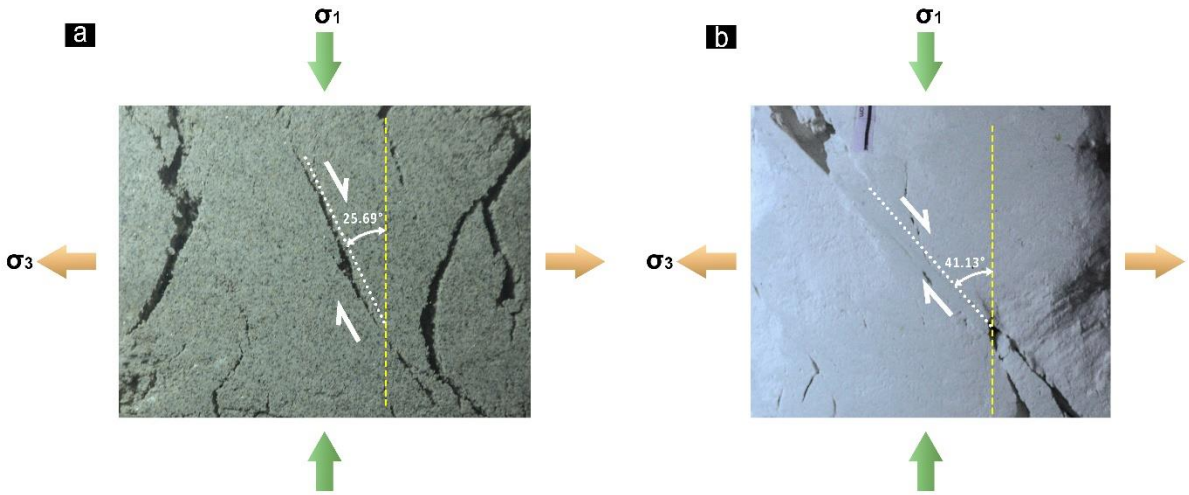

Figure 2.2. Shear fractures produced in rock analogue materials, a) sand and b) talc models under plain strain compressional deformation test. Note the angle between the shear fracture and the principal compression direction is less than 45°.

observed in tectonic belts. Crustal rocks typically show $\varphi \sim 30°$ in experiments (Anderson, 1951), which yields θ around 30°. The criterion supports Anderson's theory of faulting that predicts normal and reverse fault dips at ~60° and 30° (Fig 2.2.), respectively. The Mohr circle construction indicates that τ_0 and $\tan\varphi$ are the two fundamental material parameters that entirely determine the stress state required for shear failure and the orientation of shear fractures with respect to the stress axis.

The Coulomb-Navier criterion discussed above has again some limitations: 1) applicable essentially for brittle shear fractures in granular materials, where intergranular friction governs the failure dynamics, and 2) constant shear fracture orientations, which are hardly observed in natural cases. Recently experimental studies have shown that the same materials can undergo brittle failure

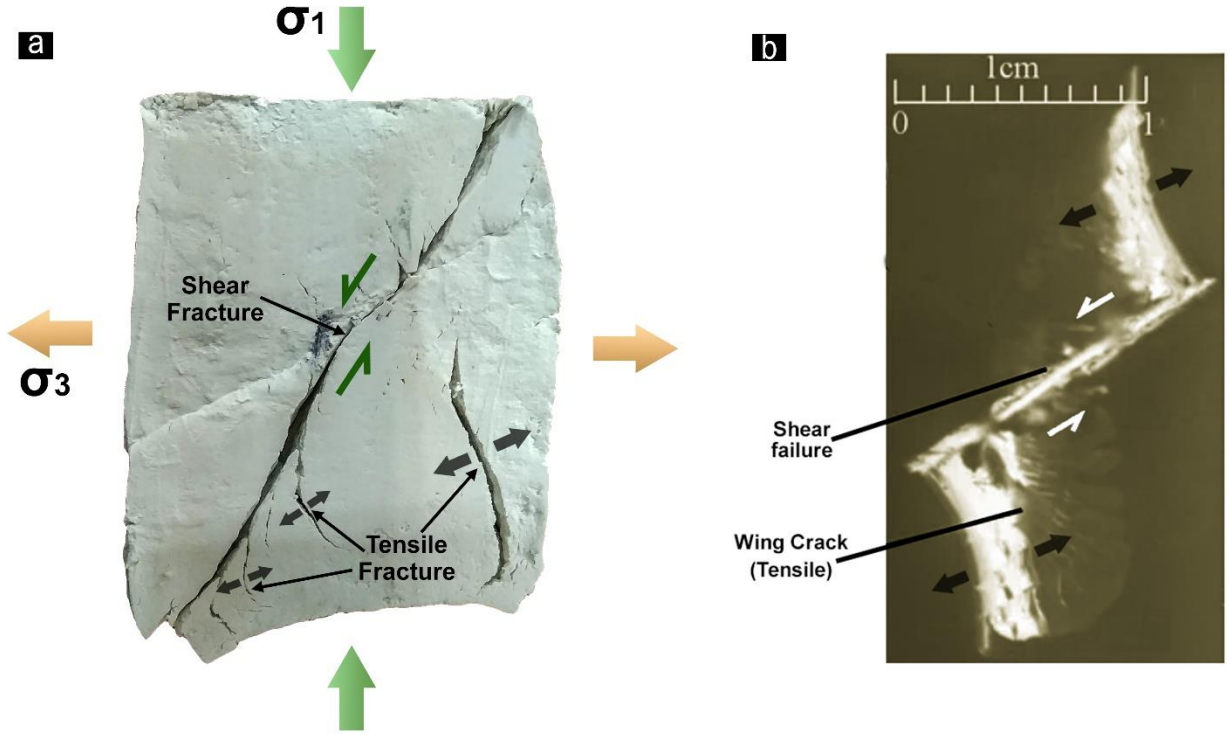

Figure 2.3. Experimental models showing generation of both shear fracture as well as tension fractures simultaneously. a) talc model under plain strain compression test, b) wing crack (tensile) formation from shear fracture in hardened epoxy resin (after *Fu et al., 2018*)

both by tensile and shear fracturing depending upon the stress conditions (Fu et al., 2018) (Fig 2.3). To overcome these limitations, researchers have later proposed new failure criteria, which are discussed in the following sections.

2.2.2. Mohr failure envelope

A Mohr failure envelope is constructed to define the critical state of stress over a range of differential stress, irrespective of the fact that the system follows Coulomb criterion or not (Fig 2.2). It is noteworthy that the Coulomb-Navier theory predicts a linear relation between the normal and shear stresses on the plane of shear failure. In contrast, Mohr postulated a nonlinear relation between σ and τ, and showed curved envelopes to define the stability fields, as illustrated in Figure 2.4.

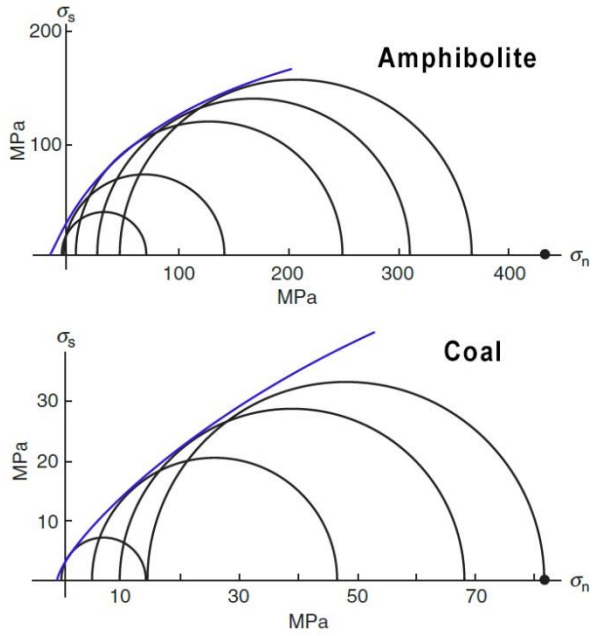

Figure 2.4. The non-linear Mohr envelope for amphibolite and coal based on triaxial tests

Mohr's theory of curved envelops agrees with the failure behavior of natural materials, such as amphibolite and coal in triaxial experiments. The tangent slope at a point on the curved envelop determines the orientation of shear fractures under a given state of stress. Evidently, the orientation varies with changing stress field as the tangent slope varies with varying differential stresses. Based on Mohr failure theory, Yu et al., (2020) showed the failure criterion behaving non-linearly in a power-law form for four rock types, granite, marble, dolomite and andesite, deformed under

triaxial compression (Fig 2.5.a). Similarly, Li and Ghassemi (2021) performed confined Brazilian test and compared with the conventional triaxial compression test (Fig. 2.5.b).

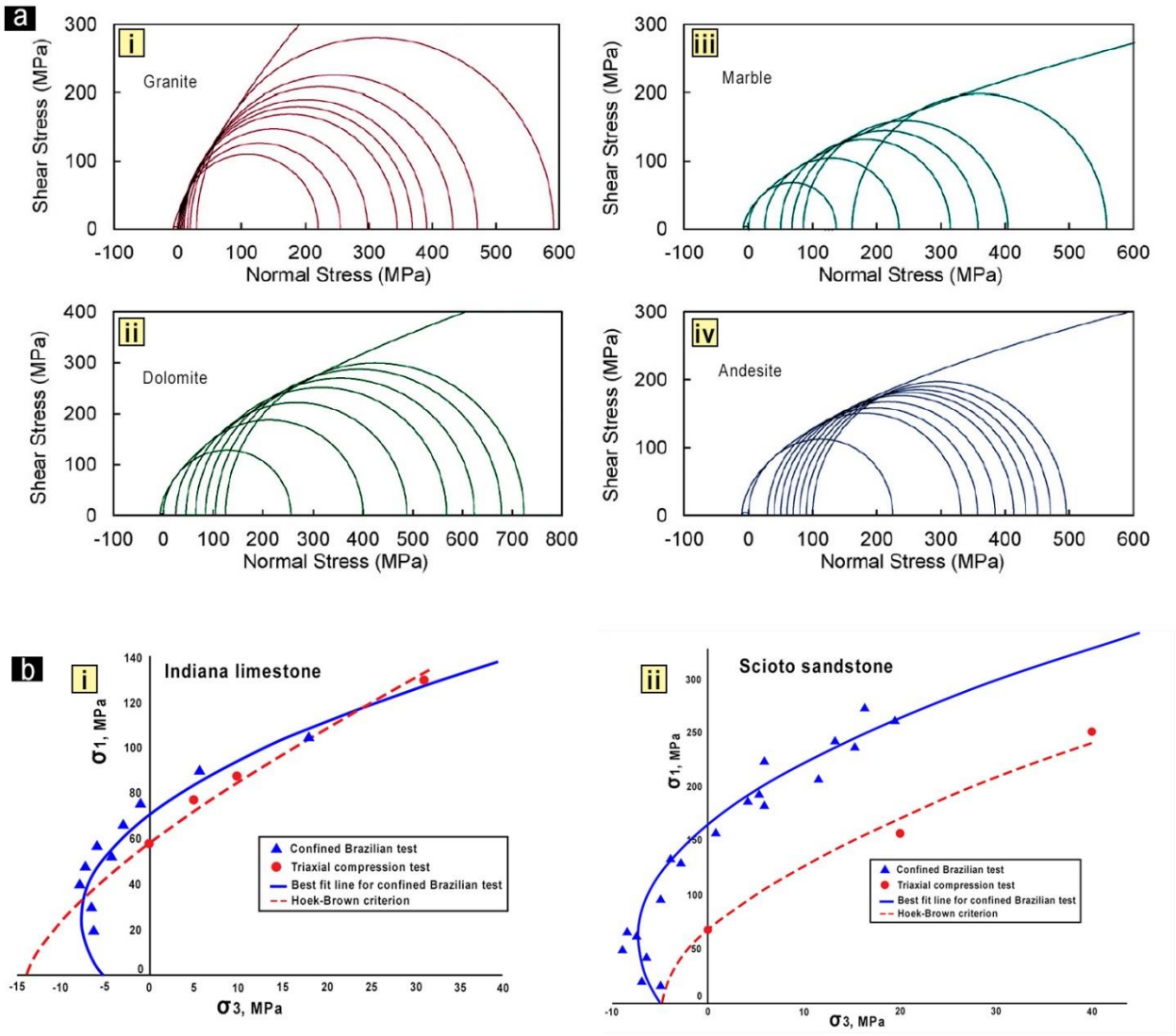

Figure 2.5. a) Curved Mohr Circle and proposed failure envelope for i) Granite, ii) Dolomite, iii) Marble, and iv) Andesite (after Yu et al., 2020) ; b) comparison of failure envelopes for confined Brazilian test and conventional compression test for i) Indiana limestone , ii) Scioto sandstone (after Li at el., 2021)

2.2.3. Drucker Prager criterion

Many granular materials, including rocks and other geological materials, such as soils show pressure dependent failure behavior, characterized by their increasing cohesive strength with pressure (Tenthorey & Cox, 2006). The Coulomb-Navier criterion as well as Mohr's theory discussed in the preceding section, however, are independent to the intermediate principal stress, secondly, both of them do not account for such pressure-induced strengthening of materials. The Drucker Prager yield criterion is a 3-dimensional pressure-dependent model to predict the critical state of stress at which the rock reaches its ultimate strength and undergo plastic yielding. This yield criterion is applied for a variety of pressure dependent materials like, rocks, concrete, polymers to estimate their strength. The Drucker-Prager yield criterion has the form

$$\sqrt{J_2} = A + B\, I_1 \,, \qquad (2.4)$$

where J_2 is the second invariant of the deviatoric part of the Cauchy stress and I_1 is the first invariant of the Cauchy stress. A and B are empirical material constants, their values are determined from experiments. The criterion can also be expressed in terms of equivalent stress and hydrostatic stress as,

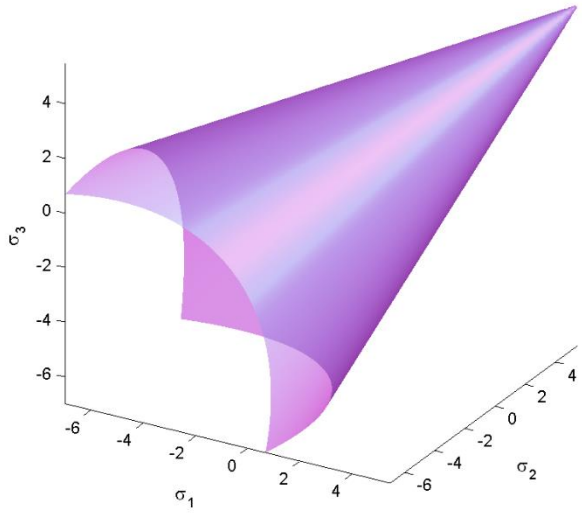

Figure 2.6. Example of a Drucker–Prager yield surface in 3D space of principal stresses obtained from experimental data.

$$\sigma_e = a + b\,\sigma_m\,, \qquad (2.5)$$

where σ_e is the equivalent stress and σ_m is the hydrostatic stress, and a and b are the constants. The Drucker-Prager yield surface is considered as a smooth version Mohr-Coulomb Yield surface (Fig 2.3).

2.2.4. Griffith Theory of fracture

The observed tensile strength of any material is much less than its theoretical value. Coulomb fracture criterion deals with the formation and propagation of the cracks in a macroscopic level. To understand the mechanics in somewhat smaller scale, i.e., in microscopic level we have to study the Griffith theory of fracture propagation. A. A. Griffith, in the early twentieth century, proposed that all solids contain innumerable microscopic to submicroscopic, randomly oriented cracks, now called Griffith Cracks, that reduce the strength of the material substantially, and forming extensional fractures on application of stress (Griffith, 1920). A Griffith crack is a small, penny-shaped or slit like crack that in cross section is much longer (a axis) than it is thick (c axis) and that has a very small radius of curvature at its tips. Griffith cracks may be imperfections within the crystal lattice of crystal grains in a rock, or they may be intergranular or grain boundary cracks. The ability of Griffith crack to reduce substantially the strength of the material comes from the fact that an applied stress in general produces a local high concentration of tensile stress near the crack tip. The smaller the radius of curvature at the crack tip, the larger the ratio a/c of the ellipsoidal crack, the higher the local concentration of tensile stress near the crack tip. Griffith found a non-linear relationship between the principal stresses for a critically stressed rock on the verge of fracture. According to Griffith's failure criterion,

$$\tau^2 = 4T_0^2 - 4T_0\sigma \quad (2.6)$$

where, T_0 is the uniaxial tensile strength.

The equation can be rewritten as,

$$\tau^2 = -4T_0(\sigma - T_0) \quad (2.7)$$

or,

$$Y^2 = -4T_0X \quad (2.8)$$

where, Y = τ , X = $\sigma - T_0$

This is a standard form of parabolic equation. There has been some argument that Griffith theory is valid for extensional fracture, and Griffith cracks tends to close in compression experiments. To overcome this, McClintock and Walsh (1962) proposed a modified form of Griffith theory :

$$|\tau| = 2T_o + \mu_s \sigma , \quad (2.9)$$

where, μ_s is the coefficient of sliding friction. This modified form of Griffith's theory holds good for fractures in the compressive stress field.

2.3. Shear failure in materials with power-law rheology

In Earth, migration of fluids and melts is greatly affected by enhanced stress by increasing the driving force of fluid movement by modifying the inherent permeability in a matrix. It has been shown by many workers that partially molten rocks, e.g., migmatites often shows signatures of strain localisation and melt concentration in melt dominant ductile shear zones (Hollister and Crawford, 1986; Burg, 1991; Brown and Solar, 1998). Kelemen and Dick (1995) showed that

strain localisation in dunites is a product of deformation localisation and melt migration, even under lower temperature conditions (1223-1373 K). Holtzman et al., 2003 studied stress driven melt segregation due to deformation localisation in partially molten rocks using simple shear experiments. In their study, they reported re-organization of melt-rich bands in preferred orientations, guided by high strain localisation, both in grain scale as well as larger than that. Permeability developed due to high strain localisation is highest for melt flowing parallel to the melt band length and lowest in the normal direction.

Other studies have also reported that highly strained localized melt bands of large porosity is developed in simple shear deformation of partially molten aggregates (B. K. Holtzman, Groebner, et al., 2003; M. E. Zimmerman et al., 1999). According to these studies, these low angle (~20°) melt bands emerge and persist over a wide range of strain rate even at large shear strains. These observations were crucial as it depicts the role of deformation localisation in magma transport in earth's mantle (Bercovici et al., 2001; Mckenzie, 1984). Some works have suggested that syntectonic melt bands evolve perpendicular to the maximum extensional strain field, assuming that matrix viscosity is a product of porosity which weakens with increase in melt fraction. Spiegelman (2003) proposed that melt bands oriented at 45° in a simple shear system will grow fastest whereas bands with high angular relationship (>90°) will decay. R. F. Katz et al., 2006considered a viscosity that includes not only porosity but also strain-rate-weakening mechanism which resulted in formation and persistence of deformational melt bands at about 20° to the maximum shear direction, which is 25° less than the previous prediction. They have use a power-law form for the strain-rate-weakening phenomenon as the constitutive relation for creep of mantle material at high temperatures, as follows

$$\eta(\varphi\,,\ \dot{\varepsilon}) = \eta_0\, e^{\alpha(\varphi-\varphi_0)}\, \dot{\varepsilon}_{II}^{\frac{1-n}{n}}\ , \qquad (2.10)$$

where η_0 is the shear viscosity at φ_0 reference porosity, α (-28 ± 3) is porosity weakening coefficient experimentally derived, $\dot{\varepsilon}_{II}$ is the second invariant of incompressible component of strain rate tensor, *n* is the power-law dependence on stress viscosity. When *n* = 1, this viscosity is Newtonian and when *n*>1 and φ = 0 , it defines a standard non-Newtonian power-law viscosity. According to their investigation, when the stress exponent *n* is 1, the porosity bands localizes at 45° and have a fast growth. But for a strain-rate-dependent viscosity, ie., *n*>1, the shear deformation causes the melt bands to localize into two orientations, one at low (~15°) and the other at high (~75°). As the deformation progresses, the high angle bands start to rotate with a positive

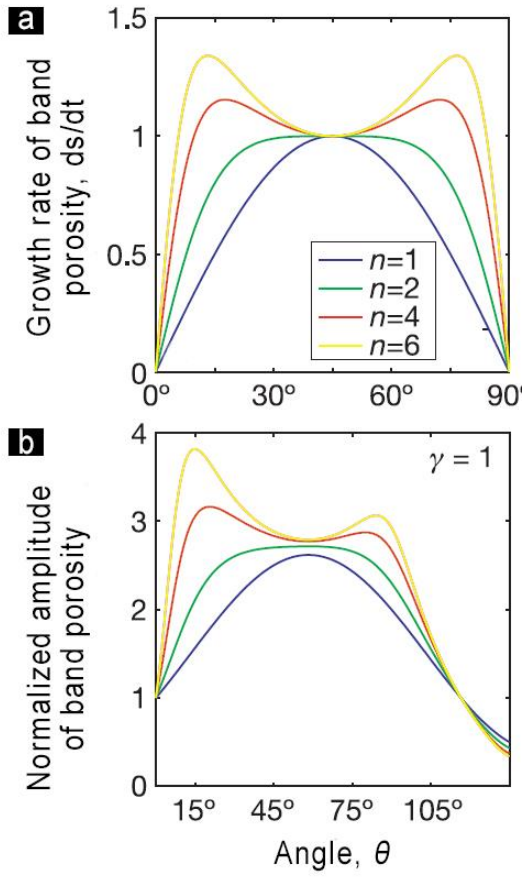

Figure 2.7. a) The growth rate of porosity as a function of angle; b) The normalized amplitude of melt-band porosity as a function of θ and *n* for γ = 1. Progressive deformation rotates the high angle shear bands towards the low-angle orientation where it becomes stable. (after *Katz et al., 2006*)

growth rate and tends to orient in the low angle band direction. Thus, their calculations and

experiments validates the magma dynamics theory as an outcome of deformation localisation, and exhibit the evolution of low-angle melt band shorter than compaction length and persist at low angle even at high shear strain. These results have huge implication in understanding of melt (magma) transport in the mantle, specially under the mid-ocean ridges. These deformation melt bands with significantly increased porosity act as feeder channels of melt that forms hundreds of kilometers away from the ridge, to form new oceanic crust. On continued deformation localisation due to shearing these bands can also form interconnected permeable network which further enhance the syntectonic melt focusing phenomenon.

2.4. Elasto-viscoplastic models of shear failure in solids

Perhaps the most crucial aspect of modelling shear failure in solids is choosing the rheological framework that approximates closest to the geological conditions of interest (Bercovici & Karato, 2002; Gerya & Yuen, 2007; A. A. Popov & Sobolev, 2008). To fulfil this criteria, researchers now

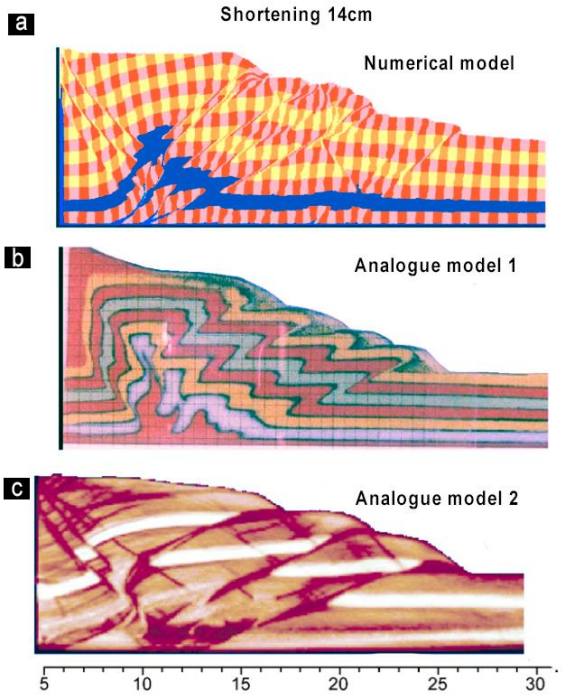

Figure 2.8. Comparison of a) numerical model (visco-elasto-plastic rheology) with analogue models b) and c) for sandbox experiments (after *Buiter et al 2006* and *Gerya and Yuen, 2007*). The numerical modelling was done in 12ELVIS.

have taken up the complex visco-elasto-plastic rheology as the preferred rheological combination. It includes all the necessary ingredients for investigating transient creep which leads to nucleation of shear zone (Regenauer-Lieb & Yuen, 2003) and shear failure in solids. Gerya & Yuen, (2007) used this visco-elasto plastic rheology to model shear failures in sand-box experiments (under compression) and compared with analogue results of the same study (Fig 2.8). They have also

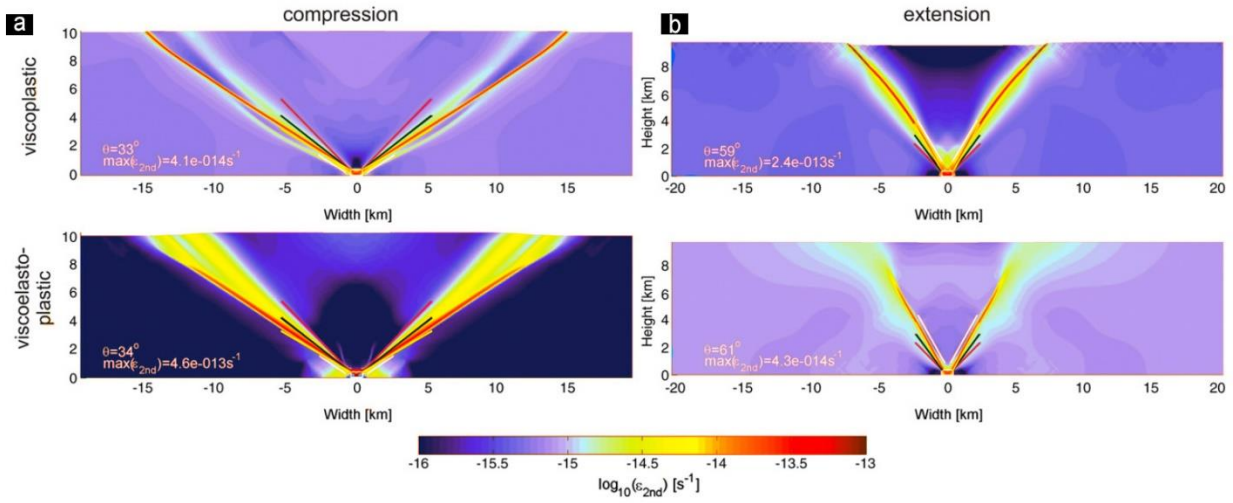

Figure 2.9. Comparison of viscoplastic versus viscoelastoplastic rheology in both a) compression and b) extension (2% finite strain). Note in both cases, shear bands formed in viscoelastoplastic sample shows a much more similar resemblance to Coloumb angle. (after *Kaus, 2010*)

provided results for extensional sandbox models. Kaus, (2010) have provided a brilliant comparison of more commonly used viscoplastic to the more efficient viscoelastoplastic rheology in both extensional and compressional conditions keeping a friction angle of 25°. He showed that there are little differences in the angles of the shear bands, with the viscoelastoplastic models showing more resemblance to the Coulomb angle (Fig 2.9). The study also showed effects of multiple heterogeneities for this rheology and showed successive developments of shear bands with increasing strain.

Chapter 3
Experimental Method

3.1. Introductory note

Geoscientists have developed the analogue modelling approach to study geological processes in the beginning of the 19th century. This technique has then emerged as an important tool, mainly due to its various advantages, such as quantitative and qualitative insights into some specific geological problems, understanding of structural evolution in long term tectonic deformations and kinematic perspectives of tectonic processes, which are often hard to obtain from any analytical solutions. In addition, analogue models can be used to investigate the effects of a physical or chemical parameter on geological processes and also to explore the possible influence of specific boundary conditions of concern. Many geoscientists have utilized this modelling approach to study the evolution of 3D complex structures in a terrain, for example, folds produced by superposed layer-parallel tectonic compression (Colletta et al., 1991; Dixon & Liu, 1992; Ghosh et al., 1992; Ghosh et al., 1993; Koyi, 1997). These physical models are designed to represent geological objects and systems on varied scales, ranging from microstructures in rocks (Gilbert, 2004) to large scale features, e.g., mountains (Bucher 1956, Ramberg 1967). The modelling demands scaling of geometrical, kinematic and dynamic parameters to replicate the natural prototypes in laboratory scale space and time. King Hubbert, (1937) gave a thorough description of the concept of scaling in terms of the above mentioned physical parameters. It is to be noted that while scaling a large geological body to experiment friendly size, the change in its several physical properties will not be necessarily proportional to the change in size of the body. The scaling of several parameters is

required to replicate nature in laboratory through specific mathematical relations, which are elaborated below.

1) *Geometrical scaling*: The most fundamental step in scaling a system concerns geometrical proportionality between the natural prototype and laboratory model, where their length dimensions hold linear proportional relations, maintaining similarity of their angular dimensions (shape conservation). Consider l_1 as the real scale length and l_2 length on laboratory scale. The geometrical scaling rule follows,

$$\frac{l_2}{l_1} = \lambda, \text{ or } \quad l_2 = \lambda l_1 \qquad (3.1)$$

where λ is the constant of proportionality (geometrical scaling factor). $\lambda > 1$ and < 1 imply that the model can represent enlargement or reduction of the real scale system, respectively. Similar to the length, the other geometrical entities, such as *area* and *volume* are to be scaled in consistent with the length scaling factor as,

$$\frac{A_2}{A_1} = \lambda^2 \qquad (3.2)$$

and,

$$\frac{V_2}{V_1} = \lambda^3 \qquad (3.3),$$

wherer, A_2 and A_1 are corresponding areas of the model and original and V_2 and V_1 are their respective volumes.

2) *Kinematic scaling*: Motion (kinematics) of a real scale system demands scaling in terms of both time and space dimensions to obtain a kinematic equivalence between the natural prototype and the corresponding geometrical scaled model. Consider first time scaling,

$$\frac{t_2}{t_1} = \tau \qquad (3.4),$$

where t_1 and t_2 are times in the real and model scales, respectively. τ represents the time scaling factor. Using scaling both the space and time dimensions, we can now scale other kinematic quantities, such as velocity and acceleration in the following steps:

$$\frac{v_2}{v_1} = \eta = \frac{\frac{l_2}{t_2}}{\frac{l_1}{t_1}} = \lambda\tau^{-1}, \qquad (3.5)$$

and,

$$\frac{a_2}{a_1} = \gamma = \frac{\frac{l_2}{t_2^2}}{\frac{l_1}{t_1^2}} = \lambda\tau^{-2} \qquad (3.6),$$

where η and γ are two kinematic scaling factors. Similarly, angular velocities can be scaled as,

$$\frac{\omega_2}{\omega_1} = \tau^{-1} \qquad (3.7)$$

3) *Dynamic scaling*: For dynamic scaling, we now need to consider mass as an additional physical attribute to arrive at a complete scaling of the model. The ratio of masses in a real scale space to that in the model scale space is denoted by μ, (termed as the mass ratio factor). Combining the mass and space scaling, the density ratio (δ) can be expressed in terms of the geometrical and mass scaling factors as,

$$\delta = \frac{\frac{dm_2}{dV_2}}{\frac{dm_1}{dV_1}} = \mu\lambda^{-3} \qquad (3.8)$$

For the dynamic similarity between a natural prototype and its corresponding model, forces acting on each element of mass dm_2 in volume dV_2 of the model, are kinematically and geometrically similar to the corresponding motion in the real scale frame. This condition is valid when each force

F_1 acting on the original system and the corresponding vector force F_2 acting on the model having same orientation have a relation as:

$$\frac{F_2}{F_1} = \varphi \qquad (3.9)$$

where φ is the model ratio of force, and remains constant for the two bodies.

4) *Strength scaling*: For the purpose of scaling, it is to be considered that strength is measured in terms of stress. For the similarity between the natural prototype and the model, the manner in which the failure occurs at a certain stress in the original body must be similar (same manner) at the corresponding scaled value of the stress in the model. So, the ratio of their strengths should be the same as the ratio of stress:

$$\frac{(strength)_2}{(strength)_1} = \frac{(stress)_2}{(stress)_1} = \sigma = \mu\lambda^{-1}\tau^{-2} \qquad (3.10)$$

Sir James Hall (1815) first demonstrated the development of tectonic fold structures in geological strata through analogue experiments and presented his findings in the Transactions of

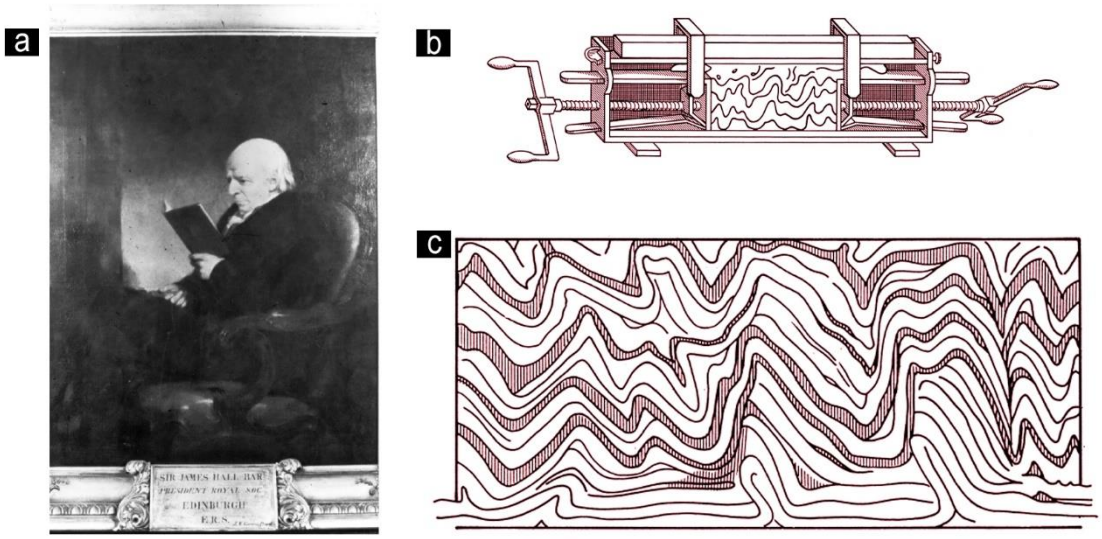

Figure 3.1. a) Portrait of Sir James Hall by Sir John J. Watson-Gordon, R.A. (from Royal Society of Edinburgh; b) Schematic of the machine used by Sir James Hall for scale modeling of folding by lateral compression; c) Result of folded model from Sir Hall's experiment. (after *Ranalli, 2001*)

the Royal Society of Edinburgh (Hall, 1815) (Fig. 3.1). He used pieces of cloth, linen and woolen fabric as rock analogue materials to simulate the fold structures (Fig. 3.1.b). Following his pioneering experiments in the early 1800's, the analogue modelling approach gained enormous popularity to study various tectonic structures, such as fractures, folds and thrusts (e.g. Favre, 1878; Daubre, 1879; Schardt, 1884; Cadell, 1889; Willis, 1893) in the late 1800's. This revolution in laboratory studies eventually led to remarkable conceptual advancement in understanding crucial geodynamic processes, e.g., subduction, mountain building, rifting, gravity spreading, indenter tectonics, escape tectonics and convection. In fact, Kuenen (1965) elegantly stated that experiments performed in the "laboratory of Nature" are too complex to comprehend the evolution of a process with convincing analyses, leaving only their end-results, which can be observed at present time. Analogue models help visualize the possible processes which may result in the "frozen" deformational result that we observe in present day rocks.

Most of the geological processes occur at high ambient temperature-pressure conditions under extremely slow rates, which can be replicated in laboratory set ups using some rock analogue materials at much faster rates to study them in short time scale experiments. Laboratory experiments can be broadly classified into two categories of analogue models: a) soft

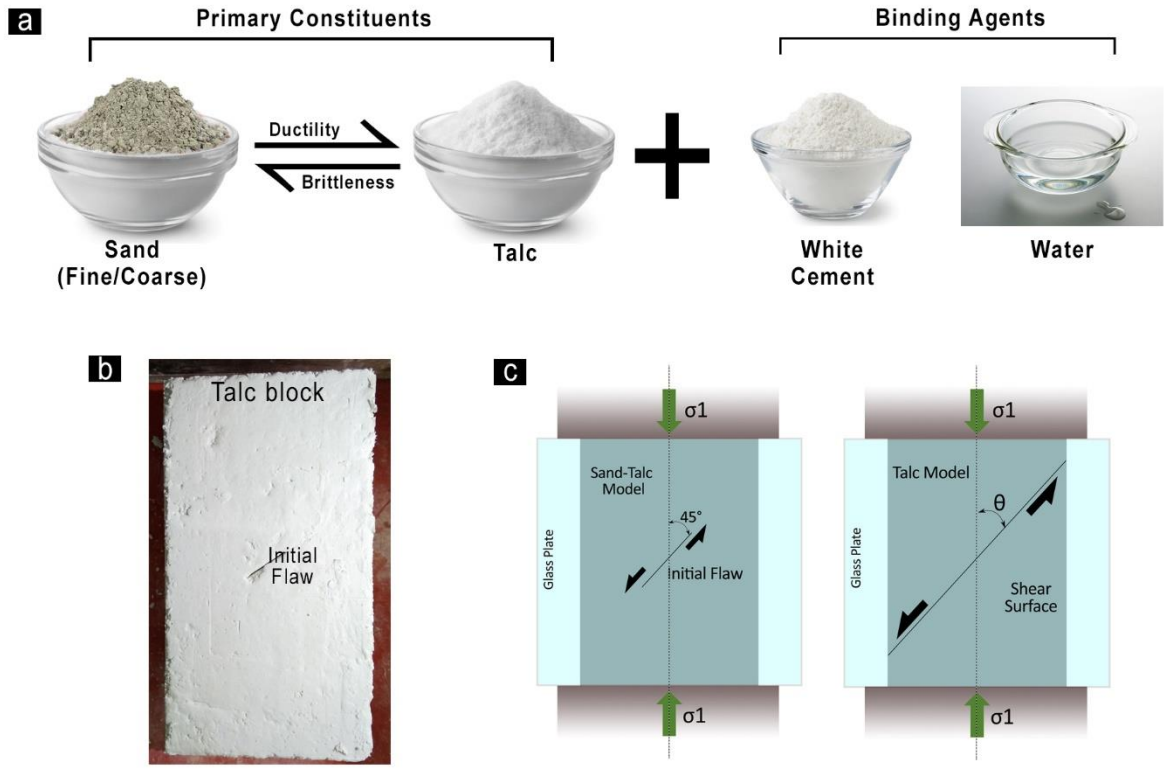

Figure 3.2. a) Major constituents and biding agents used for soft model experiments. Note that increasing talc volume increases the Ductility of the model; b) An undeformed talc block with an initial flaw; c) Schematic diagrams of the experimental setup for soft model experiments.

(mechanically weak) models and b) hard (mechanically strong) models. The first type of models uses a range of low-strength materials, e.g. sand, clay, plasticine, wax, and viscous fluids (glucose syrup, PDMS), whereas the other type uses high-strength materials, e.g., solid polymers, e.g., PMMA, PS, and PVC. Though these materials have different rheological properties than real rocks, but they reproduce approximately the behavior of real rocks at elevated temperature,

pressure and much slower strain rates (~ 10^{-15} s^{-1}) under room temperature conditions and faster strain rates (in the order of 10^{-4} s^{-1} – 10^{-6} s^{-1}). Different types of model materials that I used for analogue experiments are described in the following sections.

3.2. Soft model materials

3.2.1. Sand models

After several trials with a variety of granular materials, wet sand-talc mixtures were chosen as analogue model materials that provided good rheological approximations to brittle-ductile granular rocks (Fig. 3.2). The advantage of using this composite material is that it was possible to manipulate the model rheology by varying sand grain size as well as sand to talc volume ratio. Secondly, the ductility of sand-talc mixtures could be controlled by changing water content in the mixtures. Pure sand models (without talc) showed ideally a brittle behavior of Coulomb rheology, producing sharp shear fractures (Bratli & Rasmus, 1981; Ellis et al., 2004; Lade, 2006; Misra, Mandal, et al., 2009; Wang & Lade, 2001). In my experiments I used commercial grade coarse and fine sands with estimated modal grain sizes of 500 μm and ~150 to 200 μm, respectively. The coarse sand had a cohesive strength of ~5.26 kPa and the angle of friction of 27° (Fig. 3.3), which were measured from triaxial tests conducted in the High Pressure Temperature Laboratory, Geological Sciences Department of Jadavpur University.

3.2.2. Sand-talc mixture models

Talc was added to sand in various volume proportions (20% to 100%) to enhance ductility in the sand-talc model. Commercial grade talc used in the experiments had grain sizes ranging from 0.30 to 50 μm, with an average of ~ 20 μm. Increasing talc content resulted in a transition of typical

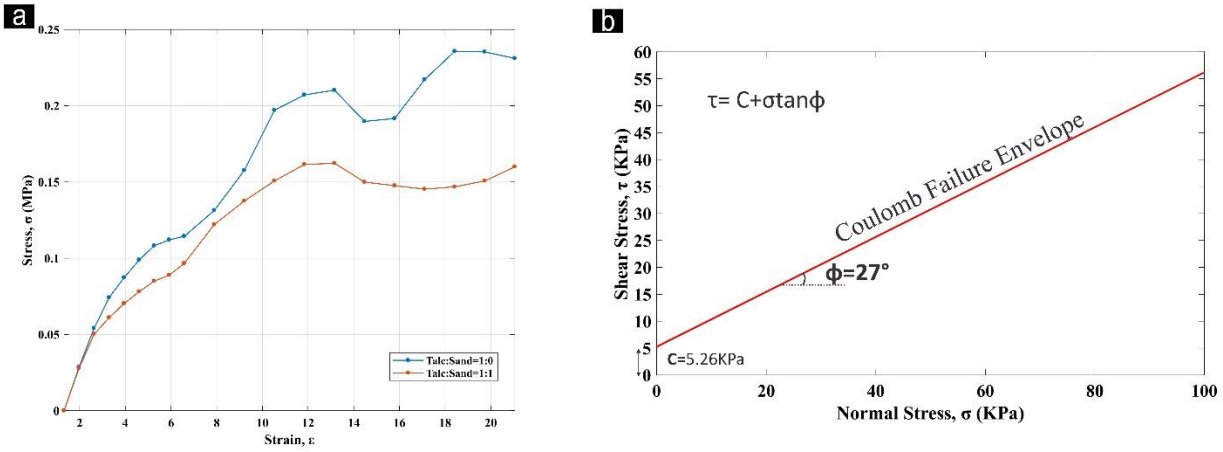

Figure 3.3. a) Yield behavior of pure talc (blue) and sand talc (orange) models under triaxial compression tests; b) Estimated coulomb failure for pure sand models.

Coulomb to plastic rheology that underwent plastic yielding at a threshold stress. I investigated the failure behavior of pure talc and sand-talc (1:1) mixtures in wet condition. They yielded at stresses of 200 and 155 kPa, respectively (Fig. 3.3.a). Both the materials showed creep with strain softening after the first yield point (Brooks et al., 1991), as reflected from a pronounced stress drop with increasing strain (Fig 3.3.a). To introduce cohesion in the model materials, white cement and water were added to the sand-talc mixture in volume ratios, 1:6 and 1:9, respectively.

3.3 Hard model materials

3.3.1. Polymethylmethaacrelate (PMMA) models

Various polymers have been widely used as rock analogues to reproduce important structures, such as fractures, folds and shear bands in laboratory conditions (Anand & Spitzig, 1980, 1982; Bowden & Raha, 1970; Misra, Burlini, et al., 2009; Misra, Mandal, et al., 2009; Misra & Mandal, 2007). The polymer-based materials are chosen in analogue experiments as they provide suitable mechanical, e.g., creep rheology and optical properties, e.g., strain dependent birefringence. I used two hard polymers: 1) polymethylmethacrylate (PMMA) and polystyrene (PS) for my experiments. PMMA is a well-known polymer, commonly available as transparent sheets of various thicknesses. They are often sold under the commercial name of fiber glass or

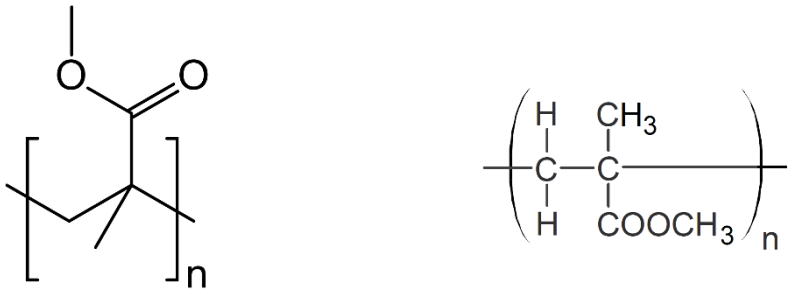

Figure 3.4. Chemical Structure of PMMA

Perspex. The IUPAC name of PMMA is Poly(methyl 2-methylpropenoate). PMMA is also known as methyl methacrylate resin. The chemical formula of PMMA is $(C_5O_2H_8)_n$. It has two typical

chemical structures (Fig 3.4). PMMA, like other polymers, is a large hydrocarbon molecule, consisting of many smaller structural units called monomers, covalently bonded together in any conceivable pattern. The long polymer chains of PMMA are thinner and smoother and can slide past each other, easily making it a softer polymer. PMMA that I used had a high mechanical strength, Young's modulus (1800-3100 MPa). It had a Poison's ratio in the range 0.35-0.4. Its creep behavior was investigated in triaxial tests. The polymer yielded at a stress of ~120MPa, and began to creep in ductile manner at room temperature condition under slow strain rates (Fig. 3.5.c). PMMA used in my experiments was optically transparent, transmitting up to 93% of the visible light, i.e., this is even more than some glasses. It had a refractive index of 1.49-1.498. The most important optical property of this polymer I utilized in my experiments is its strain sensitive optical transition. Annealed PMMA is optically isotropic and in thin sections it appears dark under cross

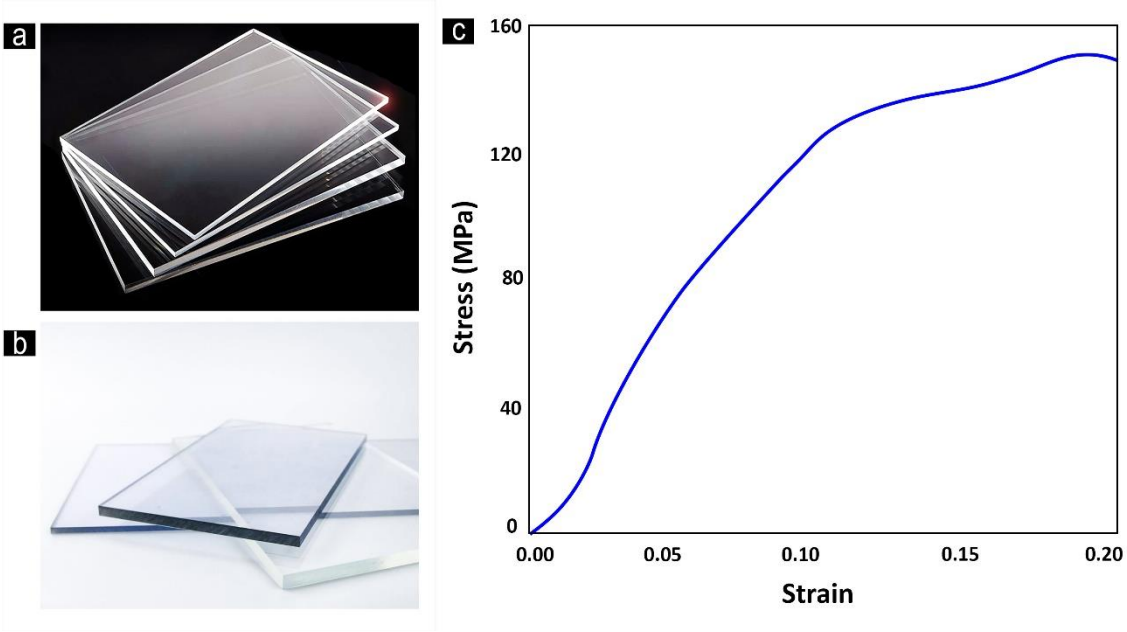

Figure 3.5. Commercially available polymers, a) PMMA; b) PS. Note a bluish tint in the PS sheets which allows us to differentiate between the two; c) Stress vs strain curve of PMMA

polarized light. The material becomes anisotropic, developing low to middle order optical birefringence under a plastic strain of ~5%. The degree of birefringence reflects the magnitude of

permanent (plastic) strain in the material. This strain dependent birefringence property is used to delineate high strain zones in the deformed PMMA models (de Joussineau et al., 2003; Küntz et al., 1998; Wong et al., 2006).

3.3.2. Polystyrene (PS) models

Polystyrene, like PMMA, is a hard polymer, extensively used in deformation experiments, especially to investigate the origin of shear bands in solids (Bowden and Raha, 1970; Bowden and Jukes, 1972; Anand and Spietzig, 1980). PS is optically transparent, often with a bluish shade, and the materials is commercially available in various forms, such as globules, block and thin sheets, usually sold under the commercial name of Styrofoam and Thermocol. The IUPAC name of PS is Poly(1-phenylethene-1,2-diyl), which is made from the monomer known as styrene. The chemical formula of PS is $(C_8H_8)_n$. Its typical chemical structure is

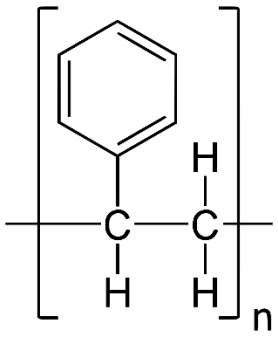

Figure 3.6. Chemical Structure of PS

PS molecules that consist thousands of atoms with the cumulative attractive force between the molecules are extremely large in size. The polymer chains can slide past each other to accommodate permanent plastic strain if the material is deformed at rapid rates, manifested in the form of shear bands.

In my study I used PS in the form of solid sheets. At room temperature, it was significantly stiffer than PMMA, where its Young's modulus was ~3000-3600 MPa, and Poison's ratio in the range 0.325 – 0.33. The material showed brittle-ductile behavior in room temperatures, forming shear bands (plastic strain localization), often associated with sharp fractures. At elevated temperatures and slow strain rates, the same PS behaved as an elasto-viscous material to produce diffused strain localization in the model. This could be utilized as an effective rock analogue material due to its strain dependent optical behavior, as in PMMA. It developed optical anisotropy with low to middle order birefringence under strain, where the degree of birefringence reflected the magnitude of permanent (plastic) strain in the material. This optical property was used to mark high strain zones in the deformed PS (Bowden and Raha 1970, Bowden and Jukes, 1972, Anand and Spitzig, 1982).

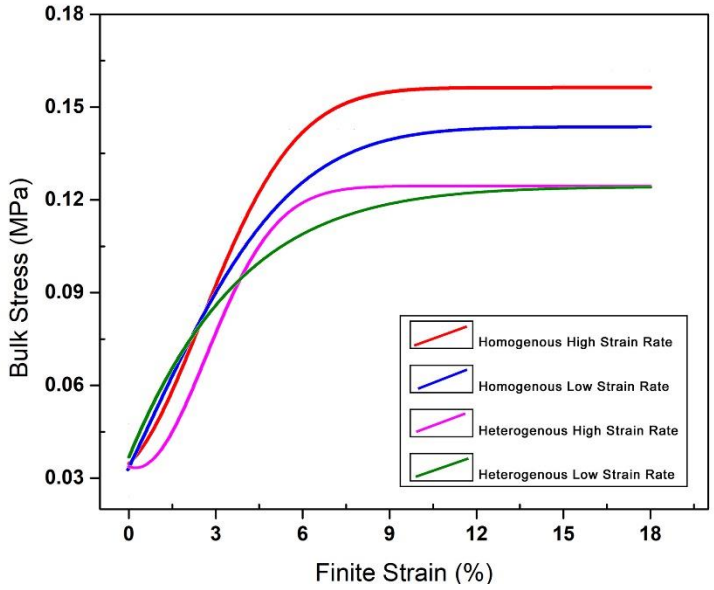

Figure 3.7. Stress versus strain relations for homogeneous and heterogeneous PS models obtained from laboratory experiments at low (2 x 10^{-5} sec^{-1}) and high (3 X 10^{-5} sec^{-1}) strain rates.

3.4 Laboratory setup

3.4.1 Soft model experiments

Talc-sand mixtures were added with a small amount of cement and water to introduce cohesion in the model, which was molded in a 17.5 cm × 9 cm × 7.62 cm rectangular box. The model was deformed in a pure shear condition (Misra, Mandal, et al., 2009; Treagus & Sokoutis, 1992) (Fig

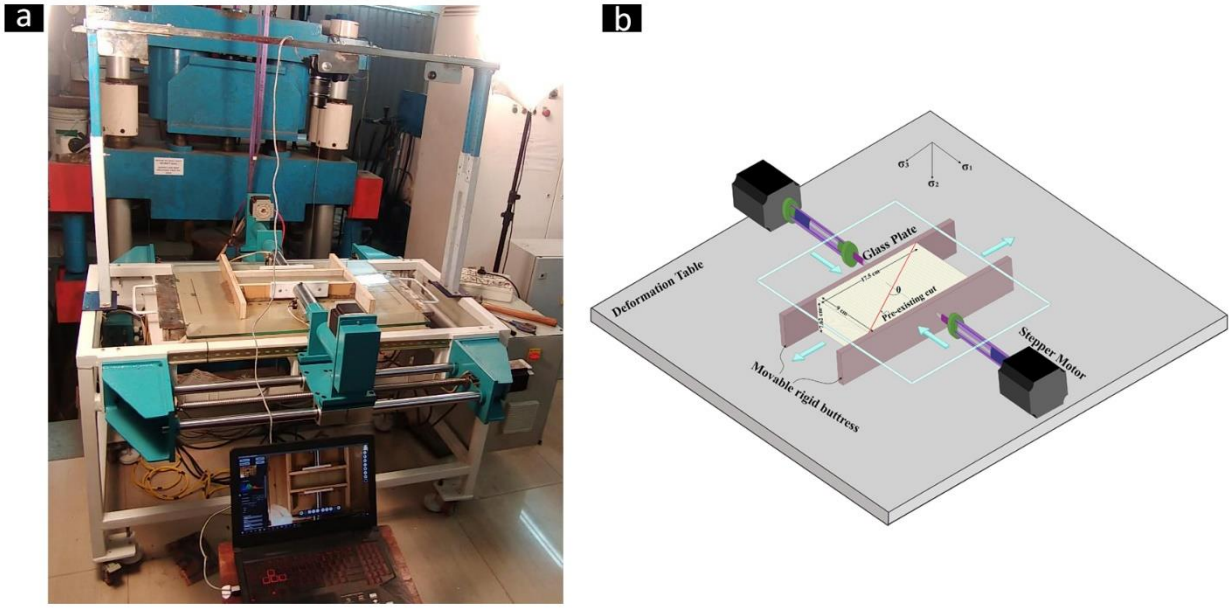

Figure 3.8. a) Shear deformation apparatus used for soft model shear experiments; b) Schematic of the laboratory setup for talc model experiments in pure shear on the shear deformation apparatus

3.8). The model was compressed by two 40 cm long, parallel vertical wooden plates, where their surfaces were lubricated with liquid soap to maintain a slip condition at their vertical interfaces, allowing horizontal extension of the model perpendicular to the compression direction (Fig 3.8.b). A thick horizontal glass plate was fixed at the top model surface to restrict the flow in the vertical direction to achieve a plane strain condition. The pure shear deformation in the model had the no-strain axis in the vertical direction. Liquid soap was used to lubricate the basal plate of the shear

box, as well as the top cover glass plate to minimize the friction during the model deformation. The convergence plate movement (6 mm/min) by two stepper motor driven pistons on opposite sides of the deformation table deformed the model at a bulk shortening rate of 0.133 min^{-1} (equivalent strain rate: 2 x 10^{-3} s^{-1} to 6 x 10^{-1} s^{-1})

3.4.2 Hard model experiments

3.4.2.1 Triaxial Test

Figure 3.9. Sample assembly in Triaxial Test Outfut for Hard Material Testing

Multiple deformation experiments were carried out under varying confining pressure and rheology to investigate the stress-strain relationship, failure mode and behavior and slip surface morphology in hard granular model materials that can replicate rock failures in laboratory conditions. The triaxial Test (Aimil Ltd. Make) was used to deform the experimental samples in a high pressure

chamber (Fig 3.10). The triaxial system consists of several parts; some of them were modified to deform hard granular materials. A brief description of the total assembly is provided below.

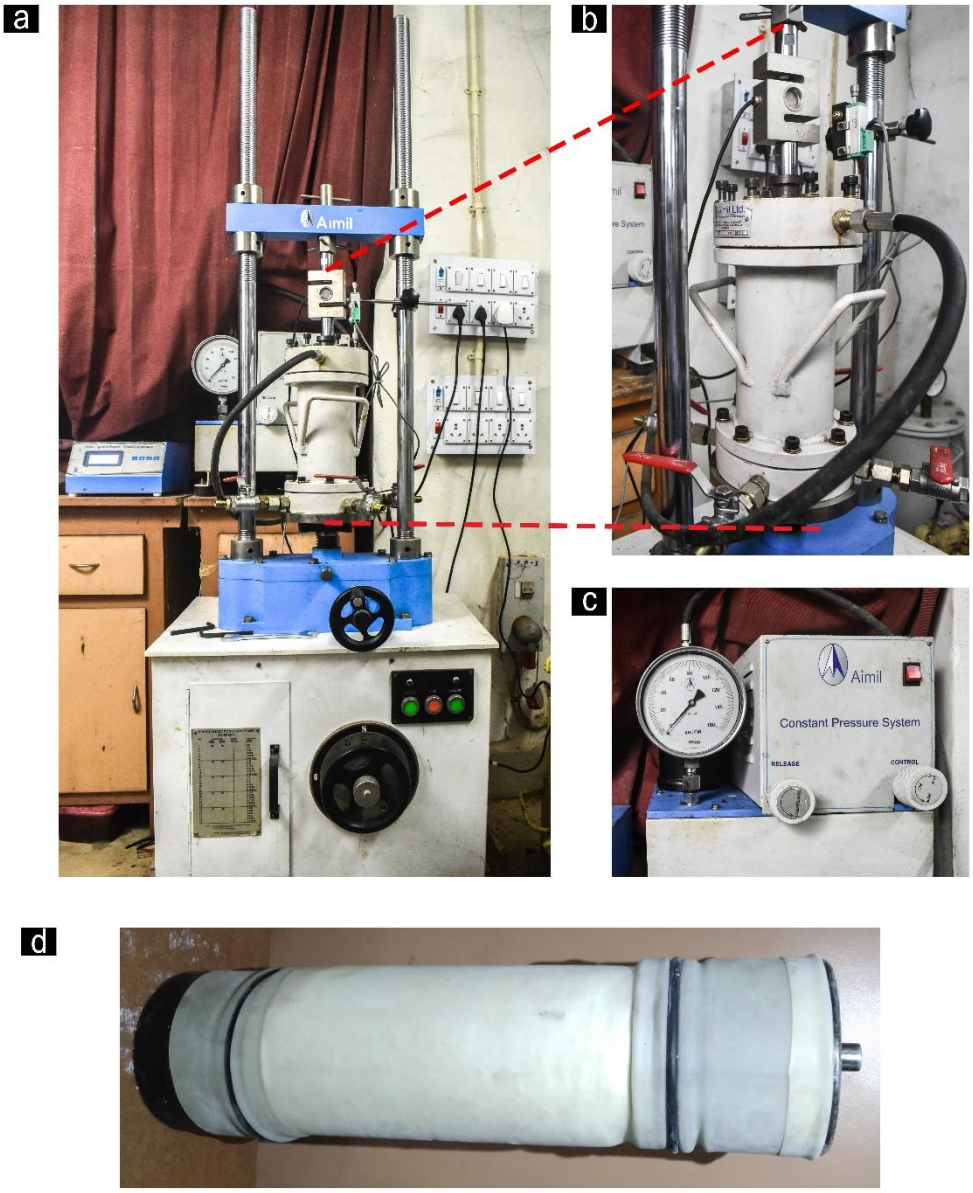

Figure 3.10. a) Triaxial test apparatus for hard talc blocks; b) enlarged view of the main sample assembly; c) Constant pressure system assembly which enable us to control the confining pressure in the main sample assembly; d) Sample assembly with two steel plates holding the hard cylindrical sample in between.

i. *150 bar AIM 211 Triaxial cell*: A metallic cylindrical chamber houses experimental models within a pressurized fluid medium (Compression Testing Machine (CTM) L-HM46 grade

hydraulic oil). The cell has a capacity to carry a maximum pressure of 150bar. The upper lid fixed to the chamber with nuts and bolts perfectly seals the fluid, and at the same time allows a vertical piston to move freely to thrust upon the top of the sample assembly. A load cell placed on the other end of the piston is used to measure the amount of load to the model during the triaxial experiment.

ii. The entire cylindrical chamber is placed on a platform that can move in the vertical direction. The platform movement is controlled by a motor-driven gear box to set the strain rate in the sample at a desired value.

iii. Motor-driven AIM 064 50kN Load frame: The 50kN load cell set upon the piston of the triaxial cell is designed to dynamically record the load on the sample and obtain the data in a digital form with a resolution of 0.01kN.

iv. The sample assembly inside the triaxial cell comprises of the sample with two steel plates and two additional iron cylinders to hold the sample in position (Fig 3.10.d). The whole arrangement is covered by a latex jacket, used to prevent oil, and at the same time transmit the confining pressure to sample. The sample is thus fixed at one end by the load cell and the piston, leaving the other end subject to movement with the moving chamber. The load cell reads the dynamic load on the sample.

v. The displacement cell (LVDT Sensor) is fixed at the upper end of the system to track the upward movement of the deformation chamber. The LLVDT is used to measure the shortening in the sample with a resolution of 0.01mm.

vi. AIM 213 Constant Pressure System for Rocks 160 bar: The deformation chamber is attached to a hydraulic pump, which drives oil into the chamber to raise the confining pressure to the sample. The confining pressure can be controlled and maintained at a fixed value during the experiment, which is recorded manually with a resolution of 1bar.

vii. AIM 085-1 Triaxial Electronic Conversion Kit: The load cell and the displacement cell readings are recorded dynamically at an interval of 1 second with the help of a data acquisition system attached to a computer. The data is processed by a software provided by Aimil.

3.4.2.2. Uniaxial Compressional Set up for Block Samples (Aimil Ltd.)

Hard analogue models were deformed at room temperature (~30°C) under a hydraulically driven compression machine (Make: Aimil Hydraulic Press) (Fig. 3.11). The Hydraulic press has a load capacity of 2000 kN, with a power pack with a manually controlled hydraulic oil injection system. The power pack is equipped with a gear to control the flow of oil in the main piston. It also has a hydraulic pressure gauge that gives us an accurate reading of the line pressure from the power pack to the piston (Fig 3.11.b). The system is capable of producing pressures at a strain rate of ~1 X 10^{-5} to ~1 X 10^{-5}. The main sample assembly consists of a jig and a T-piston (described in the following paragraph). There is a main dial gauge connected with the load cell of the system which gives the accurate reading the deformational pressure raised in the system (Fig. 3.11.c). The overall dimension of the system is 80 cm X 30 cm with the main sample assembly of 12cm X 12cm.

The compression experiments were conducted on hard models housed in a deformation jig under a plane strain condition. As mentioned above the jig is 12cm X 12cm X 9.6cm. The jig and the T-piston both are made from high strain steel to withstand the huge deformational load. They are thoroughly chrome plated to avoid rusting and subsequent damage. The sample is placed between the jig and the T-piston (Fig 3.11. a) and the whole jig setup was placed on the basal ram of the hydraulic press. Using the power pack, the ram was lifted vertically in the upward direction to thrust the jig against the top platen of the load frame. The T-piston thereby moved relatively down to the housing block of the Jig and developed a vertical compression in the sample. Under

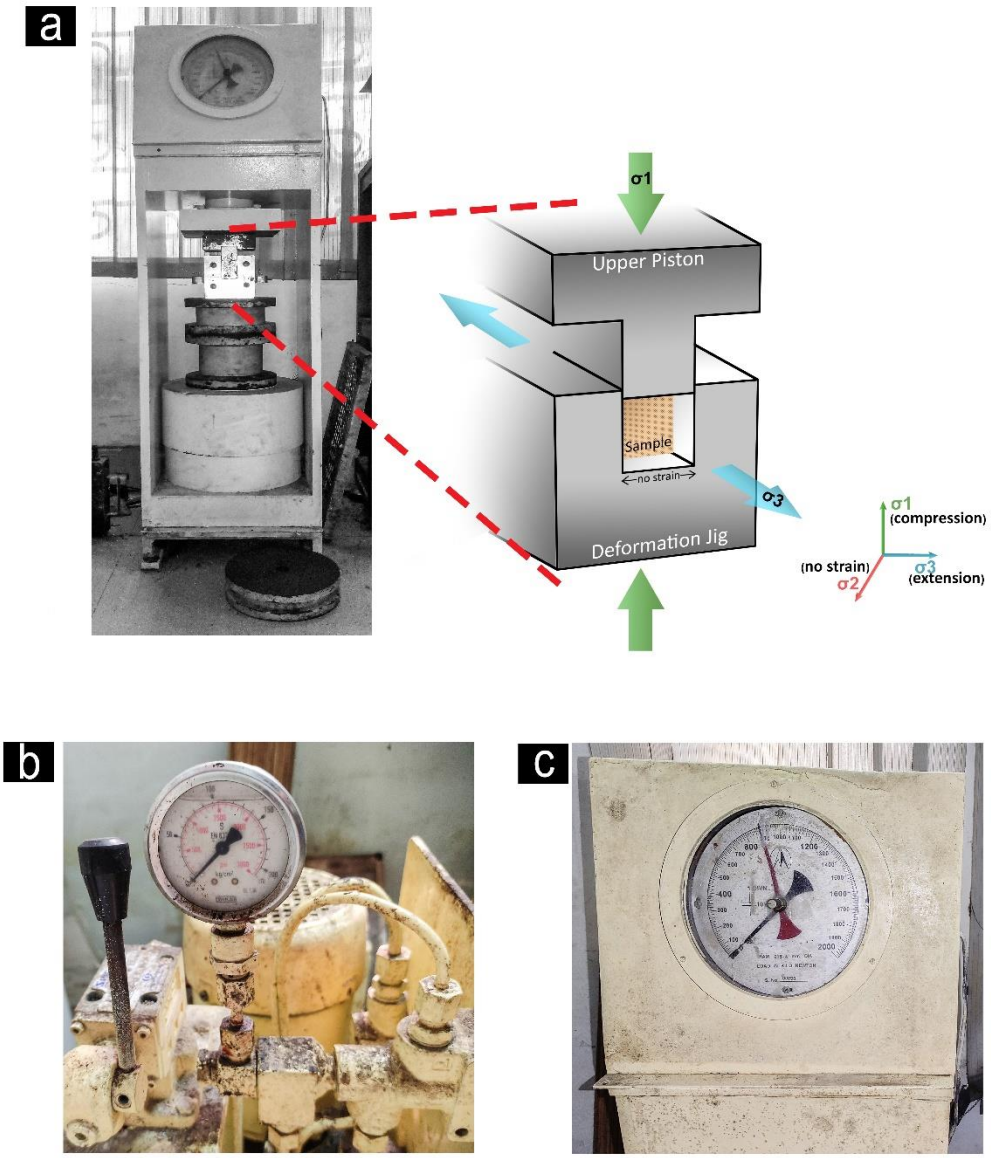

Figure 3.11. a) Uniaxial deformation apparatus used for hard model deformational experiments and zoomed in view of the metal jig for PMMA and PS model experiments in normal compression tests; b) Dial gauge for Hydraulic power pack; c) Dial gauge for load cell attached with the upper ramp.

this condition the model underwent pure shear deformation with a vertical principal axis of compression (σ_1-axis) and the least principal stress axis (σ_3) oriented along the horizontal principal model extension direction (Fig. 2.3.1.a). The intermediate principal axis of stress (σ_2) coincides with the no-strain direction, perpendicular to the jig walls. During model compression the jig walls

were greased to minimize friction to the model, and obtain homogeneity in the bulk model deformation.

3.5 LASER profilometer

A line of this thesis work focused on the problem of surface roughness properties of tectonic fractures and shear surfaces. To implement this study, I used a Laser based sensor system (OptoNCDT 1420) (Fig. 3.12.a), which offers a unique combination of speed, size, performance and application versatility in the range of compact triangulation sensors. The Laser sensor with an integrated controller is placed within a restricted installation space of a frame, as illustrated in Fig 3.12.b.

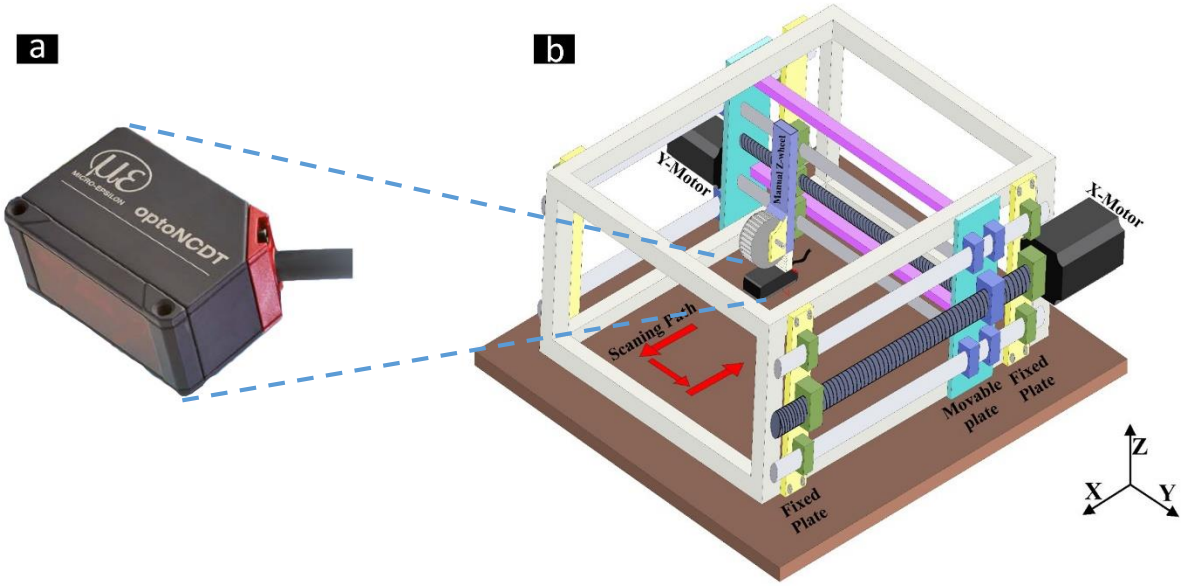

Figure 3.12. Laser System for Roughness analysis and data processing. a) The optoNCDT 1420 Laser; b) the housing framework with two draw wire sensors for controlled movement.

The frame consists of horizontal and vertical bars in a rectangular arrangement, mounted with two parallel fixed rods and a motor-driven rotating spiral rod running in the middle of the parallel rods

on one side of the frame. The rotational motion of this rod produces a translational motion along its length direction (X-axis of the reference frame). The frame has a similar mechanical arrangement on the other side, which simultaneously generates translational motion in Y direction (Fig. 3.12.b). The frame had two fixed draw-wire sensors that can be operated simultaneously to

Model		ILD1420-25
Measuring range		25mm
Start of measuring range	SMR	25mm
Midrange	MMR	37.5mm
End of measuring range	EMR	50mm
Linearity [1]		20 - 25µm
		≤±0.08 ... 0.1% FSO
Repeatability [2]		1µm
Measuring rate [3]	0.25kHz / 0.5kHz / 1kHz / 2kHz / 4kHz	
Light source	Semiconductor laser <1 mW, 670nm (red)	
Permissible ambient light		10,000 lx
Spot diameter ±10%	SMR	100 x 140µm
	MMR	120 x 130µm
	EMR	390 x 500µm

Table 3.1. Detailed technical specifications of the OptoNCDT 1420 Laser sensor.

track the X- and Y- displacements. A point laser scanner is fixed at the end of a vertical plate attached to a screw-driven holder, which moves the sensor manually in the vertical direction (Z-axis) and set it at a desired height from the surface of the sample rested on the horizontal base of the frame. The height was adjusted to keep the scanning surface within the permissible range (25 to 50 mm) of the laser sensor (Table 3.1). The Auto Target Compensation (ATC) system within

the sensor provides stable distance signal control. The high-performance optical system projects the small light spot sharply onto the measurement object which enables to even detect smallest components and every little detail reliably. The Laser sensor unit is fixed to an automated movable plate, driven by a screw-operated rod aligned in Y-direction. The entire Laser bearing system moves to-and-fro in X-direction, which is implemented with a motor-driven screw rod, as demonstrated in Figure. The frame is thus designed to move the Laser sensor at any horizontal direction by adjusting the x and y velocity components. The rotational motion of the motor can be set at a desired speed (RPM range: 1 to 1000) and scan the sample surface at a specific horizontal velocity (range 10^{-5} m sec^{-1} to 10^{-1} m sec^{-1}) of the sensor in horizontal directions. An optimum combination of the RPM was chosen and the sampling rate (500 sec^{-1}) to obtain a desired resolution of the spatial data (60 μm). The laser scanning was performed by a to-and-fro motion of the sensor

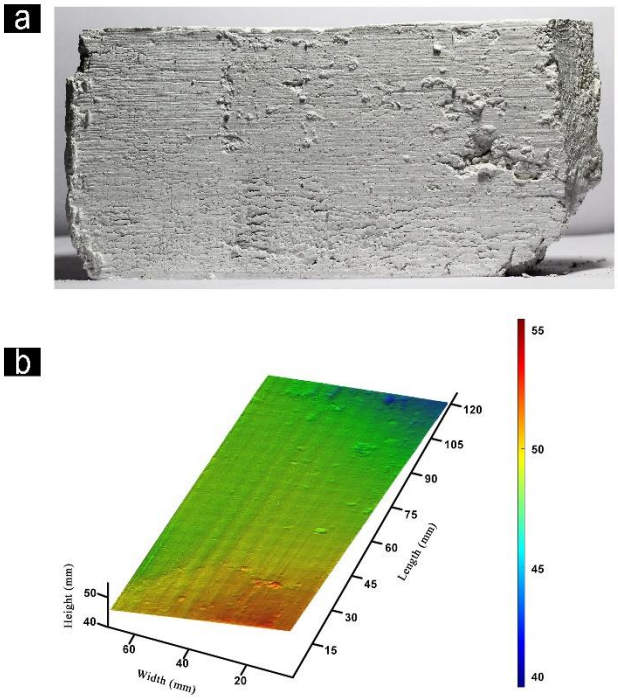

Figure 3.13. a) Deformed talc block showing the shear surface with characteristics roughness; b) 3D topological surface constructed using CloudCompare from the Laser sensor data.

in horizontal directions, forward motion to cover X full length of scanning area → forward 1step in Y direction (0.06 mm) → backward X full length of scanning area→ forward 1 step in Y

direction (0.06 mm). This sequence was repeated to cover the entire area of the sample surface. The electrical signals (voltage data) from the laser and the draw-wire position sensors were synchronously captured in a data acquisition system at the interface with a workstation. The acquired data were then processed using a software (3D Scanner by N K Instruments) code to the spatial distances, X, Y and Z. The data sets were then used to construct topographic profiles along and across the slickenlines, which were stacked to reconstruct a 3D topological surface with the help of MATLAB and Cloud Compare software. The areal occupancy of slip and stuck zones on a shear surface was evaluated using the ImageJ software (Fig. 3.13).

Chapter 4

Roughness Analysis of Shear-Failure Surfaces

4.1. An overview of the existing studies

A range of structural imprints in deformed rocks records slip activities on fault and fracture surfaces in tectonic belts. Among them, slickensides are the most prominent fingerprints of slip movements that provide critical information about the roughness making processes on faults and different types of shear surfaces. Many workers have claimed that they can be used as a reliable tool for a paleostress analysis (Allmendinger et al., n.d.; Bott, 1959; Davis et al., 2011; deformation & 1994, n.d.; Gudmundsson, 2011; Mattauer, 1980; Michael, 1984; Ramsay & Huber, 1987). Fault slickensides are typically polished, striated surfaces, often containing prominent lineations, called *slickenlines,* defined by a variety of long ridges, grooves, and directional mineral growth fibers. Slickenlines are excellent a kinematic indicator, as they grow tracking the instantaneous slip vectors. Field geologists use them extensively in the field to find the relative motion on tectonic faults (Doblas, 1998a; J. P. Petit, 1987). However, recent analyses suggested that fault surface asperities can significantly perturb the global stress field, and the local slip consequently may not track the direction of maximum resolved shear stress on the fault (Kirkpatrick & Brodsky, 2014a). Such geometrical or mechanical heterogeneities can even largely influence the large-scale slip patterns. Furthermore, such fault asperities can seriously modulate a range of slip-driven phenomena, such as bulk shear resistance to slip, seismicity patterns (Voisin et al., 2007), syn-shear variation in the slip dynamics (Candela, Renard, Bouchon, et al., 2011), and growth of fault damage zones (Kim et al., 2004; Misra et al., 2015; Shipton & Cowie, 2003).

The fault dynamics research in the last three decades has established a line of theoretical studies to quantify the roughness characteristics of fault and fracture surfaces using a variety of mathematical tools and techniques. This research has recently advanced to a great extent, primarily in the context of the analysis and prediction of fault slip dynamics. It is now a well-accepted fact that fault/fracture roughness is a geometrical phenomenon characterized by a specific statistical distribution (Stephen R. Brown & Scholz, 1985; Candela et al., 2009a; J. J. Lee & Bruhn, 1996; W L Power et al., 1987b; William L Power & Tullis, 1991; Renard et al., 2006). Geometrical asperities, such as ridges, grooves, and crystal fibers that form the surface roughness obey a definite scaling law with the fault dimensions (Stephen R. Brown & Scholz, 1985; Candela et al., 2009b, 2012a; Fondriest et al., 2013; J. J. Lee & Bruhn, 1996; W L Power et al., 1987a; Renard et al., 2006; Sagy et al., 2007a; Sagy & Brodsky, 2009b; Siman-Tov et al., 2013). Field measurements have indicated self-affine fractal properties of the roughness irregularities, showing a power-law relation of their amplitude to wavelength ratios with the scale of observations (Kirkpatrick & Brodsky, 2014b). Earlier workers used mainly mechanical profilometers for in-situ field measurements (Stephen R. Brown & Scholz, 1985; J. J. Lee & Bruhn, 1996); the techniques substantially advanced in course of time with advent of new instrumental facilities. For example, recent high-precision, high-resolution measurements have employed ground-based light detection and other optical scanning methods, such as optical profilometers to perform a quantitative analysis of fault roughness (Bistacchi et al., 2011a; Brodsky et al., 2011a; Candela et al., 2012a; Renard et al., 2006; Sagy et al., 2007a). The spectral analyses based on these new techniques also predict a power law relation of the fault-surface topography with the corresponding wavelengths (Candela et al., 2012a). Some of these field-based studies reported anisotropic properties of the

roughness, characterized by directional variability of the degree of roughness, their smoothest geometry being along the slip direction (Kirkpatrick & Brodsky, 2014b).

Several criteria, for example, roughness morphology, have been proposed to classify natural slickensides, with an objective to use them as kinematic indicators (Doblas, 1998a; J. Petit et al., n.d.; J. P. Petit, 1987). Based on the mechanisms of asperities formation, Twiss & Moores, (1992) have classified fault slickenlines broadly into three types: structural slickenlines, mineral slickenlines, and slickenfibers. Structural slickenlines originate from mechanical wearing and plowing by hard asperities on relatively softer substrates. The hard asperities can experience granulation during their movement against high frictional strength, forming a linear trail. Mineral slickenlines result from accumulation of streaks from the smearing out of mineral grains or soft asperities behind hard asperities. Fault movements often generate locally positive and negative dilation zones in the neighborhood of geometrical irregularities. At the opening (positive dilation)

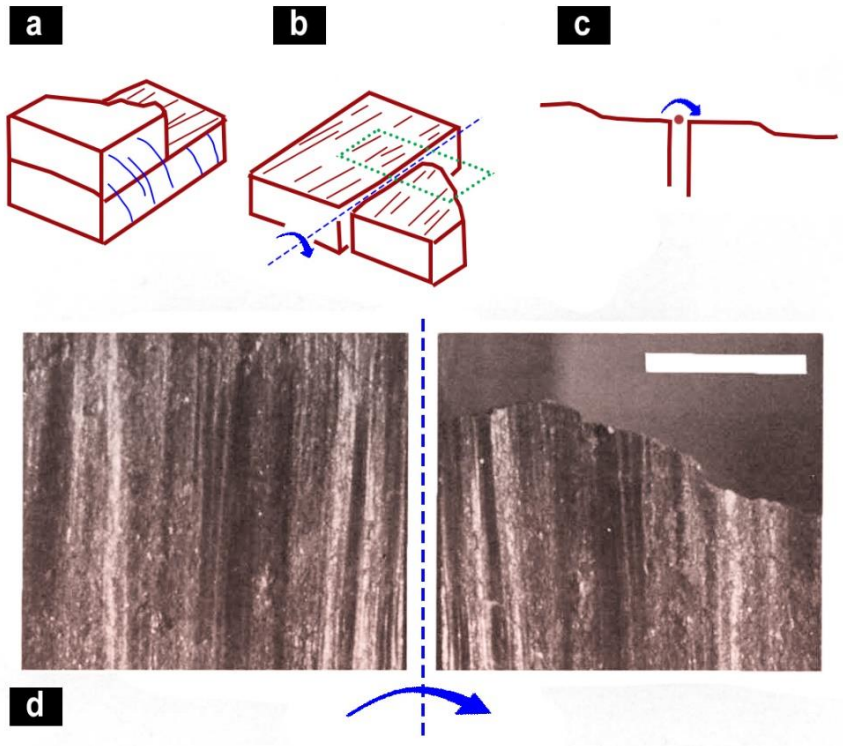

Figure 4.1 . a) Schematic representation of natural sample collected from Latham, New York (Means 1987); b) Specimen opened like a book; c) Schematic view in plane normal to the axis of opening, to show how the features nest; d) Real photograph of the sample showing the unique slickenside. *(Redrawn from Means, 1987).*

locales slicken fibers grow tracking the local displacement vectors.

Ramsay & Huber, (1987) proposed a crack-and-seal mechanism for this type of slickensides formed by progressive crystal fiber growth in the course of fault movement. Negative dilation zones undergo pressure solution, forming a type of slickenline, called slickolite (Bretz, 1940). From wax model experiments, Means, (1987) recognized a completely new type of slickenside roughness (Fig. 4.1), which cannot be explained by any of the mechanisms discussed above. This new type is characterized by the following geometrical features: (1) Ridges are as frequent as grooves, with nearly identical dimensions and shapes, and (2) the slickenside topography on one side of the fractures perfectly fits into that on the other side (Means, 1987). Furthermore, this variety is characterized by the absence of any hard asperity, which rules out the possibility of mechanical wearing as a possible mechanism. Though this type of rupture roughness was discovered way back in 1987, its mechanism remained unexplored despite a significant advance in fault studies.

The present thesis work is motivated by field observations of slickensides in the Singhbhum Shear Zone (SSZ), which separate the Proterozoic meta-sedimentary sequence thrusted over the Archean craton in eastern India (Fig. 4.2; (D. Mukhopadhyay, 2001; Saha, 1994)). This study explores the potential factors controlling shear fracture roughness with the help of analogue experiments and also address the origin of the unique type of non-abrasive slickensides discussed above. A new computational method is developed to perform a roughness analysis of the shear fractures observed in the field and analogue experiments. Based on numerical model simulations, mechanical wave instabilities in the soft interface between two walls is finally proposed as a potential mechanism of the linear irregularity formation on shear surfaces.

4.2 Field investigation

4.2.1 Study area

Slickensides in massive quartzites, exposed locally in southern parts of the SSZ and some adjoining parts of the Singhbhum Fold Belt on the north of SSZ were studied in the field (Fig. 4.2.). I chose two field locations: (1) Patherogora region near old Surda copper mines and (2) Tentuldanga region. Patherogora is a small village in Purbi Singhbhum district, Jharkhand (22°32′37.911″N, 86°26′31.223″E, altitude: 146 m, accuracy: ±3 m), and falls in the southern part of SSZ. The area has excellent outcrops of slickenside bearing massive quartzite. The second

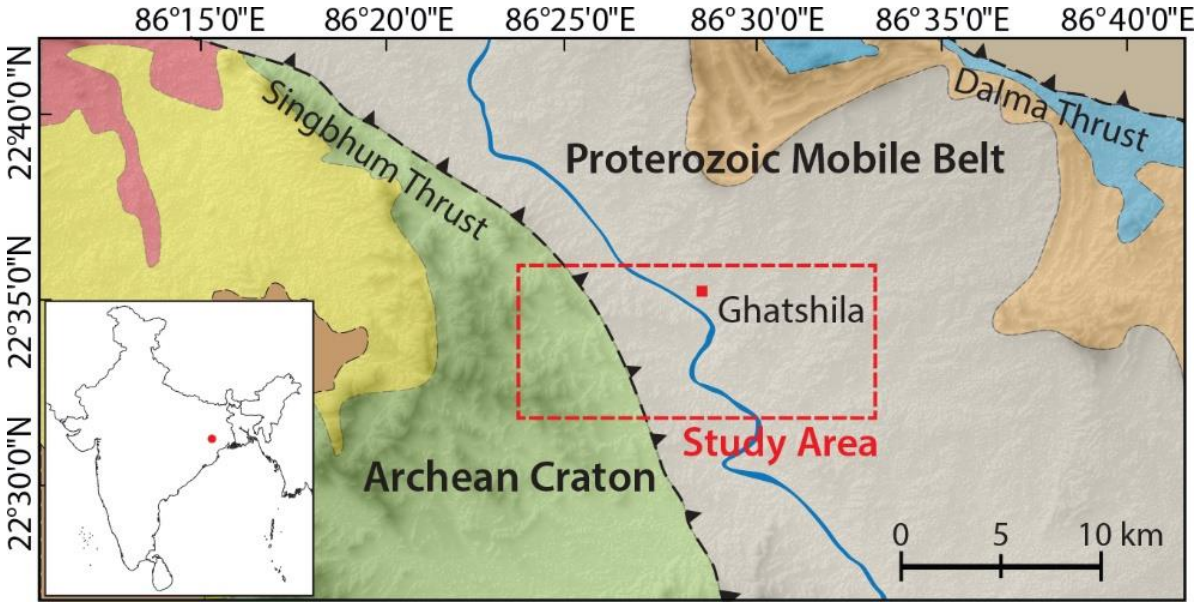

Figure 4.2. Geological map of the Precambrian Singhbhum craton in eastern India. Red line shows the north-dipping Singhbhum Shear Zone (SSZ) (after Saha, 1994). Our study area is indicated with the green box at the south eastern flank of SSZ.

outcrop is situated in a place, called Bagula (22°33′ 08.198″N, 86°30′49.819″E, altitude: 118 m, accuracy: ±3 m) near Tentuldanga village (~6 km from Ghatshila). This outcrop also shows slickensides in a massive quartzite host.

4.2.2 Geological framework of the study area (SSZ details)

The Singhbhum Shear Zone demarcates the boundary between Singhbhum Fold Belt in the north and the Singhbhum craton in east west and south (D. Mukhopadhyay & Deb, 1995).

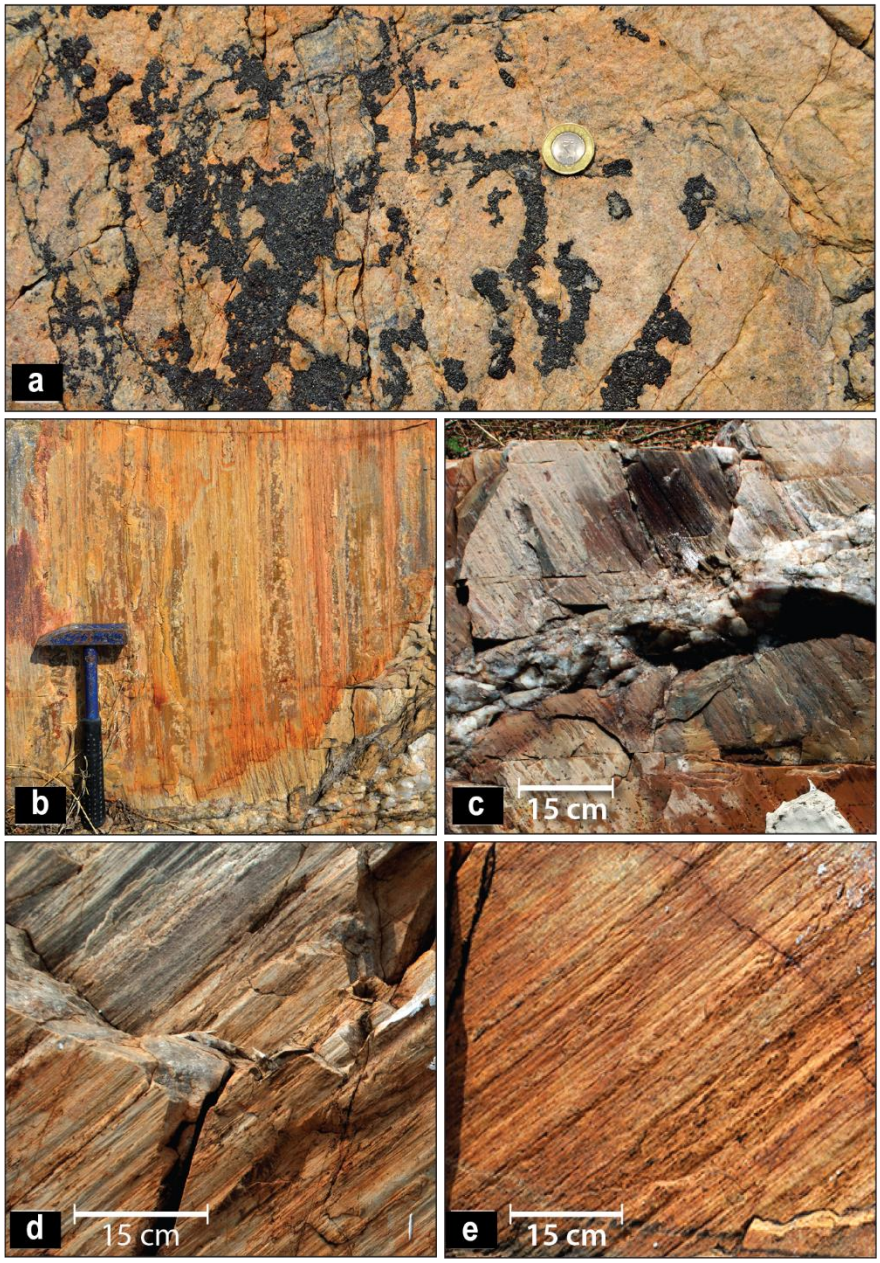

Figure 4.3. Three principal types of slickensides observed in the SSZ area. (a) Type 1: Smooth fault surfaces without any discernible linear roughness; (b) & (c)Type 2: Slickensides with lineation defined by fine scale ridges and grooves; and (d) & (e) Type 3: Slickensides with wavy linear roughness defined by ridges and grooves of varying coarseness. Dashed redlines denote the overall slip direction. The lengths of hammer and diagonal scales are 30 cm and 15 cm, respectively.

Geographically, the SSZ trend changes from E-W in the western part to NNE-SSW in its eastern segment (Mukhopadhyay and Deb, 1995), with a westerly tapering attitude (Dunn, 1929). However, according to some workers, the SSZ extends along the North-western boundary of Singhbhum Granite (Gupta et al., 1981; Sarkar & Saha, 1963). The shear zone is a strongly arcuate belt (>150km long) of intense ductile shearing, with profuse polymetallic mineralization and soda-granite magmatism. Along its entire stretch, mica schists, lenses of granite and feldspathic schists and quartzites have been sheared to mylonites and phyllonites (Ghosh & Sengupta, 1987; Sengupta & Ghosh, 1997). The thick mylonitic zone occur over a depth of more than 3km of dip length. This belt is characterized by prominent mesoscopic northerly plunging reclined to nearly reclined folds and a down-dip lineation parallel to the dominant fold axis (D. Mukhopadhyay & Deb, 1995). Though the structural evolution is presumed to be uniform, the SSZ shows strong heterogeneity, with varying intensity of ductile shearing from domain to domain and development of structures through geological time scale. SSZ is believed to have suffered two phases of brittle and four phases of ductile deformation, along-with intermediate stages.

4.2.3 Field observation and sample collection

In both the study areas: Patherogora and Bagula, the slickensides do not appear to have formed by either mechanical plowing of hard asperities or by crystal growth fibers (Fig 4.3.). Slickensides-bearing shear surfaces generally occur in sets with parallel orientations, where their spacing varies from a few millimeters to several centimeters. They locally form domains of very closely spaced

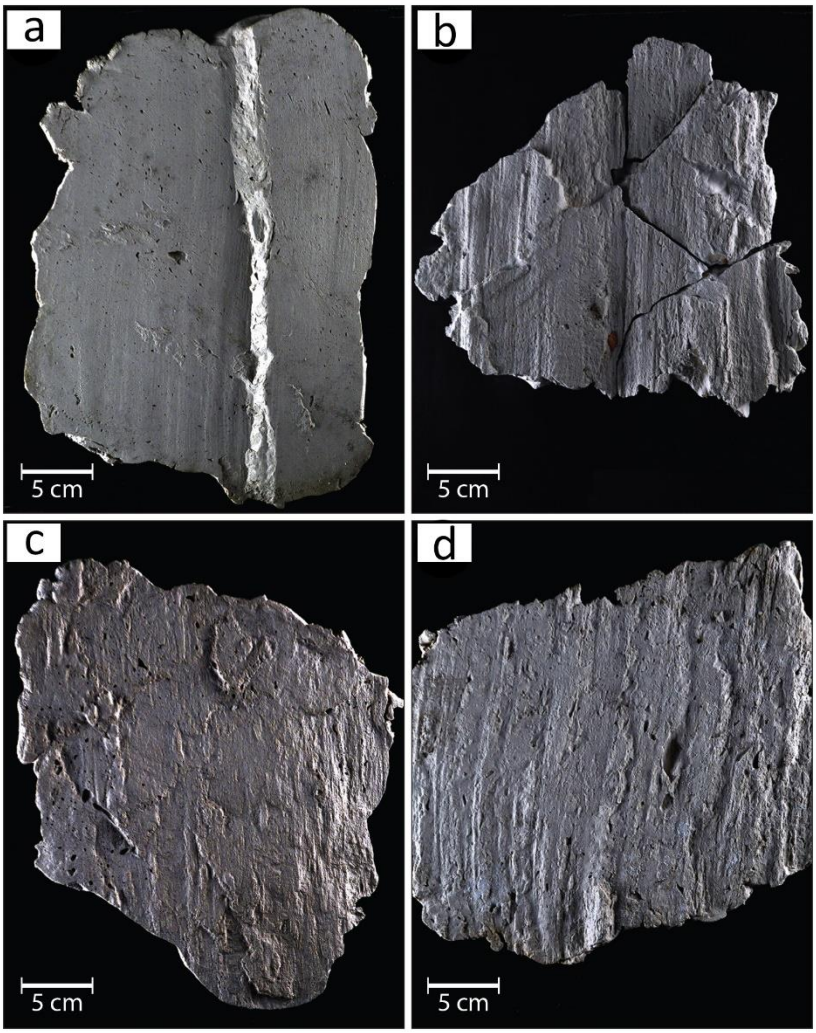

Figure 4.4. Casts of slickensides with varying roughness observed in the field. (a) Smooth shear surfaces, but with down-dipping, low-amplitudes waves, forming a distinct fine scale slickenlines structure. (b) Shear surfaces with strongly linear roughness, defined by cylindrical ridges and grooves in different orders. (c) Shear surfaces with heterogeneous linear roughness. There are patchy zones showing weak linearity in the roughness. (d) Shear surface roughness with wavy appearance of long ridges and grooves at varying spacing.

multiple shear surfaces, often showing drags on markers, for example, primary layers cutting across the shear domains.

Isolated shear surfaces at the core of thin zones of localized ductile strains were also observed in deformed rocks. They are geometrically similar to those reported from fault zones in the literature (Chester et al., 1993; R H Sibson, 1977; Richard H. Sibson, 1986). The rock

exposures in the field area show sporadically internal primary bedding and laminations, which were used to study the magnitudes of finite slip on the shear surfaces. Several locations with relatively well-preserved slip surfaces were chosen, where the macroscopic shear displacements could be estimated from offsetting of primary laminations and bedding in quartzites. The slip amounts were estimated to be ranging from 0.6 to ~2 cm. However, lack of availability of such markers extensively in these exposures posed a limitation in the systematic field study to analyze the slickenside geometry as a function of finite slip displacements, as reported in earlier studies (Brodsky et al., 2011a; Sagy et al., 2007a).

Macroscopic observations revealed no abrasion-related structural features, such as gauges and breccia along the shear surfaces (Y. Boneh et al., 2014; Chester & Logan, 1986). Their absence suggests that the shearing motion probably took place broadly in a ductile to brittle-ductile regime, as reflected locally from drag structures in their walls. This study, however, excludes any microscopic analysis of sheared rocks, which would be required to recognize the deformation mechanisms involved in the shear motion.

An extensive search for fault surfaces with well-preserved slickensides was conducted, focusing upon the varying roughness geometry. The scale of observations ranged from ~10 cm × 10 cm to ~10 m × 10 m. Special care was taken in the field while capturing photographic images, keeping a fixed day timing to obtain nearly the same natural illumination level at the exposure. For laboratory processing and analysis, I prepared in-situ casts of slickensides from the exposed fracture surface by using plaster-of-paris slurry in the following way (Fig 4.4.).

4.2.4 Casting Method on natural fracture surface

To calculate the shear fracture roughness of field samples in the laboratory, we casted some of the well exposed intact shear fractures in massive quartzite. The casting was prepared using commercial plaster of Paris (POP), compositionally gypsum powder. We cleaned the surface with fresh water and allowed it to dry. The dry surface was then brushed with coconut oil on the selected portion of the shear fracture surface. The purpose of using this oil film was to prevent sticking of the POP layer to the surface. In the next step we prepare a slurry of POP and spread over the surface to form a 1.5cm thick layer on the selected area. During this process special care was taken to avoid any air bubble trapped in the cast layer. The slurry was then left undisturbed for 23 hours, allowing the layer to harden into a solid cast. The hardened POP layer was separated from the

Figure 4.5. A plan view of the Plaster of Paris layer used to cast a natural fracture surface in quartzite.

surface carefully with the help of a chisel and a hammer. The cast eventually captured the roughness morphology of the shear fractures with minute details.

4.3 Laboratory study

4.3.1 Model set up

Several trial experiments with various types of granular materials were conducted and finally settled on a wet sand-talc mixture for the present modeling. The advantage of using such a composite material is that it is possible to manipulate the rheology of model material by varying the sand:talc volume ratio. Pure sand undergoes shear failure like a typical Coulomb material, producing sharp shear fractures (Lade, 2006; Misra, Burlini, et al., 2009; Wang & Lade, 2001).

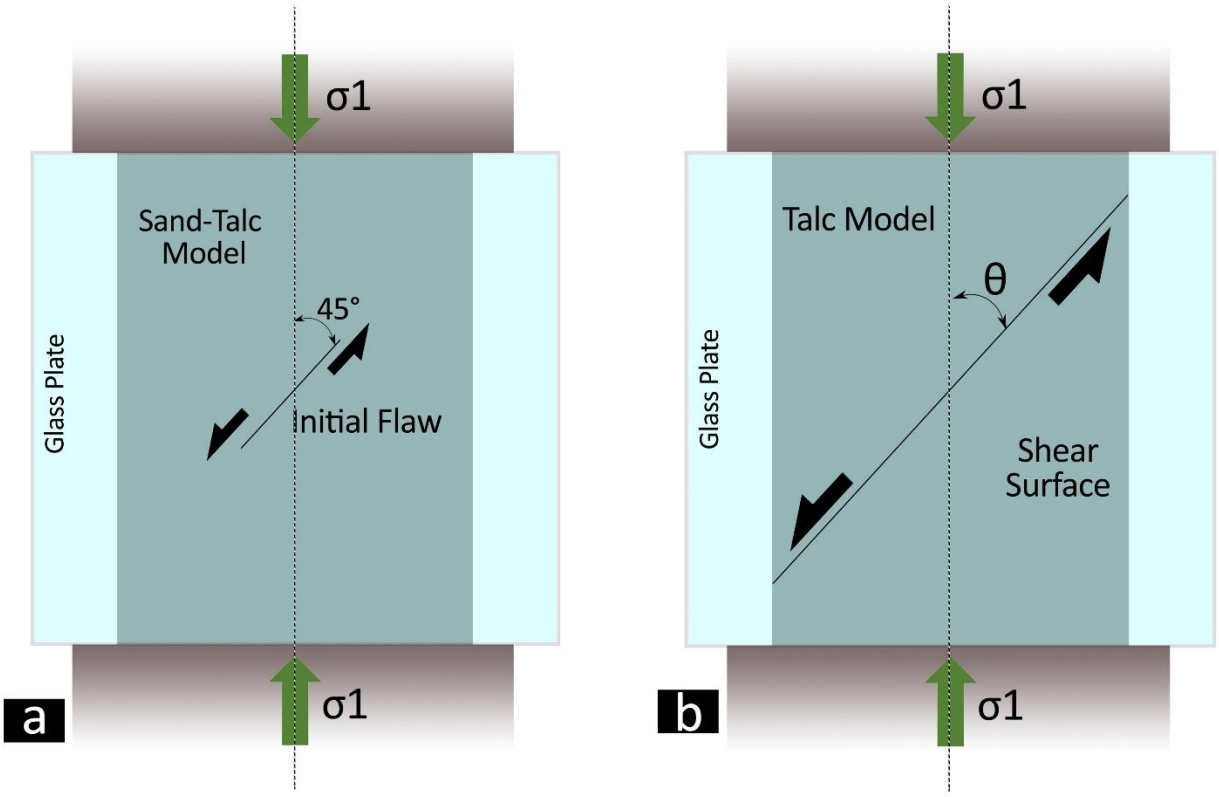

Figure 4.6. Schematic diagram of experimental set up of Sand-Talc and Talc models for a) Type I Experiment; b) Type II Experiment. Note that for Type I experiments, the initial flaw is predefined at 45 with the σ1; whereas for Type II experiments, the through-giong flaw is kept at an angle θ which varies for different models.

The cohesive strength (~5.5 kPa) and the angle of friction (27°) were measured from triaxial tests. Increasing talc content transforms the mixture to be more and more ductile, yielding plastically at a threshold stress. The failure behavior of pure talc and sand-talc (1:1) mixtures in wet condition was investigated. The materials underwent shear failure at a yield stress of 200 and 155 kPa, respectively, and had appreciable strain softening after the first yield point (Brooks et al., 1991), as reflected in a pronounced stress drop with increasing strain (Fig 3.3.a).

I chose commercial talc (grain size: 0.3 to 50 μm, average: 20 μm), and coarse (500 μm) and fine-(150 to 200 μm) grained natural sand for the experiments. To introduce cohesion in the model materials, cement and water were added to the sand-talc mixture in the volume ratios, 1:6 and 1:9, respectively. Their homogeneous mixture was then molded into a 17.5 cm × 9 cm × 7.62 cm rectangular block. The model was deformed in a pure shear condition under horizontal compression.

A thick horizontal glass plate was placed at the top model surface in order to restrict the flow in the vertical direction, allowing the material to flow entirely in the horizontal direction, perpendicular to the compression direction (Fig 4.6.). The pure shear in our model thus had the no-strain axis in the vertical direction. Liquid soap was used to lubricate the model interfaces with the vertical pushing walls as well as the top cover glass plates, significantly reducing the wall friction during the model deformation. The experiments were run on the following two types of models.

Type 1 model: This experiment had a small initial planar flaw (vertical planar cut with a length of 2 cm) in the middle of the talc-sand block at an angle of 45° to the principal compression direction ($\sigma 1$) (Fig 4.5.a) . The flaw acted as the location for shear rupture nucleation in the model. Type 1 experiments were performed in multiple sets by varying the sand:talc volume ratio: (i) 1:0

(pure coarse sand), (ii) 1:1 (coarse sand-talc mixture), (iii) 1:1 (fine sand-talc mixture), (iv) 1: 4 (fine sand-talc mixture), and (v) 0:1 (pure talc).

Type 2 model: The model had a throughgoing cut, which activated to produce a shear fracture during the compression (Fig 4.5.b). The model block was prepared by using only talc, added with cement and water. The block was cut into two halves at a desired angle (θ) to the principal compressive stress axis (σ1). The two blocks were then reunited and left undisturbed for about 2 hours, allowing the cut zone to heal sufficiently. However, the cut remained a weak zone to localize shear rupturing when the model was subjected to pure shear deformation. The main purpose of using this method was to obtain a smooth, planar slip plane, which exclusively produced roughness features due to slip motion. A series of experiments were ran on Type 2 models with varying θ (30°, 45°, and 60°).

The progressive deformation was monitored through the top glass plate in the pure shear box. The setup produced shear fractures with either dextral or sinistral sense of slip, depending upon the fracture orientation with respect to the principal compression direction. The differential horizontal movement of the walls gave rise to horizontal slickenlines on the slip surfaces. Earlier studies have shown that shear surface roughness can progressively change with increasing finite displacement (Brodsky et al., 2011a). Nearly the same amounts of finite slip on shear surfaces was maintained in all the experiments. Thus, the surface roughness variations we observed in the models could be directly attributed to the variables considered in this study. The finite displacement was ~4 cm for Type 1 models, whereas it was ~4–6 cm for Type 2 models, depending upon the initial fracture orientation. In overall, the finite slip scaled roughly 20% of the shear surface length. The deformed model was left undisturbed for about a day, allowing the block to

harden and freeze the slickensides on the slip surfaces. The two halves were then separated from each other to study the 3-D roughness characteristics of shear surfaces.

4.3.2 Model observation

Type 1 models of pure coarse sand produced excellent shear fractures, but without any prominent linear features on them (Fig 4.7.a). The models with 1:1 coarse sand-talc mixture also did not develop typical slickensides (Fig 4.7.b). They showed weak traces of slip motion, albeit locally on the shear fractures.

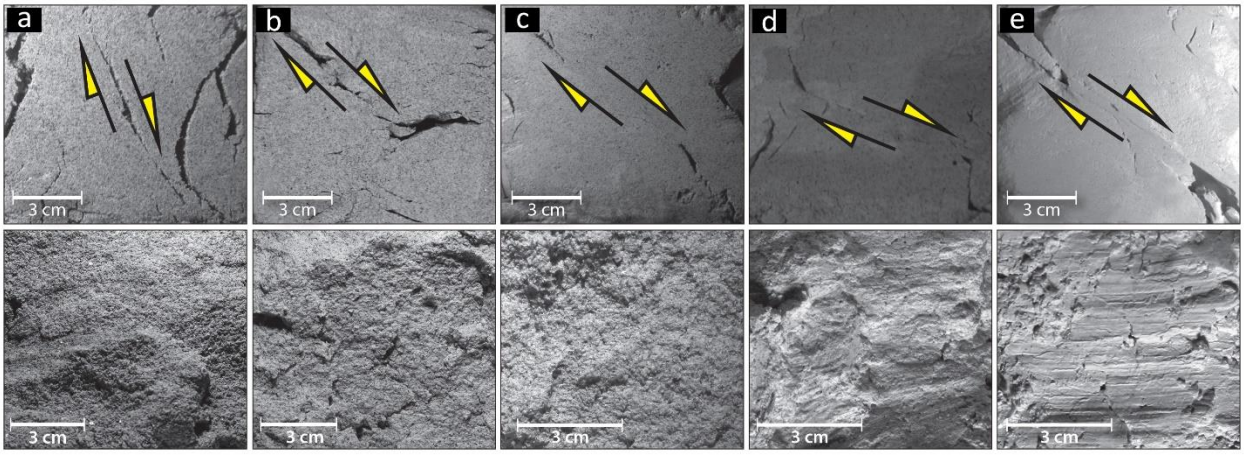

Figure 4.7. Formation of shear fractures in Type 1 sand-talc models (upper panel) under laboratory conditions (Top views). (a) Pure sand, (b) coarse sand-talc (1:1); (c) fine sand-talc (1:1); (d) fine sand-talc (1:4) and (e) pure talc. Their corresponding shear surface roughness characteristics are shown in the lower panels. Arrows in the top panel indicate the sense of slip along shear fractures in the models.

For 1:1 fine sand-talc mixture, the models yielded multiple sets of shear fractures with somewhat discernible linear irregularities (Fig 4.7.c). They also formed steps perpendicular to the movement direction on the slip surfaces. Increasing talc content strengthened the slip-induced linear features on shear fractures. Models with 1:4 sand-talc mixture produced shear fractures with bold slickenlines (Fig 4.7.d). But the linear features did not develop globally on the shear surface;

they were localized in isolated patches. Pure talc models produced excellent one-dimensional irregularities, giving an appearance of typical slickensides on the shear fractures (Fig 4.7.e).

Type 2 models produced major shear fractures along the preexisting cut along with some new shear fractures, locally branching from the cut-controlled fractures (Fig 4.8.). The fracture roughness depended largely on the angle the fracture made with the compression direction (θ).

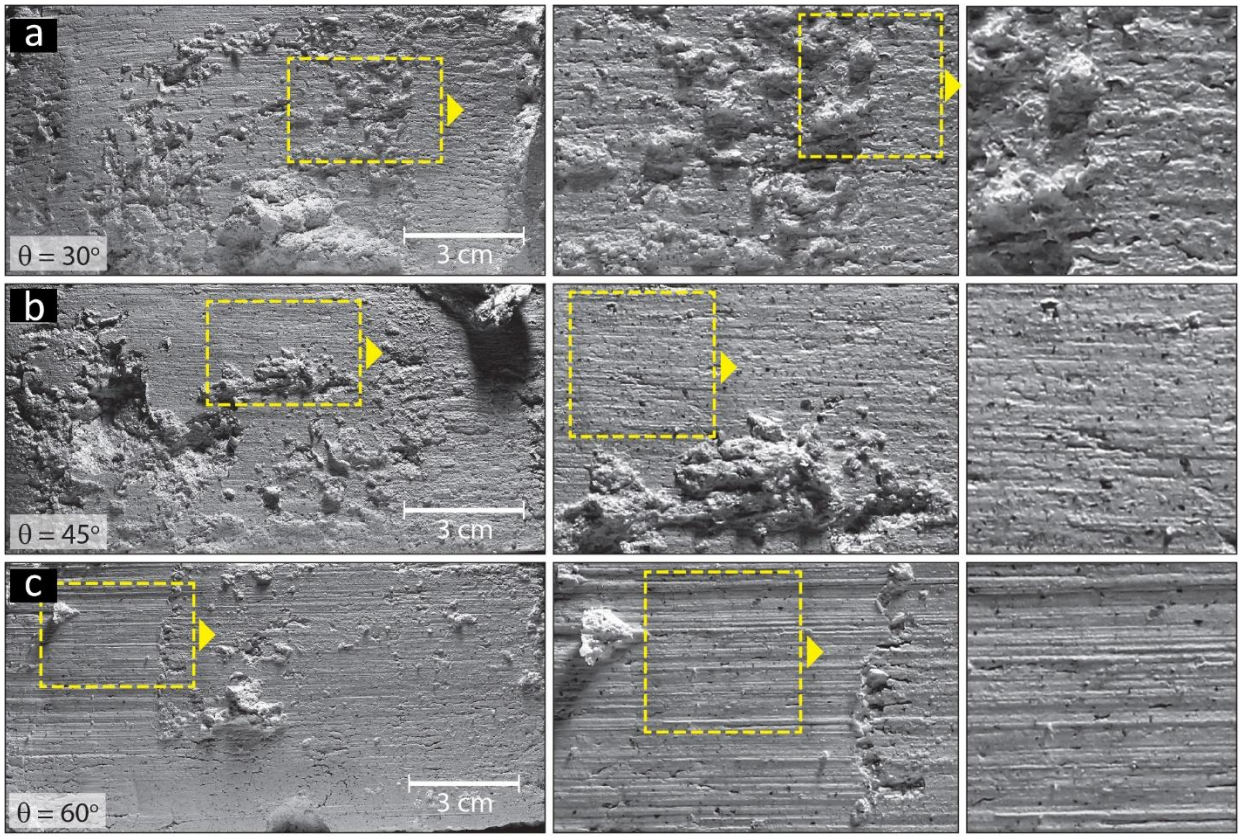

Figure 4.8. Variations of the shear fracture roughness in Type 2 pure talc models. The shear fracture angles to the compression direction (θ) were: (a) 30°, (b) 45° and (c) 60°. Notice that the rupture surfaces contain relatively smooth domains with prominent lineation (slip zones) and rough domains without any linearity (stick zones). The latter tends to die out with increasing θ. Yellow boxes show areas of observation with successive magnifications (left to right)

For θ = 30°, the slip surface form patchy slickensides, containing a distinct lineation in the slip direction. The slip produced a number of secondary features, in addition to slickensides, such

as step-like relief oriented almost normal to the slickenlines. They resemble typical steps observed on natural fault surfaces (Doblas, 1998b; Gay, 1970; Lin & Williams, 1992). The slip surfaces were dotted with isolated 3-D ridges and grooves of varying dimensions, ranging from 1 mm to 2–3 cm. A closer inspection of the rough surface reveals elongate ridges, forming a wavy pattern oriented along the slip direction. The slickenside domains are separated by large areas of either positive or negative reliefs showing no linear features. They possibly delineate locally stuck zones, allowing no relative slip during the model deformation. The estimated areal ratio of slip (slickenlines) to total area (including stuck zones devoid of lineation) is in the order of ~30% for models with $\theta = 30°$ (Fig 4.8.a). Experiments with $\theta = 45°$ produced similar roughness, but with much reduced 3-D ridges and grooves. Consequently, they developed smoother geometry (Fig 4.8.b), where the areal proportion of slip zones is ~60%. The fracture surface roughness underwent a dramatic change at $\theta = 60°$. The models produced slickensides all over the shear surfaces, marked by excellent slip-induced lineation. Enlarged views of the surface roughness reveal one-dimensional wavy roughness in multiple orders. The shear surfaces generally had little ridges or steps, leading to a large areal proportion (>80%) of slip zones (Fig 4.8.c). The slickenlines are dominated by a set of periodic waves, which look like nonfractal type of roughness (Sagy & Brodsky, 2009a). However, their distributions define nearly a fractal pattern, which is described in the coming sections. The experiments suggest that this roughness with marked linearity can be used as an indicator of ductile slickensides morphology.

To summarize the model results, Type 1 experiments indicate that increasing ductility due to higher talc content facilitates roughness formation with marked slickenlines. Conversely, Type 2 experiments reveal the control of fracture orientation on the roughness characteristics of shear fractures. Increasing fracture inclination to the principal compression direction results in a

transformation from localized to global development of slickensides, characterized by one dimensional, multi-ordered wavy irregularities when $\theta = 60°$. This effect of θ in promoting linear irregularities probably results from increasing normal stress on the shear surfaces (Badt et al., 2016; Davidesko et al., 2014). Larger compressive normal stresses favor the wavy mechanical instability in our models, which eventually produces linear geometry (details of the mechanics discussed later) to facilitate the slip motion.

4.4 Roughness analysis of field samples and laboratory models

The motivation for quantifying surface roughness has led to an enormous development of various computational methods, primarily owing to the growing demands of their applications in the studies of fault slip dynamics (Harris et al., 1991). For example, roughness can greatly influence the frictional strength of shear surfaces (Y. Boneh et al., 2014; Yuval Boneh et al., 2013; Gori & Mari, 2001), the most crucial dynamical parameter to govern the slip behavior on a fracture under a given stress field. Furthermore, several workers have shown surface irregularities as an attribute to local variations in the slip vectors on faults (Brodsky et al., 2011a). On the other hand, in many rocky terrains fracture or fault networks form permeable zones for fluid flows in solid rocks, where fracture roughness stands as an important factor to determine the heterogeneous flow patterns (S. R. Brown, 1987; R. W. Zimmerman & Bodvarsson, 1996) and the permeability (Kranzz et al., 1979) along the fracture zones. Consequently, roughness analysis of faults, fractures, and joints has emerged as an attractive area of interdisciplinary studies in Earth sciences. This present study undertakes an analysis of shear fracture roughness to investigate the degree of linearity in surface irregularities (slickensides lineation) as a function of failure behavior and fracture orientation.

Fractal analysis of fracture surfaces is performed to test whether their surface irregularities follow power law size distributions. Such analyses allow us to quantify the degree of geometrical non-uniformity and characterize their roughness properties with a quantitative approach, for example, self-similar versus self-affine (Brodsky et al., 2016; Sagy & Brodsky, 2009). In addition, the fractal dimension (*D*) is found to be an excellent proxy to the frictional properties of faults. Higher *D* values give rise to greater frictional strength (Hanaor et al., 2016; Popov & Filippov, 2010). *D* was used to provide a quantitative estimate of the roughness anisotropy, accounting the difference in *D* along and across the slip direction, as reported in several earlier studies (Candela et al., 2012b; Sagy et al., 2007a). This parameter allows to perform a comparative analysis of model roughness with the field data.

4.4.1 Fractal Method

The concept of fractal dimension was first introduced by mathematician Felix Hausdorff in 1918, though the term "fractal" was later coined by the Polish-born mathematician Benoit Mandelbrot in 1967. The concept of fractal dimension has acquired a wide range of applicability since its birth. The word fractal comes from the latin word frāctus, meaning fractured or broken, which is perhaps quite appropriate keeping in mind the fractional components that are studied using fractal. Examples of fractals can be seen in our daily lives, eg., in branches of trees, blood circulatory system, snowflakes, coastlines, lightning patterns, rivers with distributaries to name a few. In today's world, fractal dimension has found a vast array of applications, starting from pure mathematics, several aspects of engineering to biosciences and earth sciences. In its purest form, a fractal set can be defined quantitatively, by a simple mathematical definition, as:

$$N_i = \frac{C}{{r_i}^D} \qquad (4.1)$$

where, N_i is the number of fragments with r_i as the characteristic linear dimension, C is a constant of proportionality and D is the fractal dimension. In a Euclidean space, the dimensions of a point, line, square and cube are zero, one, two and three, respectively. Fractal dimension can either be an integer, where it is equivalent to any Euclidean dimension, or a non-integer, i.e., a fractional dimension. We will see both the cases, in details.

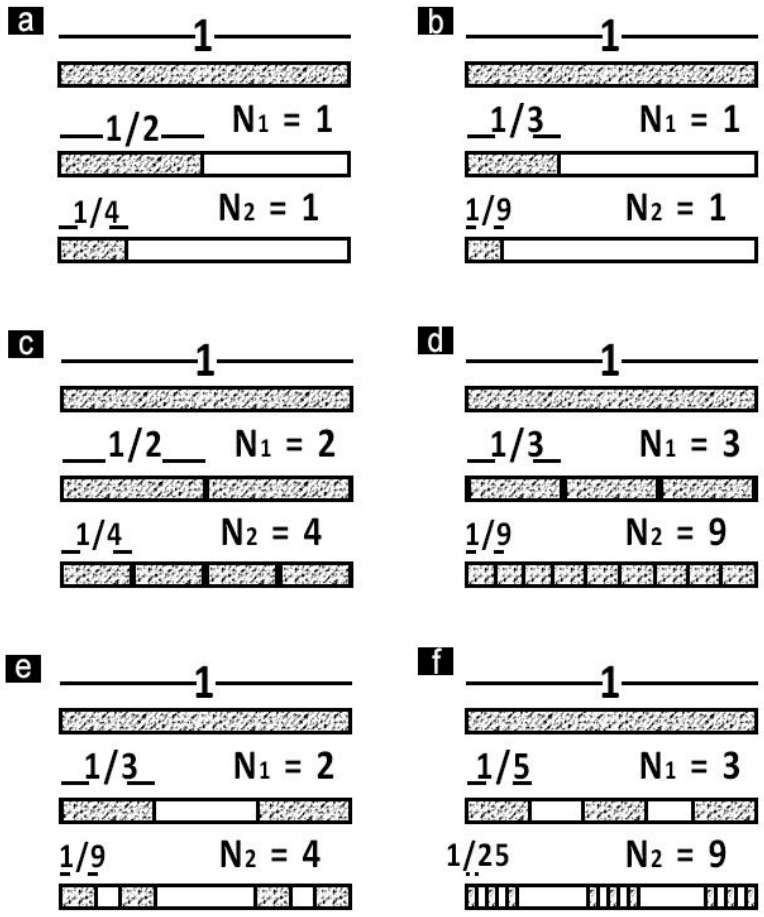

Figure 4.9. Illustrations showing one-dimensional fractal calculation from a zero order line segment. Note that: a) and b) line cut into two and three parts, respectively and one is retained. *D* is 0 for both cases; c) and d) line cut into two and three parts, respectively and all parts are retained. *D* is 1 for both cases; e) and f) line cut into three and five parts, respectively, two end segment and the center one is retained. *D* is a fractional value and lies between 0 and 1 for both cases. (*after Turcotte, 1997)*

For a detailed understanding of fractal dimension calculation, first take an example of a line segment and divide it in various ways and in increasing orders to found out the respective fractal dimensions depending upon the number of fragment and their characteristic length dimensions. Let us consider a line segment at unit length and at zero order and divide into two parts (first order), so that r_1 = ½ and N_1 = 1, when one of the parts is retained (Fig 4.9.a). The remaining segment is again divided into similar fashion (second order) to get r_2 = ¼ and N_2 = 1, when one of the part is retained again. Now to determine the *D* value, equation 4.1 can be rewritten as:

$$D = \frac{\ln\left(\frac{N_{i+1}}{N_i}\right)}{\ln\left(\frac{r_i}{r_{i+1}}\right)} = \frac{\log\left(\frac{N_{i+1}}{N_i}\right)}{\log\left(\frac{r_i}{r_{i+1}}\right)} \qquad (4.2)$$

So, from this equation, for the first example, we get, ln (N_2/N_1) = ln 1 = 0, ln (r_1/r_2) = ln 2, and thus *D* = 0. In this pattern of division, at all successive orders, we will get ln (N_{i+1}/N_i) = ln 1 = 0, and hence as the order approaches infinity the line segment approaches zero value, becoming a point. This calculation will remain exactly the same if we divide the line segment in three parts instead of two and repeat the construction (Fig 4.9.b). The story changes, when the line is divided two or three parts, but now all the parts are retained in every order. In this case, at first order, r_1 = ½ and N_1 = 2 and at second order, r_2 = ¼ and N_2 = 4. From equation 4.2, we get *D* = ln 2 / ln 2 = 1 (Fig 4.9.c). Similarly, we also get *D* = 1, when the segment is subdivided into three parts, and all the parts are retained (Fig 4.9.d). Thus, in this case, the fractal dimension is found out to be a line segment in Euclidean space. In all of the above cases, *D* is found to be an integer, however this is not always the case.

If we divide a zero-order line segment of unit length into three parts at first order and retain two end segments (Fig 4.9.e), and repeat the process at second order, we get a *D* value of ln2 / ln3

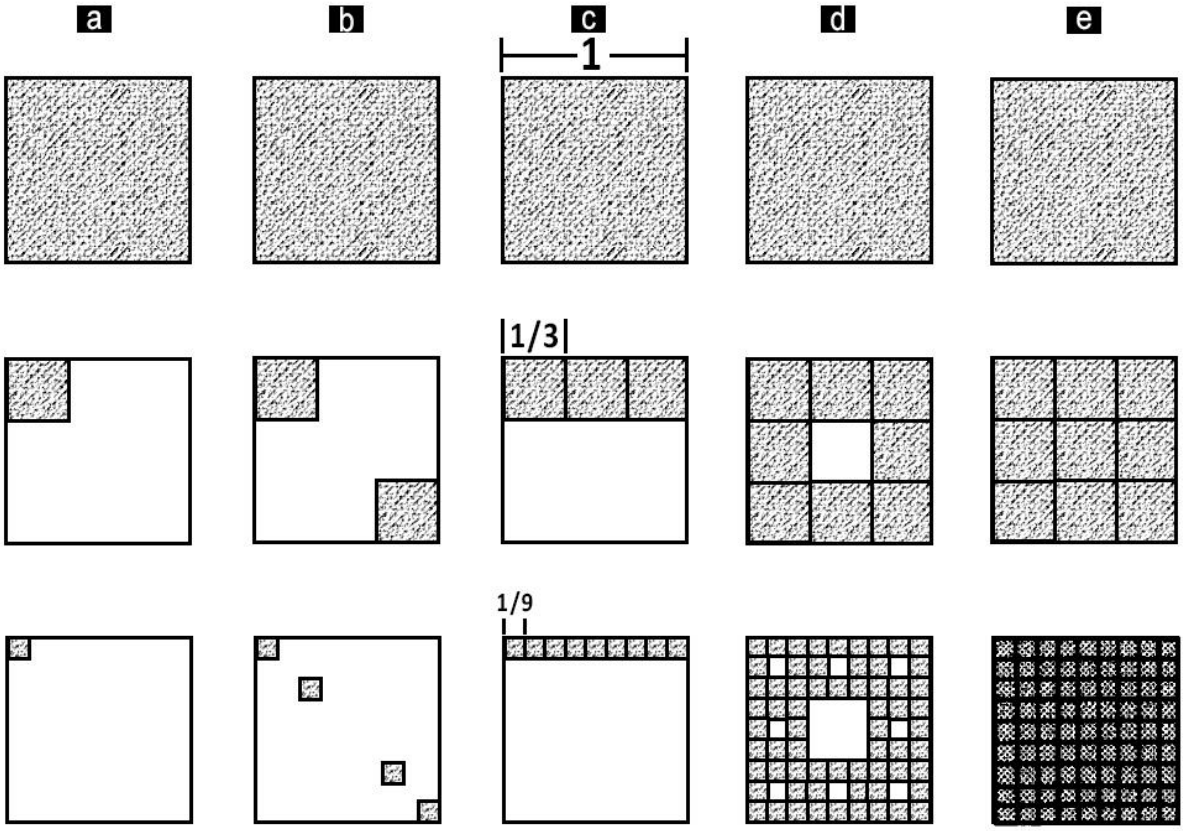

Figure 4.10. Illustrations showing five two-dimensional fractal constructions from a zero order square of unit area. In each cases at first order the squares were cut into equal sized smaller squares with 1/3rd dimension, and a fraction/fractions is/are retained and the process is repeated. *D* values were found be ranging from a) *D* = 0 to e) *D* = 2; b), c) and d) have *D* values between 0 and 2. *(after Turcotte, 1997)*

= 0.6309 from equation 4.2. Similarly, if we divide the unit length line segment in five parts and retain the two end segments and the center one, and repeat in the second order, then the *D* value obtained is ln 3 / ln 5 = 0.6826 (Fig 4.9.f). Thus, we clearly see that in these two case, *D* values are non-integers and truly have a fractional dimension. It is to be noted that all these iterations are characteristically scale invariant.

The same fractal concept can also be applied to a square (Fig 4.10). If we divide a zero order square into nine square at first order, retain one single square and the process is repeated, then from equation 4.2, we get a *D* value of 0, which is the Euclidean dimension of a point ((Fig

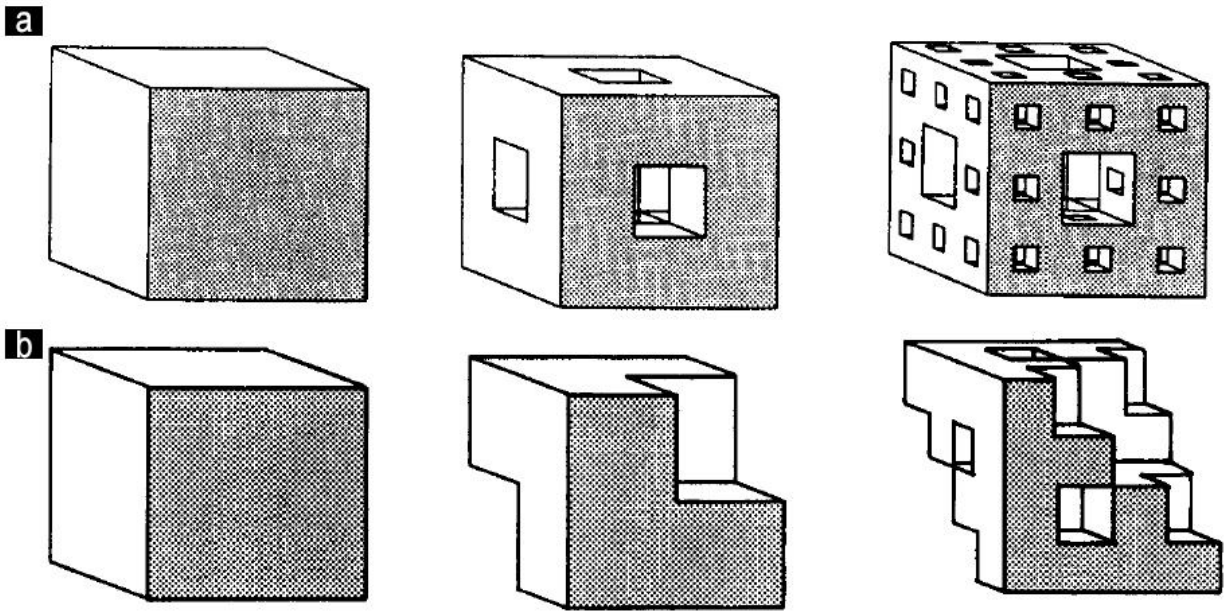

Figure 4.11. Illustrations showing two three-dimensional fractal constructions from a zero order cube of unit volume. Note that at first order, the unit cube is divided into smaller cubes with a) $r_1 = 1/3$, giving a D value of 2.727 ; b) $r_1 = 1/2$, giving a D value of 2.585. *(after Turcotte, 1997)*

4.10.a). Similarly, if we divide the square in the same fashion but retain all the nine squares, we get a *D* value of 2, which is the Euclidean dimension of a square (Fig 4.10.e). Iterative construction following pattern in between these two extremes can yield fractal dimensions between 0 and 2 (Fig 4.10.b, c & d). Fractal dimension concept can be extended to three dimensional subjects, following the same pattern, where *D* values can lie anywhere between 0 and 3, depending on the type of repetitive segmentation and retention of parts (Fig 4.11). Fractal dimension can broadly be of two types: self-similar and self-affine. A statistically self-similar fractal system is an isotropic one., i.e., in a two-dimensional *xy*-space, a self-similar fractal *f(rx, ry)* is statistically similar to *f(x,y*), where *r* is the scaling factor. Whereas, a self-affine fractal system is a rather anisotropic one, which means, in the two-dimensional space, a self-affine fractal $f(rx, r^{Ha}y)$ is statistically similar to *f(x,y)*, where Ha is Hausdorff measure.

4.4.2 Analytical approach

A quantitative approach was undertaken to the roughness analysis of shear fractures using an image processing technique based on MATLAB. This technique, in principle, applies the color shades of an object to reconstruct its three-dimensional form. Illumination is thus a critical parameter in implementing this technique for relative roughness estimation. Our laboratory setup was equipped with two flood lights, coupled to a diffuser to create a homogeneous illumination, on the surface of interest. The illumination was set at a constant level while capturing the images. The captured images were stored as JPEG format with an RGB color profile, which were processed sequentially in the following steps (Fig 4.12.). A resolution of 72 dpi was kept in digitizing the images, which enabled us to detect the finest roughness of smooth shear surfaces in the order of 85 μm. The color images were translated into a three-dimensional matrix in MATLAB

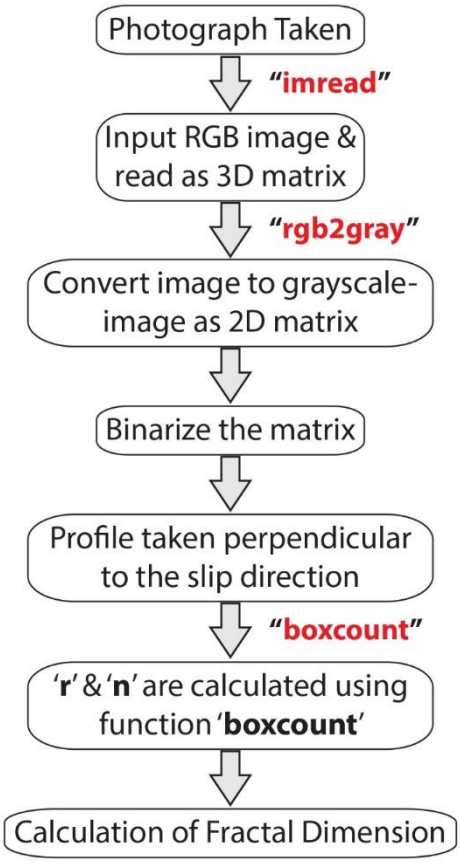

Figure 4.12. Flow chart of the sequential operations in image processing for shear surface topology mapping and fractal analysis.

environment, that is, matrix containing three layers (R = red layer, G = green layer, and B = blue layer) of two-dimensional matrices. Using the function rgb2gray they were converted from true color RGB image (3-D matrix) to gray scale intensity image (2-D matrix), eliminating the hue and saturation information, and retaining only the luminance intensity.

The gray scale image can be then expressed as a function f (x, y), where f is the intensity value stored in a pixel for any pair of x, y coordinate (Shanmugavadivu & Sivakumar, 2012). One pixel of an 8-bit gray scale image can store 256 values of intensity, where 0 stands for black, whereas 255 for white. The intensity value at a given point can be used as an apparent asperity height. Function *imagesc* was used with the gray scale 2-D matrix to obtain a color map as an output, where the color of each pixel indicates the intensity values stored in the matrix. A color bar defines the color ranges for different intensity values. For a roughness analysis of fracture surfaces, the grooves (negative elevation) were represented by lower intensity values (blue), whereas the ridges (positive elevation) were represented by higher intensity values (red-yellow). This approach was also used to generate profiles of the slickenside surfaces as a function of their elevation. A row vector was generated from the gray scale image matrix. The intensity values were plotted as a function of the position in the vector to obtain the slickenside surface profile, where the intensity values represent the relative heights.

4.5 Geometrical description of shear surfaces

4.5.1 Field casts

The color map of cast 1 (Fig 4.4.a) indicates weak roughness, containing numerous fine ridges and grooves of very low relative relief (Fig 4.13.a). Their profiles, characterized by extremely low

amplitudes (gray scale intensity [*GSI*] values: 10; ~1.5 mm), and their corresponding low fractal dimension (*D*) values (discussed separately in the next section) are in agreement with an overall smooth appearance of the shear surface. The color map of cast 2 (Fig 4.13.b) shows a distinct

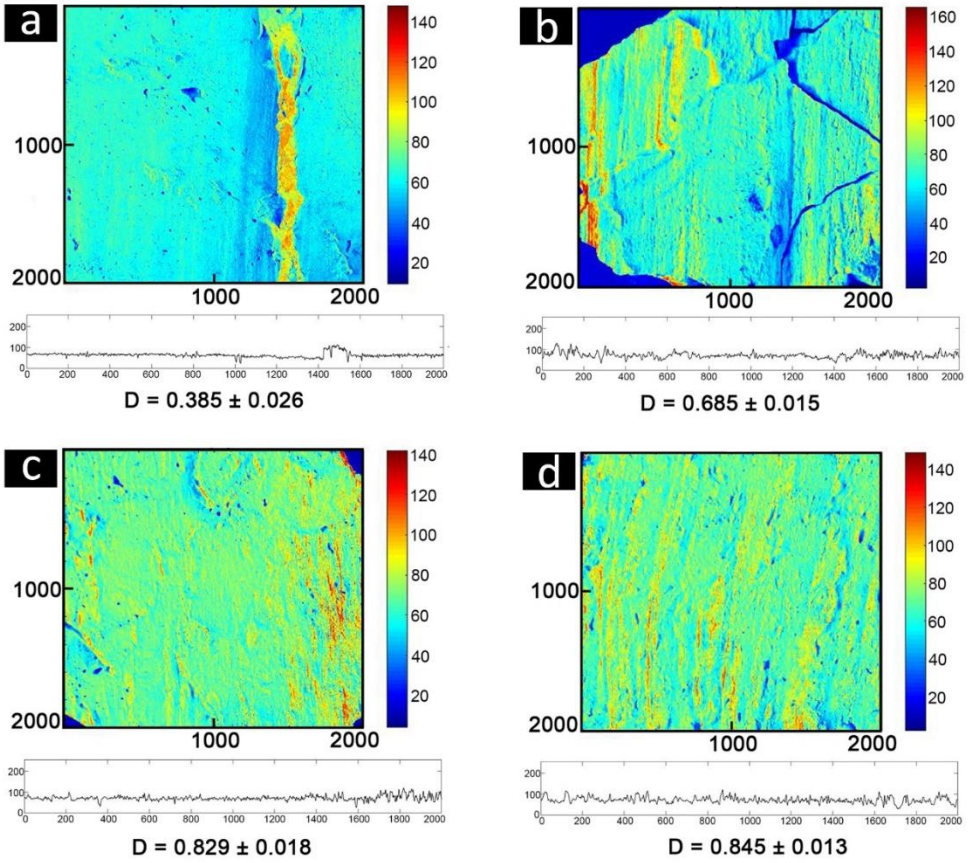

Figure 4.13. Surface geometry of shear fractures obtained from image processing of the field casts (Fig. 2). The colour bars indicate the relative relief of fracture roughness. The topological maps in (a) to (d) show increasing roughness. Horizontal and vertical scales in the map denote pixel positions, where 1000 unit represents 8.55 cm. The lower panel illustrates corresponding relief profiles perpendicular to the lineation. The elevation is in *GSI* values, where 1 *GSI* unit represents ~ 0.15 mm.

pattern of roughness marked by one-dimensional ridges and grooves (slickenlines), as one can visualize on the actual outcrop surfaces in the field (Fig 4.4.b). The broad ridges are discrete, narrowing down longitudinally to form isolated, strongly elongate relief of high amplitudes (*GSI* values: 25; ~3.6 mm). They are associated with similar fine-scale ridges and grooves, imparting a

distinct linear structure on the shear surface. The parallel arrangement of straight ridges gives rise to a prominent slickenline structure, as seen in the field outcrop (Fig 4.4.b).

The surface roughness is globally higher than that of cast 1. The map of cast 3 reveals slickenside features with numerous elongate ridges and grooves of varying scales, in both length and width dimensions (Fig 4.13.c). Such irregular geometry gives rise to prominent roughness of the shear surface, displaying relatively weak linearity, as compared to that observed in the previous cases. The color map for cast 4 shows longitudinally persistent parallel ridges constituting sharp linearity in the roughness (Fig 4.13.d). The ridge-groove frequency strongly varies across the lineation. Furthermore, they display wide variations in their relative relief (GSI values: 20 to 50; ~3 to ~7.2 mm) and give rise to higher roughness on the fracture surface, which is in agreement with the corresponding *D* value presented in the following section.

4.5.2 Type 1 experimental models

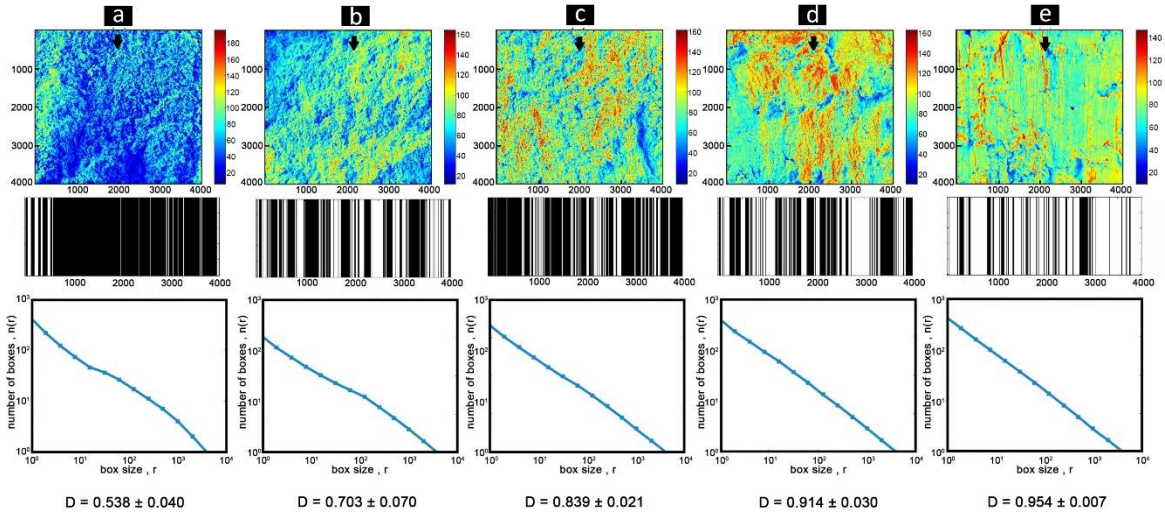

Figure 4.14. Roughness geometry of experimental shear fractures shown in Fig. 4. (a) Pure sand, (b) coarse sand-talc (1:1); (c) fine sand-talc (1:1); (d) fine sand-talc (1:4) and (e) pure talc. Horizontal and vertical scales in the map denote pixel positions, where 1000 unit represents 8.55 cm. The images (a to e) clearly reveal increasing linearity in roughness. The corresponding cantor set and fractal analyses are presented in the lower panels. *D*: one-dimensional fractal dimension. Arrows indicate the slip motion of top walls.

The same imaging technique was adopted to study the shear fracture roughness produced in the analogue experimental models. The map for a pure, coarse sand model shows that the shear rupture surface is devoid of any systematic relief variation on macroscopic scale (larger than grain size), or linearity on the surface irregularities (Fig 4.14.a), as one can visualize from the actual fractures in the model (Fig 4.7.a). The relief profiles along and across the slip direction are virtually identical.

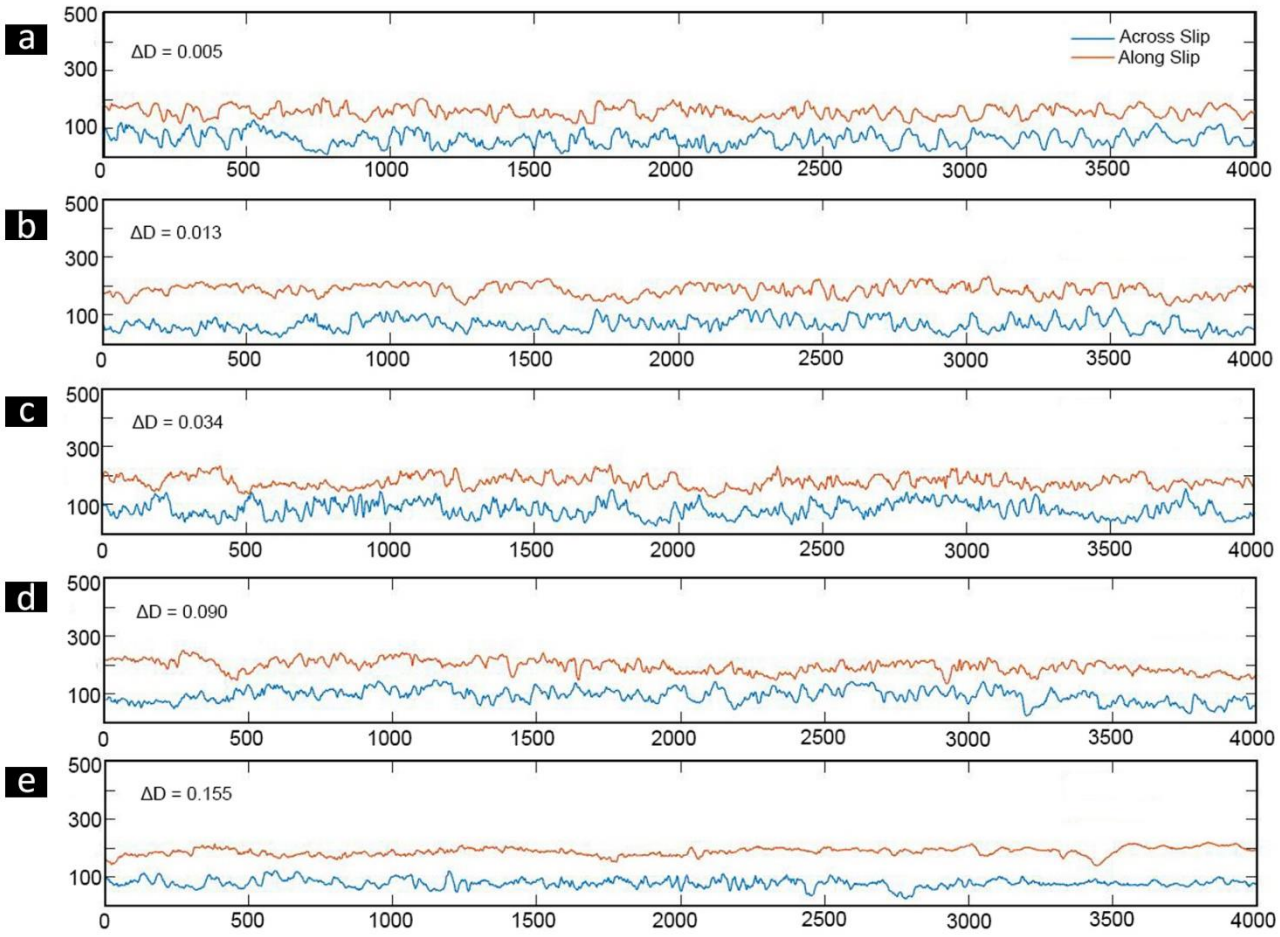

Figure 4.15. Across- and along-slip roughness profiles obtained from the topological maps (Fig. 8) of shear fractures produced in Type 1 laboratory experiments (the two graphs are plotted at a given spacing). (a) to (e): Sand:talc models with increasing talc content, as shown in Fig. 4. *ΔD* is the difference infractal dimensions estimated across and along the slip direction. Note increasing *ΔD* from (a) to (e), implying stronger anisotropy in roughness from sand to talc models. The horizontal scale is in pixel position (1000 unit = 8.55 cm), and the vertical scale in *GSI* values (1 unit ~ 0.15 mm).

The roughness characteristics remarkably change with addition of talc to coarse sand. For a 1:1 volume ratio, the fracture surface turns to be spectacularly rough (Fig 4.14.b), which is marked by large relative reliefs (maximum *GSI* values: 25 [~3.62 mm]). However, the roughness geometry displays irregular, elongate ridges with a weak preferred orientation to delineate a crude linearity in the slip direction. This is evident from the contrasting relief patterns along and across the slip direction (Fig 4.15.b). The along-slip roughness is relatively smoother than the across-slip counterpart (cf. Candela et al., 2012), which is quantitatively demonstrated later from the difference in their *D* values. The geometry of surface roughness is also sensitive to sand grain size. Models with fine sand and talc in 1:1 volume ratio show roughness with strong variations in relative relief, where the positive relief zones cluster to form elongate ridges, broadly oriented along the slip direction, forming a weak linearity in the surface roughness (Fig 4.14.c). This linearity is reflected in the contrasting profiles along and across the slip directions (Fig 4.15.c). Increase in talc content (i.e., finer size fraction) in the granular mixture again brings in changes in the surface roughness. The map for fine sand/talc in 1:4 volume ratio show distinct linear features formed by clustering of ridges in the slip direction (Fig 4.14.d). These ridge clusters ultimately define coarse slickenlines, forming conspicuous directional roughness. The surface becomes more irregular across the slip direction, as revealed from the geometrical profiles along and across the slickenlines (Fig 4.15.d).

The shear surfaces in pure talc models display excellent along-slip straight, longitudinally persistent long ridges (Fig 4.14.e). Fine-scale ridges between wide, long ridges strengthen the linearity in roughness, which is evident from a large contrast in the profiles along and across the slip direction. The surface is much smoother in the slip direction, as compared to that in the across-slip direction (Fig 4.15.e).

4.5.3 Type 2 experimental model :

The surface maps for varying θ show roughness as a function of fracture orientation (Fig 4.16.). For θ = 30°, they display strongly heterogeneous roughness, characterized by localization of two distinct domains: (1) slip zone (smooth domain containing prominent lineation) and (2) stuck zone (rough domain consisting of irregular ridges and grooves).

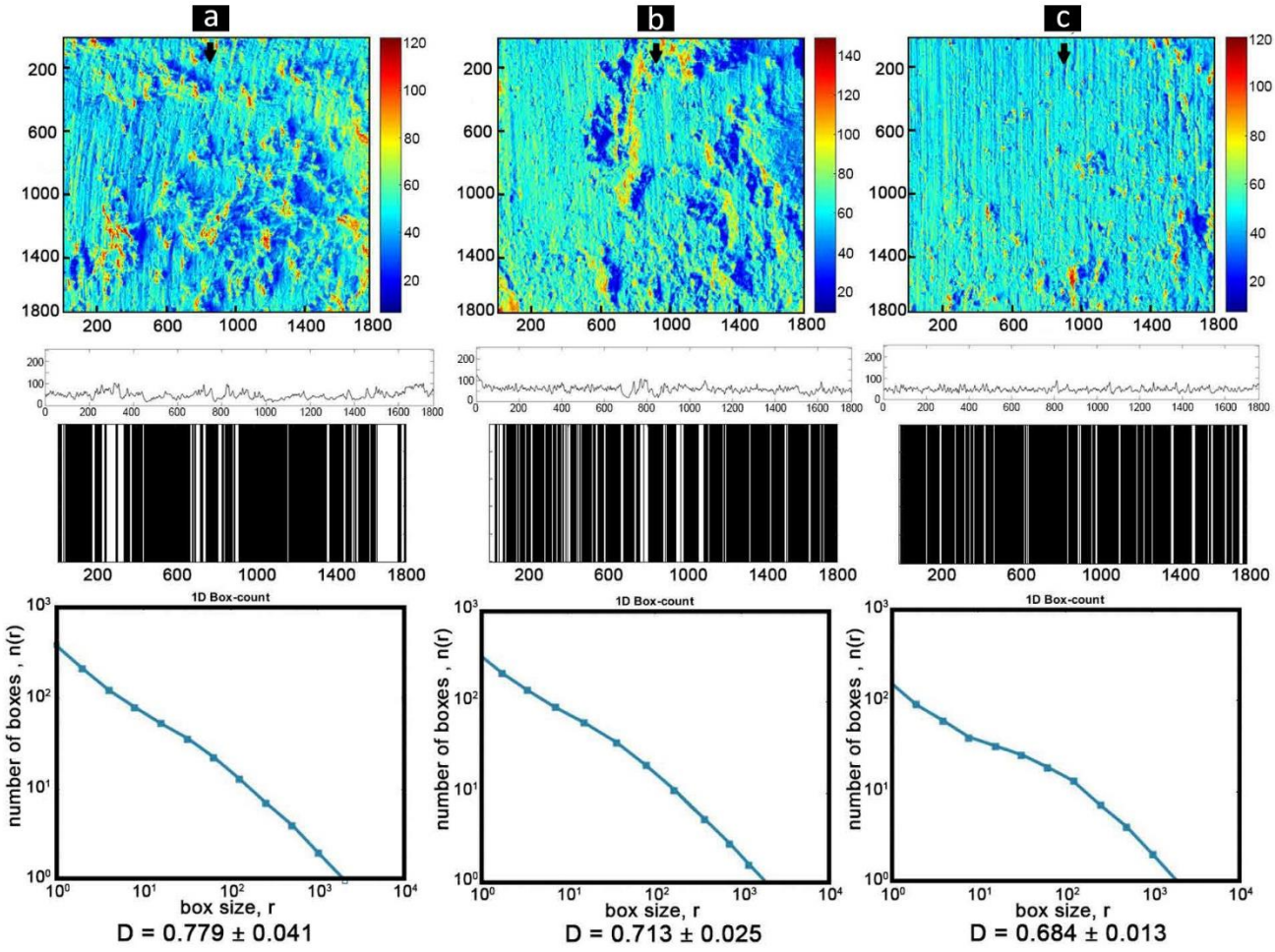

Figure 4.16. Effects of the initial fracture orientation (θ) on the surface roughness in Type 2 experiments. θ = (a) 30°; (b) 45° and (c) 60°. θ: Inclination of the fractures to the principal compression direction. The corresponding across-slip profiles, cantor sets and fractal analysis are shown below. All the scales are used as in Fig. 4.9.

In the slip zones the ridges are wide and have high relative relief, giving rise to a coarse linear feature (Fig 4.16.a). Increasing θ causes the rupture surface to become smoother, as the rough domain is reduced in its areal distribution. Second, the roughness develops strong linearity.

4.5.4 Cantor Set

Introduced by German mathematician Georg Cantor (1883), a cantor set can very simply be defined as a set of points lying on a single line segment. If we take a zero order unit length line

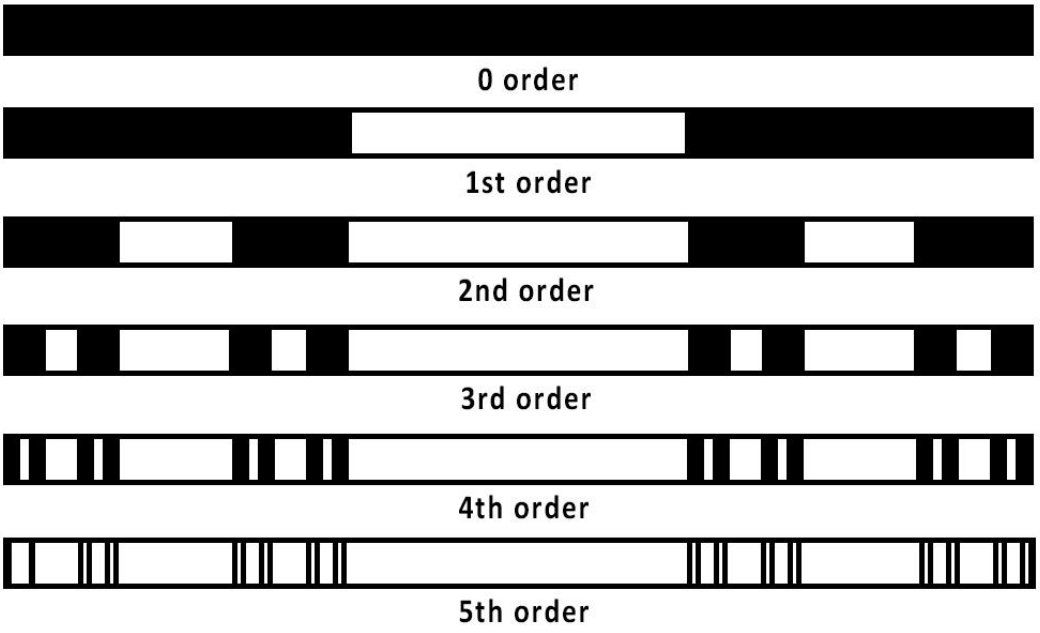

Figure 4.17. Illustration describing a cantor set formation (upto 5^{th} order), from a unit-length line segment. The first-order Cantor set is used as a generator and at order i , the line segment is replaced by the generator to get the set at order $i + 1$. *(after Turcotte, 1997)*

segment and divide it into five parts (in the first order) where two end segments and the center is retained, and the process is repeated at the second order and so one, we get a Cantor set which is related to the order of the iteration. Figure 4.17. demonstrates Cantor set upto the fifth order, i.e., $i = 5$, and can be infinite. The cantor set in the first order is used as a generator and each of the

remaining segments is replaced by the generator to obtain sets of higher orders. If *n* iterations are performed, then line length at nth step, r_n related to first iteration r_1, by $r_n/r_0 = (r_1/r_0)^n$. . As *n* tends to infinity, r_n tends to zero, and the Cantor set is then known as Cantor dust, which is an infinite cluster of points. This repetitive iteration that leads a cantor set to form a cantor dust is known as curdling.

4.6 Fractal Analysis

Fractal analysis was performed of the shear surface roughness observed in both field and laboratory models. As already mentioned, fractal set of objects can be defined as

$$N = \frac{C}{r^D} \qquad (4.3)$$

where *N* is the number of objects with linear dimension *r*, *C* is the proportionality constant, and *D* is the fractal dimension. In the equation *N* holds a power law relation with r, and their distribution on a log space shows essentially a linear regression.

Using the box counting method, the surface maps were processed in MATLAB to evaluate the geometry of their roughness. The analysis reveals that the box sizes follow nearly a power law distribution (Fig 4.14.), suggesting that the roughness obeys a fractal geometry, as shown extensively in earlier studies (S. R. Brown & Scholz, 1985; Candela et al., 2009b; J. J. Lee & Bruhn, 1996; Y. H. Lee et al., 1990; W L Power et al., 1987b; William L Power & Tullis, 1991; Renard et al., 2006). However, shear surfaces in this case had an anisotropic roughness, implying that the scale of measurement is not same in all direction; more specifically, the box shapes used for measurement are not squares (in 2-D) or cubes (in 3-D). Thus, 1-D fractal analyses was employed along and across the slip direction. The sample photographs were converted to gray

scale images, as described in section 4.4.2, and to construct a matrix for binarization by replacing all pixels in the input image with normalized luminance greater than the reference value (0.5) as 1 (white) and the rest pixels with the value 0 (black). Binarization is a process that converts the grayscale intensity image to a binary image by replacing all pixels in the input range with luminance greater than the reference level (0.5), with value 1 (white) and replacing all other pixels with the value 0 (black). In our case, the reference level value corresponds to an intensity value halfway between the minimum and maximum value of the whole image (the input matrix). This implies the maximum and minimum intensity values are normalized to 1 and 0, respectively. The reference level is calculated for each image as mean of maximum and minimum intensity. The geometrical perturbations were calculated based on the mean surface. A row vector (for across-slip 1-D fractal analysis) was created from the binarized matrix to develop a cantor set (Fig 4.12; Moisy, 2008). The function boxcount was operated on that vector to calculate N and r (equation (1)). We then determined the corresponding fractal dimension (D) from log N versus log r plots (Fig 4.14). D values were evaluated from these plots considering the fitting to the box sizes (r) in the range of 10 to 10^3. To test the accuracy of this method, we validated our results with the fractal dimensions of known curves (Lee et al., 1990).

The visual roughness of slickensides in the field agrees with the D values estimated from their corresponding casts. The cast of smooth shear surfaces containing fine-scale ridges shows low D values (0.385). Their relief profiles across the lineation provide a visual estimate of such low roughness (Fig 4.13a). Shear surfaces with strong relief variations, in contrast, give rise to higher D values (0.685; Fig 4.13b). The analysis yielded increasing D values (0.829 and 0.845) of the casts with increasing coarseness in linear ridges and grooves of the slickensides (Fig 4.13.c and 4.13.d).

The analogue models yield *D* values broadly in a similar range. The fractal analysis shows an increasing trend of *D* values from pure sand to pure talc models (Fig 4.14). Pure coarse sand models produced shear surfaces with very low fractal dimensions ($D \sim 0.538$), as also reflected in the corresponding cantor presentation (Fig 4.14.a). The fractal pattern is nearly isotropic, showing a small difference in *D* values across and along the slip direction ($\Delta D = 0.005$). Coarse sand-talc (1:1) models yield relatively larger *D* values (0.704); this difference is visually evident from the cantor plots (Fig 4.14.b). In addition, these models had an anisotropic fractal pattern, where the across-slip *D* value is significantly larger than the along-slip *D* ($\Delta D = 0.014$). Replacement of coarse sand with fine sand increased the fractal dimensions ($D = 0.83$) as well as the anisotropy ($\Delta D = 0.03$), which is obvious from their respective cantor plots. Similarly, coarse sand-talc models produced rupture roughness with further higher fractal dimensions ($D = 0.914$) and greater fractal anisotropy ($\Delta D = 0.09$) when the fine sand:talc volume ratio was increased to 1:4. Pure talc models yield the highest fractal dimensions ($D = 0.954$). Their roughness is strongly anisotropic ($\Delta D = 0.15$), which is evident from pronounced slickenlines on the rupture surface (Fig 4.7.e).

For Type 2 models, the roughness analysis suggests decreasing *D* with θ. For $\theta = 30°$, the rupture surfaces had greater roughness ($D = 0.77$) due to a mosaic of slickenline-bearing smooth domains and rough domains containing irregular ridges and grooves, as discussed earlier in section 4.3.2. The rough domains almost disappeared, leaving the entire rupture surfaces covered with slickenline-bearing smooth domains when $\theta = 60°$. Consequently, the fractures developed relatively low fractal dimensions ($D = 0.68$). We obtain an intermediate *D* value (0.71) for $\theta = 45°$. The log-log plots show increasing nonlinearity with increase in θ (Figures 4.16.a– 4.16.c). Such nonlinearity suggests weakening of the fractal character of surface roughness due to formation of well-defined, regular wavy irregularities at large θ.

4.7 Mechanical modelling of shear surface roughness

Numerical simulations were ran on 3-D computational fluid dynamic models to understand the growth mechanism of macroscale slickenlines observed in our analogue experiments. Millimeter

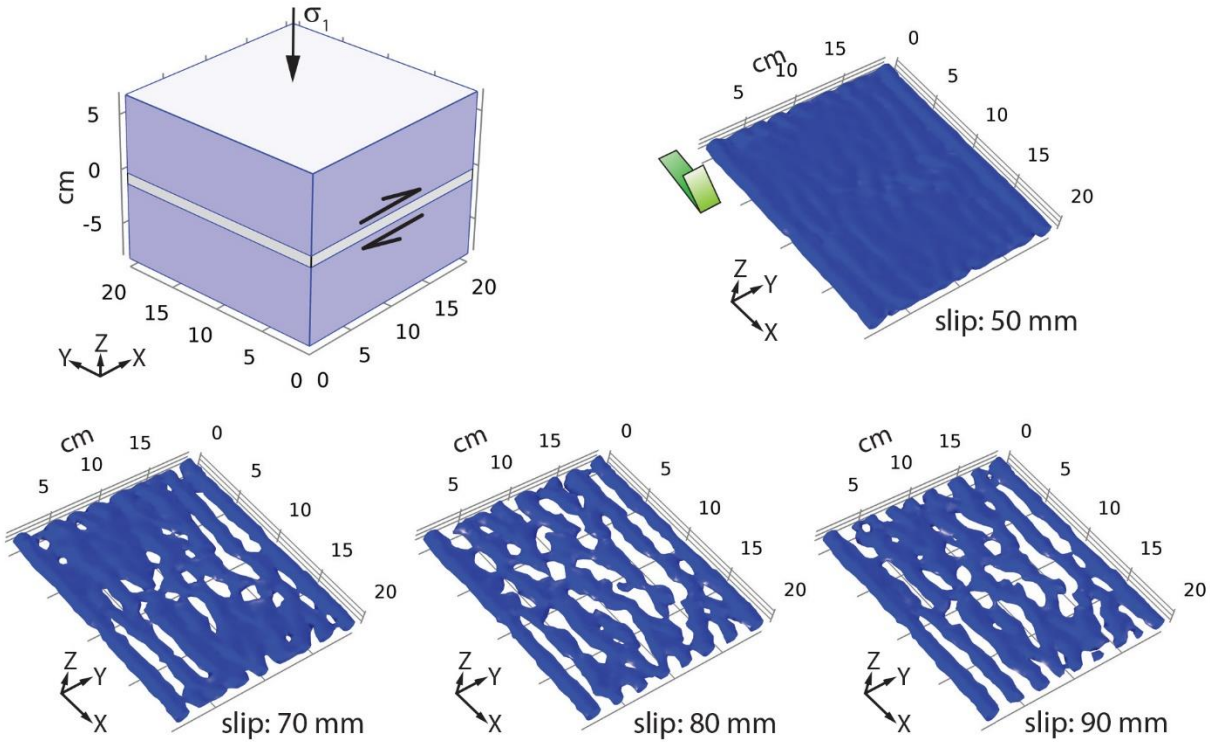

Figure 4.18. 3D computational fluid dynamic (CFD) model used for investigation of shear instability in a low-viscosity layer sandwiched between two high-viscosity blocks (viscosity ratio: 10^2) and successive stages of instability wave growth, leading to along-slip ridge and groove structures, as observed in pure talc models (Fig. 4). The model was subjected to slip movement along the soft zone. σ_1 indicates the normal stress to slip zone.

scale thick slip zones were simulated in computational fluid dynamic models, which consisted of a low-viscosity layer, sandwiched between two thick, high-viscosity blocks with coherent interfaces (Figure 4.18).

Both the wall and the layer were treated with rate-independent linear viscous rheology. In this modeling their relative viscosity is used as a non-dimensional parameter, expressed in terms of viscosity ratio (*R*). For a simulation run, the weak layer was chosen to have initially a uniform thickness (*T*), and the model was subjected to a layer parallel shear and a normal stress at the model boundaries. The deformation localized preferentially in the thin low-viscosity layer, forming a distinct slip zone, which resembled those produced in our laboratory experiments. The walls also participated in deformation but restricted within a thin zone close to the interface, where the magnitude of finite strain was significantly lower than that in the slip zone.

4.7.1 Mathematical method for Instability Simulation

The evolution of slip zones was investigated to study their geometrical irregularities with progressive shear. This was performed by mapping the interface of the weak layer with the ambient stronger wall. However, tracking the transient states of the interface is a major step in our multiphase flow analysis. Level Set (LS) method was employed that tracks the phase interface using a level set function (Osher & Sethian, 1988). The LS method employs a Eulerian technique to track the moving interface between two fluid phases with the help of a globally defined smooth continuous function, known as LS function (ø). The function ø varies smoothly from 0 to 1, where the functional values 0 and 1 denote fluid phases 1 and 2, respectively, whereas 0.5 delineates the interface. The region assigned with $ø > 0.5$ is filled with fluid phase 1 and that with $ø < 0.5$ is occupied by fluid phase 2.

The LS function (ø) is also advected in the flow field; its time-dependent expression for the moving interface is given by the advection equation:

$$\frac{\partial \emptyset}{\partial t} + v.\nabla\emptyset = 0 \qquad (4.4)$$

An abrupt jump of physical parameters across the moving interface often causes problems with conservations of mass and constant interface thickness. To overcome these problems, we used a conservative level-set (CLS) method (Osher and Sethian, 1988) to express the advection in the following form,

$$\frac{\partial \emptyset}{\partial t} + v.\nabla\emptyset = \gamma\nabla.\left(\varepsilon\nabla\emptyset - \emptyset(1-\emptyset)\frac{\nabla\emptyset}{|\nabla\emptyset|}\right) \qquad (4.5)$$

The left hand side of the Eq. 4.5 defines motion of the interface; the right side stands for reinitialization and numerical stabilization. Parameter ϵ is responsible for controlling the interface thickness and γ defines intensity of reinitialization. The model variables, such as density (ρ) and dynamic viscosity (μ) of the two phases, can be expressed in terms of the LS function as

$$\rho = \rho_1 + (\rho_2 - \rho_1)\emptyset \qquad (4.6.a)$$

$$\mu = \mu_1 + (\mu_2 - \mu_1)\emptyset \qquad (4.6.b)$$

In our simulations we consider incompressible flow conditions and momentum conservation, which are expressed by continuity equation and Navier-stokes equations, respectively, ignoring the gravity effects,

$$\nabla.\boldsymbol{u} = 0 \qquad (4.7)$$

$$\rho\frac{\partial \boldsymbol{u}}{\partial t} + \rho(\boldsymbol{u}.\nabla)\boldsymbol{u} = \nabla.[-pI + \mu(\nabla\boldsymbol{u} + \nabla\boldsymbol{u}^T], \qquad (4.8)$$

where $\boldsymbol{u}$ and p are the velocity vector and hydrostatic pressure respectively. I represent the identity matrix. In the present case, $\frac{\partial \boldsymbol{u}}{\partial t} = 0$ in Eq. (4.8). Using a commercial code (Multiphysics Comsol

5.2a) we implemented the CLS method for simulation of mechanical instability in a thin weak layer sandwiched between two stiff blocks.

The interface was initially flat but developed irregularities with progressive simulation run. In the beginning the irregularities nucleated as isolated 3-D domes and basins, without showing any linear trend. They acted as seed heterogeneities to promote subsequent growth of the surface irregularities into distinctly elongate shapes along the slip direction. Such an along-slip growth

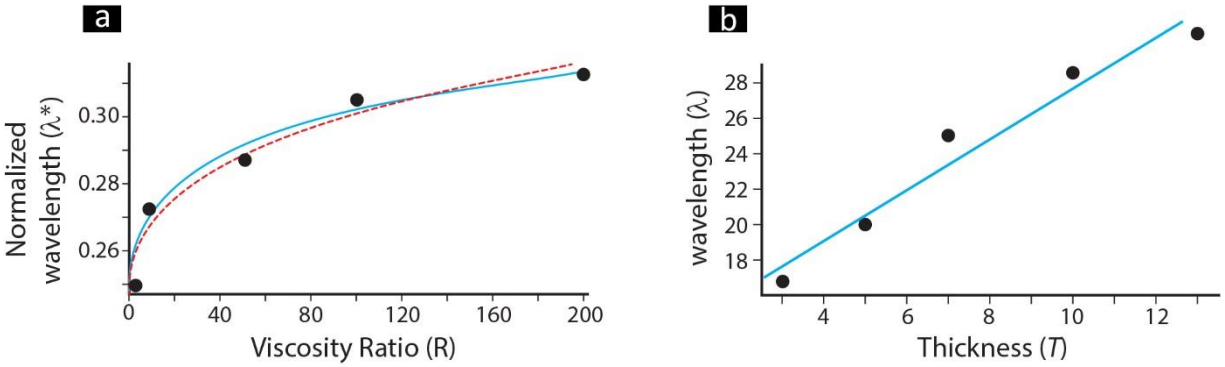

Figure 4.19. (a) Calculated plots of normalized wavelength ($\lambda^* = \lambda / T$) with viscosity ratio (R). The non-linear variation (blue line) closely follows a cubic root function of R (red dashed line). (c) Linear variation of λ with T.

involves amplification of the 3-D irregularities along with their rapid propagation and coalescence preferentially in the slip direction. This process eventually gives rise to wavy form of the interface, leading to slip-parallel ridges with more or less regular spacing. Unlike abrasion-induced slickenlines (Y. Boneh et al., 2014; Chester & Logan, 1986), these cylindrical ridges do not show any tendency to smoothen out with progressive shearing in the weak layer (Figure 4.17). However, the model run was restricted to a finite shear displacement of 100 mm.

Sets of simulations were ran by varying both R (1 to 200) and T (3 to 13 mm). These simulations aimed at analyzing the nature of mechanical instability, which will be discussed separately in section 4.8. The wavelength (λ) of irregularities becomes larger for larger R values,

as observed in case of buckling instabilities in mechanical layers under layer-parallel compression (Ramberg, 1955). For a quantitative analysis, a graphical plot of normalized wavelength (λ^*) with R (Fig 4.19.a) is presented here, which reveals a strongly nonlinear relation between them, closely agreeing with a cubic root function of R. On the other hand, a linear variation of λ with T (Fig 4.19.b) was obtained. These variations of wavelength (λ) with R and T warrant the development of cylindrical irregularities as a consequence of mechanical instability.

4.8 Theoretical interpretation

The slickenlines produced in the sand-talc models are strikingly similar to the new type reported by Means (1987) from his wax models (Fig 4.1). The shear surfaces are coherently corrugated more or less with cylindrical forms, with their axes oriented in the slip direction. Overall, the irregularities appear as a set of typical compressional folds in multiple orders (Ramberg, 1964). The antiforms on one side fit into the synforms on the other side (Means, 1987). They finally form along-slip linear structures, which grossly resemble the slickenlines produced in Means's wax and our sand-talc model experiments. Based on the numerical model results, the possible mechanism involved in the development of such geometrically coherent cylindrical irregularities is discussed here. The models consist of two mechanically distinct domains, the high-viscosity matrix and a low-viscosity thin intermediate layer embedded in the matrix. They are subjected to a layer-parallel shear, along with a layer-normal compression at their boundaries. The weak layer develops dome-basin-like fold instabilities, which act as crucial seed heterogeneities to promote the instability growth in response to the layer-parallel shear (Fig 4.17). The dome-basin-like structures were thought to initiate as a consequence of mechanical instabilities in the weak layer under layer-

normal compression. Smith (1975, 1977) has theoretically shown this type of fold-like instability, called inverse folding. From the numerical analysis, a nonlinear relation between normalized wavelength and viscosity ratio (*R*; Fig 4.19.a) was obtained, which closely corresponds to a cubic root function of *R* (Smith, 1975). In addition, a consistent linear wavelength (λ) versus thickness relation (Fig 4.19.b) was obtained. These findings support the interpretation of irregularities initiation in the thin weak layer as a result of mechanical instability, which is similar to inverse folding. However, further theoretical work is required to develop a complete conceptual framework of this unique mechanism.

In Type 2 model experiments the development of cylindrical irregularities on the shear surfaces varies with the inclination of shear surface to the bulk compression direction (θ). Increase in θ from 30 to 60° strengthens the growth of surface irregularities with well-defined waveforms (Fig 4.11). The theory of inverse folding instability discussed above can be accounted to explain this experimental finding. The normal stress component on the weak layer facilitates the initiation of such instabilities. Increase in θ gives rise to larger compressive stress normal to the weak layer, which facilitates the growth of inverse fold instabilities, required as seed heterogeneities for the development of cylindrical irregularities on the shear surfaces, as observed in our Type 2 experiments (Fig 4.16).

Numerical models presented in section 4.7 reproduce the linear irregularities along the slip direction observed in the sand-talc experiments. However, there are some differences in their geometrical characteristics. The physical experiments produced ridges with varying wavelengths, closely following their fractal distributions as revealed from our analysis, whereas numerical models show them as regularly spaced undulations of uniform dimension. This difference most probably results from the consideration of uniform slip zone thickness in our numerical model,

which is likely to be strongly non-uniform in natural conditions. Under a given mechanical condition, the instability wavelength is a function of the mechanical layer thickness. In the experiments the mechanical thickness of slip zones was likely to be heterogeneous, leading to wave instability formation with spatial irregularity.

This new type of mechanical model for the origin of slickensides has significant implications in interpreting the roughness characteristics of slip surfaces in specific settings, which do not show any imprints of abrasion, plowing, or synkinematic mineral growth, as elaborately discussed by Means (1987). For example, several studies have shown that the corrugated topography on slip surface results from plastic strain localization in the slip zones (Escartín et al., 2017; Parnell-Turner et al., 2018). This mechanical model suggests that such linear irregularities can also develop as a consequence of mechanical instabilities in the ductile slip zones. However, the growth of such instabilities demands a specific mechanical setting of the slip zones with their viscosity lower than the walls. Synkinematic rheological weakening can be a possible mechanism to lower the viscosity substantially and favors the condition required for this type of instabilities, as suggested by Smith (1975).

4.9 Experimental Advantages and Limitations

The field examples presented in this study motivated us to explore the mechanisms of slickenside lineation formation on shear surfaces without abrasion or synshearing crystal fiber growth. The slip surface irregularities characterized from the field observations provide significant information about non-abrasion type of slickensides. However, scarcity of markers indicating the finite slip puts a limitation in systematically studying the surface roughness as a function of displacement

(Brodsky et al., 2011; Sagy et al., 2007). In addition, the entire field analyses were performed on macroscopic scales, without any microscopic studies required to recognize the deformation mechanisms, such as cataclasis and crystal-plastic creeps, involved in slip processes. Despite these limitations, our field study allows us to qualitatively compare the macroscale geometry of experimental surface irregularities with nature.

The experimental approach in this study has several advantages: (1) it is possible to manipulate the rheology of models under room temperature conditions, (2) directly observe the rupture process in the models, and (3) easily study internal slip features with little or no significant alteration. Additionally, the total experimental procedure is cost-effective, and one can easily implement it in a simple laboratory setup. However, there are a number of limitations in our experimental approach: (1) the shear rupturing in experimental models does not involve secondary processes, which are commonly encountered in nature, such as synkinematic mineral growth, frictional melting, and gouge formation, and (2) the experiments do not account for the effects of varying the confining pressure and temperature.

This study offers a new technique for the quantitative analysis of fracture roughness. Generally, a range of contact and noncontact type methods are employed, but their implementation is costly. This method is simple, and easy to implement in a simple laboratory setup, equipped with a good camera and a controlled illumination facility. This technique is faster to develop surface maps for analyzing the roughness profiles. The binarization (cantor set) method allows to quantify the directional variability of fractal dimensions, which is useful for evaluating the anisotropic properties of linear roughness. This image analysis technique, however, has some limitations, and the user needs to be cautious because (1) it provides a picture of the surface roughness in terms of relative relief and (2) the D value obtained from cantor set is a measure of

roughness in the linear arrangement of geometrical perturbations, excluding the effects of other dimensions.

Chapter 5

Slip Patterns on Shear Surfaces

5.1. Introductory note

Faults and shear fractures usually accommodate large displacements preferentially along discrete zones (called slip zones), rather than uniformly on their entire surface areas (Brodsky et al., 2011a; Chester et al., 2004; Cowan et al., 2003; R H Sibson, 1977). Such slip zones on a seismic fault stores crucial information required to interpret the faulting history (Wells & Coppersmith, 1994) and rupture propagation dynamics (Scholz, 2002) of notable earthquake events. Their geometrical characteristics, such as their size and roughness as well as their spatial distributions critically determine the amount of elastic energy, and thereby the magnitude of earthquakes triggered by the fault (Biegel et al., 1992; Harrington & Brodsky, 2009; Lay et al., 1982; Rubin et al., 1999). Exposed fault and shear fractures often contain slip zones displaying linear surface roughness, formed by parallel long ridges and grooves (termed as *slickenlines*). A group of workers have demonstrated from field measurements their scale independent geometrical properties (Kirkpatrick & Brodsky, 2014a; Sagy & Brodsky, 2009a; C. H. Scholz & Aviles, 1986). Their roughness analysis not only provides a clue to the past rupture events, but opens a ground to establish the geological boundary conditions of past as well as possible future rupture events in a tectonically active region (Brodsky et al., 2016a). Moreover, slip surface analysis is extensively used for paleo-stress analysis in geological terrains (Bott, 1959; Gudmundsson, 2011; Michael, 1984; Ramsay & Huber, 1987). Several laboratory experimental studies have suggested that the

evolution of slip-surface roughness can largely influence the frictional properties and modulate the rupture propagation dynamics (Ohnaka & Shen, 1999; Okubo & Dieterich, 1984) and eventually determine the frictional stability of a fault (Harbord et al., 2017; Marone & Cox, 1994; Ohnaka, 2013). Quantifying surface roughness of faults and fractures has consequently emerged as a study of great demand in brittle tectonics research.

Most of the earlier workers employed profilometers to measure the geometrical irregularities in quantify the fault roughness (S. R. Brown & Scholz, 1985; J. J. Lee & Bruhn, 1996; W. L. Power et al., 1988; William L Power & Tullis, 1991). The surface roughness studies subsequently underwent a revolutionary development with the advent of non-contact type high-density optical scanning methods, which remarkably improved the precision of the field measurements (Bistacchi et al., 2011b; Brodsky et al., 2011a; Candela et al., 2012a; Renard et al., 2006; Sagy et al., 2007a). The quantitative analyses of fault surface roughness reveal a well-defined statistical distribution of the surface irregularities (S. R. Brown & Scholz, 1985; Candela et al., 2009b; J. J. Lee & Bruhn, 1996; W L Power et al., 1987a; Renard et al., 2006). These topological studies lead to two primary findings: 1) roughness on a slip surface is not isotropic, rather there is a appreciable difference in irregularities along and across-slip direction, a much smoother roughness along the slip direction than that across the slip direction, on a particular length scale (Renard et al., 2006); and 2) this roughness defines a statiscally self-affine property, rather than self-similarity. It has been shown from analogue model experiments that the degree of anisotropy has a tendency to increase with increase in slip on the shear surfaces. Additionally, M. Mukhopadhyay et al., (2019) also demonstrated that the mode of shear failure and the initial shear surface orientation can dictate this degree of roughness anisotropy, as defined by the difference in one-dimensional fractal dimension (ΔD) in the along and across slip direction. On the other hand,

2D profiles of roughness from several studies have reported self-affine fractal property, obeying a transformation $\delta x \rightarrow \mu\delta x$, $\delta z \rightarrow \mu H \delta z$ (Candela et al., 2012), where δx = profile length, δz = asperity height and H = roughness exponent, commonly termed as the Hurst exponent ($H \neq 1$). It can be inferred from this law, that the geometry of profiles of the surface irregularities or asperities varies with the scale of observations.

5.2 Field studies

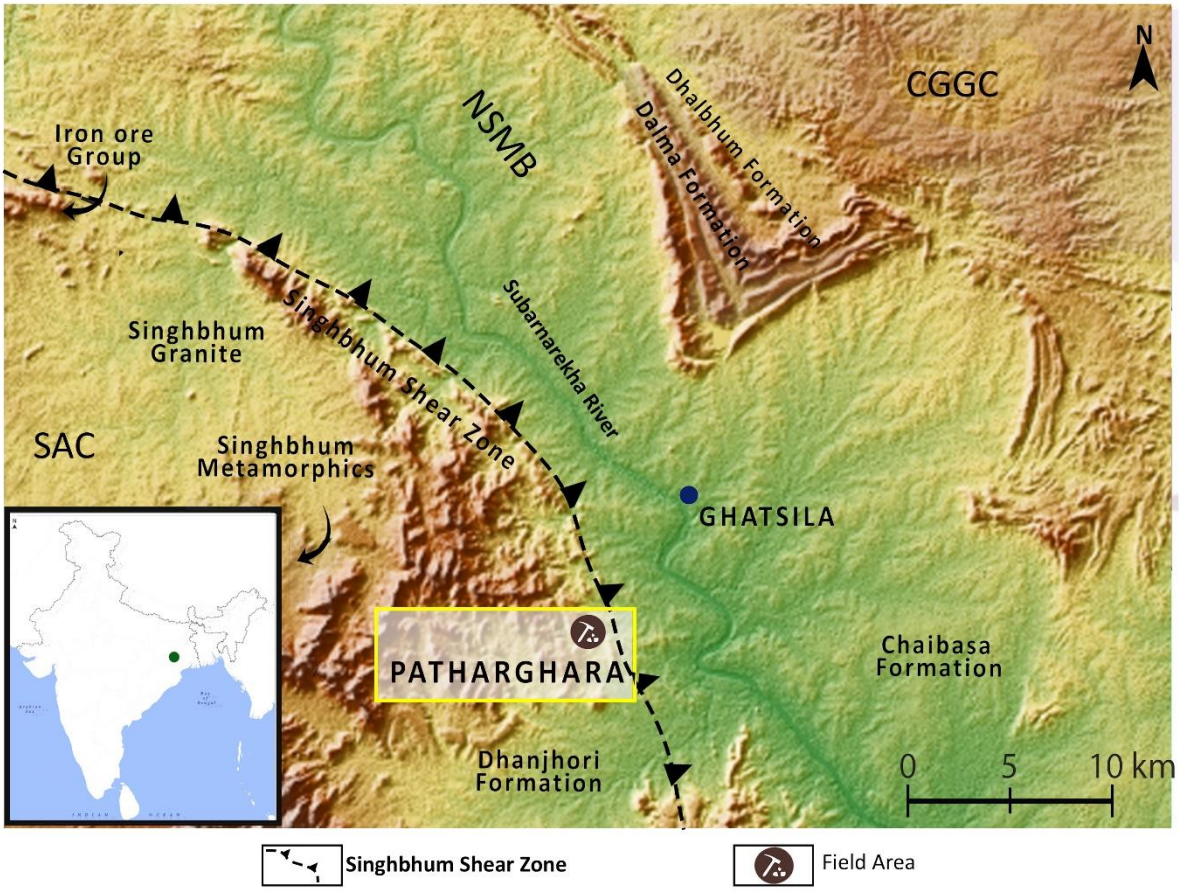

Figure 5.1. Geological framework of the Singhbhum Craton in the eastern part of India (location marked by green dot in the inset). The Singhbhum Shear Zone (SSZ) separates the Archean Singhbhum Craton and the North Singhbhum Proterozoic mobile belt (NSMB). The yellow box demarcates the study area in the SSZ. SAC: Singhbhum Archean Craton ; CGGC : Chhotanagpur Granit Gneissic Complex.

The present field investigation was carried out in the Singhhum Shear Zone (SSZ), which is a ~200 km long, about 2 km wide arcuate ductile to brittle-ductile shear zone (Ghosh & Sengupta, 1987; Sengupta & Ghosh, 1997) in the eastern Precambrian terrain (Fig1a). The SSZ delineates the boundary between the North Singhbhum Mobile Belt (NSMB) of Proterozoic age in the north and the Archaean cratonic (Singhbhum Craton) nucleus to the south (Saha, 1994), as described in the previous chapter (Chapter 4). It trends NW-SE in the eastern flank, turning to E-W in the central part and finally to NE-SW on the opposite flank, and always maintains northerly steep dips (40° to 60°). Micro- to macro-scale structural analyses suggest strong deformation localization over the entire stretch, however, with some local variations in the intensity of ductile to brittle-ductile shearing (Roy et al., 2021; Sengupta & Ghosh, 1997).

Field analyses were concentrated in an elegant exposure of sheared quartzite at Patharghara village, located (22°32′37.911″N, 86°26′31.223″E, altitude: 143 m, accuracy: ±3 m) near the old Surda copper mines in the south-eastern flank of SSZ (Fig. 5.1). The Patharghara-Surda area constitutes an undulating plateau, showing a spectacular range of scattered hills with an average altitude of about 200m. Geographically, the area lies between Mosabani in the east, Surda in the west, Dhobani ranges on the south and in the north, and can be accessed from the Mosabani-Tatanagar Road running parallel to the SSZ. In these scattered hills there are large outcrops of sheared quartzite, providing an excellent scope for studying slip-surface features on slickensides. Fresh shear surfaces with no significant weathering effects were chosen.

5.2.1 Field-study approach

Sheared quartzite outcrops displaying well-developed slickensides on a few centimeters to several meters scale, were chosen to analyze slip zones by using linear features (slickenlines).

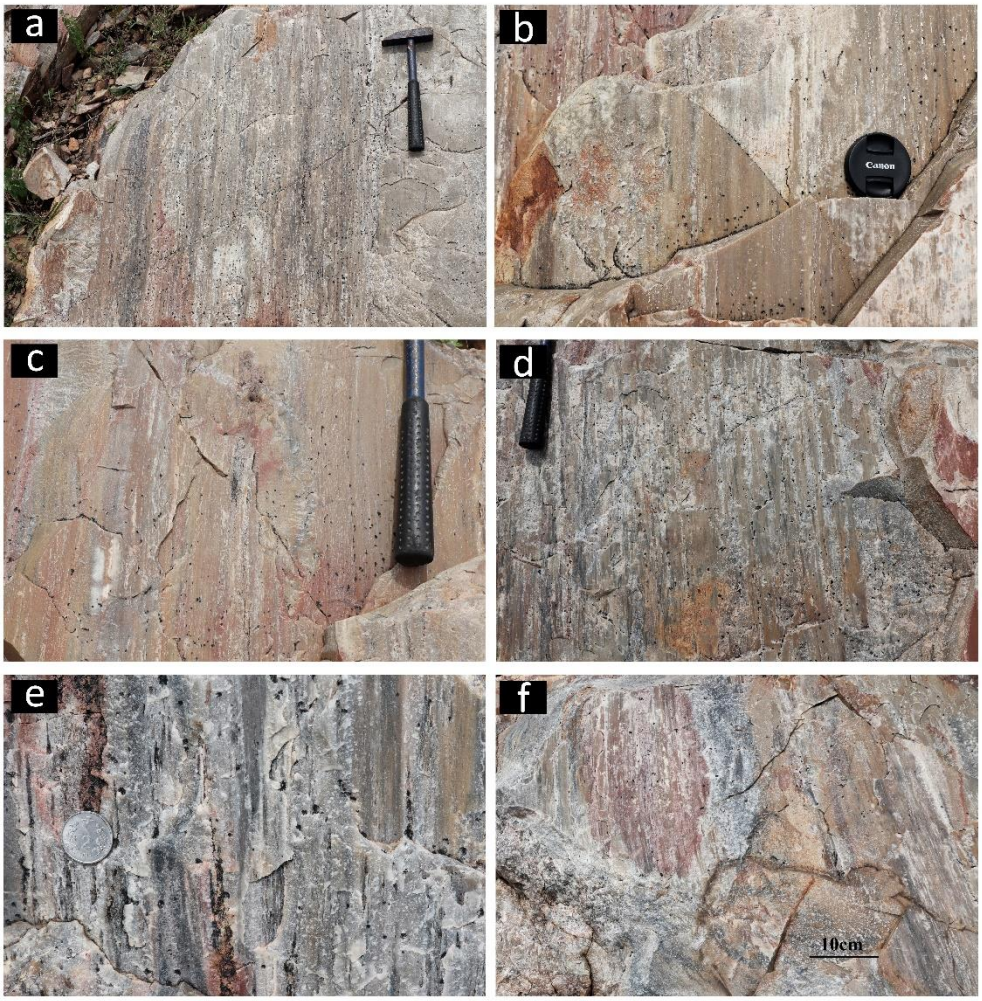

Figure 5.2. Field photographs of slickensides showing different geometrical relationships between slip zone (strongly lineated region) and stuck zones (regions with weak or no lineations). (a) Slip and stuck zones separated by a linear divisor. (b) and (c) Stuck zones surrounded by slip dominated zones on all sides. (d) and (e) Slip and stuck zones distributed all over the shear surface, forming a network. (f) Circular slip zones rimmed by an annular stuck region. (The hammer length= 33 cm, hammer handle length= 17.5 cm, camera cap diameter= 5.5cm, coin diameter= 2.5cm.)

Slickensides surfaces strike broadly parallel to the NW-SE trend of SSZ in its eastern flank, and the slickenlines on them plunge in the NE direction. They could be recognized by their strong linear features in the field. They occur in discrete patches with intervening stuck zones, which are

either devoid of prominent slip parallel lineation or contain weakly developed lineation. Slip and stuck zones were seen to coexist in several forms, such as random, irregular patches, alternate elongate bands, pits and grooves and circular slip zones, surrounded by lineation-free stuck zones. Detailed photographs were taken to capture these patterns on varied scales to study the slip heterogeneity on shear surfaces. For a quantitative 3D analysis of shear surface roughness, their casts were taken from selected locations (Figs 5.3.a-d) and prepared their three-dimensional topography using a laser scan system in the laboratory.

5.2.2 Slip zone patterns

Based on the surface roughness characteristics of slickensides, the two principal domains were demarcated: 1) slip zone and 2) stuck zone. The main feature used to characterize them is the anisotropic surface roughness, defined by ridge-groove 3D wave geometry in single or multiple orders of wavelengths, to form strong linearity in the roughness characteristics. The roughness becomes almost isotropic in stuck zones, represented by smooth or pitted or irregularities without any directional attribute. Understanding the fault surface topography is an essential step to deal with the heterogeneous stress field that plays a critical role in the nucleation of isolated slip zones, triggering earthquakes (Campillo et al., 2001; Voisin et al., 2002), and propagation and arrest of the ruptures (Voisin et al., 2002). In the field studies, it was thus meticulously observed how slip and stuck zones are spatially correlated on slickenside surfaces. Their distributions are found to be neither uniform throughout the outcrop nor entirely random, rather they form specific geometrical patterns. The slip zones are often separated by linear stuck zones parallel to the lineation (Fig. 5.2a). In places, the stuck zones occur sporadically as discrete patches on the shear surface. These patches appear like islands surrounded by slip zones on all sides (Fig. 5.2.b and c). Slip and struck

zones also occur alternately to form a band structure almost parallel to the overall slip direction (Fig. 5.2.d and e). Shear surfaces occasionally contain large slip zones surrounded on all sides by no-slip domains in the form of an annular ring (Fig. 5.2.f).

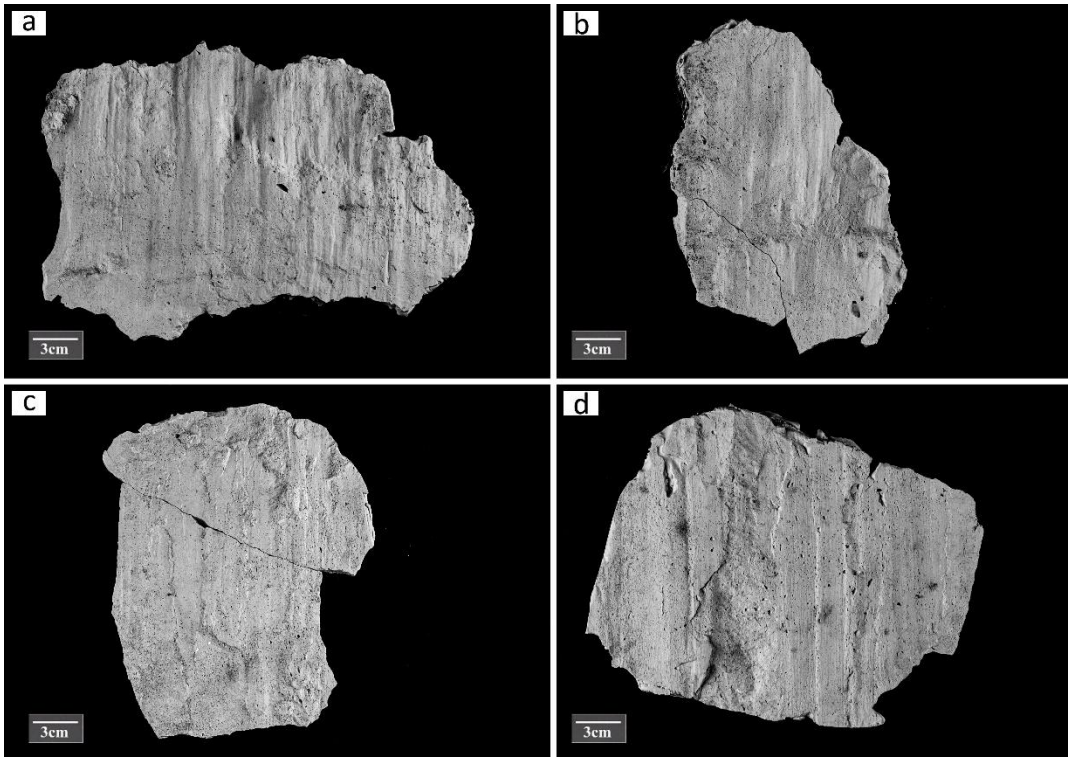

Figure 5.3. Field casts of slickensides with various spatial slip-stuck zone patterns. (a) Shear surfaces containing linear roughness on wavelengths, ranging from a fraction of millimeter to a centimeter, and sporadic small non-lineated (stuck) regions. (b) Shear surface with wavy irregularities, as in (a), but showing more prominent stuck zones (> 45% in area coverage). (c) Slip-parallel lenticular stuck domains (> 53% in area coverage), often fingering inside the slip zones. d) Shear surface dominated by slip zones, leaving stuck zones as a minor component (20% in area coverage).

Several 1D analyses of natural fault-surface topology have indicated the roughness as a scale invariance phenomenon (J. J. Lee & Bruhn, 1996; W. L. Power et al., 1988; W L Power et al., 1987b; W L Power & Durham, 1997; William L Power & Tullis, 1991; Schmittbuhl et al., 1993). Such scale invariance characteristics can be described by self-affine geometry with a

roughness scaling exponent. Field observations reveal similar scale independent geometrical properties of slip and stuck zones on slickensides. The different types of their geometrical patterns described above can be found on a wide range of spatial scales, from outcrop (tens of meters) (Fig. 5.2.b) to hand specimen (a few centimeters) (Fig. 5.2d). Laser scanned images of the field casts further suggest that similar geometrical patterns of the slip and stuck zones persist even in much smaller scales.

5.3 Laboratory modelling of slip zones

5.3.1 Experimental design

Analogue experiments were conducted on wet talc blocks, mixed with a small amount of white cement to introduce initial cohesion in the block. This wet talc material reproduced brittle-ductile rheology, and underwent shear failure at yield stress of 162 kPa, followed by a stress drop with increasing strain, i.e., strain softening after the first yield point (Brooks et al., 1991). The shear surfaces in talc models developed excellent one dimensional irregularities, giving rise to typical slickensides features (Mukhopadhyay et al., 2019).

Commercial talc powder (grain size: 0.3 to 50 μm, average: 20 μm) was used to prepare the analogue model in the following way. White cement and water were added to the pure talc powder in volume ratios, 1:6 and 1:9, respectively. The wet homogeneous mixture was then molded in a rectangular box of desired dimensions [17.5 cm × 9 cm × 7.62 cm] to form a solid block. The purpose of using a little amount of white cement was also to retain the slip-induced geometrical irregularities produced shear surfaces after the experimental run and study them under the laser scanner system. The talc model was deformed in pure shear under a plane strain condition. The

deformation setup is schematically illustrated in Figure 3b. In order to restrict the flow in the vertical direction, a horizontal toughened glass plate was fixed at the top model surface, allowing the model extension entirely in the horizontal direction, perpendicular to the horizontal shortening direction. This kinematic configuration sets a stress frame, defined by a vertical intermediate principal axis of stress (σ_2) and horizontal major and minor principal axes of stress (σ_1 and σ_3). To minimize friction at the basal and top model interfaces, liquid soap (viscosity ~ 1.5 Pa s) was applied at the model base and the bottom face of the top cover glass plate.

The talc model had an initial cut which reactivated to localize a shear surface during the experimental run. The purpose of introducing this cut was to simulate a shear surface at a desired inclination (θ) to the compression direction (σ_1-axis). It is noteworthy that the slip mechanism mediated by stuck and slip zone formation is sensitive to θ. This approach was implemented in the following way. The talc block was cut into two halves at a desired orientation (θ). The two halves were then reunited, leaving the setup undisturbed for about ~2 hours and allowing the cut zone to heal sufficiently. The cut zone, however, remained as a weak planar heterogeneity, and facilitated the shear failure to localize in the talc model preferentially along its trend during pure shear deformation. A series of experiments were ran by systematically varying θ in the range 30° to 60°.

The convergence movement (6 mm/min) of two stepper motor driven pistons on opposite sides of the deformation table gave rise to a bulk shortening in the model at a rate of 2.2×10^{-3} sec^{-1}. An experimental run was continuously monitored and photographed through the top glass plate, keeping the camera attached to an adjustable vertical stand, which was fixed to the deformation table. A computer-controlled automated shutter operation was used to capture successive snaps of the ongoing model deformation at regular intervals. Under compression, shear deformation localized along the vertical initial cut in the model to produce a laterally persistent shear surface.

It was not possible to undertake in-situ observations of the shear surface topography during the experimental run. Earlier studies showed that shear surface features can significantly change with increasing finite slip (Brodsky et al., 2011). In the experiments, model shortening was kept low so that the finite slip remained roughly below 20% of the shear surface length. The deformed block was left untouched for about a day, allowing the block to harden and freeze the slickensides on the slip surfaces. The two halves were separated from each other with special care to preserve the geometrical features on the shear surface. The shear surface features were photographed to study the slip and stuck zone patterns. For their quantitative geometrical analysis, the model slip surface was also scanned under Micro-Epsilon opto NCDT ILD1420-25 Laser Sensor. Finally, a fractal analysis of the stuck and slip domains was conducted. The details of the Laser and the Fractal Analysis will be discussed in section 5.4.

5.3.2 Laboratory observation

Sand-talc models localized slip preferentially along the pre-existing weak planes under pure shear, producing major shear fractures. Some secondary fractures locally branched from the principal shear surface. The shear surface roughness, defined by irregularities of ridge and groove structures, produce a lineation in the slip direction. The slickenside surface also developed some secondary features, like step-like reliefs oriented at high angles to the slickenlines, closely resembling the typical steps observed on natural fault surfaces (Doblas, 1998b; Gay, 1970; Lin & Williams, 1992). Varying fracture inclination θ resulted in a spectacular transition of the roughness characteristics. The experimental slickenside surfaces form two prominent domains: isolated slip zones and stuck zones (Fig. 5.4), as observed in natural rock samples (Fig. 5.2.a-f and 5.3). The slip zones occur sporadically, leaving isolated stuck zones, which are devoid of any slip-induced

lineation and show either positive or negative reliefs. Isolated stuck zones show a wide variation in their normalized dimensions (equivalent circular diameter), ranging as low as 0.79 mm to 59.18 mm. The relative area of stuck domains in the total shear surface reduces with increasing θ (Fig. 5.4.a - c). For $\theta > 45°$, the smaller size population of stuck zones dominates in the system, and the

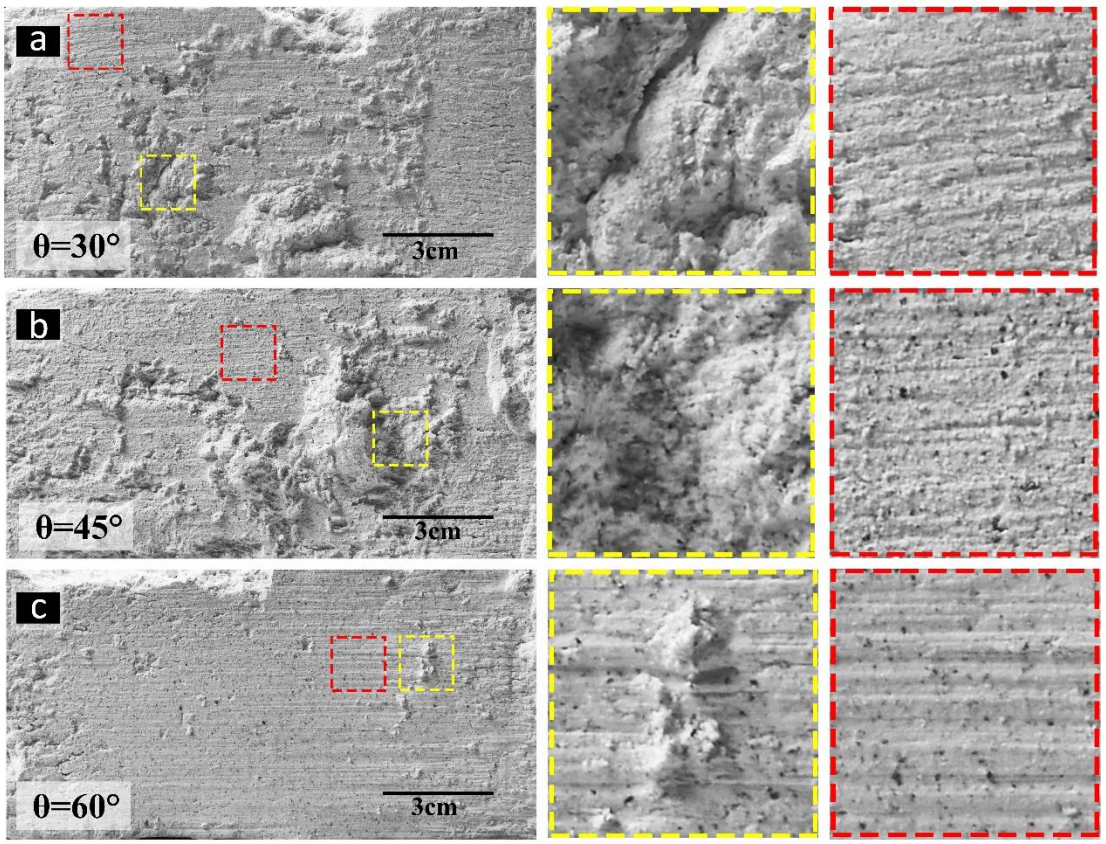

Figure 5.4. Shear surface roughness produced in talc model experiments, conducted with varying initial shear-surface inclinations (θ) to the compression direction. The yellow and red boxes demarcate stuck and slip zones, respectively chosen for magnified views (corresponding right panels). (a) $\theta = 30°$; shear surface with abundant stuck zones, characterized by roughness without any directionality. Notice intervening slip zones showing persistent slickenlines. (b) $\theta = 45°$; nearly equal development of stuck and slip zones. (c) $\theta = 60°$; extensive growth of slip zones, leaving small isolated stuck zones

shear surfaces develop mostly slip zones, characterized by strong slickenlines when $\theta = 60°$ (Fig. 5.4c). The stuck zones become a minor component, covering less than 10% of the total shear surface area. Based on the stuck-zone distributions, the shear surface roughness in the experiments

can be grouped into the following three categories. a) Shear surfaces contain random discrete stuck zones within a spatially vast slip zone. b) Shear surfaces consists of stuck and slip zones in the form of alternate bands oriented parallel to the slip direction; c) Shear surfaces form a network of stuck zones with slip domains.

5.4 Quantitative analysis of slip zone patterns

Topographical fluctuations on shear surfaces was measured to characterize their roughness properties (Renard & Candela, 2017), such as scale invariance and fractal dimension. The slickenline formation in slip zones results in surface irregularities with linearity, which is found to be a characteristic parameter of slickensides in fault zones (Mukhopadhyay et al., 2019; Renard and Candela, 2017). Several studies have shown that fault roughness can satisfy power-law size distributions of the geometrical irregularities (Candela et al., 2009b; Mandelbrot et al., 1984; W L Power et al., 1987b). Interestingly, the fractal dimensions (*D*) of such power-law distributions are often used to estimate the frictional properties of fracture surfaces; more the *D* values more the frictional strength (Hanaor et al., 2016; V. L. Popov & Filippov, 2010). In the present study, a laser-based roughness analysis was undertaken to quantitatively describe the characteristic geometrical properties of the two shear-surface domains: slip and stuck zones. This analysis uses the fractal dimension as a measure of roughness anisotropy in demarcating them.

Two methods were used: 1) MATLAB based image processing (Mukhopadhyay et al., 2019) and 2) laser profilometer to perform roughness analyses on outcrop and laboratory scales, respectively. In case of the image-based technique, surface illumination is the most crucial factor, where it must be sufficiently homogeneous over the surface area of interest. In a field environment,

sunlight is the prime source of illumination, where its pattern varies during the day time due to a change of illuminating angle to the surface. To avoid this uncertainty, a specific time of the day was chosen to capture images of slickenside surfaces of more or less uniform orientations (dip angle variation within ±3°). Special care was taken to set the DSLR camera in a fixed setting while capturing the images. The images were then processed in the MATLAB platform using the Gray Scale Intensity (*GSI*) values to prepare the topographic profiles of shear surfaces (Mukhopadhyay et al., 2019). A specially designed laser profilometer was used for the roughness analysis of experimental models and slickenside casts from the field. Details of this is given in Chapter 3.

5.4.1 Field Samples

As described in section 5.2.2, the exposed shear surfaces display linear roughness, formed by a preferred orientation of fine ridges and groves (slip zones), but they are locally devoid of any type of linearity in patches (stuck zones). Figure 5.5 illustrates different varieties of roughness in natural shear surfaces, where the stuck zones are delineated in transparent yellowish colour. A type of roughness contains distinct slip and stuck zones; the latter occupies ~36 % of the shear surface area. A field example is presented to show two contrasting roughness domains, anisotropic slip zone and isotropic stuck zone, with their boundary parallel to the slip direction (Fig. 5.5.a). The corresponding profiles reveal a similar contrast between them in the *GSI* (Gray Scale Intensity) values, where the slip zones show higher amplitudes (*GSI*: ~50) than the stuck zones (*GSI*: ~25). The profile of slip parallel and perpendicular direction of the stuck zone shows a similar pattern (Difference in amplitude ~ 5 *GSI* values), implying an isotropic roughness characteristic. Another variety contains stuck zones with patchy appearance. They are relatively rougher (*GSI* values: ~70) than the surrounding slip zones (*GSI* values: ~30) due to the presence of large-amplitude abundant

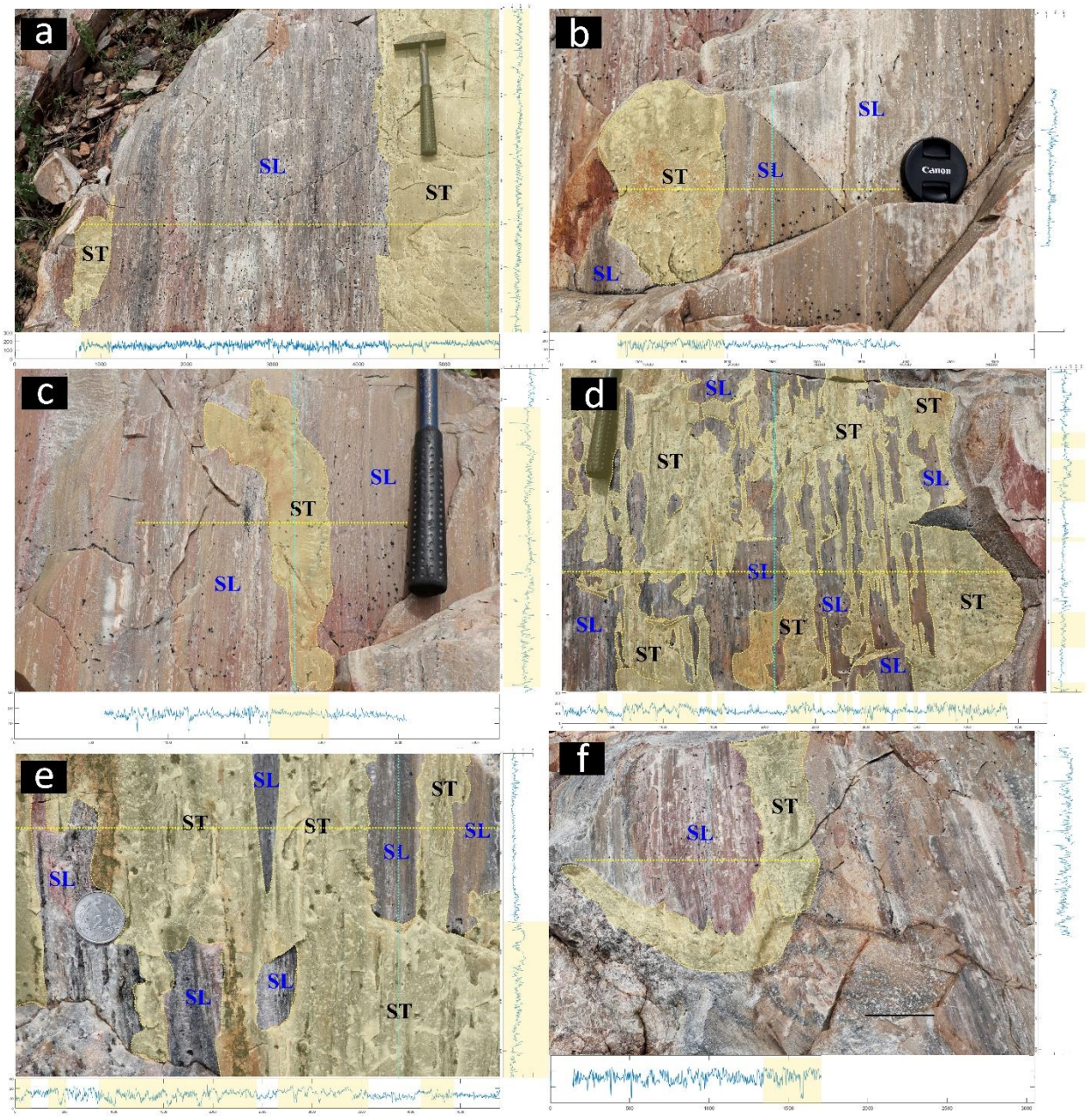

Figure 5.5. Field examples of varying roughness on shear surfaces in quartzite. Stuck zones (little or no lineation) are highlighted by light yellow shades. Corresponding across- (dotted yellow line) and along-slip (dotted cyan line) profiles are shown at the bottom and the right sides of each panel, respectively. ST: stuck zone, SL: slip zone.

ridges and grooves without any directionality. Along-slip profile of the slip zone is markedly smoother (*GSI*: 10-15) than an across-slip profile (Fig. 5.5b and c). Slickensides also show a

network of stuck zones with slip zones, broadly aligned in the slip direction. The corresponding across- and along-slip profiles show a hybrid pattern of contrasting roughness, where the stuck zones occur as bands of rougher irregularities in both the directions (*GSI* values ~ 60), which indicate their isotropic roughness property. In contrast, the slip zone profiles are characterized by a strong anisotropic roughness (across *GSI*: ~ 55 and along *GSI*: ~ 25) (Fig 5.5.d and 6e). In places, slickensides display a unique roughness characteristic, where the slip zones occur in isolated patches, surrounded by stuck zones (Fig. 5.5.f). The slip zones show a large difference in the GSI values along and across the lineation.

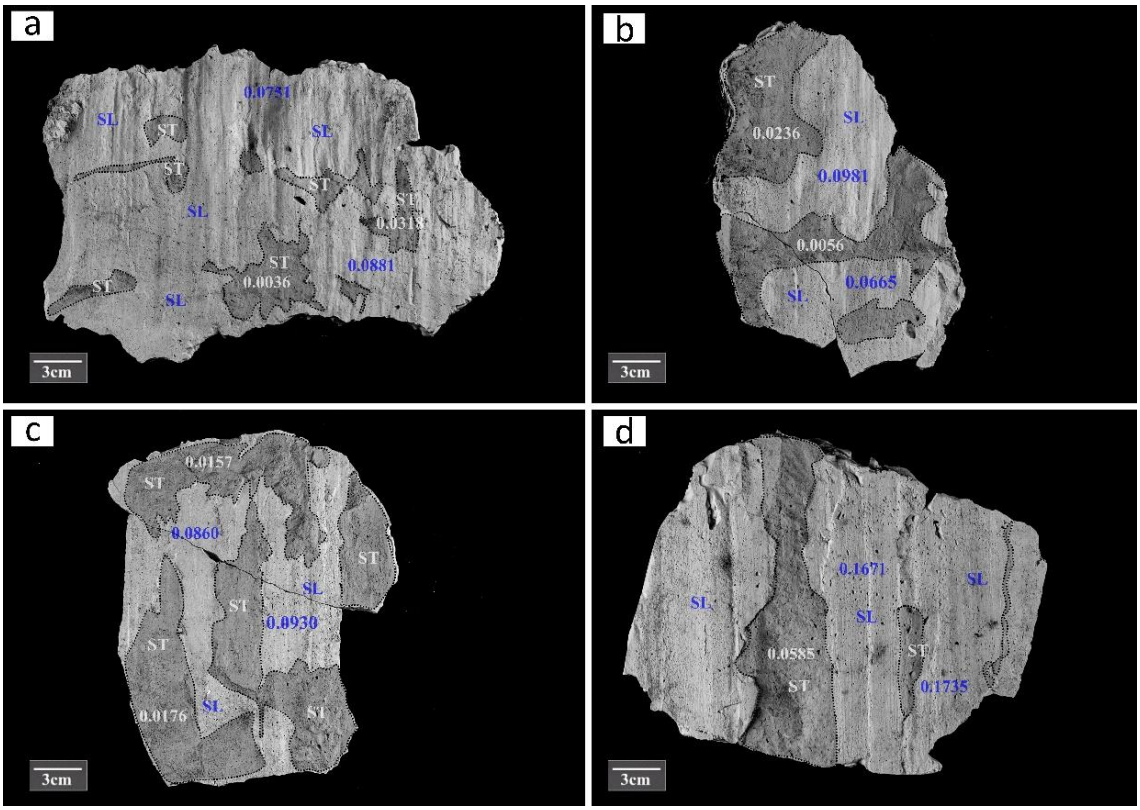

Figure 5.6. (a-d) Stuck zone mapping (highlighted by grey shades) on shear surfaces from field casts. Δ*D* values are plotted in the stuck zones and slip zones (numbers in white and blue, respectively) to show a clear difference in their roughness anisotropy. ST: stuck zone, SL: slip zone

The field casts were used for the roughness analysis in the laboratory with the help of the laser profilometer. A set of cast samples is presented in Figure 5.6.a-d, highlighting the stuck zones in transparent grey colour to describe typical features of slip-stuck zones association. A sample shows slip-dominated shear surfaces with minor stuck zones (areal coverage: ~15 %) as isolated patches (Fig. 5.6a). The calculated 3D topography ensures the dominance of linear roughness, represented by a preferred orientation of alternate ridges and grooves, leaving small lineation-free domains

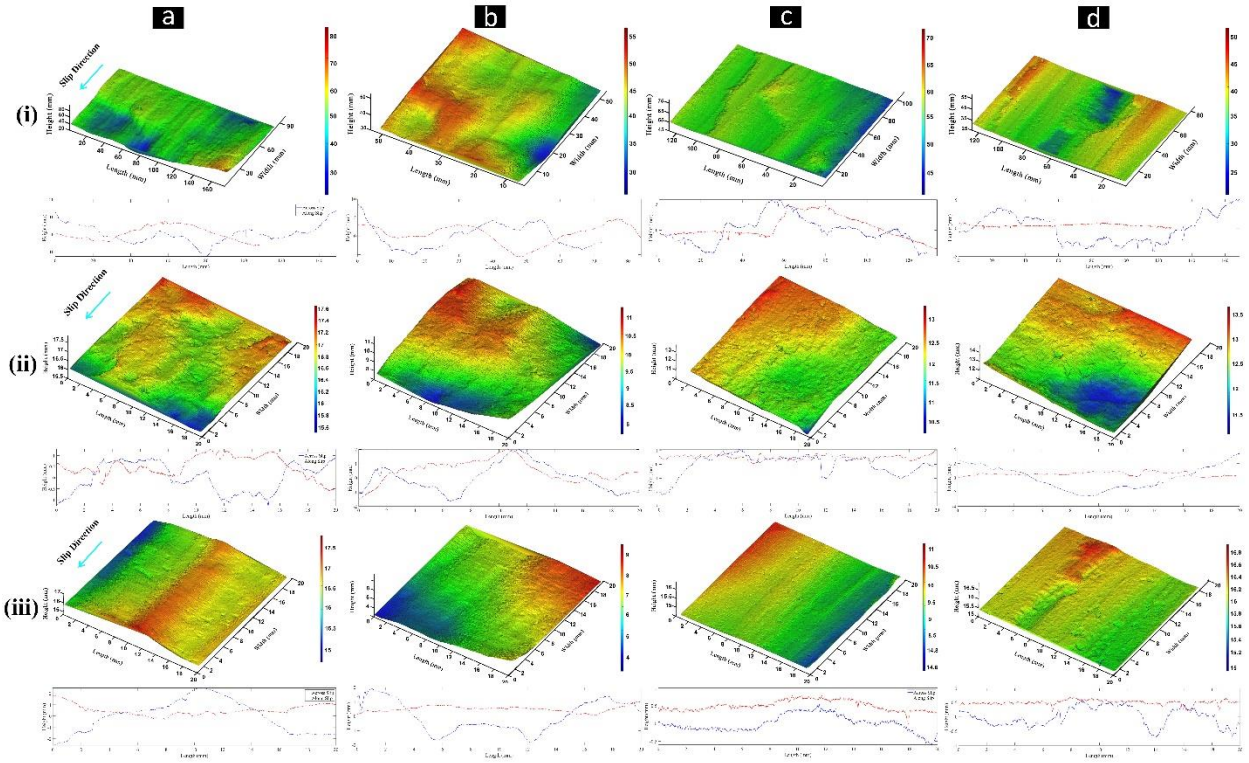

Figure 5.7. 3D topography of cast samples showing varying shear-surface roughness. Row-wise panels: (i) Surface topography containing stuck and slip zones (ii) and (iii) Close views of stuck and slip zones, respectively. The corresponding across- and along-slip profiles are shown in red and blue lines at the bottom of each panel.

(stuck zones) (Fig. 5.7.a). A magnified 3D view of the stuck zones reveals isotropic roughness characteristics, giving rise to similar across- and along-slip profiles (amplitude ~ 1mm). In contrast, the slip zones consist of alternate linear ridges and grooves (see parallel colour bands in the topographic map) with a strong topographic anisotropy, which is evident from across- and

along-slip profiles (slip perpendicular maximum amplitude ~ 3mm, whereas and slip parallel maximum amplitude ~1.5mm).

Figure 5.6.b shows a field cast of shear surfaces characterized by competing slip and stuck zones, which occupy 55 % and 45 % of the total shear surface area. The irregularities in lineated slip zones occur in two dominant wavelengths (~1 mm and ~ 10 mm), forming a multi-ordered topographic structure. The 3D topographic map also demarcates high lands, which are devoid of linearity (i.e. stuck zones) and relatively flat regions of strong linearity (i.e., slip zones) (Fig. 5.7.b). The domain-wise topographic mapping also allows us to distinguish between a stuck zone and a slip zone in terms of their roughness characteristics. The directional topographic profiles of stuck zones are almost identical (amplitude difference between across and along profiles ~0mm), but show a large variation in relatively smooth slip domains (amplitude difference ~ 1.9mm).

Another example of field cast topography is presented in Figure 5.7.c. The shear surface consists of stuck zones as multiple bands, separated by slip zones. Their band structure is oriented broadly in the slip direction. The 3D maps show almost homogenous colour distribution, implying relatively a smaller variation of irregularity elevations (0.1 mm). The two domains: slip and stuck zones, cover an area of 47% and 53% of the total surface area, respectively (Fig. 5.6.c). The stuck zone topography is characterized by uneven distribution of round pits and islands. Their corresponding profiles also show alternate but irregular valleys and peaks. In contrast, slip zones show fine scale slickenlines, giving rise to a remarkable difference in across- and along-slip topographic profiles. In extreme cases, slip zones far dominate (covering 80% of the total area) and stuck zones localize in a few locations (Fig. 5.6.d). The 3D topographical map shows a similar difference between the two domains (Fig. 5.7.d), as described above.

5.4.2 Laboratory Samples

In laboratory experiments, shear surfaces produced stuck zones mainly in the form of patchy domains. Their areal abundance varies inversely with the shear surface inclination (θ), reducing from ~ 56 % to 9% with θ = 30° to 60° (Fig. 5.8.a-c). Their 3D topography, generated by laser profilometer shows a marked geometric difference between stuck and slip zones, as observed in the field casts. Stuck zones form high or low lands without any directionality in their roughness, whereas slip zones in the model are relatively smooth, characterized by persistent linear roughness (Fig. 5.9.a-c). The θ = 30° model shows topographically irregular domains (stuck zones) spread

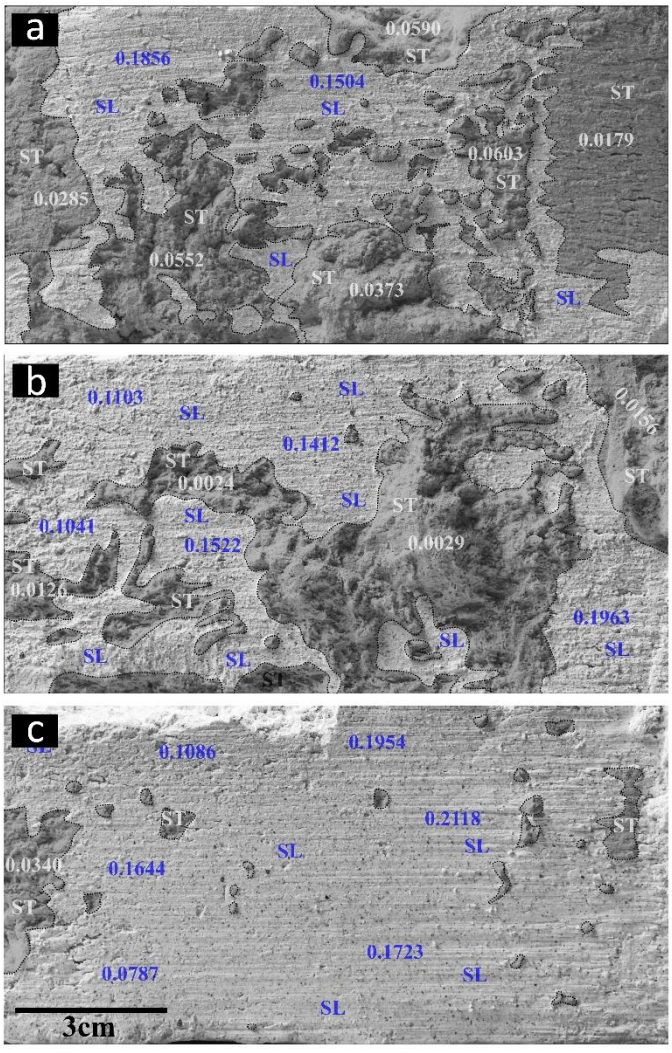

Figure 5.8. Stuck zone mapping (highlighted by grey shades) of the shear surfaces produced in laboratory experiments. (a) θ = 30°; (b) θ = 45° and (c) θ = 60°. Numbers in white and blue color denote ΔD values of the stuck and slip zones, respectively. ST: stuck zone, SL: slip zone. It is noteworthy that stuck zones decrease in area, whereas slip zones increase ΔD with increasing θ.

over the shear surface, leaving relatively flat, isolated regions (slip zones) with linear topographic structures (ridge-groove) parallel to the slip direction (Fig. 5.9.a(i)). Low-amplitude perturbations on the mean surface (5mm) of along-slip profiles clearly indicates smooth topography, as compared to that observed on an across-slip profile, which shows large amplitudes (8.5mm) of topographic roughness. This contrasting profile characteristics ensures the presence of linear

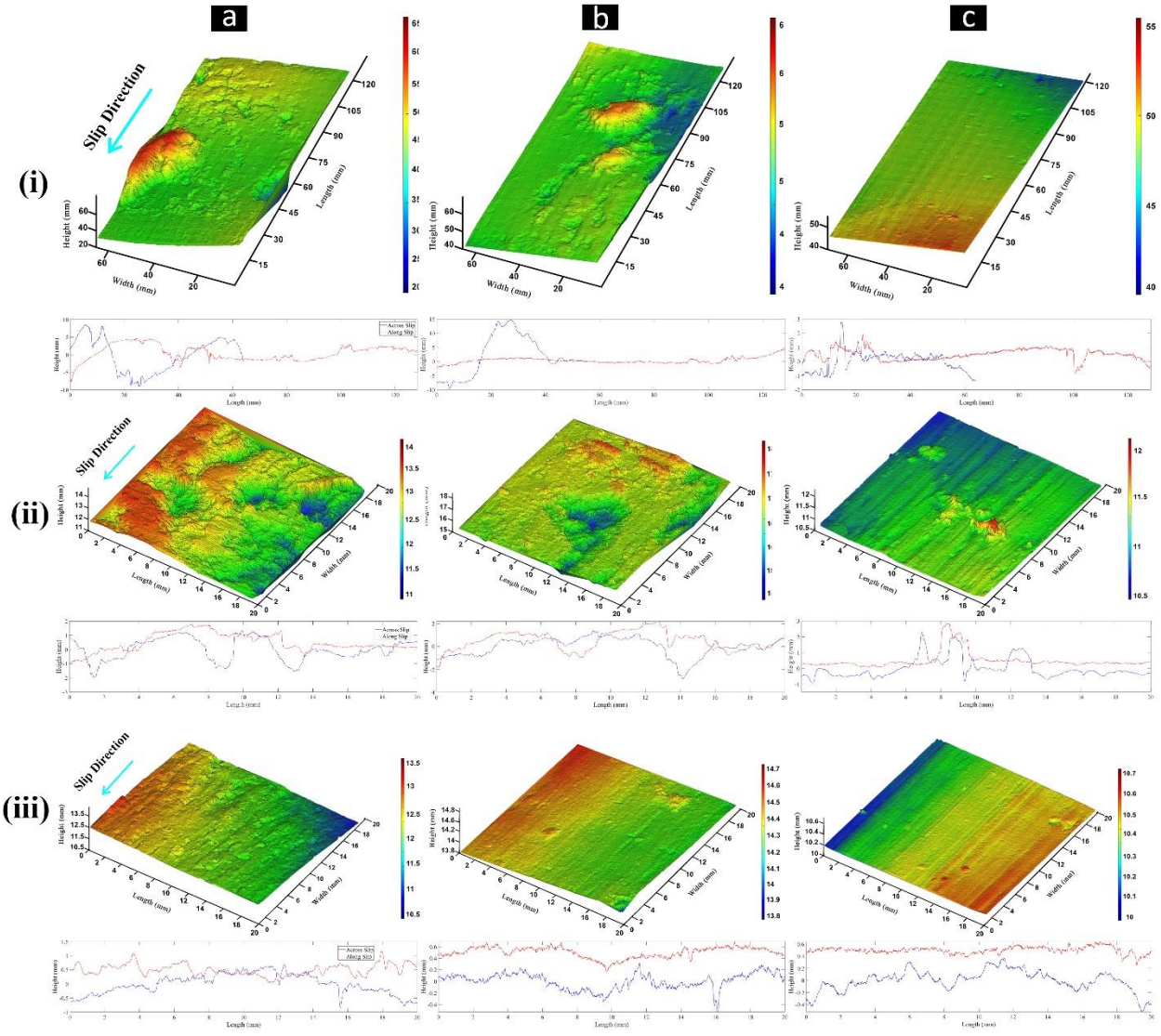

Figure 5.9. Calculated 3D shear-surface topography in experimental models with θ = 30° (a), 45° (b) and 60° (c). Corresponding row-wise panels: (i) topography of the entire shear surfaces. (ii) and (iii) Selected portions of the shear surfaces to show the details of stuck and slip zone topography, respectively. Their across- (red lines) and along- (blue lines) slip profiles are placed below each panel.

roughness in slip zones, which is completely absent in stuck zones, as revealed from similar along- and across-slip topographic profiles (Fig. 5.9.a(ii)). The slip zones, however, show strong heterogeneity in the degree of roughness anisotropy, especially weak in regions of irregular shear surface topography (Fig. 5.9.a(iii)). The 3D shear surface topography produced for $\theta = 45°$ consists of two major topographic highs and a few small highs, along with numerous topographic low regions (Fig. 5.9.b(i)). All these topographic elements represent stuck zones with isotropic irregularities, which are broadly smoother (Fig. 5.9.b(ii)) than those produced in the previous model ($\theta = 30°$) (Fig. 5.9.a(ii)). The slip zones display coarse linearity, resulting in conspicuous roughness anisotropy in the 3D topology, which is also obvious from the difference in along- and across-slip roughness (Fig. 5.9.b(iii)). The $\theta = 60°$ model produces slip zones to capture virtually the entire shear surface, leaving stuck zones as a minor element (a few sporadic topographic highs and small pits) (Fig. 5.9.c(i)). The enlarged views also reveal small islands of stuck parts (Fig. 5.9.c(ii)). The shear surfaces are remarkably smooth, but contain rod-like linear structures (dominantly in two wavelengths), forming a strong roughness anisotropy (Fig. 5.9.c(iii)).

To summarize, increasing θ facilitates slip zones at the cost of stuck zone areas, decreasing from 56% to 9%. The 3D stuck zone topography develops increasing anisotropy with increasing θ (amplitude difference changes from 0.1mm to 0.7mm). An increase in θ intensifies the roughness anisotropy of shear surfaces.

5.5 A synthesis of field and laboratory slip patterns

Fractal analysis of shear surface roughness was carried out for both the field casts and laboratory models, aiming to find distinctive geometrical properties of the stuck and slip zones. A

fractal population of objects must obey a power law function: $N = C/r^D$, where N is the number of objects with linear dimension r, C is the proportionality constant and D is the fractal dimension (Turcotte, 1997). The number of objects, N will thus vary linearly with their corresponding size r in a log-log space. The principal two domains of a shear surface: stuck and slip zones develop contrasting roughness anisotropy, as described in the earlier section. Using a box counting method, a one-dimensional fractal analysis was performed to show the degree of anisotropy in terms of D.

D was calculated along and across the slip directions and considered their difference ΔD as a measure of roughness anisotropy. ΔD was evaluated independently for slip dominated and stuck dominated zones in the field cast samples as well as laboratory models. The calculations yielded distinctive ΔD values in the two domains of shear surfaces (Figures 5.6 and 5.8). The stuck zones in natural casts had ΔD (0.0036 to 0.0585) significantly lower than that in the corresponding slip zones (0.0665 to 0.1735). The contrasting ΔD is visually reflected in the difference of their roughness profiles along and across the slip direction (Fig. 5.7). Slip zones with strong slickenlines produce large ΔD values (~ 0.1735), implying quantitatively greater roughness anisotropy. On the other hand, low ΔD (= 0.0036) characterizes weak roughness anisotropy in stuck zones, which agrees with the lack of directionality in their topographic irregularities. However, some of them had weak linearity, and gave rise to slightly higher ΔD values (ΔD = 0.0751 and 0.0881; Fig. 5.6a), albeit much lower than those obtained from slip zones with strong slickenlines (ΔD=0.1671 and 0.1735; Fig. 5.6.d).

The fractal analysis of analogue models produced ΔD values of shear surfaces strikingly in the similar ranges of ΔD for natural casts. The θ = 30° model yields ΔD in the range of 0.0179 to 0.0603 within stuck zones, which is elevated to a range of 0.1504 to 0.1856 in slip zones (Fig. 5.8.a). ΔD maintains a similar difference between the stuck and slip zones in the θ = 45° model;

stuck zones: 0.0024 to 0.0156 and slip zones: 0.1041 to 0.1963 (Fig. 5.8.b). As discussed earlier (section 3.2), stuck zones were drastically reduced in area, from ~ 45% to ~ 9% of the shear surface when $\theta = 60°$ (Fig. 5.8.c). Individual stuck domains became so small in size it was hard to perform their roughness analysis using the box count method in a resolution required to find ΔD. Some of them occurred as islands of relatively larger size, which allowed us to calculate their ΔD (= 0.0340). Strongly lineated slip zones that covered most of the surface area (~ 91%) had large ΔD values in the range 0.0787 to 0.2118.

In summary, the slip domains of a shear surface are characterized by large ΔD values (> 0.07). Stuck domains, in contrast, form regions of low ΔD (< 0.06). Laboratory experiments suggest that increasing θ facilitates higher ΔD, implying an increase in the degree of roughness anisotropy of shear surfaces, as visualized from the difference between across- and along-slip profiles in their 3D topography (Fig. 5.9a(iii), b(iii), c(iii)).

5.6 Experimental Advantages and Limitations

The experimental method used in this study has a number of advantages. For example, the shear surface could be set at varied orientations to investigate how the slip versus stuck zone processes can change with the initial shear surface orientations with respect to the compression direction. In addition, the experimental models allowed us to study the actual 3D topography produced on the shear surfaces using the laser profiling technique. Apart from these, the experimental method is cost-effective and can easily be implemented in a simple laboratory setup. However, there are a number of limitations, which are listed in the following. The experimental approach does not account for the role of frictional heating and associated phases changes, such as melting (Brown,

1998). These processes are reported to largely control the fault slip behavior (S. K. Lee et al., 2017). Secondly, it was not possible to simulate other secondary processes like synkinematic mineral growth that often influences the shear surface roughness (Twiss & Moores, 1992). Finally, the effects of confining pressure and temperatures on the creep mechanisms that might operate during sliding movement along faults were excluded in the experiments.

Chapter 6

Deformation localisation in mechanically heterogeneous media

6.1. Failure in solids: a review of existing theories and models

The shear failure mechanics is crucial to understand a wide spectrum of geodynamic phenomena, ranging from crustal scale tectonic deformation localization to earthquake dynamics. According to the classical theories, deforming elastic solids under increasing stresses attain a critical state, marked by a sharp jump in the displacement gradient across specific surfaces (strain localization) to undergo failure in the form of shear bands (Anand & Spitzig, 1980, 1982; Hutchinson & Tvergaard, 1980; Rice, 1976; Rudnicki & Rice, 1975; Tvergaard et al., 1981). Such band structures generally occur as narrow, linear regions on a wide range of scales (a few microns to hundreds of kilometers) and accommodate large plastic creeps to form high-strain zones in Earth's lithosphere (Mancktelow & Pennacchioni, 2005; Meyer et al., 2017; Rogowitz et al., 2016; Christopher H. Scholz & Choi, 2021; Snyder & Kjarsgaard, 2013; Vauchez et al., 2012). A direction of recent studies focuses upon the growth mechanisms of deformation bands, primarily to address a number of key rock physics issues, such as composite structures of fault damage zones (Mitchell & Faulkner, 2009), porosity enhancement versus reduction in deformation bands (H. Fossen, 2010), and localized melt or fluid transport pathways (B. K. Holtzman, Groebner, et al., 2003; Benjamin K. Holtzman et al., 2005; R. F. Katz et al., 2006). A significant part of their insights has come from laboratory experiments (Bowden & Raha, 1970; Camwell & Hull, 1973; Nizolek et al., 2021; Reber et al., 2020; Sagapuram et al., 2018; Zielinski & Ast, 1983). For

example, Bowden and Raha's experiments with polymer materials, e.g., polystyrene (PS) and polymethyl methacrylate (PMMA) recognize temperature (T) and strain rates ($\dot{\varepsilon}$) as principal physical factors to determine the mode of shear band localization in elasto-plastic solids under compression. At room temperature (T = 21°C) their PS experiments produced numerous sharp micro shear bands of ~1μm thickness, replaced by relatively wide, diffused shear bands at increasing temperature (T = 70°C) or reducing strain rates ($\dot{\varepsilon}$: 6×10^{-3} sec^{-1} to 4×10^{-3} sec^{-1}). The other polymer showed a similar transition in the mode of shear band localization as a function of T and $\dot{\varepsilon}$. A range of various practical materials, e.g., steel and rocks have also been used to study their failure behavior under laboratory conditions (Anand & Spitzig, 1980; David L. Kohlstedt & Holtzman, 2009). The shear band mechanisms in geological conditions are found to be intricately complex due to various factors, such as syn-shearing rheological transformations, fluid-assisted mineralogical changes, and long-time scale growth with changing ambient conditions (Bauer et al., 2018; Condit & Mahan, 2018; Haakon Fossen & Cavalcante, 2017; Putnis, 2021). To tackle such complexities, geoscientists have used numerical models to understand the evolution of shear localization on geological time scales (Beall et al., 2019; Gerya & Yuen, 2007; Meyer et al., 2017; A. A. Popov & Sobolev, 2008; Roy et al., 2021; Willis et al., 2019).

The studies discussed in the preceding paragraph dealt with shear failure in mechanically homogeneous solids. On the contrary, geological terrains can hardly be treated as homogeneous continua as they mostly contain inherent compositional or mechanical heterogeneities on macroscopic (e.g., igneous intrusives, faults or fracture zones, localized melt pockets, xenoliths) to microscopic (e.g., intragranular fractures/cracks, soft mineral aggregates, strong xenocrysts) scales. Field evidences, in fact, suggest that such heterogeneities can crucially influence the process of shear localization (Grujic & Mancktelow, 1998; Pennacchioni & Mancktelow, 2007) in

forming isolated shear bands, as observed in analogue experiments (Grujic & Mancktelow, 1998; Mancktelow et al., 2002; Misra & Mandal, 2007). Laboratory experiments predicted the geometry and orientations of shear bands that localize preferentially against mechanical flaws, such as, voids and rigid inclusions (Misra & Mandal, 2007). Earlier studies, however, provided little insights into the composite band evolution, characterized by multiple sets of primary and secondary shear bands, as commonly observed in tectonic belts (Y. Katz et al., 2004; Meyer et al., 2017; Misra & Mandal, 2007; Roy et al., 2021).

6.2. Aims and objectives of the present work

The evolution of complex internal band structures discussed in the preceding section is virtually unexplored, and the present experimental study aims to meet this gap. To understand the role of pre-existing flaws in determining the mode of plastic strain localisation and the deformation pattern, two types of experimental studies were performed on two types of models: *Type 1 and Type 2 models*. Type 1 experiments were done on Poly(methyl methacrylate) or PMMA, with two inherent cracks in the initial models under room temperature laboratory condition. PMMA was used as a proxy for real world rocks and several experiments were done to observe the various patterns of strain localization around the induced crack tips. This study also investigated the various features that develop as a result of the strain localizations and ultimately the failure of the rocks, like the wing cracks, their orientations, their formation mechanisms and the conditions of their formations.

Type 2 experiments (strain-rated controlled compression tests) were carried out on Polystyrene (PS) sheets under room temperature laboratory condition. The experiments

reproduced the typical plastic creep behaviour of common rocks reported from rock deformation experiments at elevated temperatures and pressures (B. K. Holtzman, Groebner, et al., 2003; B. K. Holtzman, Kohlstedt, et al., 2003; David L. Kohlstedt & Holtzman, 2009). From these experiments, how pre-existing mechanically weak flaws can control the shear band mechanisms (numerous sharp narrow to composite wide band formation) in heterogeneous elasto-plastic rocks, was demonstrated. The experimental findings were supported with the results obtained from real scale numerical simulations within a framework of visco-elasto-plastic rheology. Finally, this chapter presents a set of geological field examples to discuss different types of internal band structures in the light of laboratory experiments.

6.3. Experimental design

6.3.1. Type 1 Model preparation

For the first set three or four PMMA sheets of dimension (55mm X 35mm) and 12mm thickness were taken. To simulate the predefined crack, two PMMA blocks were cut at desired position and angle each halfway through, in a way that when they were stacked one above another, they form a single through going crack within two sheets. The crack transects entirely the width of the model (35mm). Two such cracks were made for each block. A thin saw (~1mm thickness) was used to cut the flat crack surface (Fig 6.1.a). I then filled the crack with commercially available epoxy with an intention to replicate the secondary filling materials, as found in geological cavities and fractures. An epoxy of extremely low yield strength, compared to that of PMMA, was chosen to reproduce the mechanical setting of a weak flaw in the host. These two sheets were then stacked one above another with a thin film of chloroform as adhesive. This combined stack of two sheets

containing the flaw, was then sandwiched between two intact layers of PMMA of the same dimension to complete the block. Chloroform was again used to adhere these two intact sheets. This whole stack was then kept under pressure, for about 12 hours, in a vice system overnight to ensure complete adhesion between the sheets and can now be used as a single homogenous block with two pre-defined cracks in the middle at desired angle, and also to ensure the complete hardening of the epoxy resin.

PMMA models were further subdivided into two subsets or types. In the first type of experiments, a considerable amount of gap was kept between the two flaws, to avoid any overlapped portion between the two flaws. Models with two predefined cracks of different lengths were studied in this type, 1cm and 1.5cm each respectively, for this study. This was done to investigate that whether multiple flaws occurring in the same pressure regime but at a distance from one another interacts with one another under compression or behaves individually, and if the difference in crack length makes any difference in the deformation pattern. Crack orientation angle α was kept at 60° with σ_1 and all the other parameters were kept constant.

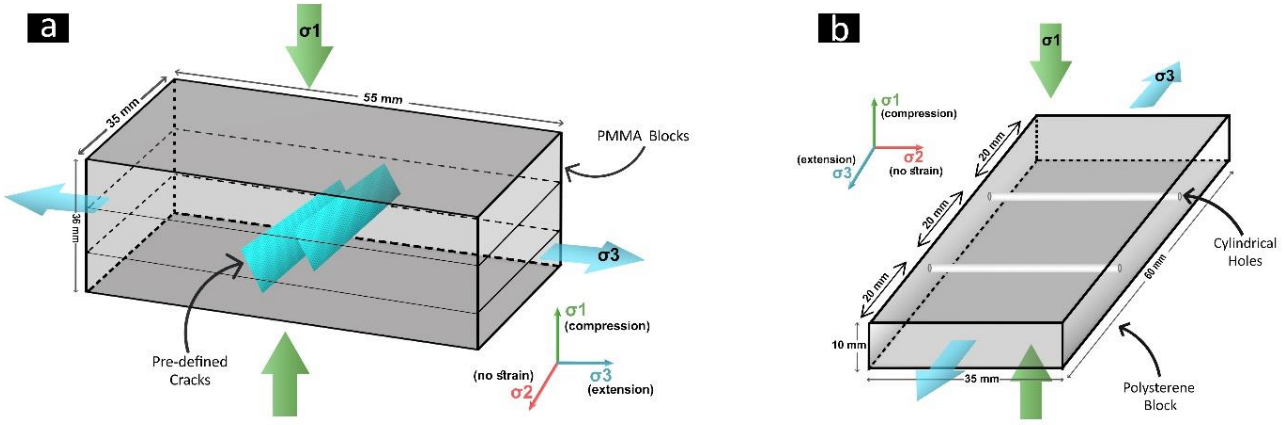

Figure 6.1. A perspective view of heterogeneous Polymer models. a) PMMA model, and b) PS model, containing two through-going planar cracks (for PMMA) and cylindrical weak flaws (for PS) with their axes perpendicular to the principal compression direction (σ_1-axis) and aligned along the direction of no strain (σ_2-axis). The blocks were allowed to extend in the horizontal direction (σ_3-axis) at right angle to the flaw axis

In the second type, the crack orientation angle α was varied between 30°, 45° and 60° with respect to σ_1 to investigate the effect of α under applied load in the deformation sequence. In this subtype, the flaws were kept close to one another to have a considerable amount of overlapping area (~50%) between them with respect to the σ_1. All the other parameters were kept constant.

6.3.2. Type 2 Model preparation

Compressional test experiments were conducted on fabricated polystyrene (PS) models (Fig 6.1.b) to study the mechanisms of shear band formation in laboratory conditions. I used commercial grade PS, which was selected after several trial experiments, ensuring that the material could produce sharp shear bands under our experimental conditions (room temperature and strain rates). Fig 3.7. shows its plastic creep behavior at slow ($2x10^{-5}$ sec^{-1}) and relatively fast strain rates ($3x10^{-5}$ sec^{-1}). The material yields at a stress of ~0.13 MPa at the low strain-rate, whereas at ~0.15MPa at the high strain-rate under the ambient temperature condition (27°C). PS samples containing circular mechanical flaws reduce their yield stresses to ~0.1MPa and ~0.12MPa at low and high strain rates, respectively (Fig 3.7.). We prepared the entire batch of PS models from the same PS sheet

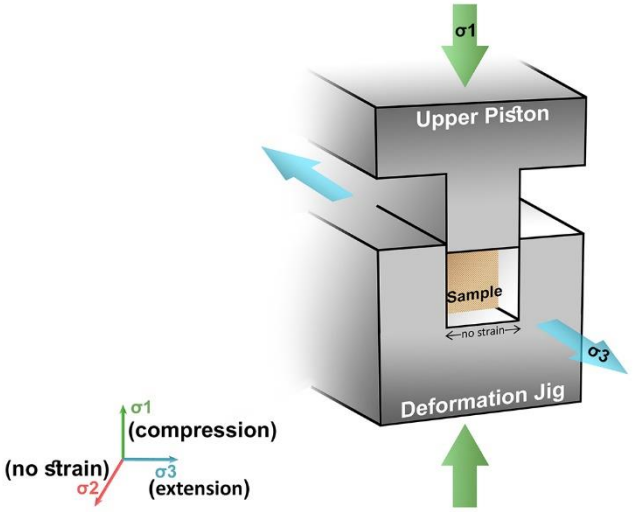

Figure 6.2. Schematic presentation of the deformation zig used for compression tests under plane strain condition. The orientations of the principal stress axes are shown in the corresponding panel

to avoid the possibility of any inherent variations in their rheological properties, e.g., yield strength, depending on the manufacturing history of the polymer. A 9 mm thick, rectangular (60 mm x 35 mm) block was cut out from a large PS sheet, and its vertical face was drilled to create a through-going cylindrical hole of ~1mm diameter, as illustrated in Fig. 6.1.b. Similar to the PMMA models, epoxy was used to fill up the holes to replicate the secondary filling materials. The models were left undisturbed overnight to allow the epoxy inside the hole to set in and form a mechanically weak solid region.

The crack/hole -normal vertical faces of the PMMA and PS model were polished by P80 grit sandpaper to minimize the contact friction between the model block and the metal jig (Fig 6.2.). The vertical model faces were gridded by passive 2 mm × 2 mm square grids to visualize the macro-scale heterogeneous strain fields around the hole in the deformed sample. Models were deformed under a hydraulically driven compression machine (Aimil Hydraulic Press, with 1200kN load frame), equipped to control the strain rate during an experimental run by a flow-controlled valve. A sample housing system (jig) was specially designed (Fig 6.2.) to run the deformation under a plane strain condition. The model was placed in the jig, keeping the flaw axis normal to the jig walls, and compressed with a vertical load (σ_1) under a biaxial stress condition, allowing the model to stretch perpendicular to the flaw axis (direction of no strain). To minimize the jig friction, we applied grease (viscosity 115 Pa s) at the model-jig wall interface prior to the beginning of model deformation. The experiments were run at ambient pressure and temperature (~27°C), keeping the σ_2 and σ_3 axes in horizontal directions, where σ_2 was oriented along the flaw axis direction (Fig 6.2.b). The vertical load (σ_1) was applied to the jig by moving the load frame in the upward direction against the stationary piston at the top, and continuously tracked by the 1200kN load cell attached at the top of the load frame. Under a given strain rate we ran a set of experiments

for varying finite strains (6%, 12% and 18%, for PS blocks) to study the progressive shear band structures with increasing deformation.

To study the role of pre-existing heterogeneity in shear band development, I first ran a set of reference experiments on homogeneous PS models (devoid of induced cylindrical flaw) and compared the results with those obtained from heterogeneous models. Both the homogeneous and the heterogeneous model experiments were conducted at low ($2x10^{-5}$ sec^{-1}) and high ($3x10^{-5}$ sec^{-1}) strain rates, with an aim to explore the possible effects of deformation rates on the mechanism of flaw-controlled shear band localization. The compression experiments occasionally produced tensile fractures in the models during the sample unloading, which was minimized by keeping the PS model inside the jig and allowing the hydraulic pressure to release at an extremely slow rate ($2x10^{-3}$ mm/sec).

6.4. Techniques for model observation

After the successful unloading process, the model was cleaned and its vertical faces parallel to the σ_1-σ_3 plane were photographed to record the deformation patterns in the model, revealed from the deformed grids. The laboratory study then took up post-processing of the deformed models for microscopic analyses, where each model was cut into thin slices (~0.5mm thick), perpendicular to the flaw axis, which was mounted on a glass slide. The thin section was observed under cross-polarized light to study the shear band patterns, characterized by their strong optical birefringence. Degree and areal extent of the birefringence can be used to visualize the degree and positions of strain localisation in the media, which can in turn be used to understand the behavior of shear band formation and deformation pattern of the models.

6.5. Experimental results

6.5.1. Type 1 (PMMA)

1st set: In the first set of experiments on PMMA models, the pair of induced cracks was oriented at an angle of 60° to the principal compression direction (σ_1). To study whether and how multiple

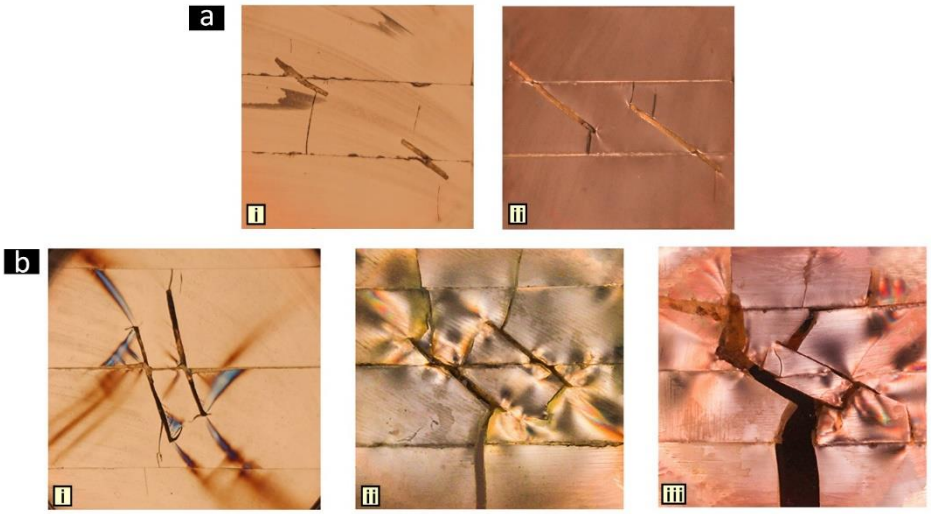

Figure 6.3. Deformation localisation pattern manifested by shear band growth and wing crack development in PMMA models. a) PMMA models without any areal overlap with crack length i) 1cm and ii) 1.5cm ; b) PMMA models with significant overlapped area with orientation α as i) 30° , ii) 45° and iii) 60°

inherent flaws, at a distance to each other, behave in a single deformational event, no common overlapped area was kept between them. The cracks were placed in the middle of the block. The model was free to extend in σ_3 direction. The models were deformed upto 20% finite strain.

Two subsets of experiments were done by keeping the predefined crack length at 1cm and 1.5cm. The gap between the cracks, and all the other parameters were kept constant for both the subsets. It was interesting to note that keeping a considerable amount of gap between the cracks, lead them to behave individually. They failed to interact with one another in a single event. As a

result, each crack produced its own deformational history. For both the subsets, brittle failure was found to be the permanent mode of deformation. Models carrying cracks of 1cm length produced only brittle failure, defined by the formation of wing cracks (Fig 6.3.a.i). The blocks did not show any signs of viscous strain localisation. In contrast, experiments done with crack length of 1.5cm produced small zones of strain localisation as seen from the birefringence around the crack tips (Fig 6.3.a.i). Though, in this subset also, the major mode of deformation was found to be of brittle wing cracks. However, in both of these models, there were no evidence of prominent interaction between the inherent cracks.

2nd set: In natural systems, incipient crack and fractures are the most abundant heterogeneities in rocks, and they generally occur in populations. Under a particular tectonic regime these highly fractured rocks behave in a different manner than the rocks without any flaw, or with flaws separated by a considerable distance. A second set of experiments was performed to understand the behavior of rocks containing closely spaced preexisting fractures. In this set of experiments PMMA blocks were induced with two cracks with significant amount of overlaps (~>50%) to account for their mutual interactions. Moreover, the orientation of the cracks with the principal stress direction (σ1) was also varied. Keeping the overlapped area similar, the angle for three models were kept 30°, 45° and 60°. Notable differences were seen in these models where the orientation angle played a major role in determining the mode of deformation localization (Fig 6.3.b).

As the crack orientation increased from 30° to 60°, the portion of ductile strain localisation decreased, giving way to prominent wing cracks. In 30° models, the main mode of shear

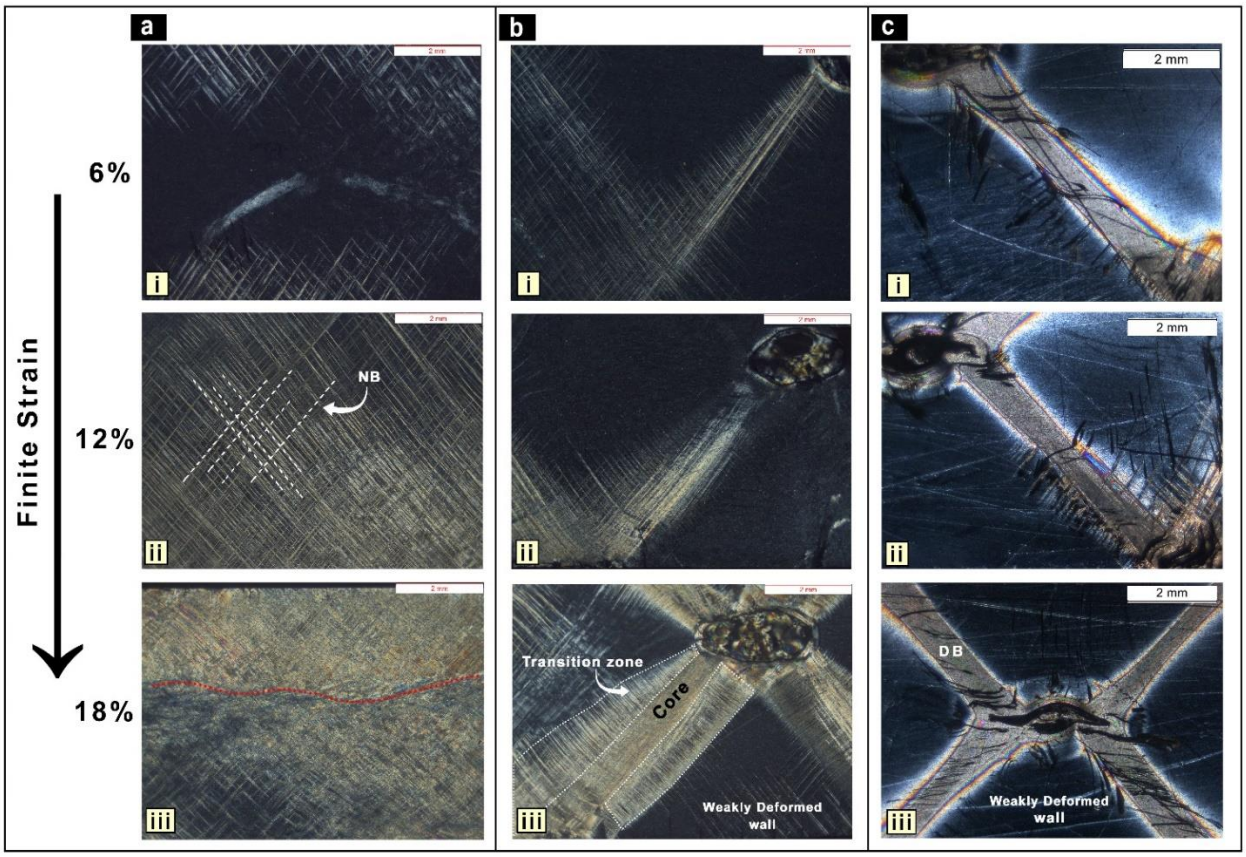

Figure 6.4. Shear band growth in PS model experiments with increasing finite strain. a) Uniform development of closely spaced, conjugate narrow bands (NBs) in homogenous PS models deformed at high strain rate ($\dot{\varepsilon} = 3 \times 10^{-5}\ sec^{-1}$). Note at higher finite strain, shear zone forms at a high angle to the compression direction, marked by dotted red line. b) Formation of wide composite bands (CBs) preferentially against the weak flaws in a heterogeneous PS model at a high strain rate. The composite structure consists of a core and a transition zone, dominated by band-parallel and orthogonal NBs. c) Formation of homogeneously sheared bands (HBs), bordered by narrow zones of gradational shear contacts with the weakly strained walls. The heterogeneous PS model was deformed at a low strain rate ($2 \times 10^{-5}\ sec^{-1}$). The photographs are obtained from thin sections of deformed PS blocks observed under cross polarized light.

localisation is by the formation of shear zones, dominantly around the crack tips. Very fine wing cracks were produced from opposite ends of each crack (Fig 6.3.b.i). These changes were particularly notice in notable the 60° model that deformed mainly by the formation of wider wing cracks, and much reduced ductile shear zones, as seen from reduced birefringence around crack

tips (Fig 6.3.b.iii). The model results indicate that increasing initial fracture angle results in transition in the model of deformation localization.

6.5.2. Type 2 (PS)

Homogenous models

Homogeneous PS models, deformed under high strain rates ($3x10^{-5}$ sec^{-1}), produced numerous closely spaced, narrow shear bands (NBs), distributed more or less uniformly in the entire model region. Each band characteristically had exceptionally long (*L*), narrow (*W*) geometry (*L/W* > 25), defined by sharp boundaries (Fig 6.4.a). They grew in length much faster than in width, as revealed from increasing L/W with model strain. The narrow bands form typically in conjugate sets (Fig 6.6.a-i), with their dihedral angles (Φ) varying with increasing finite strain (ε). For $\varepsilon \sim 6\%$, the modal Φ lies in the range 70°-75°, which increases to ~80°-85° for $\varepsilon \sim 12\%$, and to ~85°-88° at $\varepsilon = 18\%$ (Fig 6.6.b-i). Another interesting observation is that this type of bands multiplies in number to increase their P20 (Mauldon et al., 2001) estimated density (from $<4 \times 10^{-3}$ mm^{-2} at 6% to 18×10^{-3} mm^{-2} at 18%), with progressive compressional strains. To study such a spatio-temporal band evolution, we prepared band density maps from deformed models corresponding to $\varepsilon \sim 18\%$ (Fig. 6.6.c-i), and found the following features: 1) the bands do not cluster in specific zones; they are more or less homogeneously distributed; 2) progressively increasing new band formation facilitates the degree of homogeneity; and 3) at large finite strains it is hard to recognize individual bands as the band density is extremely high. For large $\varepsilon > 18\%$, the PS model produced a few isolated domains that accommodated plastic strains in the bulk model, forming shear zones at a high angle to the compression direction (Fig 6.4.a-iii).

An additional set of experiments was run to test the sensitivity of homogenous PS blocks to strain rate in forming shear band structures (Fig 6.5.). The experiments were run at a lower strain rate, 3 X 10^{-5} sec^{-1} to 2 X 10^{-5} sec^{-1}, as compared to those presented in the main text (Fig 6.4.a). This range of strain rates produced sharp and narrow bands that are finely spaced and uniformly distributed in the entire model. They typically formed in conjugate sets, symmetrically oriented with respect to the compression direction. The bands multiplied in number with increasing finite strain, as observed in similar experiments at relatively higher rates, and they had no tendency to widen, but grow in length. The PS produced distributed narrow bands in its

Figure 6.5. Uniform development of closely spaced, conjugate narrow bands (NBs) in homogenous PS models deformed at low strain rate ($\dot{\varepsilon} = 2 \text{ X } 10^{-5}\ sec^{-1}$). Note that strain rate doesn't have any effect on shear band formation in homogeneous model.

homogeneous state under the entire range of strain rate conditions used in the laboratory experiments. To conclude the experimental finding, uniformly thick bands of homogeneous shear (HBs) in low-strain rate experiments are hard to produce in homogeneous models without any pre-existing weak flaws in the model.

Heterogenous Models

Heterogeneous model experiments produced band structures markedly different from those formed

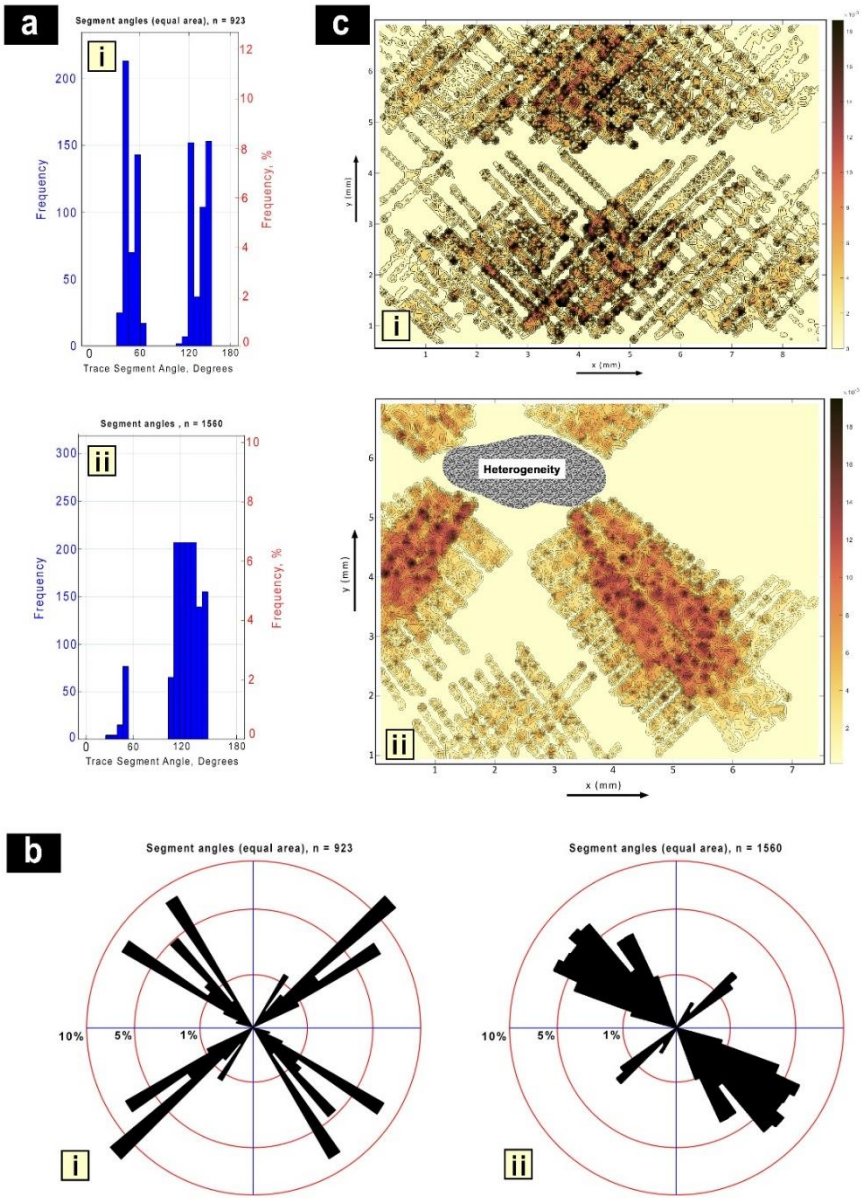

Figure 6.6. a) Band density mapping (Estimated Density (P20), mm^{-2}), b) histogram and c) rose diagrams of band orientations for i) homogenous PS models and ii) PS models containing cylindrical weak flaws. Note that the band density plots show a clear transition of distributed NBs in homogenous model to localized CBs in a PS model with weak flaws, where the band core regions have the highest band concentrations.

in homogeneous models, irrespective of the strain rate ($\dot{\varepsilon}$) and the amount of finite strain (ε).

However, $\dot{\varepsilon}$ critically controlled the mode of shear localization in the neighborhood of mechanical flaws, which is discussed later. Compression under high strain-rates ($\dot{\varepsilon}$ = 3 x 10^{-5} sec^{-1}) developed plastic strains in the form of wide shear bands that localized preferentially at the extensional faces of the pre-existing heterogeneity. These plastic zones contained numerous narrow shear bands (NBs) in conjugate sets (Fig 6.6.a-ii) with Φ = ~ 98° (Fig 6.6.b-ii), forming a composite shear band (CB) structure (Fig 6.4.b). In a CB one set of NBs formed nearly parallel or at low angles (~ 10° - 15°) to the overall CB trend, whereas the other at high angles (~ 85° - 95°), almost orthogonally oriented to the CB. Interestingly, the two sets had competing growth in the CB evolution; the low-angle set increased its band density by multiplying the number of NBs and at the same time grew in length to form a well-defined core zone, which was practically devoid of high-angle shear bands. Such a differential NB growth gave rise to a characteristic two-layer composite structure of CBs: a core zone of low-angle bands, flanked by zones of high angle bands (called transition zone in the foregoing description). The transition zones represent an intermediate region between the strongly sheared core and the strain-free walls (revealed from weak or no optical birefringence and sharp termination of across-band NBs). Both the core and the transition zones increase their NB densities and formed a well-developed composite structure of CB at large ε (= 18%). A CB eventually shows a complete segregation of the two band populations in the core and the transition zones, which can be seen in the band density map (Fig 6.6.c-ii). CBs had a lateral growth of their core zone at the cost of the transition zones, but they hardly change their overall band thickness. Consequently, the composite CB structure consistently increased the core/transition zone thickness ratio (T_r) with increasing ε, for example, T_r = 0.887 and 1.914 at ε = 6% and 18%, respectively.

To describe the overall band structure of a heterogeneous PS model under high strain rates ($\dot{\varepsilon}$ = 3 x 10^{-5} sec^{-1}), each circular heterogeneity localizes a conjugate pair of CBs, symmetrically

oriented at an angle of ~35° to the compression direction. Their core zones do not exactly follow the CB trend, but consistently form an oblique relation at an angle of ~10° to 15° (Fig. 6.4.b-iii). They have dihedral angles (~75°), significantly lower than that of the corresponding CBs (~93°). As the loading progresses, the circular flaw is deformed into an oval shape and the CBs increase their dihedral angles by ~6°- 8°. The degree of shear partitioning between the core and transition zones of a CB, calculated from the across-band NB deflections, suggests contrasting shear localisation in the two domains of the CB. For a given model compression, e.g., ε = 6%, the estimated shear in the core is ~0.72, which becomes extremely low (~0.11) in the transition zone. However, the transition zones progressively increase their shear at a large finite deformation (ε = 18%), e.g. their estimated shear is ~0.31 when the finite shear at the core is ~1.2.

Under a low compression rate (2 x 10^{-5} sec^{-1}) the same heterogeneous PS model produced a symmetrical pair of nearly tabular conjugate bands, radiating from the heterogeneity at an angle of ~40° to the compression direction (Fig 6.4.c). In contrast to CBs, they are completely devoid of NBs, and develop distributed plastic strains, giving rise to the characteristics of homogeneous shear bands (HB). Secondly, the dihedral angle of HBs (Φ = ~80°) is lower than those of CBs. They have a narrow transition zone (T_r = ~0.3mm), revealed from the birefringence bands, on either side of the homogeneous core. The birefringence variations across the band length suggest a diffused boundary of the transition zone with the unstrained walls (Fig 6.4.c-iii). Models at increasing ε from 6% to 18% show little modifications in the HBs, implying that they grow in thickness with increasing ε. Similarly, their transition zones remain unchanged, allowing the core zone to entirely accommodate the plastic strain in the model.

In summary, the PS model experiments yield three distinct types of shear band structures: narrow bands (NBs), wide composite bands (CBs) and wide homogeneous bands (HBs) (Fig 4).

NBs are defined by their extremely long, narrow band geometry ($L/W > 25$) with sharp boundaries (Fig 6.7.a). They occur as densely penetrative band structures in a homogeneous medium. The

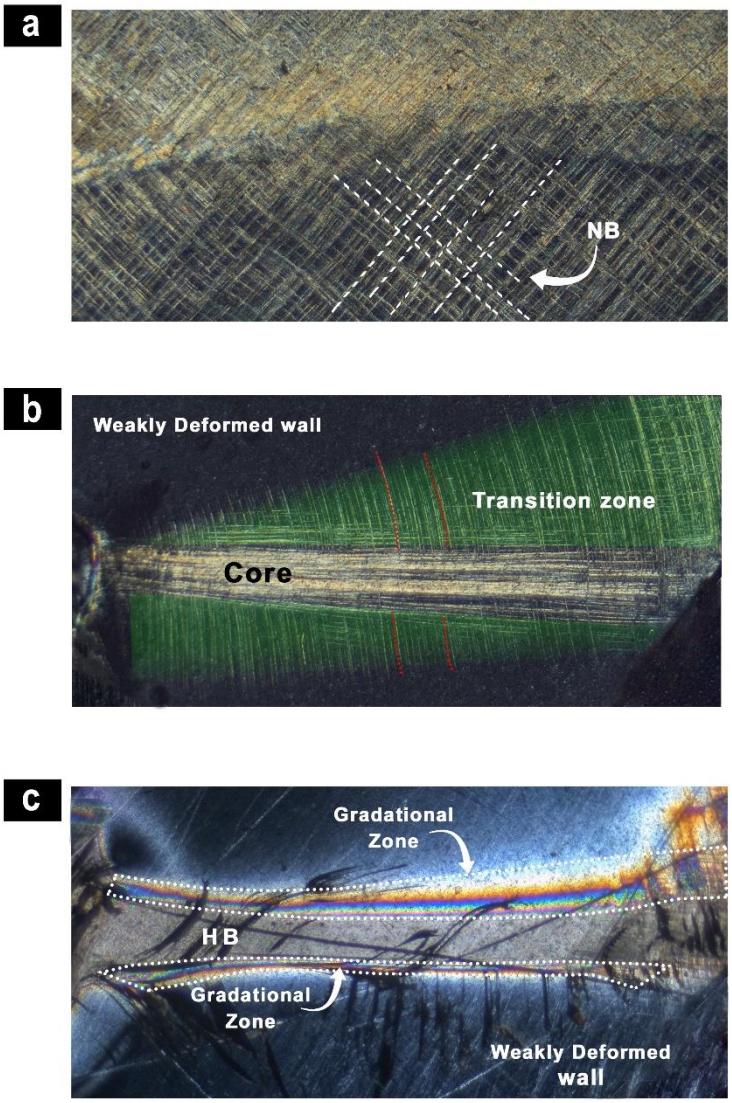

Figure 6.7. Structural characteristics of the three types of shear bands in PS models (thin sections under cross polars). a) Uniformly distributed NBs in homogeneous PS deformed at high $\dot{\epsilon}$ (3 x 10^{-5} sec^{-1}). Note that the bands define conjugate orientations (white dotted lines) with dihedral angle (Φ) of ~85°-88° b) Composite band (CB) in a PS block containing weak flaws deformed at high $\dot{\epsilon}$ (3 x 10^{-5} sec^{-1}). The CB structure is composed of a core zone (cluster of finely spaced parallel narrow bands), bounded by transition zone (marked by green color), containing a dominant set of orthogonal NBs. The red lines show the accommodated viscous drag in the transition zone. The core zone generally forms at a low angle (~ 10°-15°) to the overall CB trend. c) Homogeneous shear band (HB) in a PS block with weak flaws deformed at low $\dot{\epsilon}$ (2 x 10^{-5} sec^{-1}) Note that the band shows a wide core zone of homogeneous internal shear strain, and a narrow zone of gradational shear, as revealed from optical birefringence.

presence of a mechanical heterogeneity results in a transition of the shear localization mechanism to form either CBs or HBs, depending on the bulk strain rates ($\dot{\varepsilon}$). A CB consists of two orthogonal sets of NBs, forming a composite structure: core (cluster of densely packed, sub-parallel NBs that accommodates maximum plastic strain) and transition zones (set of closely spaced orthogonal NBs showing shear drags) (Fig 6.7.b). HBs are always produced relatively at lower strain rate, and they are characterized by a thick band of homogenous shear localization, bounded by narrow zones showing gradational shear boundary with the walls (Fig 6.7.c).

6.6. Field Study

6.6.1. Approach

To further understand and cross examine the effects of heterogeneity on the deformation behavior of rocks, as seen in PS model experiments, I conducted extensive field work in shear zones. Both the laboratory experiments and FE model simulations (Chapter 7) suggest that pre-existing mechanical flaws are necessary agents to form isolated shear band/zones, as commonly encountered in most of the geological terrains. A flaw-free, homogeneous rock at the yield stress would produce numerous, spatially distributed narrow shear bands (cf. NBs observed in homogeneous PS experiments), but not isolated wide shear zones in host rocks. However, it is difficult to recognize the nucleation of a shear zone in relation to pre-existing flaws in the field because the length scale of shear zones eventually far exceeds the flaw dimension, leaving the flaws geometrically almost unrecognizable objects, as seen in the numerical simulations. But, some of their characteristic features can reflect their flaw-controlled origin. The thesis discusses

here outcrop scale shear zones from the Chotonagpur Granite Gneissic Complex (CGGC) in the light of our heterogeneous model experiments.

A few centimetres to tens of metres long ductile shear zones in the Chotonagpur Granite Gneissic Complex (CGGC) were studied, focusing upon regions north of the South Purulia Shear Zone (SPSZ). The shear zones are associated with alkali granite, brecciated quartzite, apatite-magnetite bearing chert, U-Th mineral-bearing pegmatite and mafic-ultramafic rocks (Mandal &

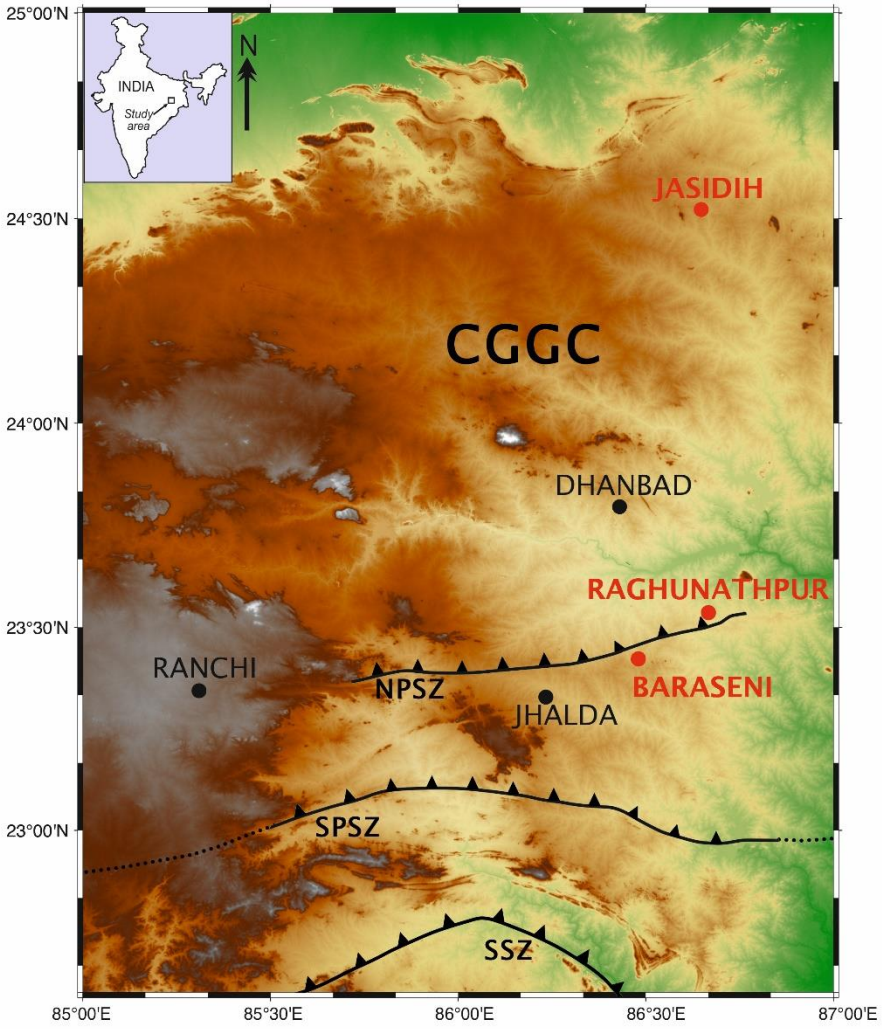

Figure 6.8. A simplified geological map of the East Indian Precambrian craton, showing the locations of the Singhbhum Shear Zone (SSZ), the South Purulia Shear Zone (SPSZ), the North Purulia Shear Zone (NPSZ) and the Chotanagpur Granite Gniess Complex (CGGC). Field areas are marked by red dots in the map.

Ray, 2009). The host rock types include banded, porphyritic and augen granite gneisses, garnet-bearing quartzo-feldspathic gneisses, khondalite, amphibolites and mafic granulites, which generally contain penetrative tectonic foliations of single or multiple generations. The host foliations act as markers, showing sharp deflections across shear bands that allow us to identify the mode of shear localization. In places we could recognize mechanical heterogeneities as nucleating agents of shear zones. For example, high-temperature metamorphic rocks in the Jasidih area show band localization in the vicinity of quartzo-feldspathic aggregates, which possibly represent melt lenses (weak zones) produced by partial melting during the granulite facies metamorphism. This kind of field examples support our experimental interpretation that mechanically weak heterogeneities can be a crucial factor for the formation of isolated shear zones in continua.

Three prominent locations were chosen: 1) Bero Hillocks (23°32'09.5" N, 86°40'01.3" E) near Raghunathpur town, 2) Purulia-Asansol Road transect near Baraseni (23°25'20.9"N 86°28'48.8"E), and 3) Jasidih (24° 31′ 19.2″ N, 86° 38′ 51.72″ E) (Fig 6.8.). Location 1 is predominantly composed of biotitic granite gneiss, which shows excellent shear band structures with thick strongly shear core, sometimes flanked by excellent drag zones on both sides, while some shows relatively weakly deformed matrix. Lithologically, Location 2 is a fine-grained granulite-facies rock, primarily composed of alkali-feldspar, with minor amounts of quartz, mica, garnet and tourmaline. Classically this rock type is also termed as Leptynite and they often show a planar gneissic structure. Location 2 exhibits extensive micro shear band structures with a cross cutting relationship throughout the exposure (Fig 6.9.a). Location 3 is situated near the Jasidih area, which lies in the northernmost part of CGGC. Lithologically, this area is predominantly of migmatitic felsic orthogneiss origin, with random enclaves of meta -sedimentary and meta-mafic

rocks. Excellent shear bands were found to localize in the vicinity of elliptical to semi-elliptical heterogenous clasts (Fig 6.9.b), that can be well correlated with the present heterogenous models (Fig 6.4.b).

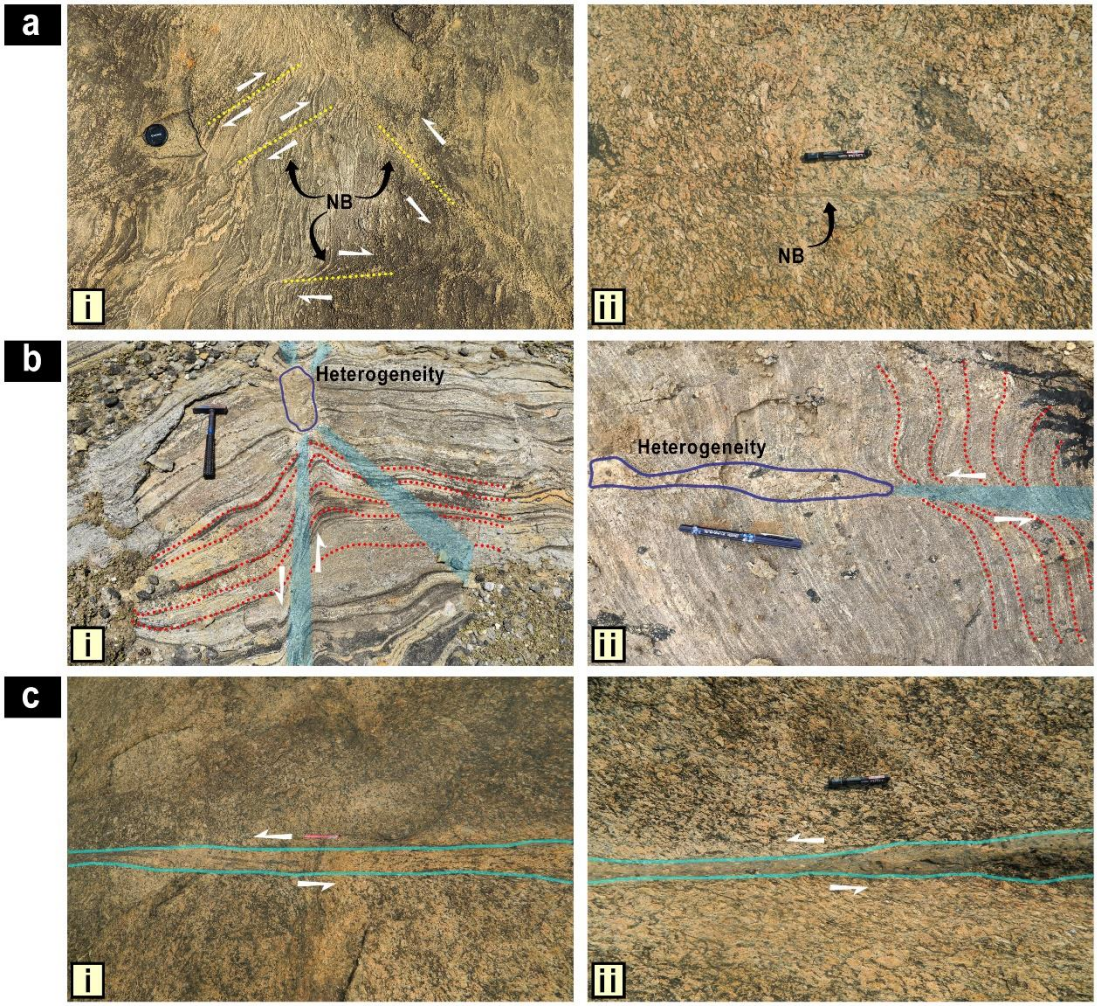

Figure 6.9. Field photographs of outcrop-scale shear zones in the Chotonagpur Granite Gneissic Complex (CGGC), Eastern India showing a) Narrow shear Bands (NBs), b) Composite shear Bands (CBs) and c) Homogenous shear Bands (HBs). a-i) Multiple narrow shear zones of conjugate orientations (NBs) distributed in a single ~ 100 m x 50 m outcrop of homogeneous quartzo-feldspathic rocks. a-ii) A single NB (3mm thickness) in an outcrop of banded gneiss. b-i) Heterogeneity (quartzo-feldspathic aggregates) controlled localization of composite shear bands in conjugate sets, radiating from the heterogeneity. Each band shows a core of strongly sheared rocks, flanked by foliation drag zones. b-ii) A single CB formed along an inherent heterogeneity with prominent drag zone and strongly sheared core. c-i) and ii) Shear zones containing a wide band of homogeneous shear strain (core), bordered by narrow zones of relatively weak shear, grading into unsheared wall rocks.

6.6.2. Field Observations and their synthesis

Three distinct types of shear zones were recognized based on their internal shear structures and the nature of contact with the relatively less deformed host rock: Type I – isolated, narrow shear zones with maximum shear focused in the central zone, forming sharp boundaries with the unsheared walls (Fig 6.9.a), Type II – broad shear zones, consisting of a sheared core, defined by a cluster of narrow shear bands, where the entire composite structure is bounded by a drag zone on its either side (Fig 6.9.b), and Type III - thick homogeneous shear zones with a narrow diffused zone, forming a gradational boundary with the unsheared host (Fig 6.9.c). As these contrasting types occur in the same rocks, the lithology does not seem to be a prime factor in controlling the varying modes of band formation in our study area. Type I shear structures, observed in an outcrop of garnet-bearing quartzo-feldspathic gneissic rocks (location 2) near Purulia town, characteristically show intense shear localization ($\varepsilon > 12$) in narrow (thickness: ~2mm - ~5cm), linear zones, with their strike length on a few centimeters (Fig 6.9a). High-resolution structural mapping {scale 1:100} (Fig 6.10.a-i) reveals that they are spatially distributed over the entire outcrop, and their statistical orientations define a conjugate set (Fig 6.10.a-ii) with a dihedral angle of ~70°-75° (Fig 6.10.a-iii). In overall, this type of shear zones resembles narrow shear bands (NBs) produced in homogeneous PS models (Fig 6.4.a) and numerical simulations that typically show an abrupt transition of shear strain across them (Fig 6.10.b-i), without showing any significant drag zone. In many places of our study area, such as Raghunathpur - Bero Hills (Location 1) and Jasidih (Location 3) we observed Type II shear zones in granite gneissic hosts. This type of shear zone structures often localizes against quartzo-feldshapthic lenses in conjugate sets (Fig 6.9.b), as in the heterogeneous PS model experiments under high compression rates (Fig. 6.4b). The bands contain

a strongly sheared core (~20 – 50 cm), flanked by wide transition zones (~5-10 cm to ~1-2 m) that

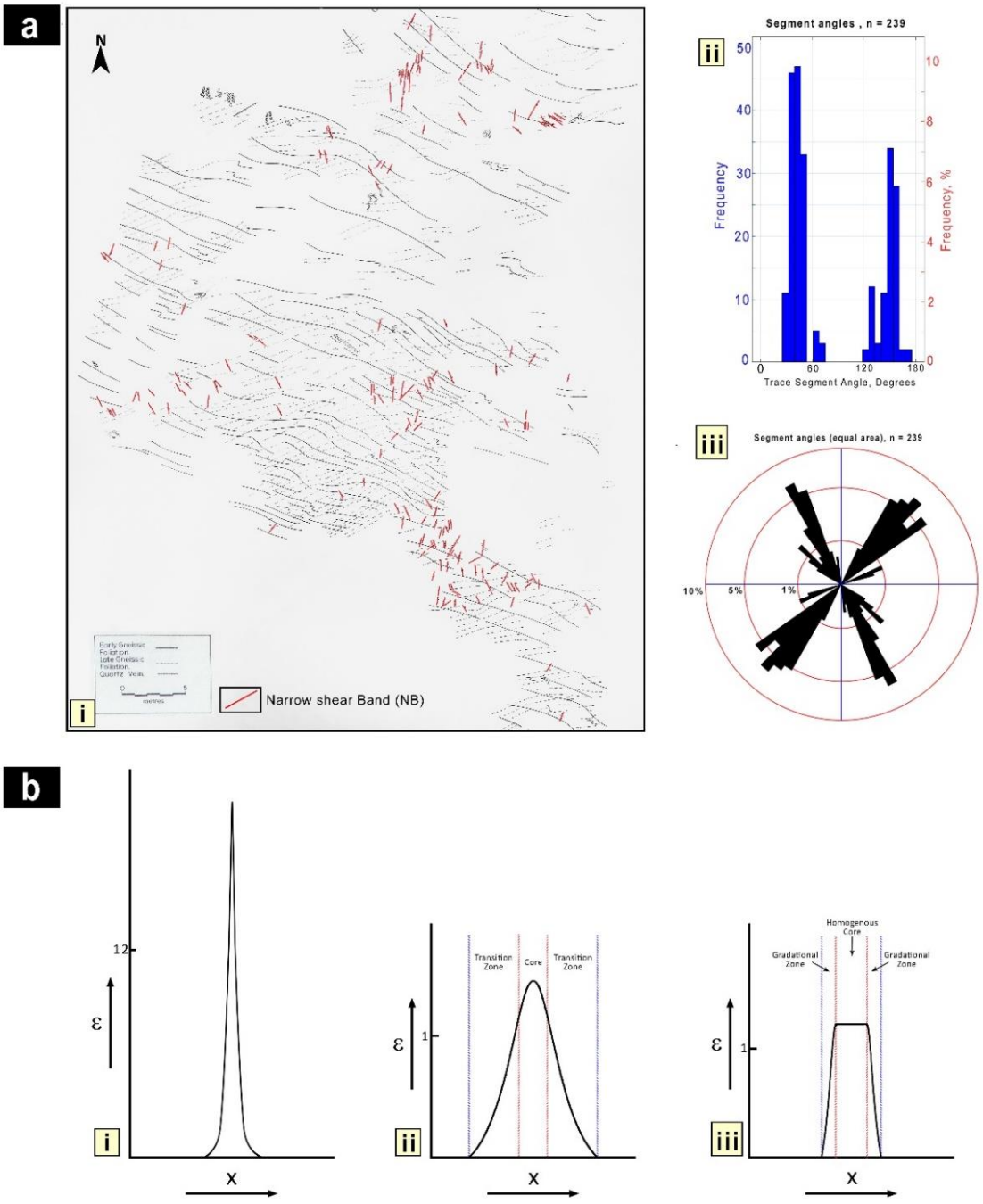

Figure 6.10.. a-i) High-resolution structural map (1:100) of a homogeneous quartzo-feldspathic outcrop showing spatially distributed numerous NBs (marked by red color) in conjugate sets. a ii) Corresponding histogram and (a-iii) rose diagram of the shear band orientations shown in the map. b) Construction of across-band strain profiles based on field measurements: i) Type I, ii) Type II and iii) Type III shear zones.

gradually reduce shear strain from the core to unsheared walls. Although the shear zones are devoid of orthogonal NBs on macro-scales, they form typically a core - drag zone complex structure, which is comparable to CBs produced in the heterogeneous PS models at high shear rates (Fig 6.4.b). Type III shear zones contain a thick, homogeneously sheared core (~15-20cm), bordered by a narrow zone of gradational shear on either side of the core (Fig 6.9.c). They look like flaw-controlled HBs in PS experiments under relatively slow rates. Both Type II and III shear zones had long strike lengths, ranging from a fraction to tens of meters, irrespective of their core thickness.

Strain profiles were obtained by calculating the finite strain (ε) across various types of shear zones. Type I shear zones containing narrow shear bands observed in an area near Purulia town, showed a characteristic curve with a high peak showing large ε values implying intense shear localisation across the narrow shear bands (Fig 6.10.b-i). Type II shear zones showed gradational shear strain variation from weakly deformed wall to highly sheared core forming a typical bell-shaped curve (Fig 6.10.b-ii). On the contrary, Type III shear zones are characterized by a plateau like strain profile with very narrow gradational zone (Fig 6.10.b-iii). This characteristic shape results due to formation of a very narrow drag zone on both sides of the homogenous core zone.

Chapter 7

Numerical modelling of flaw-controlled deformation localization

7.1 Theoretical consideration

In this thesis 2D finite element (FE) models were developed to reproduce the mechanisms of shear band localization as a function of mechanical heterogeneities on the natural scale, with an aim to show the validity of laboratory experimental results (described in Chapter 6) for geological

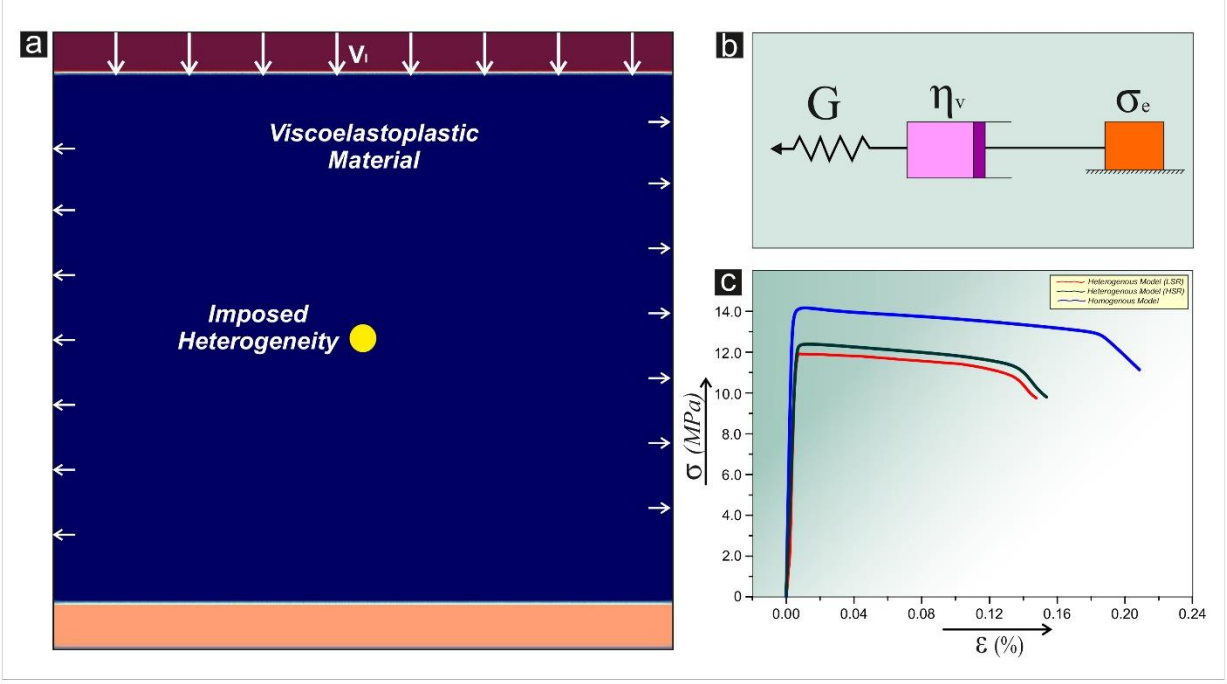

Figure 7.1. a) Initial finite element (FE) model setup used for numerical experiments. The circle (yellow) at the center represents a weak flow in the FE model domain. Arrows indicate the kinematic boundary conditions imposed at the model boundaries. b) 1D rheological representation of the FE modelling. This decomposition can be interpreted as Maxwell visco-elasto-plastic rheology, where plastic, viscous and elastic components are connected in series. σe, ηv, and G: plastic yield stress, material viscosity and shear modulus of the material, respectively. c) Stress versus strain relations obtained from progressive deformations of visco-elasto-plastic numerical models. Note that the model with an initial weak flaw yields at a lower stress than a homogenous model (free from any initial flaw).

strain rates. The FE modelling uses the open-source, particle-in-cell, finite element code Underworld2 (http://www.underworldcode.org/) that solves the incompressible Stokes equations for visco-plastic materials in combination with the energy conservation equation (Mansour et al.,

Parameters	***Symbol***	***Natural Values***	***Numerical Input Values***
Model length	L	60 km	6
Model width	W	40 km	4
Model reference strain rate	$\dot{\gamma}_o$	$1.00e^{-15}$	1
Model reference density	ρ	2700 kg m^{-3}	1
Model reference viscosity	η_0	$1e^{20}$ Pas	1
Initial Cohesion	C_i	20 Mpa	0.08
Cohesion after Softening	C_s	5 Mpa	0.02
Angle of friction	ϕ	25° - 30°	25° - 30°
Maximum Yield stress	σ_{max}	1000 Mpa	3.7
Minimum Yield stress	σ_{min}	10 Mpa	0.04
Elastic shear module	G	5×10^9 Pa	18.5

Table 7.1. Parameters used for Numerical Simulation and their values

2020; Moresi et al., 2007). A rectangular, visco-elasto-plastic domain was chosen in a Cartesian space subjected to pure shear deformation (Fig 7.1.a), as in the laboratory setting.

I used a 1D rheological model, consisting of an elastic (spring), a plastic (frictional block) and a viscous (dashpot) element in series (Fig 7.1.b), and chose the Drucker-Prager yield criterion for plastic strain localization in the FE model at the given yield stress. The model domain is discretized into quadrilateral meshes, comprising 564 x 328 elements. Mesh refinement tests were

performed to find the level of mesh resolution required to attain a steady model output. The simulation results hardly changed with further mesh refinement. Table 7.1 shows the various mechanical parameters used for numerical simulations.

The plastic yielding condition was defined by the first I_1 and second I_2 invariants of stress tensor (σ_{ij}) in the model. Their expressions follow:

$$I_1 = \sigma_{jj}; \quad (7.1)$$

$$I_2 = \frac{\sigma_{ii}\sigma_{jj} - \sigma_{ij}\sigma_{ij}}{2} \quad (7.2)$$

Decomposing σ_{ij} into the isotropic ($\sigma^o{}_{ij}$) and the deviatoric stress ($\sigma^s{}_{ij}$) tensors, we get

$$\sigma^o{}_{ij} = \frac{1}{3}\sigma_{kk}\delta_{ij} \text{ and } \sigma^s{}_{ij} = \sigma_{ij} - \sigma^o{}_{ij} \quad (7.3)$$

where δ_{ij} is Kronecker delta. From Eq. (2) and (3), the second stress invariant, I_2 is expressed as

$$I_2 = 3\sigma^o{}_{jj}{}^2 - \frac{1}{2}\sigma_{ij}\sigma_{ij} \quad (7.4)$$

Considering incompressible rheology, the total strain-rate tensor is a sum of elastic ($\dot{\varepsilon}^e_{ij}$), plastic ($\dot{\varepsilon}^p_{ij}$) and viscous ($\dot{\varepsilon}^v_{ij}$) strain-rates:

$$\dot{\varepsilon}_{ij} = \dot{\varepsilon}^v_{ij} + \dot{\varepsilon}^p_{ij} + \dot{\varepsilon}^e_{ij}, \quad (7.5)$$

where $\dot{\varepsilon}^v_{ij} = \frac{1}{2}\frac{\sigma^s{}_{ij}}{\eta_v}$,

$$\dot{\varepsilon}^p_{ij} = \begin{cases} 0, & I_2 < \sigma_{yield} \\ \chi\left(\frac{1}{2}\frac{\sigma^s{}_{ij}}{I_2}\right), & I_2 \geq \sigma_{yield} \end{cases},$$

$$\dot{\varepsilon}^e_{ij} = \frac{1}{2G}\frac{D\sigma^s{}_{ij}}{Dt}$$

σ_{yield} denotes the yield strength of the material, *G* is the Elastic shear module, η_v is the bulk viscosity of the material, and χ is a plastic multiplier, satisfying the yield condition, $I_2 = \sigma_{yield}$.

If we had considered only viscous and elastic component of a material, then the deformation rate is the sum of both the parts, which means:

$$\frac{\sigma^s ij^{\Delta}}{2G} + \frac{\sigma^s ij}{2\eta} = \hat{\Sigma}_v + \hat{\Sigma}_e = \Sigma \qquad (7.6)$$

and,

$$\sigma^s ij^{\Delta} = \dot{\sigma}^s_{ij} + \sigma^s_{ij} M - M\sigma^s_{ij} \qquad (7.7),$$

where, Σ is the matrix of material properties, $\hat{\Sigma}$ is the deviatoric part of Σ, $\sigma^s ij^{\Delta}$ is the Jaumann corotational stress rate, η is the shear viscosity and *M* is the material spin tensor, where $M_{ij} = \frac{1}{2}\left(\frac{\partial V_i}{\partial x_j} - \frac{\partial V_j}{\partial x_i}\right)$

Now to determining the value of effective viscosity η_{eff}, the plastic part is to be incorporated. From equation (7.5) and (7.6), we get,

$$\frac{\sigma^s ij^{\Delta}}{2G} + \frac{\sigma^s ij}{2\eta} + \chi\frac{\sigma^s ij}{2|I_2|} = \hat{\Sigma}_v + \hat{\Sigma}_e + \hat{\Sigma}_p = \hat{\Sigma} \qquad (7.8)$$

The constitutive law for the plastic flow introduces a non-linearity, and needs iterations to get to the equilibrium state. From equation (7.8), the Jaumann stress rate is expressed in the first order difference form:

$$\sigma^s ij^{t+\Delta t^e}\left[\frac{1}{2G\Delta t^e} + \frac{1}{2\eta} + \frac{\chi}{2|I_2|}\right] = \hat{\Sigma}^{t+\Delta t^e} + \frac{1}{2G\Delta t^e}\sigma^s ij^t + \frac{1}{2G}(M^t\sigma^s ij^t - \sigma^s ij^t M^t) \qquad (7.9)$$

At yield, $|\sigma^s ij| = \sigma^s ij_{yield}$, to get the form :

$$\sigma^s ij^{t+\Delta t^e} = \eta_{eff}\left[2\Sigma\hat{}^{t+\Delta t^e} + \frac{1}{G\Delta t^e}\sigma^s ij^t + \frac{1}{G}(M^t\sigma^s ij^t - \sigma^s ij^t M^t)\right] \quad (7.10)$$

using η_{eff} (effective viscosity), given by

$$\eta_{eff} = \frac{\eta\sigma^s ij_{yield} G\Delta t^e}{\eta\sigma^s ij_{yield} + \sigma^s ij_{yield} G\Delta t^e + \chi\eta G\Delta t^e} \quad (7.11)$$

χ is determined by equating the value of $\left|\sigma^s ij^{t+\Delta t^e}\right|$ with the yield stress in equation (7.10). In this case, the η_{eff} is obtained directly as:

$$\eta_{eff} = \frac{\sigma^s ij_{yield}}{\left|\Sigma\hat{}_{eff}\right|} \quad (7.12)$$

where,

$$\Sigma\hat{}_{eff} = 2\Sigma\hat{}^{t+\Delta t^e} + \frac{1}{G\Delta t^e}\sigma^s ij^t + \frac{1}{G}(M^t\sigma^s ij^t - \sigma^s ij^t M^t) \quad (7.13)$$

and $|\Sigma| = \left(2\Sigma_{ij}\Sigma_{ij}\right)^{1/2}$.

The χ and η_{eff} values are iterated for redistribution of stress from points which becomes unloaded.

As the model domain is chosen to replicate a portion of the crust, we consider a linear dependence of the yield limit (σ_{yield}) on lithostatic pressure (p), similar to the Drucker-Prager plasticity criterion. This is comparable to the Mohr-Coulomb plasticity in 2-D for incompressible plane strain deformation (Roy et al., 2021; Snell et al., 2020), written as

$$\sigma_{yield} = C(\gamma_{pl}) + tan\emptyset p\,, \quad (7.15)$$

where $p = -\frac{1}{3}I_1$, and $C(\gamma_{pl})$ is the material cohesion, expressed as a function of plastic strain γ_{pl} , and $\emptyset$ is the angle of internal friction. The cohesion is assumed to weaken with increasing accumulated plastic strain:

$$C = C_i + (C_f - C_i)\min(1, \frac{\gamma_{pl}}{\gamma_o}), \qquad (7.16)$$

where C_i is the initial cohesion and C_f is the final cohesion of the shear zone material. Also, $\gamma_{pl} = \int_0^t \dot{\varepsilon}_p \, dt$, indicates accumulated plastic strain in regions where the yield limit is reached and $\gamma_o = 0.1$ is taken as the reference strain. No syn-deformational healing of the cohesion is implemented in this model.

7.2 Model Setup

Three different sets of numerical simulations were performed: 1) Model Simulations (MS1) to reproduce the reference laboratory experiments with homogeneous PS models; 2) Model Simulation (MS2) to replicate heterogeneous laboratory model containing a circular cylindrical flaw at high strain rates ($\dot{\varepsilon}$ = 2 x 10^{-12} sec^{-1}), and 3) Model Simulation (MS3) similar to MS2, but run at a significantly low strain rates ($\dot{\varepsilon}$ = 5 x 10^{-14} sec^{-1}). Figure 5c presents the typical stress-strain curves obtained from these three kinds of model simulations run at room temperature, where all of them show the stress to rise with increasing finite strain and reach the maximum yield stress, followed by a drop to the lower yield stress. This stress variation broadly agrees with the laboratory findings. The simulated models start to produce narrow shear bands (NBs) at finite strains of about 3% - 4%, which commences prior to a proportionality limit of the stress-strain curve. However,

NBs appear in large density only when the upper yield stress is attained at about 6% -7% strain. Sporadic NBs that initiated at a pre-upper yield stress might have resulted from local stress concentrations due to some mesh configurations.

7.3 Simulation Results

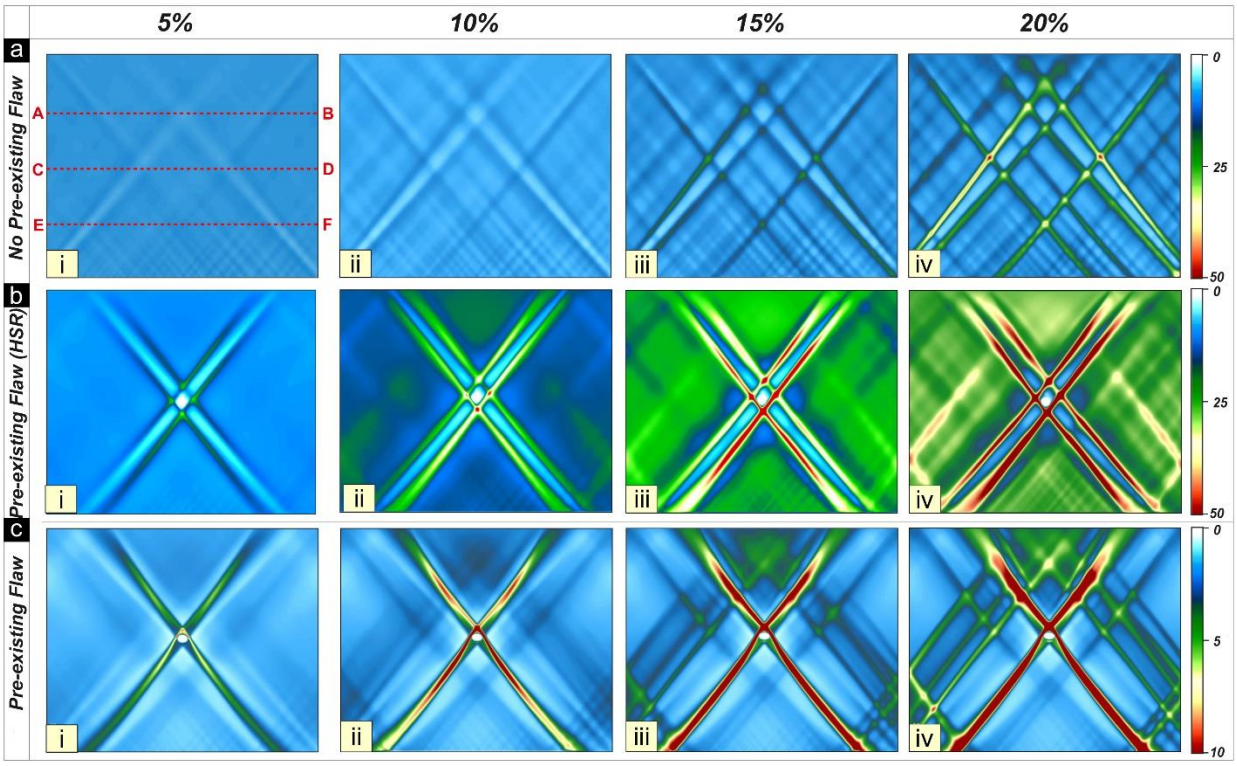

Figure 7.2. Progressive development of shear bands in a) a homogeneous model and b) a heterogeneous model with an initial weak flaw, deformed at high strain rates (3 x 10-5 sec-1), and c) a similar heterogeneous model, but deformed under a relatively low strain rate (2 x 10-5 sec-1). The color bar represents the magnitude of strain rate 2nd invariant. The finite model shortening is indicated at the top of each panel. Note that the core zones (red regions) in bands produced in the heterogeneous model under high strain rates (b) form at an angle (~7°-10°) to the overall band trend, as in the laboratory models (Fig 2b-iii)

MS 1: The homogeneous model initially (ε = ~4%) produced two sets of narrow shear bands (NBs), symmetrically oriented to the compression direction with a dihedral angle (Φ) of ~70°. They do not cluster in specific locations, but show a uniform spatial distribution in the model domain. They grow in length and at the same time, multiply in number to increase their spatial density with increasing ε (Fig 7.2.a). A set of strain profiles were constructed along a number of transects in the simulated band structures to find the spatial patterns of band distributions (Fig 7.2.a-i). A profile for ε = 5% does not show any peaks (Fig 7.4.a-i), i.e., strain perturbations by shear band formation. In an advanced stage (ε > 10%) the simulation produces numerous peaks that amplify with increasing ε, but remain in low amplitudes (Fig 7.4.a). Their spatial patterns suggest a distributed development of band structures in the model simulations at ε = 15 – 20% (Fig. 7.4.a-iv). However, a few bands selectively localise larger plastic strains, and gain prominence in the

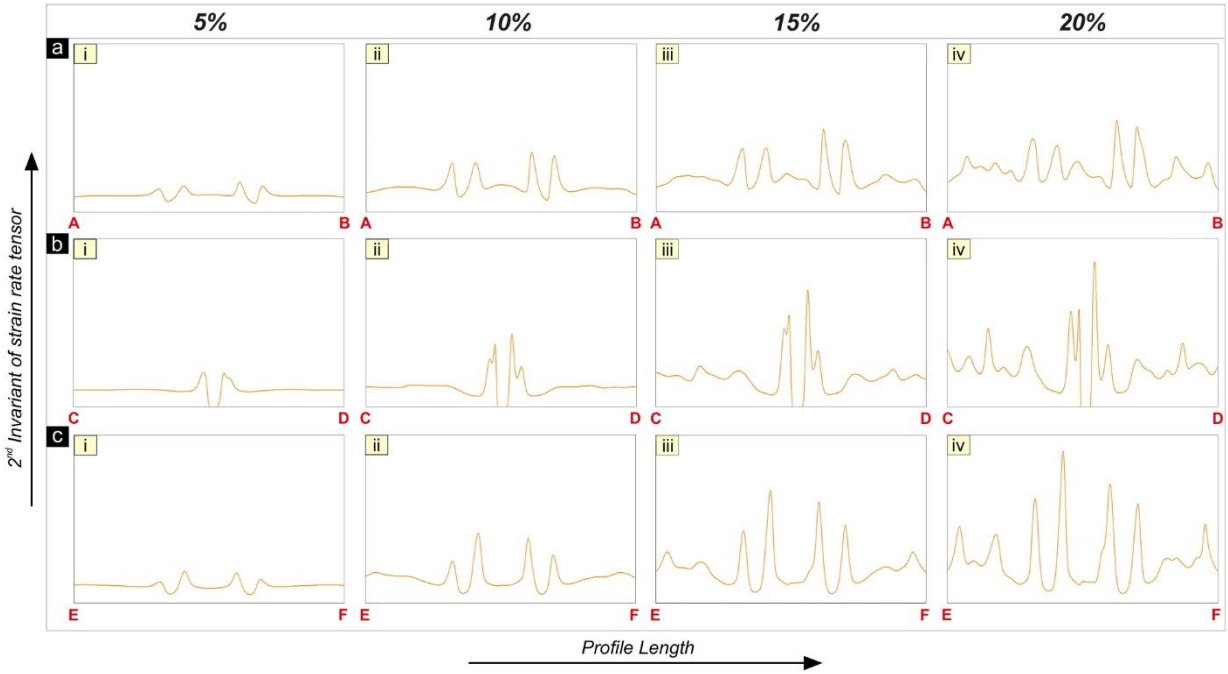

Figure 7.3. Across-band strain profiles in MS2 (locations of the profile lines: AB, CD, and EF, shown in Fig 7.2). Note that the strain profiles show multiple peaks signifying the formation of multiple shear bands in the core zone

matrix of homogeneously distributed numerous bands. The shear bands hardly widen with progressive deformations.

MS 2: This simulation run at a higher strain-rate generates a pair of composite shear bands, radiating from the flaw boundary at a model strain (ε) < 5% (Fig 7.2.b). The shear bands are symmetrically oriented at an angle of ~40° to the compression direction, forming $\Phi \sim 80°$. A close view of the model reveals a characteristic internal structure of the conjugate bands, each of them forms a narrow core zone of the greatest plastic strains, oriented obliquely to the overall band trend, as observed in CBs of the laboratory experiments (Fig 7.2.b-iii). Two core zones on either flank of the flaw thus form a dihedral angle ($\Phi \sim 75°$) lower than that described by the overall conjugate band structures. They continue to accumulate plastic strain, leaving the rest part relatively unstrained. This model shows partitioning of the plastic strain equally into two parallel pairs of identical bands. Strain profile across the model shows four distinct and almost equal peaks which demonstrates that the plastic deformation is accommodated into several bands (~4) of equal intensity (Fig 7.3).

MS 3: The simulation at a low model strain rate produces a pair of conjugate shear bands ($\Phi \sim 75°$) that localize preferentially at the extensional flaw boundary when (ε < 5%) (Fig 7.2.c-i), as manifested in two high-amplitude, sharp peaks in the corresponding strain profile (Fig 7.4.b, c). The time series simulations reveal that each shear band grows in length and concurrently multiplies the magnitudes of their maximum strain localization, eventually to form a core of homogeneously distributed strain, as observed in experimental HBs. Such a band evolution is well reflected from the corresponding strain profiles (Fig 7.4), marked by two outstanding peaks of nearly equal amplitudes in the low-amplitude spectrum. The peak density distribution indicates a large part of plastic strain partitioning selectively in the flaw-controlled conjugate bands. As the model

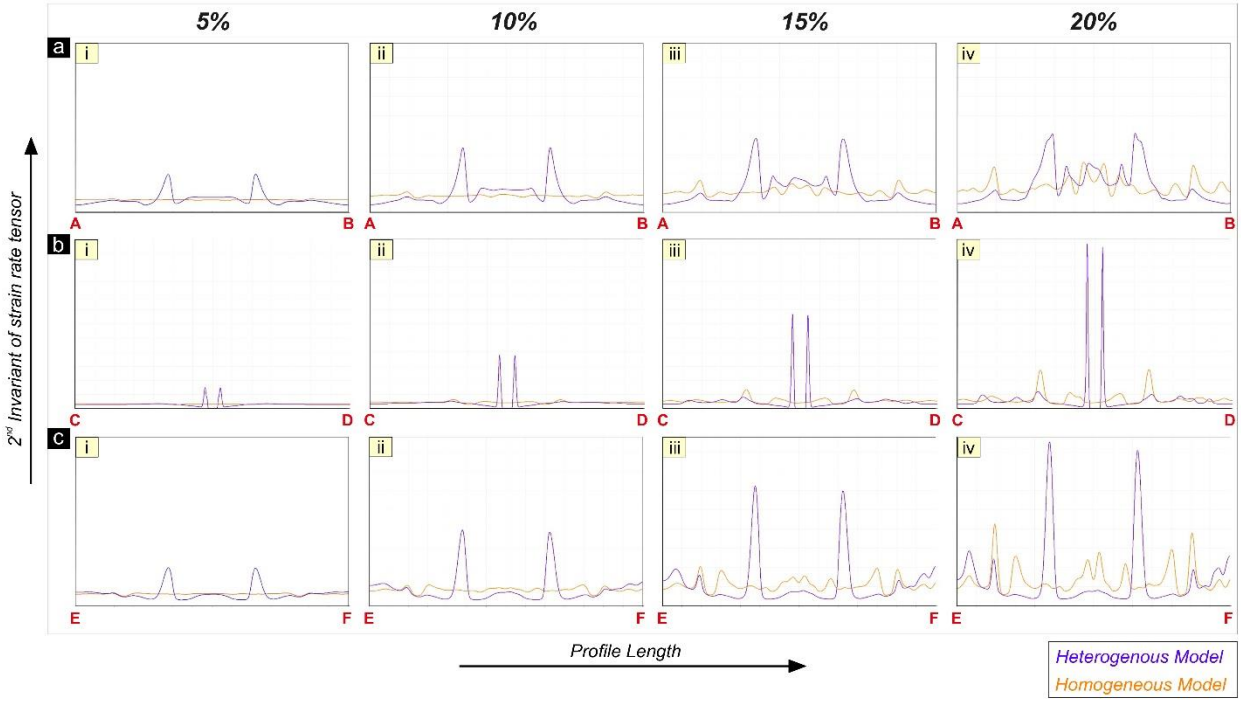

Figure 7.4. Across-band strain profiles in deformed numerical models (locations of the profile lines: AB, CD, and EF, shown in Fig 6 ai). The profiles reveal systematic variations of the 2nd invariant strain rate tensor, where the peaks demarcate the locations of shear band localization in a homogeneous and a heterogeneous model simulation: MS1 and MS3.

deformation progresses, the circular flaw is deformed into an elliptical shape, and the model produces several secondary shear bands, although of much lower thickness in conjugate sets at ϵ > 15% (Fig 7.2.c-iii). This complex band structure is evident from multiple peaks in the strain profiles (Fig. 7.4.c-iv), where the secondary peaks have amplitudes much lower than the principal peaks, implying that the flaw-controlled bands mainly accommodate the bulk strain, even after localization of the secondary bands. The calculated stress-strain curve (Fig 7.1.c) for MS3 indicates that the heterogeneous model attains the state of complete failure much earlier than MS1.

Thus the real scale (both space and time) 2D finite element models, based on visco-elasto plastic rheology support the following laboratory findings: 1) transition in the mechanism of band formation (spatially distributed NBs to localized CBs) depending on the absence or presence of an inherent weak flaw, and 2) CB to HB transformation with reducing global strain rates.

Chapter 8

Discussions and Conclusions

8.1 Roughness Analysis of Shear-failure Surfaces

8.1.1 Implications of the Experimental Results

The laboratory experiments presented in this thesis aim to explain the possible factors responsible for varying roughness characteristics of shear surfaces observed in the SSZ. Earlier frictional slip experiments on solid materials of different rheological properties demonstrated contrasting roughness on slip surfaces. For example, experiments with marble (Badt et al., 2016) and granite (Amitrano & Schmittbuhl, 2002) showed that the slip in the brittle regime produces greater roughness (Hurst exponent values >0.7), attributed to plow-related processes, such as gouge formation and striations. Similar slip experiments on halite and limestone, in contrast, develop relatively smoother roughness (Hurst exponent < 0.5), where asperities cause plastic strain localization in their neighborhood (Renard & Candela, 2017; Sagy et al., 2017). In both the cases plowing and gouge formation primarily determined the roughness characteristic on slip surfaces. The sand-talc models, however, dealt with roughness produced on a shear surface without any action of inherent mechanical asperities. These new models suggest that failure behavior can be a crucial factor in controlling the roughness defined by the linear irregularities. In Type 1 experiments increasing talc to sand volume ratio promotes creep behavior in the sand-talc models, leading to a transition from Coulomb failure in a brittle regime to plastic yielding in the ductile regime. This rheological transition is manifested by the formation of abundant linear irregularities

(slickenlines) on shear fractures. Pure coarse sand models that underwent Coulomb failure produced sharp shear fractures devoid of any macroscopic linearity in their roughness, as observed in some of the field examples (Fig 4.3). Consequently, the fractures had roughness with weak linear irregularities. Coulomb rheology thus cannot give rise to pronounced slickenlines unless the shear fractures involve slip-induced secondary processes, such as asperity plowing, growth fibers, and pressure solution. However, these possibilities were ruled out in the field area as the slickenlines were all found in quartzite host rocks containing no sign of growth fiber or asperity-driven scours or pressure solution-related features. On the other hand, talc-rich or pure talc models of Type 1 produced shear fractures with excellent one-dimensional wavy slickenlines (Fig 4.7.e), strikingly similar to those observed in the field area (Fig 4.3.a). The triaxial tests showed that these models underwent failure by plastic yielding (Fig 3.3.a), involving a substantial strain softening, which seems to have the most potential for slip-induced slickenline generation. A mechanical model was proposed later that a thin soft zone sandwiched between two stiffer walls can develop a slip-parallel wave instability under shear motion, leading to linear irregularities, as observed in the field and laboratory models.

Tectonic faults and fractures often undergo reactivation when they are exposed to a new stress field (Erickson et al., 2001; Mandal & Chattopadhyay, 1995; Misra, Mandal, et al., 2009; Morris et al., 1996; Richard & Krantz, 1991; Richard H. Sibson, 1985). The slip motion during such reactivation can also produce a new set of slickenlines. Type 2 experiments suggest that the surface roughness is sensitive to their initial orientation (θ). For low θ values, the shear fractures are very rough (Fig 4.7.a), characterized by high fractal dimensions (D = 0.77). With increase in θ the roughness is reduced to produce smoother geometry of low fractal dimensions (D = 0.68 when $\theta = 60°$). This change in θ also promotes the formation of slickenlines along the slip direction (Fig

4.7.c). Based on these experimental findings, old shear fractures or faults at angles >45° to the principal compression axes of the new stress field are found to be potential slip surfaces to extensively produce slickensides.

8.1.2 Fractal Dimension: A Measure of Linearity in Slickenside Roughness

Earlier studies have extensively used the concept of fractal geometry in characterizing the fracture roughness employing different techniques, for example, power spectral density (Brodsky et al., 2011b, 2016b; Candela et al., 2012a; Y. H. Lee et al., 1990) and divider fractal methods (Andrle, 1992; Hyslip & Vallejo, 1997; Y. H. Lee et al., 1990). Most of these fractal analyses dealt with length (L) and height dimensions of geometrical asperities to express the degree of roughness of

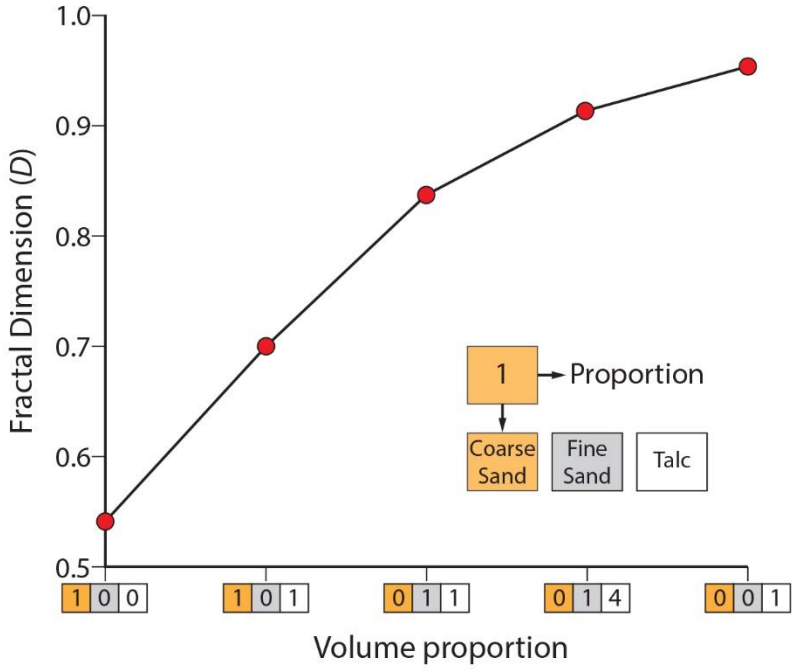

Figure 8.1. Calculated plot of the fractal dimension (D) as a function of the sand-talc volume proportions (shown in the corresponding boxes) in experimental models. With increasing talc content, the transition of Coulomb failure to plastic yielding leads to more prominent linearity in the roughness from shear fractures.

fracture surfaces (e.g., Brodsky et al., 2011, 2016) and yielded fractal dimension, $1 < D < 2$ (Schmittbuhl et al., 1993). 1-D fractal analysis of the field samples and laboratory models was used to analyze the directional variability of roughness on the shear surface because the linear structural elements with preferred orientations introduces a strong anisotropy in the roughness geometry, as reported in many earlier studies (e.g., Candela et al., 2012, and references therein). The differences in fractal dimensions along and across the lineation directly provide us a quantitative measure of the degree of roughness linearity. Cantor set method was adopted for this 1-D analysis (Turcotte, 1997), which fundamentally transforms the system into a binary form (Figure 4.8). This method enables us to characterize the roughness in terms of the frequency distribution of geometrical perturbations, for example, ridges and grooves. This approach was taken as the frequency density of linear features manifests the roughness characteristics of slip surfaces. For example, shear surfaces in talc models form densely packed linear features, as compared to those in pure sand models (Fig 4.7.). The cantor method is thus a handy method to assess the strength of linearity on shear rupture surface.

To discuss the implications of fractal dimension for the linearity analysis, the fracture surface features of pure sand and pure talc models are compared here. Fractures in the sand models show some roughness (D = 0.5), which is evident from the surface map (Fig 4.14.a). However, this roughness occurs on a broad scale, that too spatially quite irregular, displaying no directionality in its geometrical manifestation. Consequently, the relief profiles along and across the slip directions are virtually identical, and the rupture surface, even it is visually rough, completely lacks any slickenlines. Measurement of ΔD attests the visual perception; it is always less than 0.005. On the other hand, pure talc models produced shear fractures, which are apparently smooth. However, their cantor constructions clearly suggest a significant increase in their

roughness compared to those in sand models. Such roughness results from numerous linear features along the slip direction. There is a large contrast in their relief profiles along and across the lineation (Fig 4.15.e). A large value of ΔD (0.15) is obtained, which is consistent with the physical appearance of extensively developed slickenlines in the models (Fig 4.7.e). To sum up, the fractal dimension parameter, ΔD, can be used to express quantitatively the anisotropy of geometrical roughness on shear fractures (Candela et al., 2012; Sagy et al., 2007).

8.1.3 Fractal Dimension versus Slip Behavior

Understanding the slip dynamics of shear fractures helps inform failure studies for a wide range of phenomena, such as fracture propagation, earthquake generation, and scale-dependent frictional properties (Dalguer et al., 2003; Harris et al., 1991; Heaton, 1990; Ruina, 1983; Tsutsumi & Shimamoto, 1997). A line of research focuses upon the control of fracture roughness on the frictional behavior of fracture interface, accounting their geometrical asperities in fractal form. Fractal dimension (D) has been shown from theoretical and experimental models as a critical roughness parameter in determining the frictional strength of shear fractures (Andrle, 1992; Brodsky et al., 2011a, 2016a; Candela et al., 2012b; Hyslip & Vallejo, 1997; Y. H. Lee et al., 1990). The coefficient of friction (μ) increases with D, implying that the slip on shear fractures faces larger frictional resistance if they have roughness of higher fractal dimensions. Based on 2-D fractal analysis, it has been estimated that μ increases substantially, by nearly 50% on an increase of D from 1.025 to 1.055 (Gori & Mari, 2001). Evidently, the slip dynamics are expected to greatly vary depending on the inherent fractal dimensions of rupture surfaces. Pure talc models yielded a large difference in D across and along the lineation ($\Delta D \sim 0.1$). Such directionality in roughness would promote slip in the direction of weakest frictional strength, corresponding to the lowest D.

8.1.4 Concluding points

The principal findings of this study are concluded along the following points.

- The shear fractures in massive quartzite of the SSZ display atypical slickenlines, giving no sign of plowing, mineral growth, or pressure solution lineation. The surfaces show mainly three types of roughness patterns: Type 1—smooth surfaces without any distinct linear irregularities, Type 2—linear roughness with fine scale ridges of small amplitudes, and Type 3—linear roughness with coarse ridges of relative large amplitudes.
- The present sand-talc experiments suggest that the mode of failure and the initial inclination of fractures to the principal compression direction are the potential factors in controlling the linear roughness patterns of shear surfaces. Coulomb failure in pure sand models develops sharp fractures containing no discernible linearity in their roughness, whereas the plastic yielding in pure talc models produces fractures with prominent linear irregularities (slickenlines).
- Initial fracture orientation (θ) with the principal compression direction greatly influences the degree of shear surface roughness is another important factor. Increase in θ promotes the formation of smooth slickenlines at the cost of rough zones.
- This study develops an innovative optical image processing method for estimation of surface roughness. This method provides a measure of roughness topology in terms of relative relief. The Cantor construction (binarization) method is successfully implemented to determine 1-D fractal dimension (D) of a shear surface roughness, which is found to be effective in estimating the degree anisotropy in surface roughness.
- Shear fractures produced by Coulomb failure in brittle regime show roughness with D = 0.53, whereas those produced by plastic yielding in ductile regime display roughness with larger

D (0.95). D holds an inverse relation with the initial fracture inclination (θ); D = 0.77 for θ = 30°, which decreases to 0.68 when θ = 60°.

- The difference (ΔD) in 1-D fractal dimension across and along the slip direction is used as a measure of roughness anisotropy (cf. Sagy et al., 2007; Candela et al., 2012). Increasing ductility promotes ΔD values.
- Based on numerical models, this thesis proposes mechanical instability as a potential mechanism for formation of roughness with marked linearity in the slip zones.

8.2 Mechanism of slip on shear surface

8.2.1 Geological and Geophysical implications

During a fault event, two blocks slide past each other either on a single surface or along a set of surfaces with some variations in their relative orientations. Their sliding motion leaves behind a variety of slip-driven structural marks, forming characteristic roughness on the fault surface. The roughness study has accelerated in recent time due to its implications for interpreting or predicting a range of important geological and geophysical phenomena, e.g., aseismic slip, sub-shear ruptures and occurrence of earthquakes on varied scales (Angheluta et al., 2011). Quantifying the surface topography of natural faults is now a central theme of this study. Power et al., (1987) first developed a movable profilometer technique to construct one dimensional profiles of a fault surface. The topological studies underwent a revolutionary change with the progress of instrumental facilities, e.g., high-resolution laser profilometer, interferometer and field scale mobile LiDAR (Light Detection and Ranging), which led to a dramatic improvement of both the precision and measurement density in the surface roughness calculations (Bistacchi et al., 2011a; Brodsky et al., 2011b; Candela et al., 2012; Renard et al., 2006; Sagy et al., 2007).

This study provides a new insight into the analysis of fault surface roughness that can be used to track heterogeneous slip kinematics and interpret a range of important fault-related geological phenomena, such as fluid permeability and earthquake locations. Roughness characteristics allows us to recognize two principal kinematic domains: stuck zones (little or no slip) and slip zones (relative sliding motion). This work discusses here, albeit in a qualitatively way to show how the ratio of slip to stuck zone area (Ψ) would be a crucial parameter to determine these phenomena. Slip zone localization and their synkinematic growth enhance permeability in fault zones, which in turn facilitate fluid migration activities along the fault (S. R. Brown, 1987; R. W. Zimmerman & Bodvarsson, 1996). Experiments suggest that Ψ increases steeply with increasing initial fault inclination (θ) to the compression direction (Fig 5.8). For example, $\Psi = 0.785$ at $\theta = 30°$, whereas $\Psi = 10.111$ when $\theta = 60°$. Faults oriented at high angles to the regional tectonic compression would be thus potential to develop area-wise extensive slip zones, and thereby act as preferential sites for more intense fluid activities. To summarize this discussion, this study recognizes slip to stuck zone ratio as a possible factor for varying fault-driven fluid activities, as often encountered in many terrains (Faulkner et al., 2010).

The stuck zone versus slip domains can also control the magnitude of strain accumulation on a fault surface. A stuck zone acts as a locking agent to build elastic strains during fault movement partitioned in slip zones. Evidently, the amount of slip depends on the slip area, larger the slip zones larger the slip amount (Pollard & Segall, 1987). Small stuck zones on fault surfaces are likely to fail to lock large slip movement and allow frictional displacements to dissipate mechanical energy, mediated by a number of secondary processes, such as frictional heating and secondary rupture formation. Stuck zones thus must form to cover a significant area of the shear surface so that they can act as an effective source for locking of the fault motion to develop large

strains. On the other hand, the J integral analysis suggests that the amount of strain energy accumulated on a fault depends on the slip area (Atkinson, 1987). A large accumulation of strain energy required for high-magnitude earthquake generation demands slip zones on a large area. An optimum combination of slip and stuck zones is thus a necessary condition to facilitate elastic strain accumulation and trigger earthquakes at the moment slip zones propagate by destabilizing their neighboring stuck zones (Atkinson, 1987). The spatial distribution of stuck zones on the fault surface will eventually determine the temporal patterns of earthquake occurrence in a region. Experiments suggest that stuck and slip zones represent two competing processes, which would be controlled by the fault orientation with respect to the principal compression direction (θ). Stuck zones become extremely weak in their abundance when $\theta > 60°$. Faults with large θ would be thus less effective in the strain accumulation process, which play the most critical role in triggering earthquakes.

8.2.2 Fractal dimensions in the slip versus stuck zone analysis

By combining field and experimental observations, the thesis identifies two geometrical domains of a fault surface, characterized by their distinctive surface roughness properties. Their detailed analyses provide a quantitative difference in roughness anisotropy, measured from along and across-slip profile amplitudes (Fig. 5.5, 5.7 and 5.9). Fractal dimension analysis shows that it can be an effective method to quantify the degree of roughness anisotropy. There are several other ways to measure contrasting roughness across and along slip profiles of irregular surfaces (Renard & Candela, 2017); one of them is Hurst exponent (H), where $H = 1.0$ indicates a self-similar roughness property (i.e., scale independent profile shapes), and $H < 1.0$ implies a self-affine roughness property (i.e., scale dependent profile shapes, becoming more and more smoother on

increasing scale size). Renard and Candela (2017) performed a fractal analysis of synthetic 2D rough surfaces without any linear geometric elements and obtained equal H values in all directions.

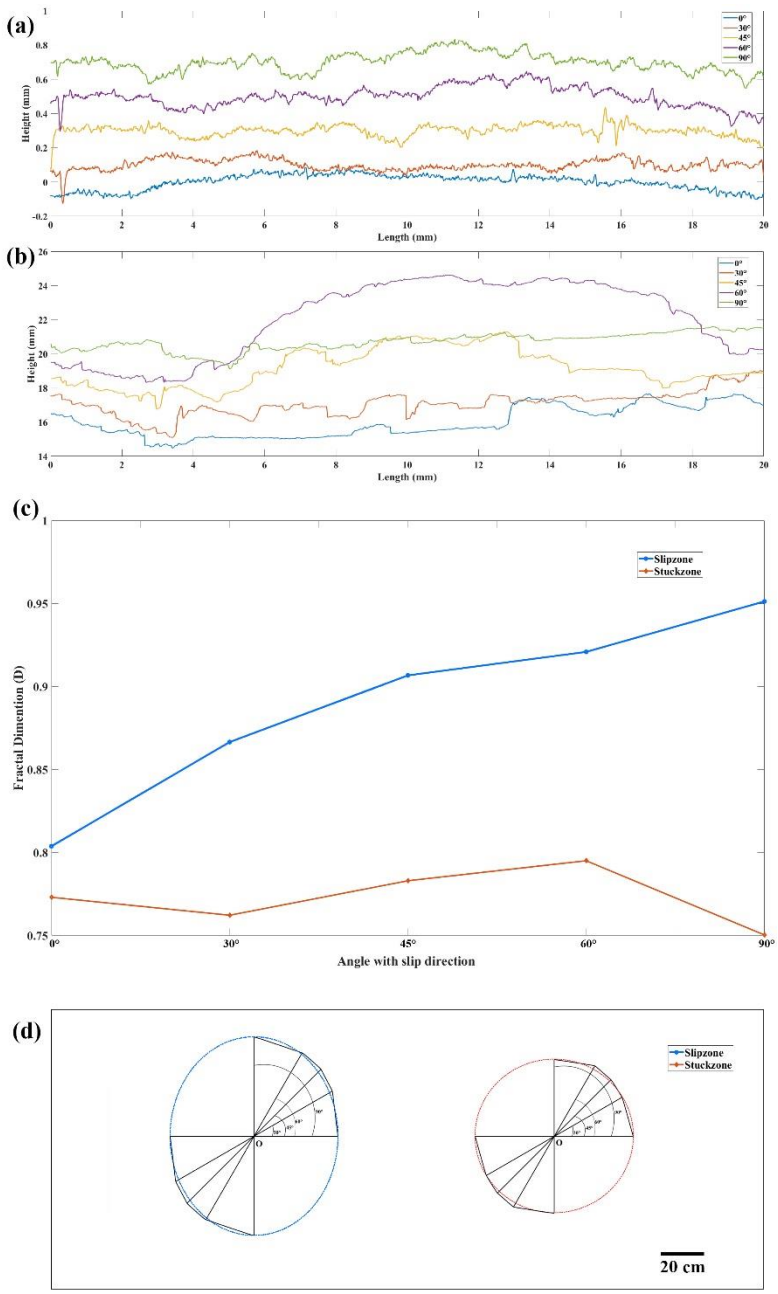

Figure 8.2. (a) Variations of 2D roughness in slip zones with the profile orientation, 0° (parallel) to 90° (perpendicular) to the slip direction. Notice increasing roughness amplitude of the profiles from bottom to top. (b) Roughness profiles in a stuck zone for varying profile orientations. The profiles do not show any systematic roughness variation with the profile orientation. (c) Calculated plots of one-dimensional fractal dimension (*D*) of slip and stuck zone roughness as a function of the profile orientation. Notice a steady increase of *D* from parallel to perpendicular profile orientations in slip zones, but not in stuck zones. (d) Graphical presentations of the directional variability of *D* in slip and stuck zones. The radial length dimension represents the absolute value of *D*. The best-fit ellipse clearly reveals strong roughness anisotropy in slip zones, which becomes isotropic in stuck zones, as indicated by the circular graphical plot.

Their calculations yielded varying *H* with direction when the shear surfaces had slip induced

lineation; *H* value (0.6) in along-slip direction was found to be less than *H* value (0.8) across-slip direction.

This study exercises a 1D fractal analysis, taking into account the frequency of irregularity amplitudes to quantify the degree of roughness anisotropy. The difference between across- ($D\perp$) and along-slip ($D/\!/$) profile fractal dimensions ($\Delta D = D\perp \sim D/\!/$) is found to be significantly high (up to ΔD= 0.1735 in natural samples and 0.2118 in laboratory models) for slip zones, implying strong anisotropy in their roughness. Figure 8.2.a shows a set of profiles at varying orientations to the slip direction. Their calculated fractal dimensions continuously increase from the parallel to perpendicular orientations ($D/\!/$ = 0.8037 to $D\perp$ = 0.9513; Fig. 8.2.c). In contrast, stuck zones show remarkably weak anisotropy, as reflected from little or no variation of *D* with the profile direction (ΔD = 0.0036 for casts and ΔD=0.0024 for laboratory models; Figs. 8.2.b and c). Based on the field observations and their experimental validation, this work proposes ΔD as an effective parameter in identifying slip and stuck domains on a fault surface, as illustrated in Figure 8.2.d. This can be a handy approach to calculate their relative abundance (stuck to slip zone area ratio), which is a critical factor in controlling the pattern of earthquake events on a fault, as discussed in section 8.2.1.

8.2.3 Heterogeneous Slip-localization model

Frictional slip along well-defined shear surfaces and shear zones play a major role in the process of strain energy dissipation during crustal-scale tectonic deformations. As discussed in the preceding section (8.2.1), the morphological characteristics of shear surfaces can mediate the stress build-up and strain release cycles. Classical Coulomb-friction models account for uniform slip on

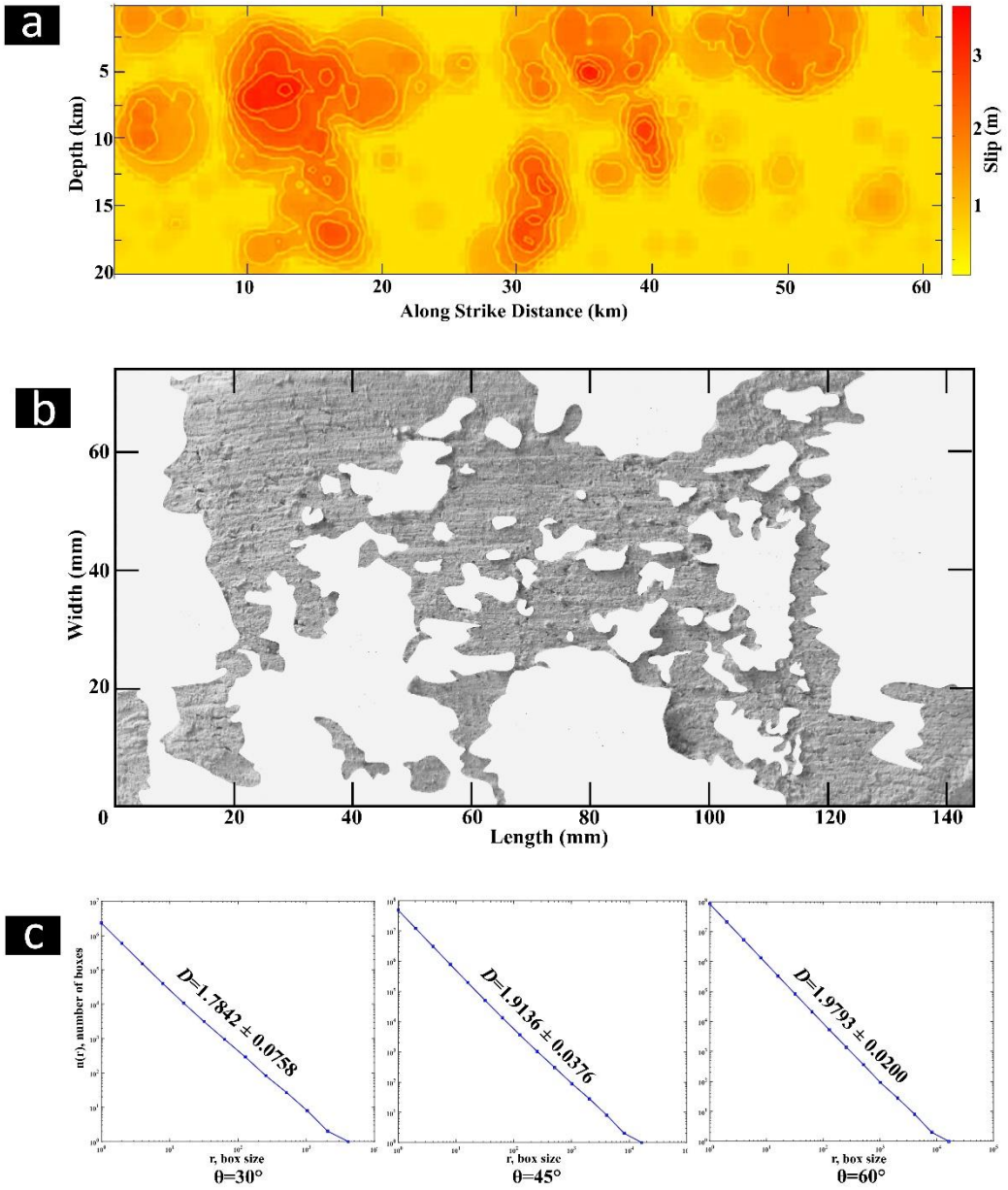

Figure 8.3. (a) Spatial distribution of slip zones on a fault surface during the Kobe earthquake (modified after Zeng & Anderson, 2000). (b) Similar slip zone pattern in analogue experimental model with θ = 30°. (c) Log-log plots of surface irregularities and their corresponding frequencies and the spatial fractal dimension, based on a 2D box-counting method. The linear plots indicate a power-law characteristic of the slip zones. Note that D increases with increasing θ.

a flat fault surface (Anderson, 1905; Angelier, 1979; Richard H. Sibson, 2003). However, the slip behavior during a seismic event as well as in the aseismic period is found to be extremely complex

(Archuleta, 1984; Candela, Renard, Bouchon, et al., 2011; Candela, Renard, Schmittbuhl, et al., 2011; Mai & Beroza, 2002; Rockwell & Klinger, 2013), hard to be predicted by such smooth-fault theory. It is now well-documented that faults always contain scale independent geometrical irregularities of the slip zones (Fig. 8.3.a) (Zeng & Anderson, 2000), as observed in the present laboratory experiments (Fig 8.3.b) and many earlier studies (Candela, Renard, Bouchon, et al., 2011; Candela, Renard, Schmittbuhl, et al., 2011; Manighetti et al., 2005; Renard & Candela, 2017). The fault-slip fields are also strongly heterogeneous, both in terms of their magnitudes and directions. Theoretical studies demonstrated self-similar slip patterns (Hurst exponent of the spatial distribution, $HS = 1$) (Andrews, 1980; Frankel, 1991; Herrero & Bernard, 1994). But, several field observations show self-affine characteristics of faults with HS between 0 and 1 (Candela et al., 2011b). For example, Mai & Beroza, 2002 reported a self-affine analysis with average $HS = 0.71 \pm 0.23$. The kinematic inversion models also suggest size dependence of the slip distributions and their governing factors (Causse et al., 2010). Geometrical analysis of the irregular slip zones in experimental models was performed and an excellent power law distribution was obtained, irrespective of θ value (Fig. 8.3.c). Their estimated 2D fractal dimensions, $D = 1.7842$, 1.9136 and 1.9793 for $\theta = 30°$, 45° and 60° respectively.

The field observations at outcrop to hand specimen scales reveal variability in slickenlines characteristics, implying that the slip is not only heterogeneous, but also the shear surface is morphologically dissimilar in two principal domains: slip zones and stuck zones. The laboratory experiments show their relative spatial occupancy varying with the shear surface orientation θ (Fig. 5.8). The stuck zones are reduced in area, from 56% to 9% with an increase of θ from 30° to 60°, but their pattern continue to follow a power-law distribution (Fig. 8.3.c). Based on this experimental observation, this work hypothesizes that slip first localizes at isolated points on the

surface, which independently grow in area to form a number of distinct zones with progressive bulk shearing. These slip zones continue to grow, and some of them break the stuck zone barrier to coalesce with one another. This sequential process takes place randomly at all scales to produce a self-affine property of slip-stuck zone distributions.

Earlier theoretical and real slip data analysis as well as stress distribution models showed slip heterogeneity on the rupture surface of earthquake events (Candela et al., 2011b), as observed in analogue model experiments. According to the pulse slip model, slip zones continue to propagate until they encounter a strong barrier (Brodsky & Mori, 2007). Stuck zones, characterized by isotropic surface roughness produced during a slip event can act as a barrier in the next sequence of slip events. Stuck zones can thus largely control the first order spatial patterns of coseismic slip localization during an earthquake event (Peyrat & Olsen, 2004). On the other hand, strong roughness anisotropy in slip zones, as shown from both field observations and analogue experiments, can contribute to directional stress accumulation on a fault surface (Marsan, 2006; Schmittbuhl et al., 2006).

8.2.4 Concluding points

The main outcomes of this study follow:

- Intensely sheared quartzite in the Singhbhum shear zone extensively contains slickensides showing heterogeneous surface roughness, characterized by two distinct roughness domains: striated zones and non-striated zones. The striated zones display strong anisotropy in their roughness due to the presence of linear structural elements (parallel ridges and grooves), whereas non-striated zones are devoid of any significant directionality in their roughness.

- These two roughness domains constitute various geometrical patterns, such as sporadic island-like non-striated zones surrounded by striated zones, network structures, and isolated striated zones bordered by non-striated bands.
- The fractal analysis suggests that ΔD (difference in 1D fractal dimension across and along the slip direction) is an effective parameter to express the degree of anisotropy in surface roughness and delineate striated and non-striated zones in field. ΔD attains its lowest value (0.0036) in non-striated zones, whereas the highest value (0.1735) in the striated zones. This field analysis is validated by the experimental data, where ΔD = 0.0024 (lowest value) and 0.2118 (highest value) in non-striated and striated zones, respectively. Increase of ΔD value with θ in experiments suggests enhancement of roughness anisotropy with strengthening of striated zones.
- The spatial association of the two roughness domains is a manifestation of the heterogeneous slip distribution on the shear surface; the striated domains represent slip zones, whereas the non-striated domains reveal the zones of little or no significant slip (i.e., stuck zones).
- Heterogeneity in roughness anisotropy is found to be a good indicator of non-uniform slip fields of faults.

8.3 Deformation localisation in mechanically heterogeneous media

8.3.1 Physical factors controlling the band growth patterns

Earlier studies demonstrated the evolution of micro-bands (cf. NBs) from plane-strain compression experiments on various solids, such as steels and polymers (Anand & Spitzig, 1982; Bowden & Raha, 1970). The micro-bands generally multiply their number with increasing compressional strain, hardly showing any growth in thickness. Bowden and Raha's (1970) elaborate experiments

with PMMA and PS show a transition from micro- to diffuse shear band formation as a function of temperature and strain rate. For example, their experiments find the micro-band mechanism as the dominant mechanism of plastic strain localization in PS at room temperature (21°C), completely replaced by diffuse shear bands at higher temperatures (60°C to 70°C). They showed the same transition by lowering the strain-rate of the test from 2.3 x 10^{-2} sec^{-1} to 6.0 x10^{-3} sec^{-1}. These experimental results can be used to predict the band transition conditions, in terms of thermal or kinematic conditions, but it is applicable for mechanically homogeneous materials. Rocks and natural materials, such as soils are, however, heterogeneous due to various geological reasons (discussed later), and their heterogeneities can largely influence the process of shear-band formation in them (Grujic & Mancktelow, 1998; Pennacchioni & Mancktelow, 2007). This work thus includes pre-existing heterogeneities as an additional factor in this study, with an aim to widen the applicability of the previous experimental findings for inherently heterogeneous material systems. PS model experiments suggest that the presence of mechanical flaws can result in a transition of the shear band mechanism under the same temperature and bulk strain conditions. For example, homogeneous PS models produce spatially distributed narrow shear bands (cf. micro-bands of Bowden and Raha) with a dihedral angle ~85° at room temperature condition and a strain rate of 3 x 10^{-5} sec^{-1} (Fig 6.4.a). The same experimental condition produces band formation in a localized mode, forming a composite band (CB) structure when the material contains a tiny circular flaw. The CBs form in conjugate sets with a dihedral angle of ~86°-90°. It follows from this discussion that the transition from distributed to localized band formation may not always reflect a drop in strain rate or lowering in temperature, as interpreted in earlier studies (Bowden & Raha, 1970). This can occur in the same location under the same physical condition, depending on the availability of inherent mechanical heterogeneities, as observed in the study area discussed in the

preceding section. Structural overprinting relations, e.g. shear localization and foliation of particular generations, suggest that they formed in the same phase of deformation. In addition, the temperature and the strain rate conditions are unlikely to change to a large extent in an outcrop or a small part of the study area. This work suggests that varying shear band patterns observed in the CGGC might have originated from inherent mechanical heterogeneities in gneissic granites.

8.3.2 Geological origin of mechanical heterogeneities

Geological terrains evolve through complex petrogenetic and tectonic processes that eventually result in heterogeneous characteristics of the rocks on a wide range of scales: micro-scale, such as mechanically contrasting mineral grains and grain scale fractures, to kilometer scales, such as magma bodies (plutons) and fault zones. This study deals with weak flaws in a continuum, as they represent the most common type of mechanical heterogeneities encountered in the rock systems. This discussion thus focuses upon the origin of mechanically weak flaws in crustal rocks. A group of such flaws originate from petrological processes, such as partial melting, hydrothermal fluid enrichment and localized hydrolytic weakening. Partial melting in high-grade metamorphic conditions (p = ~3-4 Kb and T = ~750°C – 900°C) produces isolated melt pockets on macroscopic scale (a few millimeters to several centimeters), as reported from many field studies (Dijkstra et al., 2002; Kelemen & Dick, 1995; A. L. Lee et al., 2018; Piazolo et al., 2020). Both theoretical and experimental estimates suggest that the viscosity of quartzo-feldspathic melts ranges 3.9×10^{-3} to 1×10^{-2} Pa s, depending upon the volume content of solid crystals in them (Holtz et al., 1999). Assuming the viscosity of granitic crust in the order of 10^{21} Pa s at the corresponding P-T condition (D. L. Kohlstedt, 2007), the viscosity ratio of melt pockets to their host is found to be extremely low (~0.22), implying that the melt pockets would mechanically act almost like holes in the bulk

rocks, similar to the consideration in the PS models. Interestingly, such weak zones can be effective agents to localize outcrop scale shear zones in metamorphic terrains. Hydrothermal alteration is another important weak-zone forming mechanism at shallow to mid-crustal depths (Adak et al., 2021; Kalczynski & Gates, 2014; Rolland et al., 2003). Such alteration generally produces a variety of phyllosilicates, depending upon the geochemical composition and temperature of the hydrothermal fluids. Experimental studies suggest that phyllosilicate enrichments can lower the viscosity by several orders (Misra, Burlini, et al., 2009), forming isolated weak mechanical heterogeneities, especially in crustal terrains that undergo intense fluid activities, as imprinted in abundant pegmatite bodies.

Another group of weak heterogeneities originate from mechanical processes, such as crack development and fracturing of rocks. Tensile fractures, for example, often form with a finite length, and they subsequently open out, forming lenticular zones, filled with leucosome materials. Field studies have reported localization of conjugate shear zones against such leucosome pods (Grujic & Mancktelow, 1998) and nodal veins of boudinage structures, formed by tensile fractures. With continued deformations the opening fractures act as weak zones to cause stress concentrations (Misra, Mandal, et al., 2009). Such mechanical heterogeneities provide seeds for preferential plastic yielding to initiate shear bands in the bulk continua (Eshelby, 1959; Rutter et al., 1986), as also reported in several geological studies (Grujic & Mancktelow, 1998; Meyer et al., 2017; Misra & Mandal, 2007; Roy et al., 2021). This article advances this line of study by showing the role of weak zones to shear band formation in three mechanisms: distributed narrow shear bands (NBs), localized composite shear bands (CBs) and internally homogeneous shear bands (HBs) as the typical patterns of the shear zones formed due to mechanical heterogeneities.

8.3.3 Macroscopic rheology in shear zone modelling

To model purely ductile or brittle-ductile shear zones in rocks, the crucial step demands an appropriate rheological framework with a close approximation to the geological conditions of interest (Bercovici & Karato, 2002; Gerya & Yuen, 2007; A. A. Popov & Sobolev, 2008). Previous works have used a wide spectrum of rheologies in shear zone modelling, ranging from power-law viscous (Fleitout & Froidevaux, 1980; D. A. Yuen et al., 1978; David A. Yuen & Schubert, 1977) to complex visco-elasto-plastic rheology (Babeyko & Sobolev, 2008; Gerya & Yuen, 2007; Kaus, 2010). However, visco-plastic and elasto-plastic rheologies are perhaps the most commonly used rheological classes. Both of them have certain drawbacks for ductile shear zone modeling. On one hand, the non-associative plasticity for visco-plastic media applies to weak and narrow brittle fault zones that can hardly represent the entire lithosphere. Furthermore, modelling based on this rheological consideration produces transient shear bands that fail to grow steadily to attain a mature state as they are immediately replaced by new generation of bands in the course of progressive deformation (Regenauer-Lieb & Yuen, 2003). The other drawback concerns the exaggeration of brittle responses in the model over the ductile contribution that critically determines the growth of shear zones in ductile or brittle-ductile regimes, as applicable to lithospheric deformations. To overcome these shortcomings, an elasto-visco-plastic rheology was used to model ductile shear zones around a weak zone. This rheological approximation simulates them in agreement with the field observations reported earlier (Grujic & Mancktelow, 1998; Meyer et al., 2017; Misra & Mandal, 2007; Roy et al., 2021) and in this study.

8.3.4 Concluding points

The main outcomes of this study are as follows:

- Analogue laboratory experiments confirm earlier geological observations that inherent mechanical heterogeneities in rocks act as potential nucleating seeds for shear zone formation. At a threshold stress rocks and similar solids without any inherent heterogeneities would always produce spatially distributed numerous narrow, sharp bands (NBs) in conjugate sets with a dihedral angle of ~75°-85° to the compression direction. Their overall pattern is unlike isolated or solitary wide shear zones commonly observed in tectonic belts.
- In homogeneous solids NBs begin to form at ~5% finite strain and multiply in number to increase their spatial density with increasing finite strain, and at the same time they grow in length with nearly a constant thickness.
- The presence of weak heterogeneities results in a transition of spatially distributed NBs to isolated wide composite shear bands (CBs). The CBs radiate from the circular flaw in conjugate pairs with a dihedral angle of ~85°-90°. A typical CB develops a characteristic internal band structures, consisting of a strongly sheared core (cluster of extremely close spaced sub-parallel NBs, flanked by a region of orthogonal NBs on either side of it. The CB core accommodates most of the plastic strain in the band, leaving its flank regions for weak shear localization.
- The mechanism of heterogeneity-controlled shear band localization is sensitive to the global strain rate ($\dot{\varepsilon}$). Reducing $\dot{\varepsilon}$ replaces composites bands (CBs) with wide, homogeneous shear bands (HBs), which are completely devoid of NBs.
- The real scale (both space and time) 2D finite element models, based on visco-elasto plastic rheology validate the following laboratory findings: 1) transition in the mechanism of band

formation (spatially distributed NBs to localized CBs) depending on the absence or presence of an inherent weak flaw, and 2) CB to HB transformation with reducing global strain rates.

- Heterogeneous mechanical models explain the diverse types of shear zones commonly observed in many geological terrains, like CGGC.

References

Adak, S., Pal, D. C., Upadhyay, D., & Mondal, R. (2021). Textural re-equilibration, hydrothermal alteration and element redistribution in Fe-Ti oxide pods, Singhbhum Shear Zone, eastern India. *Geochemistry*, *81*(1), 125679. https://doi.org/10.1016/j.chemer.2020.125679

Aki, K. (1989). Ideal probabilistic earthquake prediction. Tectonophysics, 169(1-3), 197-198.

Allmendinger, R. W., Gephart, J. W., & Marrett, R. A. (n.d.). *Notes on Fault Slip Analysis*.

Amitrano, D., & Schmittbuhl, J. (2002). Fracture roughness and gouge distribution of a granite shear band. *Journal of Geophysical Research: Solid Earth*, *107*(B12), ESE 19-1-ESE 19-16. https://doi.org/10.1029/2002jb001761

Anand, L., & Spitzig, W. A. (1980). Initiation of localized shear bands in plane strain. *Journal of the Mechanics and Physics of Solids*, *28*(2), 113–128. https://doi.org/10.1016/0022-5096(80)90017-4

Anand, L., & Spitzig, W. A. (1982). Shear-Band Orientations in Plane Strain. *Acta Metallurgica*, *30*(2), 553–561.

Anderson, E. M. (1942). *The dynamics of faulting and dyke formation with applications to Britain*. Oliver and Boyd.

Anderson, E. M. (1905). The Dynamics of Faulting. *Transactions of the Edinburgh Geological Society*, *8*(3), 387–402. https://doi.org/https://doi.org/10.1144/transed.8.3.387

Andrews, D. J. (1980). Fault impedance and earthquake energy in the Fourier transform domain. *Bulletin of the Seismological Society of America*, *70*(5), 1683–1698. https://doi.org/https://doi.org/10.1785/BSSA0700051683

Andrle, R. (1992). Estimating fractal dimension with the divider method in geomorphology. *Geornorphology*, (3), 131–141. https://doi.org/10.1016/0033-5894(92)90047-M

Angelier, J. (1979). Determination of the mean principal directions of stresses for a given fault population. *Tectonophysics*, *56*(3–4), T17–T26. https://doi.org/https://doi.org/10.1016/0040-1951(79)90081-7

Angheluta, L., Candela, T., Mathiesen, J., & Renard, F. (2011). Effect of surface

morphology on the dissipation during shear and slip along a rock-rock interface that contains a visco-elastic core. *Pure and Applied Geophysics*, *168*(12), 2335–2344. https://doi.org/10.1007/s00024-011-0272-8

Archuleta, R. J. (1984). A faulting model for the 1979 Imperial Valley earthquake. *Journal of Geophysical Research*, *89*(B6), 4559–4585. https://doi.org/10.1029/JB089iB06p04559

Atkinson, B. K. (1987). Introduction to fracture mechanics and its geophysical applications. In B. K. Atkinson (Ed.), *Fracture Mechanics of rock* (pp. 1–26). Academic Press.

Babeyko, A. Y., & Sobolev, S. V. (2008). High-resolution numerical modeling of stress distribution in visco-elasto-plastic subducting slabs. *Lithos*, *103*(1–2), 205–216. https://doi.org/10.1016/j.lithos.2007.09.015

Badt, N., Hatzor, Y. H., Toussaint, R., & Sagy, A. (2016). Geometrical evolution of interlocked rough slip surfaces: The role of normal stress. *Earth and Planetary Science Letters*, *443*, 153–161. https://doi.org/10.1016/j.epsl.2016.03.026

Barnhoorn, A., Bystricky, M., Burlini, L., & Kunze, K. (2004). The role of recrystallisation on the deformation behaviour of calcite rocks: Large strain torsion experiments on Carrara marble. *Journal of Structural Geology*, *26*(5), 885–903. https://doi.org/10.1016/j.jsg.2003.11.024

Bauer, H., Rogowitz, A., Grasemann, B., & Decker, K. (2018). Intracrystalline deformation of calcite in the upper brittle crust. *Geology*, *46*(4), 375–378. https://doi.org/10.1130/G39990.1

Beall, A., Fagereng, Å., & Ellis, S. (2019). Fracture and Weakening of Jammed Subduction Shear Zones, Leading to the Generation of Slow Slip Events. *Geochemistry, Geophysics, Geosystems*, *20*(11), 4869–4884. https://doi.org/10.1029/2019GC008481

Bercovici, D., & Karato, S. I. (2002). Theoretical analysis of shear localization in the lithosphere. *Reviews in Mineralogy and Geochemistry*. https://doi.org/10.2138/gsrmg.51.1.387

Bercovici, D., Ricard, Y., & Schubert, G. (2001). A two-phase model for compaction and damage 1. General Theory. *Journal of Geophysical Research: Solid Earth*, *106*(B5), 8887–8906. https://doi.org/10.1029/2000jb900430

Biegel, R. L., Wang, W., Scholz, C. H., Boitnott, G. N., & Yoshioka, N. (1992). Micromechanics of rock friction: 1. Effects of surface roughness on initial

friction and slip hardening in Westerly granite. *Journal of Geophysical Research*, *97*(B6), 8951–8964. https://doi.org/10.1029/92JB00042

Bistacchi, A., Ashley Griffith, W., Smith, S. A. F., di Toro, G., Jones, R., & Nielsen, S. (2011a). Fault roughness at seismogenic depths from LIDAR and photogrammetric analysis. *Pure and Applied Geophysics*, *168*(12), 2345–2363. https://doi.org/10.1007/s00024-011-0301-7

Bistacchi, A., Ashley Griffith, W., Smith, S. A. F., di Toro, G., Jones, R., & Nielsen, S. (2011b). Fault roughness at seismogenic depths from LIDAR and photogrammetric analysis. *Pure and Applied Geophysics*, *168*(12), 2345–2363. https://doi.org/10.1007/s00024-011-0301-7

Blenkinsop, T. G. (2008). Relationships between faults, extension fractures and veins, and stress. *Journal of Structural Geology*, *30*(5), 622-632. https://doi.org/10.1016/j.jsg.2008.01.008

Boneh, Y., Chang, J. C., Lockner, D. A., & Reches, Z. (2014). Evolution of Wear and Friction Along Experimental Faults. *Pure and Applied Geophysics*, *171*(11), 3125–3141. https://doi.org/10.1007/s00024-014-0801-3

Boneh, Yuval, Sagy, A., & Reches, Z. (2013). Frictional strength and wear-rate of carbonate faults during high-velocity, steady-state sliding. *Earth and Planetary Science Letters*, *381*, 127–137. https://doi.org/10.1016/j.epsl.2013.08.050

Bott, M. H. P. (1959). The mechanics of oblique slip faulting. *Geological Magazine*, *96*(2), 109–117. https://doi.org/https://doi.org/10.1017/S0016756800059987

Bowden, P. B., & Raha, S. (1970). The formation of micro shear bands in polystyrene and polymethylmethacrylate. *Philosophical Magazine*, *22*(177), 463–482. https://doi.org/10.1080/14786437008225837

Bratli, K. R., & Rasmus, R. (1981). Stability and Failure of Sand Arches. *Society of Petroleum Engineers Journal*, *21*(2), 236–248.

Bretz, H. J. (1940). Solution cavities in the Joliet limestone of northeastern Illinois. *The Journal of Geology*, *48*(4), 337–384.

Brodsky, E. E., & Mori, J. (2007). Creep events slip less than ordinary earthquakes. *Geophysical Research Letters*, *34*(16). https://doi.org/10.1029/2007GL030917

Brodsky, E. E., Gilchrist, J. J., Sagy, A., & Collettini, C. (2011a). Faults smooth

gradually as a function of slip. *Earth and Planetary Science Letters*, *302*(1–2), 185–193. https://doi.org/10.1016/j.epsl.2010.12.010

Brodsky, E. E., Gilchrist, J. J., Sagy, A., & Collettini, C. (2011b). Faults smooth gradually as a function of slip. *Earth and Planetary Science Letters*, *302*(1–2), 185–193. https://doi.org/10.1016/j.epsl.2010.12.010

Brodsky, E. E., Kirkpatrick, J. D., & Candela, T. (2016a). Constraints from fault roughness on the scale-dependent strength of rocks. *Geology*, *44*(1), 19–22. https://doi.org/10.1130/G37206.1

Brodsky, E. E., Kirkpatrick, J. D., & Candela, T. (2016b). Constraints from fault roughness on the scale-dependent strength of rocks. *Geology*, *44*(1), 19–22. https://doi.org/10.1130/G37206.1

Brooks, N. W., Duckett, R. A., & Ward, I. M. (1991). Investigation into double yield points in polyethylene. *Polymer*, *33*(9), 1872–1880. https://doi.org/https://doi.org/10.1016/0032-3861(92)90486-G

Brown, S. R. (1987). Fluid flow through rock joints: the effect of surface roughness. *Journal of Geophysical Research*, *92*(B2), 1337–1347. https://doi.org/10.1029/JB092iB02p01337

Brown, S. R., & Scholz, C. H. (1985). Broad bandwidth study of the topography of natural rock surfaces. *Journal of Geophysical Research*, *90*(B14). https://doi.org/10.1029/jb090ib14p12575

Brown, Stephen R., & Scholz, C. H. (1985). Broad bandwidth study of the topography of natural rock surfaces. *Journal of Geophysical Research*, *90*(B14), 12575. https://doi.org/10.1029/JB090iB14p12575

Campillo, M., Favreau, P., Ionescu, I. R., & Voisin, C. (2001). On the effective friction law of a heterogeneous fault. *Journal of Geophysical Research: Solid Earth*, *106*(B8), 16307–16322. https://doi.org/10.1029/2000jb900467

Camwell, L., & Hull, D. (1973). Crazing and fracture associated with the interaction of shear bands in polystyrene. *Philosophical Magazine*, *27*(5), 1135–1150. https://doi.org/10.1080/14786437308225822

Candela, T., Renard, F., Bouchon, M., Brouste, A., Marsan, D., Schmittbuhl, J., & Voisin, C. (2009a). Characterization of fault roughness at various scales: Implications of three-dimensional high resolution topography measurements. *Pure and Applied Geophysics*, *166*(10–11), 1817–1851. https://doi.org/10.1007/s00024-009-0521-2

Candela, T., Renard, F., Bouchon, M., Brouste, A., Marsan, D., Schmittbuhl, J., & Voisin, C. (2009b). Characterization of fault roughness at various scales: Implications of three-dimensional high resolution topography measurements. *Pure and Applied Geophysics*, *166*(10–11), 1817–1851. https://doi.org/10.1007/s00024-009-0521-2

Candela, T., Renard, F., Schmittbuhl, J., Bouchon, M., & Brodsky, E. E. (2011). Fault slip distribution and fault roughness. *Geophysical Journal International*, *187*(2), 959–968. https://doi.org/10.1111/j.1365-246X.2011.05189.x

Candela, T., Renard, F., Bouchon, M., Schmittbuhl, J., & Brodsky, E. E. (2011). Stress drop during earthquakes: Effect of fault roughness scaling. *Bulletin of the Seismological Society of America*, *101*(5), 2369–2387. https://doi.org/10.1785/0120100298

Candela, T., Renard, F., Klinger, Y., Mair, K., Schmittbuhl, J., & Brodsky, E. E. (2012a). Roughness of fault surfaces over nine decades of length scales. *Journal of Geophysical Research: Solid Earth*, *117*(8), 1–30. https://doi.org/10.1029/2011JB009041

Candela, T., Renard, F., Klinger, Y., Mair, K., Schmittbuhl, J., & Brodsky, E. E. (2012b). Roughness of fault surfaces over nine decades of length scales. *Journal of Geophysical Research: Solid Earth*, *117*(8). https://doi.org/10.1029/2011JB009041

Causse, M., Cotton, F., & Mai, P. M. (2010). Constraining the roughness degree of slip heterogeneity. *Journal of Geophysical Research: Solid Earth*, *115*(5). https://doi.org/10.1029/2009JB006747

Chester, F. M., & Logan, J. M. (1986). Implications for mechanical properties of brittle faults from observations of the Punchbowl fault zone, California. *Pure and Applied Geophysics PAGEOPH*, *124*(1–2), 79–106. https://doi.org/10.1007/BF00875720

Chester, F. M., Evans, J. P., & Biegel, R. L. (1993). Internal structure and weakening mechanisms of the San Andreas Fault. *Journal of Geophysical Research*, *98*(B1), 771–786. https://doi.org/10.1029/92JB01866

Chester, J. S., & Fletcher, R. C. (1997). Stress distribution and failure in anisotropic rock near a bend on a weak fault. *Journal of Geophysical Research: Solid Earth*, *102*(B1), 693-708. https://doi.org/10.1029/96JB02791

Chester, F. M., & Chester, J. S. (2000). Stress and deformation along wavy frictional faults. *Journal of Geophysical Research: Solid Earth*, *105*(B10),

23421-23430. https://doi.org/10.1029/2000JB900241

Chester, F. M., Chester, J. S., Kirschner, D. L., Schulz, S. E., & Evans, J. P. (2004). Structure of Large-Displacement, Strike-Slip Fault Zones in the Brittle Continental Crust. In *Rheology and Deformation of the Lithosphere at Continental Margins* (pp. 223–260). https://doi.org/https://doi.org/10.7312/karn12738-009

Colletta, B., Letouzey, J., Pinedo, R., Ballard, J. F., & Bale, P. (1991). Computerized X-ray tomography analysis of sandbox models: examples of thin-skinned thrust systems. *Geology*, *19*(11), 1063–1067. https://doi.org/10.1130/0091-7613(1991)019<1063:CXRTAO>2.3.CO;2

Condit, C. B., & Mahan, K. H. (2018). Fracturing, fluid flow and shear zone development: Relationships between chemical and mechanical processes in Proterozoic mafic dykes from southwestern Montana, <scp>USA</scp>. *Journal of Metamorphic Geology*, *36*(2), 195–223. https://doi.org/10.1111/jmg.12289

Cowan, D. S., Cladouhos, T. T., & Morgan, J. K. (2003). Structural geology and kinematic history of rocks formed along low-angle normal faults, Death Valley, California. *GSA Bulletin*, (10), 1230–1248. https://doi.org/https://doi.org/10.1130/B25245.1

Dalguer, L. A., Irikura, K., & Riera, J. D. (2003). Simulation of tensile crack generation by three-dimensional dynamic shear rupture propagation during an earthquake. *Journal of Geophysical Research: Solid Earth*, *108*(B3). https://doi.org/10.1029/2001JB001738

Davidesko, G., Sagy, A., & Hatzor, Y. H. (2014). Evolution of slip surface roughness through shear. *Geophysical Research Letters*, *41*, 1492–1498. https://doi.org/10.1002/ 2013GL058913.Received

Davis, G., Reynolds, S., & Kluth, C. (2011). *Structural geology of rocks and regions*. Retrieved from https://books.google.co.in/books?hl=en&lr=&id=EYzzOKLRT-8C&oi=fnd&pg=PA2&dq=Davis,+G.H.,+1984.+Structural+Geology+of+Rocks+and+Regions.+Wiley,+New+York,+NY,+492+pp&ots=2B0TRmDduo&sig=Uk5z8AUXT_r3zesU__5xI5oNkXU

deformation, J. A.-C., & 1994, undefined. (n.d.). Fault slip analysis and paleostress reconstruction. *Ci.Nii.Ac.Jp*. Retrieved from https://ci.nii.ac.jp/naid/10023913594/

Dibblee, T. W. (1977). STRIKE-SLIP TECTONICS OF THE SAN ANDREAS FAULT AND ITS ROLE IN CENOZOIC BASIN EVOLVEMENT.

Dijkstra, A. H., Drury, M. R., & Frijhoff, R. M. (2002). Microstructures and lattice fabrics in the Hilti mantle section (Oman Ophiolite): Evidence for shear localization and melt weakening in the crust-mantle transition zone? *Journal of Geophysical Research: Solid Earth*, *107*(B11), ETG 2-1-ETG 2-18. https://doi.org/10.1029/2001jb000458

Dixon, J. M., & Liu, S. (1992). Centrifuge modelling of the propagation of thrust faults. *Thrust Tectonics*, 53–69. https://doi.org/10.1007/978-94-011-3066-0_5

Doblas, M. (1998a). Slickenside kinematic indicators. *Tectonophysics*, *295*(1–2), 187–197. https://doi.org/10.1016/S0040-1951(98)00120-6

Doblas, M. (1998b). *Slickenside kinematic indicators*. *Tectonophysics* (Vol. 295).

Dunn, J.-M. G. S., & 1929, undefined. (1929). The geology of north Singhbhum including parts of Ranchi and Manbhum districts. *Mem. Geol. Surv. India*. Retrieved from https://ci.nii.ac.jp/naid/20000875780/

Ellis, S., Schreurs, G., & Panien, M. (2004). Comparisons between analogue and numerical models of thrust wedge development. *Journal of Structural Geology*, *26*(9), 1659–1675. https://doi.org/10.1016/j.jsg.2004.02.012

Hancock, P. L., & Engelder, T. (1989). Neotectonic joints. *Geological Society of America Bulletin*, *101*(10), 1197-1208. https://doi.org/10.1130/0016-7606(1989)101%3C1197:NJ%3E2.3.CO;2

Engelder, J. T. (1974). Cataclasis and the generation of fault gouge. *Geological Society of America Bulletin*, *85*(10), 1515-1522. https://doi.org/10.1130/0016-7606(1974)85%3C1515:CATGOF%3E2.0.CO;2

Erickson, S. G., Strayer, L. M., & Suppe, J. (2001). Initiation and reactivation of faults during movement over a thrust-fault ramp: Numerical mechanical models. *Journal of Structural Geology*, *23*(1), 11–23. https://doi.org/10.1016/S0191-8141(00)00074-2

Eshelby, J. D. (1959). The elastic field outside an ellipsoidal inclusion. *Proceedings of the Royal Society of London. Series A. Mathematical and Physical Sciences*, *252*(1271), 561–569. https://doi.org/10.1098/rspa.1959.0173

Faulkner, D. R., Jackson, C. A. L., Lunn, R. J., Schlische, R. W., Shipton, Z. K., Wibberley, C. A. J., & Withjack, M. O. (2010, November). A review of recent

developments concerning the structure, mechanics and fluid flow properties of fault zones. *Journal of Structural Geology*. https://doi.org/10.1016/j.jsg.2010.06.009

Finch, M., Hasalová, P., Weinberg, R. F., & Fanning, C. M. (2014). Switch from thrusting to normal shearing in the Zanskar shear zone, NW Himalaya: Implications for channel flow. *Bulletin of the Geological Society of America*, *126*(7–8), 892–924. https://doi.org/10.1130/B30817.1

Fleitout, L., & Froidevaux, C. (1980). Thermal and mechanical evolution of shear zones. *Journal of Structural Geology*, *2*(1–2), 159–164. https://doi.org/10.1016/0191-8141(80)90046-2

Flinn, D. (1977). Transcurrent faults and associated cataclasis in Shetland. *Journal of the Geological Society*, *133*(3), 231-247. https://doi.org/10.1144/gsjgs.133.3.0231

Fondriest, M., Smith, S. A. F., Candela, T., Nielsen, S. B., Mair, K., & Toro, G. Di. (2013). Mirror-like faults and power dissipation during earthquakes. *Geology*, *41*(11), 1175–1178. https://doi.org/10.1130/G34641.1

Fossen, H. (2010). *Structural Geology*. Cambridge University Press.

Fossen, Haakon, & Cavalcante, G. C. G. (2017). Shear zones – A review. *Earth-Science Reviews*, *171*(May), 434–455. https://doi.org/10.1016/j.earscirev.2017.05.002

Frankel, A. (1991). High-frequency spectral falloff of earthquakes, fractal dimension of complex rupture, b value, and the scaling of strength on faults. *Journal of Geophysical Research*, *96*(B4), 6291–6302. https://doi.org/10.1029/91JB00237

Fusseis, F., & Handy, M. R. (2008). Micromechanisms of shear zone propagation at the brittle-viscous transition. *Journal of Structural Geology*, *30*(10), 1242–1253. https://doi.org/10.1016/j.jsg.2008.06.005

Fusseis, F., Handy, M. R., & Schrank, C. (2006). Networking of shear zones at the brittle-to-viscous transition (Cap de Creus, NE Spain). *Journal of Structural Geology*, *28*(7), 1228–1243. https://doi.org/10.1016/j.jsg.2006.03.022

Gay, N. C. (1970). The formation of step structures on slickensided shear surfaces. *The Journal of Geology*, *78*(5), 523–532. Retrieved from http://www.jstor.org/stable/30061389 Accessed:

Gerya, T. V., & Yuen, D. A. (2007). Robust characteristics method for modelling

multiphase visco-elasto-plastic thermo-mechanical problems. *Physics of the Earth and Planetary Interiors*, *163*(1–4), 83–105. https://doi.org/10.1016/j.pepi.2007.04.015

Ghosh, S. K., & Sengupta, S. (1987). Progressive development of structures in a ductile shear zone. *Journal of Structural Geology*, *9*(3), 277–287. https://doi.org/https://doi.org/10.1016/0191-8141(87)90052-6

Ghosh, S. K., Mandal, N., Khan, D., & Deb, S. K. (1992). Modes of superposed buckling in single layers controlled by initial tightness of early folds. *Journal of Structural Geology*, *14*(4), 381–394. https://doi.org/10.1016/0191-8141(92)90100-B

Gori, U., & Mari, M. (2001). The correlation between the fractal dimension and internal friction angle of different granular materials. *Soils and Foundations*, *41*(6), 17–23.

Griggs, D. T., Turner, F. J., & Heard, H. C. (1960). Deformation of Rocks at 500° to 800° C. https://doi.org/10.1007/978-1-4939-6911-1

Grujic, D., & Mancktelow, N. S. (1998). Melt-bearing shear zones: analogue experiments and comparison with examples from southern Madagascar. *Journal of Structural Geology*, *20*(6), 673–680. https://doi.org/10.1016/S0191-8141(98)00006-6

Gudmundsson, A. (2011). *Rock fractures in geological processes*. Cambridge University Press.

Gupta, A., Basu, N., & Srivastava, D. (1981). Mafic and ultramafic volcanism of Ongarbira greenstone belt, Singhbhum, Bihar. *Journal Geological Society of India*, *22*(12), 593–596.

Hanaor, D. A. H., Gan, Y., & Einav, I. (2016). Static friction at fractal interfaces. *Tribology International*, *93*, 229–238. https://doi.org/10.1016/j.triboint.2015.09.016

Handin, J., & Fairbairn, H. W. (1955). EXPERIMENTAL DEFORMATION OF HASMARK DOLOMITE. *BULLETIN OF THE GEOLOGICAL SOCIETY OF AMERICA*, *66*, 1257–1274.

Handin, J., & Hager, R. V. J. (1957). EXPERIMENTAL DEFORMATION OF SEDIMENTARY ROCKS UNDER CONFINING PRESSURE: TESTS AT ROOM TEMPERATURE ON DRY SAMPLES. *BULLETIN of the AMERICAN ASSOCIATION OF PETROLEUM GEOLOGISTS*, *41*(1).

Handin, J., & Hager, R. V. J. (1958). EXPERIMENTAL DEFORMATION OF SEDIMENTARY ROCKS UNDER CONFINING PRESSURE: TESTS AT HIGH TEMPERATURE. *BULLETIN OF THE AMERICAN ASSOCIATION OF PETROLEUM GEOLOGISTS*, *42*(12), 2892–2934.

Harbord, C. W. A., Nielsen, S. B., De Paola, N., & Holdsworth, R. E. (2017). Earthquake nucleation on rough faults. *Geology*, *45*(10), 931–934. https://doi.org/10.1130/G39181.1

Harrington, R. M., & Brodsky, E. E. (2009). Source duration scales with magnitude differently for earthquakes on the San Andreas fault and on secondary faults in Parkfield, California. *Bulletin of the Seismological Society of America*, *99*(4), 2323–2334. https://doi.org/10.1785/0120080216

Harris, R. A., Archuleta, R. J., & Day, M. (1991). Stepover, *18*(5), 893–896.

Heaton, T. H. (1990). Evidence for and implications of self-healing pulses of slip in earthquake rupture. *Physics of the Earth and Planetary Interiors*, *64*(1), 1–20. https://doi.org/10.1016/0031-9201(90)90002-F

Herrero, A., & Bernard, P. (1994). A kinematic self-similar rupture process for earthquakes. *Bulletin of the Seismological Society of America*, *84*(4), 1216–1228. https://doi.org/https://doi.org/10.1785/BSSA0840041216

Holtz, F., Roux, J., Ohlhorst, S., Behrens, H., & Schulze, F. (1999). The effects of silica and water on the viscosity of hydrous quartzofeldspathic melts. *American Mineralogist*, *84*(1–2), 27–36. https://doi.org/10.2138/am-1999-1-203

Holtzman, B. K., Kohlstedt, D. L., Zimmerman, M. E., Heidelbach, F., Hiraga, T., & Hustoft, J. (2003). Melt segregation and strain partitioning: Implications for seismic anisotropy and mantle flow. *Science*, *301*(5637), 1227–1230. https://doi.org/10.1126/science.1087132

Holtzman, B. K., Groebner, N. J., Zimmerman, M. E., Ginsberg, S. B., & Kohlstedt, D. L. (2003). Stress-driven melt segregation in partially molten rocks. *Geochemistry, Geophysics, Geosystems*, *4*(5). https://doi.org/10.1029/2001GC000258

Holtzman, Benjamin K., Kohlsted, D. L., & Morgan, J. P. (2005). Viscous energy dissipation and strain partitioning in partially molten rocks. *Journal of Petrology*, *46*(12), 2569–2592. https://doi.org/10.1093/petrology/egi065

Hutchinson, J. W., & Tvergaard, V. (1980). Surface instabilities on statically strained plastic solids. *International Journal of Mechanical Sciences*, *22*(6),

339–354.

Hyslip, J. P., & Vallejo, L. E. (1997). Fractal analysis of the roughness and size distribution of granular materials. *Engineering Geology*, *48*(3–4), 231–244. https://doi.org/10.1016/S0013-7952(97)00046-X

de Joussineau, G., Petit, J. P., & Gauthier, B. D. M. (2003). Photoelastic and numerical investigation of stress distributions around fault models under biaxial compressive loading conditions. *Tectonophysics*, *363*(1–2), 19–43. https://doi.org/10.1016/S0040-1951(02)00648-0

Kalczynski, M. J., & Gates, A. E. (2014). Hydrothermal alteration, mass transfer and magnetite mineralization in dextral shear zones, western Hudson Highlands, New York, United States. *Ore Geology Reviews*, *61*, 226–247. https://doi.org/10.1016/j.oregeorev.2014.02.007

Katz, R. F., Spiegelman, M., & Holtzman, B. (2006). The dynamics of melt and shear localization in partially molten aggregates. *Nature*, *442*(7103), 676–679. https://doi.org/10.1038/nature05039

Katz, Y., Weinberger, R., & Aydin, A. (2004). Geometry and kinematic evolution of Riedel shear structures, Capitol Reef National Park, Utah. *Journal of Structural Geology*, *26*(3), 491–501. https://doi.org/10.1016/j.jsg.2003.08.003

Kaus, B. J. P. (2010). Factors that control the angle of shear bands in geodynamic numerical models of brittle deformation. *Tectonophysics*, *484*(1–4), 36–47. https://doi.org/10.1016/j.tecto.2009.08.042

Kelemen, P. B., & Dick, H. J. B. (1995). Focused melt flow and localized deformation in the upper mantle: juxtaposition of replacive dunite and ductile shear zones in the Josephine peridotite, SW Oregon. *Journal of Geophysical Research*, *100*(B1), 423–438. https://doi.org/10.1029/94JB02063

Kim, Y. S., Peacock, D. C. P., & Sanderson, D. J. (2003). Mesoscale strike-slip faults and damage zones at Marsalforn, Gozo Island, Malta. *Journal of Structural Geology*, *25*(5), 793-812. https://doi.org/10.1016/S0191-8141(02)00200-6

Kim, Y. S., Peacock, D. C. P., & Sanderson, D. J. (2004). Fault damage zones. *Journal of Structural Geology*, *26*(3), 503–517. https://doi.org/10.1016/j.jsg.2003.08.002

King Hubbert, M. (1937). Theory of scale models as applied to the study of geologic structures. *Bulletin of the Geological Society of America*, *48*(10), 1459–1520. https://doi.org/10.1130/GSAB-48-1459

Kirkpatrick, J. D., & Brodsky, E. E. (2014a). Slickenline orientations as a record of fault rock rheology. *Earth and Planetary Science Letters*, *408*, 24–34. https://doi.org/10.1016/j.epsl.2014.09.040

Kirkpatrick, J. D., & Brodsky, E. E. (2014b). Slickenline orientations as a record of fault rock rheology. *Earth and Planetary Science Letters*, *408*, 24–34. https://doi.org/10.1016/j.epsl.2014.09.040

Kohlstedt, D. L. (2007). Properties of Rocks and Minerals - Constitutive Equations, Rheological Behavior, and Viscosity of Rocks. *Treatise on Geophysics*, *2*, 389–417. https://doi.org/10.1016/B978-044452748-6.00043-2

Kohlstedt, David L., & Holtzman, B. K. (2009). Shearing melt out of the earth: An experimentalist's perspective on the influence of deformation on melt extraction. *Annual Review of Earth and Planetary Sciences*, *37*, 561–593. https://doi.org/10.1146/annurev.earth.031208.100104

Koyi, H. (1997). Analogue modelling: From a qualitative to a quantitative technique - A historical outline. *Journal of Petroleum Geology*, *20*(2), 223–238. https://doi.org/10.1111/j.1747-5457.1997.tb00774.x

Kranzz, R. L., Frankel, A. D., Engelder, T., & Scholz, C. H. (1979). The permeability of whole and jointed Barre Granite. *International Journal of Rock Mechanics and Mining Sciences And*, *16*(4), 225–234. https://doi.org/10.1016/0148-9062(79)91197-5

Küntz, M., Lavallée, P., & Mareschal, J. C. (1998). Steady-state flow experiments to visualise the stress field and potential crack trajectories in 2D elastic-brittle cracked media in uniaxial compression. *International Journal of Fracture*, *92*(4), 349–357. https://doi.org/10.1023/A:1007537222483

Lade, P. V. (2006). Assessment of test data for selection of 3-D failure criterion for sand. *International Journal for Numerical and Analytical Methods in Geomechanics*, *30*(4), 307–333. https://doi.org/10.1002/nag.471

Lay, T., Kanamori, H., & Ruff, L. (1982). The asperity model and the nature of large subduction zone earthquakes. *Earthquake Prediction Research*, *1*, 3–71. Retrieved from https://www.researchgate.net/publication/247782044

Lee, A. L., Torvela, T., Lloyd, G. E., & Walker, A. M. (2018). Melt organisation and strain partitioning in the lower crust. *Journal of Structural Geology*. https://doi.org/10.1016/j.jsg.2018.05.016

Lee, J. J., & Bruhn, R. L. (1996). Structural anisotropy of normal fault surfaces. *Journal of Structural Geology*, *18*(8), 1043–1058.

https://doi.org/10.1016/0191-8141(96)00022-3

Lee, S. K., Han, R., Kim, E. J., Jeong, G. Y., Khim, H., & Hirose, T. (2017). Quasi-equilibrium melting of quartzite upon extreme friction. *Nature Geoscience*, *10*(6), 436–441. https://doi.org/10.1038/ngeo2951

Lee, Y. H., Carr, J. R., Barr, D. J., & Haas, C. J. (1990). The fractal dimension as a measure of the roughness of rock discontinuity profiles. *International Journal of Rock Mechanics and Mining Sciences And*, *27*(6), 453–464. https://doi.org/10.1016/0148-9062(90)90998-H

Lin, S., & Williams, P. F. (1992). The origin of ridge-in-groove slickenside striae and associated steps in an S-C mylonite. *Journal of Structural Geology*, *14*(3), 315–321. https://doi.org/10.1016/0191-8141(92)90089-F

Lockner, D. A., & Madden, T. R. (1991). A multiple-crack model of brittle fracture: 1. Non-time-dependent simulations. *Journal of Geophysical Research: Solid Earth*, *96*(B12), 19623-19642. https://doi.org/10.1029/91JB01642

Mai, P. M., & Beroza, G. C. (2002). A spatial random field model to characterize complexity in earthquake slip. *Journal of Geophysical Research: Solid Earth*, *107*(B11), ESE 10-1-ESE 10-21. https://doi.org/10.1029/2001jb000588

Mancktelow, N. S., & Pennacchioni, G. (2005). The control of precursor brittle fracture and fluid-rock interaction on the development of single and paired ductile shear zones. *Journal of Structural Geology*, *27*(4), 645–661. https://doi.org/10.1016/j.jsg.2004.12.001

Mancktelow, N. S., Arbaret, L., & Pennacchioni, G. (2002). Experimental observations on the effect of interface slip on rotation and stabilisation of rigid particles in simple shear and a comparisons with natural mylonites. *Journal of Structural Geology*, *24*(3), 567–585. https://doi.org/10.1016/S0191-8141(01)00084-0

Mandal, A., & Ray, A. (2009). Petrology of Mafic-Ultramafic Rocks Along North Puruliya Shear Zone, West Bengal. *Journal of the Geological Society of India*, *74*(1), 108–118. https://doi.org/10.1007/s12594-009-0161-2

Mandelbrot, B. B., Passoja, D. E., & Paullay, A. J. (1984). Fractal character of fracture surfaces of metals. *Nature*, *308*(5961), 721–722. https://doi.org/https://doi.org/10.1038/308721a0

Manighetti, I., Campillo, M., Sammis, C., Mai, P. M., & King, G. (2005, May 4). Evidence for self-similar, triangular slip distributions on earthquakes:

Implications for earthquake and fault mechanics. *Journal of Geophysical Research: Solid Earth*. Blackwell Publishing Ltd. https://doi.org/10.1029/2004JB003174

Mansour, J., Giordani, J., Moresi, L., Beucher, R., Kaluza, O., Velic, M., et al. (2020). Underworld2: Python geodynamics modelling for desktop, HPC and cloud. *Journal of Open Source Software*, *5*(47). https://doi.org/10.1130/G39943.1

Marone, C., & Cox, S. J. D. (1994). Scaling of rock friction constitutive parameters: The effects of surface roughness and cumulative offset on friction of gabbro. *Pure and Applied Geophysics* , *143*(3), 359–385. https://doi.org/https://doi.org/10.1007/BF00874335

Marsan, D. (2006). Can coseismic stress variability suppress seismicity shadows? Insights from a rate-and-state friction model. *Journal of Geophysical Research: Solid Earth*, *111*(6). https://doi.org/10.1029/2005JB004060

Mattauer, M. (1980). Les déformations des matériaux de l" écorce terrestre. Retrieved from https://infoscience.epfl.ch/record/27138

Mauldon, M., Dunne, W. M., & Rohrbaugh, M. B. (2001). Circular scanlines and circular windows: New tools for characterizing the geometry of fracture traces. *Journal of Structural Geology*, *23*(2–3), 247–258. https://doi.org/10.1016/S0191-8141(00)00094-8

Mckenzie, D. (1984). The generation and compaction of partially molten rock. *Journal of Petrology*, *25*(3), 713–765. https://doi.org/10.1093/petrology/25.3.713

Means, W. D. (1987). A newly recognized type of slickenside striation. *Journal of Structural Geology*, *9*(5–6), 585–590. https://doi.org/10.1016/0191-8141(87)90143-X

Meyer, S. E., Kaus, B. J. P., & Passchier, C. (2017). Development of branching brittle and ductile shear zones: A numerical study. *Geochemistry, Geophysics, Geosystems*, *18*, 2054–2075. https://doi.org/10.1002/2016GC006793.Received

Michael, A. J. (1984). Determination of stress from slip data: faults and folds. *Journal of Geophysical Research: Solid Earth*, *89*(B13), 11517–11526. https://doi.org/https://doi.org/10.1029/JB089iB13p11517

Misra, S., & Mandal, N. (2007). Localization of plastic zones in rocks around rigid inclusions: Insights from experimental and theoretical models. *Journal of Geophysical Research: Solid Earth*, *112*(9), 1–15.

https://doi.org/10.1029/2006JB004328

Misra, S., Mandal, N., & Chakraborty, C. (2009). Formation of Riedel shear fractures in granular materials: Findings from analogue shear experiments and theoretical analyses. *Tectonophysics*, *471*(3–4), 253–259. https://doi.org/10.1016/j.tecto.2009.02.017

Misra, S., Burlini, L., & Burg, J. P. (2009). Strain localization and melt segregation in deforming metapelites. *Physics of the Earth and Planetary Interiors*, *177*(3–4), 173–179. https://doi.org/10.1016/j.pepi.2009.08.011

Misra, S., Ellis, S., & Mandal, N. (2015). Journal of Geophysical Research : Solid Earth. *AGU: Journal of Geophysical Research, Solid Earth*, *120*, 5432–5452. https://doi.org/10.1002/2014JB011780.Received

Mitchell, T. M., & Faulkner, D. R. (2009). The nature and origin of off-fault damage surrounding strike-slip fault zones with a wide range of displacements: A field study from the Atacama fault system, northern Chile. *Journal of Structural Geology*, *31*(8), 802–816. https://doi.org/10.1016/j.jsg.2009.05.002

Moresi, L., Quenette, S., Lemiale, V., Mériaux, C., Appelbe, B., & Mühlhaus, H. B. (2007). Computational approaches to studying non-linear dynamics of the crust and mantle. *Physics of the Earth and Planetary Interiors*, *163*(1–4), 69–82. https://doi.org/10.1016/j.pepi.2007.06.009

Morris, A., Ferrill, D. A., Henderson, D. B., Morris, A., Ferrill, D. A., & Henderson, D. B. (1996). Slip-tendency analysis and fault reactivation. *Geology*, *24*(3), 275–278. https://doi.org/10.1130/0091-7613(1996)024<0275

Mukherjee, S., & Koyi, H. A. (2010). Higher Himalayan Shear Zone, Zanskar Indian Himalaya: Microstructural studies and extrusion mechanism by a combination of simple shear and channel flow. *International Journal of Earth Sciences*, *99*(5), 1083–1110. https://doi.org/10.1007/s00531-009-0447-z

Mukhopadhyay, D. (2001). The Archaean Nucleus of Singhbhum: The Present State of Knowledge. *Gondwana Research*, *4*(3), 307–318. https://doi.org/10.1016/S1342-937X(05)70331-2

Mukhopadhyay, D., & Deb, G. K. (1995). Structural and textural development in Singhbhum shear zone, eastern India. *Proceedings of the Indian Academy of Sciences - Earth and Planetary Sciences*, *104*(3), 385–405. https://doi.org/10.1007/BF02843404

Mukhopadhyay, M., Biswas, U., Mandal, N., & Misra, S. (2019). On the development of shear surface roughness. *Journal of Geophysical Research:*

Solid Earth, *124*(2), 1273–1293. https://doi.org/10.1029/2018JB016677

Nizolek, T. J., Pollock, T. M., & McMeeking, R. M. (2021). Kink band and shear band localization in anisotropic perfectly plastic solids. *Journal of the Mechanics and Physics of Solids*, *146*(July 2019), 104183. https://doi.org/10.1016/j.jmps.2020.104183

Ohnaka, M. (2013). *The physics of rock failure and earthquakes*. *The Physics of Rock Failure and Earthquakes* (Vol. 9781107030060). Cambridge University Press. https://doi.org/10.1017/CBO9781139342865

Ohnaka, M., & Shen, L. (1999). Scaling of the shear rupture process from nucleation to dynamic propagation: Implications of geometric irregularity of the rupturing surfaces. *Journal of Geophysical Research: Solid Earth*, *104*(B1), 817–844. https://doi.org/10.1029/1998jb900007

Okubo, P. G., & Dieterich, J. H. (1984). Effects of physical fault properties on frictional instabilities produced on simulated faults. *Journal of Geophysical Research*, *89*(B7), 5817–5827. https://doi.org/10.1029/JB089iB07p05817

Osher, S., & Sethian, J. A. (1988). Fronts propagating with curvature-dependent speed: Algorithms based on Hamilton-Jacobi formulations. *Journal of Computational Physics*, *79*(1), 12–49. Retrieved from https://ntrs.nasa.gov/archive/nasa/casi.ntrs.nasa.gov/19880001113.pdf

Parnell-Turner, R., Escartín, J., Olive, J. A., Smith, D. K., & Petersen, S. (2018). Genesis of corrugated fault surfaces by strain localization recorded at oceanic detachments. *Earth and Planetary Science Letters*, *498*, 116–128. https://doi.org/10.1016/j.epsl.2018.06.034

Paterson, M. S., & Wong, T. F. (2005). *Experimental rock deformation: the brittle field* (Vol. 348). Berlin: Springer.

Paterson, M. S. (1958). EXPERIMENTAL DEFORMATION AND FAULTING IN WOMBEYAN MARBLE. *BULLETIN OF THE GEOLOGICAL SOCIETY OF AMERICA VOL.*, *69*(April).

Pennacchioni, G., & Mancktelow, N. S. (2007). Nucleation and initial growth of a shear zone network within compositionally and structurally heterogeneous granitoids under amphibolite facies conditions. *Journal of Structural Geology*, *29*(11), 1757–1780. https://doi.org/10.1016/j.jsg.2007.06.002

Petit, J., Proust, F., Société, P. T.-B. de la, & 1983, undefined. (n.d.). Critères de sens de mouvement sur les miroirs de failles en roches non calcaires. *Pubs.Geoscienceworld.Org*. Retrieved from

https://pubs.geoscienceworld.org/sgf/bsgf/article-abstract/S7-XXV/4/589/111198

Petit, J. P. (1987). Criteria for the sense of movement on fault surfaces in brittle rocks. *Journal of Structural Geology*, *9*(5–6), 597–608. https://doi.org/10.1016/0191-8141(87)90145-3

Peyrat, S., & Olsen, K. B. (2004). Nonlinear dynamic rupture inversion of the 2000 Western Tottori, Japan, earthquake. *Geophysical Research Letters*, *31*(5). https://doi.org/10.1029/2003gl019058

Piazolo, S., Daczko, N. R., Silva, D., & Raimondo, T. (2020). Melt-present shear zones enable intracontinental orogenesis. *Geology*. https://doi.org/10.1130/G47126.1

Pollard, D. D., & Segall, P. (1987). Theoretical displacements and stresses near fractures in rock: with applications to faults, joints, veins, dikes, and solution surfaces. In B. K. Atkinson (Ed.), *Fracture Mechanics of rocks* (pp. 277–349). Academic Press.

Popov, A. A., & Sobolev, S. V. (2008). SLIM3D: A tool for three-dimensional thermomechanical modeling of lithospheric deformation with elasto-visco-plastic rheology. *Physics of the Earth and Planetary Interiors*, *171*(1–4), 55–75. https://doi.org/10.1016/j.pepi.2008.03.007

Popov, V. L., & Filippov, A. É. (2010). Force of friction between fractal rough surface and elastomer. *Technical Physics Letters*, *36*(6), 525–527. https://doi.org/10.1134/S1063785010060118

Power, W. L., Tullis, T. E., & Weeks, J. D. (1988). Roughness and wear during brittle faulting. *Journal of Geophysical Research*, *93*(B12). https://doi.org/10.1029/jb093ib12p15268

Power, W L, & Durham, W. B. (1997). Topography of natural and artificial fractures in granitic rocks: Implications for studies of rock friction and fluid migration. *International Journal of Rock Mechanics and Mining Sciences*, *34*(6), 979–989. https://doi.org/https://doi.org/10.1016/S1365-1609(97)80007-X

Power, W L, Tullis, T. E., Brown, S. R., Boitnott, G. N., & Scholz, C. H. (1987a). ANatural Joint Surfaces, *14*(1), 29–32.

Power, W L, Tullis, T. E., Brown, S. R., Boitnott, G. N., & Scholz, C. H. (1987b). Roughness of natural fault surfaces. *Geophysical Research Letters*, *14*(1), 29–32. https://doi.org/https://doi.org/10.1029/GL014i001p00029

Power, William L, & Tullis, T. E. (1991). *Euclidean and Fractal Models for the Description of Rock Surface Roughness*. *JOURNAL OF GEOPHYSICAL RESEARCH* (Vol. 96).

Putnis, A. (2021). Fluid-Mineral Interactions: Controlling Coupled Mechanisms of Reaction, Mass Transfer and Deformation. *Journal of Petrology*, *62*(12), 1–27. https://doi.org/10.1093/petrology/egab092

Ramsay, J. G., & Huber, M. I. (1987). *The Techniques of Modern Structural Geology, Volume 2_ Folds and Fractures* (Vol. 2). London: Academic Press.

Reber, J. E., Cooke, M. L., & Dooley, T. P. (2020). What model material to use? A Review on rock analogs for structural geology and tectonics. *Earth-Science Reviews*, *202*(September 2019), 103107. https://doi.org/10.1016/j.earscirev.2020.103107

Regenauer-Lieb, K., & Yuen, D. A. (2003). Modeling shear zones in geological and planetary sciences: Solid- and fluid-thermal-mechanical approaches. *Earth-Science Reviews*, *63*(3–4), 295–349. https://doi.org/10.1016/S0012-8252(03)00038-2

Renard, F., & Candela, T. (2017). Scaling of fault roughness and implications for earthquake mechanics. In *Fault zone dynamic processes: Evolution of fault properties during seismic rupture* (pp. 197–216). https://doi.org/10.1002/9781119156895.ch10

Renard, F., Voisin, C., Marsan, D., & Schmittbuhl, J. (2006). High resolution 3D laser scanner measurements of a strike-slip fault quantify its morphological anisotropy at all scales. *Geophysical Research Letters*, *33*(4). https://doi.org/10.1029/2005GL025038

Rice, J. R. (1976). Localization of Plastic Deformation. *Theoretical and Applied Mechanics*, *1*, 207–220. https://doi.org/10.4028/www.scientific.net/ssp.3-4.347

Rice, J. R., Sammis, C. G., & Parsons, R. (2005). Off-fault secondary failure induced by a dynamic slip pulse. *Bulletin of the Seismological Society of America*, *95*(1), 109-134. https://doi.org/10.1785/0120030166

Richard, P., & Krantz, R. W. (1991). Experiments on fault reactivation in strike-slip mode. *Tectonophysics*, *188*(1–2), 117–131. https://doi.org/10.1016/0040-1951(91)90318-M

Rispoli, R. (1981). Stress fields about strike-slip faults inferred from stylolites and tension gashes. *Tectonophysics*, *75*(3-4), T29-T36.

https://doi.org/10.1016/0040-1951(81)90274-2

Robertson, B. E. C. (1955). EXPERIMENTAL STUDY OF THE STRENGTH OF ROCKS. *Bulletin of the Geological Society of America*, *66*(October), 1275–1314.

Rockwell, T. K., & Klinger, Y. (2013). Surface rupture and slip distribution of the 1940 Imperial Valley earthquake, Imperial fault, Southern California: Implications for rupture segmentation and dynamics. *Bulletin of the Seismological Society of America*, *103*(2 A), 629–640. https://doi.org/10.1785/0120120192

Rogowitz, A., White, J. C., & Grasemann, B. (2016). Strain localization in ultramylonitic marbles by simultaneous activation of dislocation motion and grain boundary sliding (Syros, Greece). *Solid Earth*, *7*(2), 355–366. https://doi.org/10.5194/se-7-355-2016

Rolland, Y., Cox, S., Boullier, A. M., Pennacchioni, G., & Mancktelow, N. (2003). Rare earth and trace element mobility in mid-crustal shear zones: Insights from the Mont Blanc Massif (Western Alps). *Earth and Planetary Science Letters*, *214*(1–2), 203–219. https://doi.org/10.1016/S0012-821X(03)00372-8

Roy, A., Roy, N., Saha, P., & Mandal, N. (2021). Factors Determining Shear-Parallel Versus Low-Angle Shear Band Localization in Shear Deformations: Laboratory Experiments and Numerical Simulations. *Journal of Geophysical Research: Solid Earth*, *126*(10), 1–23. https://doi.org/10.1029/2021JB022578

Rubin, A. M., Gillard, D., & Got, J.-L. (1999). Streaks of microearthquakes along creeping faults. *Nature*, *400*(6745), 635–641. https://doi.org/https://doi.org/10.1038/23196

Rudnicki, J. W., & Rice, J. R. (1975). Conditions for the localization of deformation in pressure-sensitive dilatant materials. *Journal of the Mechanics and Physics of Solids*, *23*(6), 371–394. https://doi.org/10.1016/0022-5096(75)90001-0

Rudnicki, J. W. (1980). Fracture Mechanics Aplied to the Earth's Crust. *Annual Review of Earth and Planetary Sciences*, *8*, 489.

Ruina, A. (1983). Slip instability and state variable fricion laws. *Journal of Geophysical Research*, *88*(B12), 10,310-359,370.

Rutter, E. H., & Hadizadeh, J. (1991). On the influence of porosity on the low-temperature brittle—ductile transition in siliciclastic rocks. *Journal of Structural Geology*, *13*(5), 609-614. https://doi.org/10.1016/0191-

8141(91)90047-M

Rutter, E. H., Maddock, R. H., Hall, S. H., & White, S. H. (1986). Comparative microstructures of natural and experimentally produced clay-bearing fault gouges. *Pure and Applied Geophysics PAGEOPH*, *124*(1–2), 3–30. https://doi.org/10.1007/BF00875717

Sagapuram, D., Viswanathan, K., Trumble, K. P., & Chandrasekar, S. (2018). A common mechanism for evolution of single shear bands in large-strain deformation of metals. *Philosophical Magazine*, *98*(36), 3267–3299. https://doi.org/10.1080/14786435.2018.1524586

Sagy, A., & Brodsky, E. E. (2009a). Geometric and rheological asperities in an exposed fault zone. *Journal of Geophysical Research*, *114*(B2), B02301. https://doi.org/10.1029/2008JB005701

Sagy, A., & Brodsky, E. E. (2009b). Geometric and theological asperities in an exposed fault zone. *Journal of Geophysical Research: Solid Earth*, *114*(2). https://doi.org/10.1029/2008JB005701

Sagy, A., Brodsky, E. E., & Axen, G. J. (2007a). Evolution of fault-surface roughness with slip. *Geology*, *35*(3), 283–286. https://doi.org/10.1130/G23235A.1

Sagy, A., Brodsky, E. E., & Axen, G. J. (2007b). Evolution of fault-surface roughness with slip. *Geology*, *35*(3), 283–286. https://doi.org/10.1130/G23235A.1

Sagy, A., Tesei, T., & Collettini, C. (2017). Fault-surface geometry controlled by faulting mechanisms: Experimental observations in limestone faults. *Geology*, *45*(9), 851–854. https://doi.org/10.1130/G39076.1

Saha, A. K. (1994). *Crustal evolution of Singhbhum-North Orissa, Eastern India*. Geological Society of India.

Sarkar, S. N., & Saha, A. K. (1963). On the Occurrence of Two Intersecting Pre-Cambrian Orogenic Belts in Singhbhum and Adjacent Areas, India. *Geological Magazine*, *100*(1), 69–92. https://doi.org/10.1017/S0016756800055060

Saucier, F., Humphreys, E., & Weldon, R. (1992). Stress near geometrically complex strike-slip faults: Application to the San Andreas fault at Cajon Pass, southern California. *Journal of Geophysical Research: Solid Earth*, *97*(B4), 5081-5094. https://doi.org/10.1029/91JB02644

Schmid, S. M., Paterson, M. S., & Boland, J. N. (1980). Resawck School of Earth Sciences, Australia (A ustmliu) Natiionnl. *Tectonophysics*, *65*, 245–280.

Schmittbuhl, J., Gentier, S., & Roux, S. (1993). Field Measurements of the Roughness of Fault Surfaces. *Geophysical Research Letters*, *20*(8), 639–641. https://doi.org/https://doi.org/10.1029/93GL00170

Schmittbuhl, J., Chambon, G., Hansen, A., & Bouchon, M. (2006). Are stress distributions along faults the signature of asperity squeeze? *Geophysical Research Letters*, *33*(13). https://doi.org/10.1029/2006GL025952

Scholz, Christopher H., & Choi, E. (2021). What comes first: The fault or the ductile shear zone? *Earth and Planetary Science Letters*, *577*, 117273. https://doi.org/10.1016/j.epsl.2021.117273

Scholz, C. H., Dawers, N. H., Yu, J. Z., Anders, M. H., & Cowie, P. A. (1993). Fault growth and fault scaling laws: Preliminary results. *Journal of Geophysical Research: Solid Earth*, *98*(B12), 21951-21961. https://doi.org/10.1029/93JB01008

Scholz, C. H., & Aviles, C. A. (1986). The fractal geometry of faults and faulting (pp. 147–155). https://doi.org/10.1029/gm037p0147

Sengupta, S., & Ghosh, S. K. (1997). The kinematic history of the Singhbhum shear zone. *Proceedings of the Indian Academy of Sciences-Earth and Planetary Sciences*, *106*(4), 185–196.

Shanmugavadivu, P., & Sivakumar, V. (2012). Fractal dimension based texture analysis of digital images. *Procedia Engineering*, *38*, 2981–2986. https://doi.org/10.1016/j.proeng.2012.06.348

Shipton, Z. K., & Cowie, P. A. (2003). A conceptual model for the origin of fault damage zone structures in high-porosity sandstone. *Journal of Structural Geology*, *25*(3), 333–344. https://doi.org/10.1016/S0191-8141(02)00037-8

Sibson, R H. (1977). Fault rocks and fault mechanisms. *Journal of the Geological Society*, *133*(3), 191–213. https://doi.org/https://doi.org/10.1144/gsjgs.133.3.0191

Sibson, Richard H. (1985). A note on fault reactivation. *Journal of Structural Geology*, *7*(6), 751–754. https://doi.org/10.1016/0191-8141(85)90150-6

Sibson, Richard H. (1986). Brecciation processes in fault zones: Inferences from earthquake rupturing. *Pure and Applied Geophysics PAGEOPH*, *124*(1–2), 159–175. https://doi.org/10.1007/BF00875724

Sibson, Richard H. (2003). Brittle-failure controls on maximum sustainable overpressure in different tectonic regimes. *American Association of Petroleum Geologists Bulletin*, *87*(6), 901–908. https://doi.org/10.1306/01290300181

Siman-Tov, S., Aharonov, E., Sagy, A., & Emmanuel, S. (2013). Nanograins form carbonate fault mirrors. *Geology*, *41*(6), 703–706. https://doi.org/10.1130/G34087.1

Smith, R. B. (1975). Unified theory of the onset of folding, boudinage, and mullion structure. *Bulletin of the Geological Society of America*, *86*(11), 1601–1609. https://doi.org/10.1130/0016-7606(1975)86<1601:UTOTOO>2.0.CO;2

Snell, T., De Paola, N., van Hunen, J., Nielsen, S., & Collettini, C. (2020). Modelling fluid flow in complex natural fault zones: Implications for natural and human-induced earthquake nucleation. *Earth and Planetary Science Letters*, *530*, 115869. https://doi.org/10.1016/j.epsl.2019.115869

Snyder, D. B., & Kjarsgaard, B. A. (2013). Mantle roots of major precambrian shear zones inferred from structure of the great slave lake shear zone, northwest Canada. *Lithosphere*, *5*(6), 539–546. https://doi.org/10.1130/L299.1

Spyropoulos, C., Scholz, C. H., & Shaw, B. E. (2002). Transition regimes for growing crack populations. *Physical Review E*, *65*(5), 056105. https://doi.org/10.1103/PhysRevE.65.056105

Tenthorey, E., & Cox, S. F. (2006). Cohesive strengthening of fault zones during the interseismic period : An experimental study, *111*(September), 1–14. https://doi.org/10.1029/2005JB004122

Thatcher, W., & Bonilla, M. G. (1989). Earthquake fault slip estimation from geologic, geodetic and seismologic observations: implications for earthquake mechanics and fault segmentation. United States Geological Survey Open-File Report, 89(315), 386-399.

Tran, T. P. H., Bouissou, S., Chemenda, A., Ambre, J., Vacher, P., & Michel, P. (2019). Initiation and Evolution of a Network of Deformation Bands in a Rock Analogue Material at Brittle–Ductile Transition. *Rock Mechanics and Rock Engineering*, *52*(3), 737–752. https://doi.org/10.1007/s00603-018-1641-8

Tran, T. P. H., Nguyen, S. H., & Bouissou, S. (2020). Experimental Study of the Strain Localization in a Rock Analogue Material at Brittle-Ductile Transition. *Proceedings of 2020 5th International Conference on Green Technology and Sustainable Development, GTSD 2020*, 224–231. https://doi.org/10.1109/GTSD50082.2020.9303057

Treagus, S. H., & Sokoutis, D. (1992). Laboratory modelling of strain variation across rheological boundaries. *Journal of Structural Geology*, *14*(4), 405–424. https://doi.org/10.1016/0191-8141(92)90102-3

Tsutsumi, A., & Shimamoto, T. (1997). High-velocity frictional properties of gabbr, *5*(i), 10.

Turcotte, D. L. (1997). *Fractals and chaos in geology and geophysics* (2nd ed.). Cambridge, UK: Cambridge University Press. https://doi.org/https://doi.org/10.1017/ CBO9781139174695

Tvergaard, V., Needleman, A., & Lo, K. K. (1981). Flow localization in the plane strain tensile test. *Journal of the Mechanics and Physics of Solids*, *29*(2), 115–142. https://doi.org/10.1016/0022-5096(81)90019-3

Twiss, R., & Moores, E. (1992). Structural geology. Retrieved from https://scholar.google.co.in/scholar?hl=en&as_sdt=0%2C5&q=Twiss+and+Moores%2C+1992&btnG=

Vauchez, A., Tommasi, A., & Mainprice, D. (2012). Faults (shear zones) in the Earth's mantle. *Tectonophysics*, *558–559*, 1–27. https://doi.org/10.1016/j.tecto.2012.06.006

Vermilye, J. M., & Scholz, C. H. (1998). The process zone: A microstructural view of fault growth. *Journal of Geophysical Research: Solid Earth*, *103*(B6), 12223-12237. https://doi.org/10.1029/98JB00957

Voisin, C., Campillo, M., Ionescu, I., Hassani, R., & Nguyen, Q.-L. (2002). Process and signature of initiation on a finite fault system: a spectral approach. *Geophysical Journal International*, *148*(1), 120–131. https://doi.org/https://doi.org/10.1046/j.1365-246x.2002.01571.x

Voisin, C., Renard, F., & Grasso, J. R. (2007). Long term friction: From stick-slip to stable sliding. *Geophysical Research Letters*, *34*(13), 1–5. https://doi.org/10.1029/2007GL029715

Wang, Q., & Lade, P. V. (2001). SHEAR BANDING IN TRUE TRIAXIAL TESTS AND ITS EFFECT ON FAILURE IN SAND. *Journal of Engineering Mechanics*, *127*(8), 1–17.

Wells, D. L., & Coppersmith, K. J. (1994). New empirical relationships among magnitude, rupture length, rupture width, rupture area, and surface displacement. *Bulletin of the Seismological Society of America*, *84*(4), 974–1002. https://doi.org/https://doi.org/10.1785/BSSA0840040974

Wibberley, C. A., & Shimamoto, T. (2003). Internal structure and permeability of major strike-slip fault zones: the Median Tectonic Line in Mie Prefecture, Southwest Japan. Journal of Structural Geology, 25(1), 59-78.

Willis, K., Houseman, G. A., Evans, L., Wright, T., & Hooper, A. (2019). Strain localization by shear heating and the development of lithospheric shear zones. *Tectonophysics*, *764*(December 2018), 62–76. https://doi.org/10.1016/j.tecto.2019.05.010

Wilson, J. E., Chester, J. S., & Chester, F. M. (2003). Microfracture analysis of fault growth and wear processes, Punchbowl Fault, San Andreas system, California. *Journal of Structural Geology*, *25*(11), 1855-1873. https://doi.org/10.1016/S0191-8141(03)00036-1

Wong, R. H. C., Guo, Y. S. H., Li, L. Y., Chau, K. T., Zhu, W. S., & Li, S. C. (2006). Anti-wing crack growth from surface flaw in real rock under uniaxial compression. *Fracture of Nano and Engineering Materials and Structures - Proceedings of the 16th European Conference of Fracture*, *2*, 825–826. https://doi.org/10.1007/1-4020-4972-2_408

Yuen, D. A., Fleitout, L., Schubert, G., & Froidevaux, C. (1978). Shear deformation zones along major transform faults and subducting slabs. *Geophysical Journal of the Royal Astronomical Society*, *54*(1), 93–119. https://doi.org/10.1111/j.1365-246X.1978.tb06758.x

Yuen, David A., & Schubert, G. (1977). ASTHENOSPHERIC SHEAR FLOW: THERMALLY STABLE OR UNSTABLE? *Geophysical Research Letters*, *4*(11).

Zeng, Y., & Anderson, J. (2000). Evaluation of Numerical Procedures for Simulating Near-Fault Long-Period Ground Motions Using Silva Method, (July).

Zhang, P., Slemmons, D. B., & Mao, F. (1991). Geometric pattern, rupture termination and fault segmentation of the Dixie Valley—Pleasant Valley active normal fault system, Nevada, USA. *Journal of Structural Geology*, *13*(2), 165-176. https://doi.org/10.1016/0191-8141(91)90064-P

Zielinski, P. G., & Ast, D. G. (1983). Slip bands in metallic glasses. *Philosophical Magazine A: Physics of Condensed Matter, Structure, Defects and Mechanical Properties*, *48*(5), 811–824. https://doi.org/10.1080/01418618308236546

Zimmerman, M. E., Zhang, S., Kohlstedt, D. L., & Karato, S. I. (1999). Melt distribution in mantle rocks deformed in shear. *Geophysical Research Letters*,

26(10), 1505–1508. https://doi.org/10.1029/1999GL900259

Zimmerman, R. W., & Bodvarsson, G. S. (1996). Hydraulic conductivity of rock fractures. *Transport in Porous Media*, *23*(1), 1–30. https://doi.org/https://doi.org/10.1007/BF00145263